

Dissertation  
submitted to the  
Combined Faculty of Natural Sciences and Mathematics  
of Heidelberg University, Germany  
for the degree of  
Doctor of Natural Sciences

Put forward by  
Keerthan Subramanian  
Born in: Bangalore, India  
Oral Examination: 09.02.2024



# Correlations in two-dimensional few-fermion systems

Referees: Prof. Dr. Selim Jochim  
Prof. Dr. Markus Oberthaler



---

## Summary

This thesis presents experiments with few-fermion systems in quasi-2D. Starting with spin-balanced systems, the emergence of a few-body precursor of a phase transition is presented. The microscopic origins of the precursor, namely Pauli blocking and Cooper pair formation at the Fermi surface, are observed using single particle microscopy of in situ momenta. Using matterwave techniques, a microscopy scheme to measure in situ positions of particles in a regime where the system size is smaller than the effective imaging resolution is presented. This matterwave microscope is characterized and its performance is demonstrated by measuring correlations across the BEC-BCS crossover in a few-body spin-balanced system. Spin-imbalanced few-fermion systems are then studied. The preparation of such systems in the motional ground state using interaction mediated spin-motion coupling is demonstrated. A simple model system consisting of a single impurity immersed in a few-body Fermi sea is studied and correlations of in situ positions beyond second order are used to infer a few-body precursor of the polaron-molecule transition. The effect of fermion number on the molecular state and the stability of the metastable excited state are studied. The effect of mismatched Fermi surfaces at finite impurity concentrations on the center-of-mass (COM) momentum of pairs are then explored by accessing correlations.

## Zusammenfassung

In dieser Arbeit werden Experimente mit Wenig-Fermionen Systemen in quasi-2D vorgestellt. Ausgehend von spin-ausgeglichenen Systemen wird das Auftreten eines Wenig-Teilchen Vorläufers eines Phasenübergangs vorgestellt. Die mikroskopischen Ursprünge des Vorläufers, nämlich Pauli-Blockierung und Cooper-Paar-Bildung an der Fermi-Oberfläche, werden mit Hilfe der Einzelteilchenmikroskopie im Impulsraum beobachtet. Unter Verwendung von Materiewellen-Techniken wird ein Mikroskopieschema zur Messung im Ortsraum von Teilchen in einem Bereich vorgestellt, in dem die Systemgröße kleiner ist als die effektive Bildauflösung. Dieses Materiewellenmikroskop wird charakterisiert und seine Leistungsfähigkeit wird durch die Messung von Korrelationen über den BEC-BCS-Übergang in einem spin-ausgeglichenen System mit wenigen Teilchen demonstriert. Anschließend werden spin-unausgeglichene Systeme mit wenigen Fermionen untersucht. Die Präparation solcher Systeme im Bewegungsgrundzustand durch wechselwirkungsvermittelte Spin-Bewegungs-Kopplung wird demonstriert. Ein einfaches Modellsystem, das aus einer einzelnen Störstelle besteht, die in ein Wenig-Teilchen-Fermi-See eingetaucht ist, wird untersucht, und Korrelationen im Ortsraum jenseits der zweiten Ordnung werden verwendet, um einen Wenig-Teilchen-Vorläufer des Polaron-Molekül-Übergangs abzuleiten. Die Auswirkungen der Fermionenzahl auf den molekularen Zustand und die Stabilität des metastabilen angeregten Zustands werden untersucht. Die Auswirkung nicht angepasster Fermi-Flächen bei endlichen Störstellenkonzentrationen auf den Massenmittelpunkt (COM) von Paaren wird dann durch den Zugriff auf Korrelationen untersucht.

---



# Contents

<b>1</b>	<b>Introduction</b>	<b>1</b>
1.1	Spin-balanced few-fermion systems . . . . .	2
1.2	Matterwave microscope . . . . .	3
1.3	Spin-imbalanced few-fermion systems . . . . .	3
1.4	Outline . . . . .	5
<b>2</b>	<b>Experimental Details</b>	<b>7</b>
2.1	Introduction . . . . .	7
2.2	Level structure . . . . .	8
2.2.1	Eigenstates of the $2^2S_{1/2}$ manifold . . . . .	11
2.2.2	Eigenstates of the $2^2P_{1/2}$ manifold . . . . .	11
2.2.3	Eigenstates of the $2^2P_{3/2}$ manifold . . . . .	14
2.3	Magnetic dipole transitions . . . . .	16
2.4	Electric dipole transitions . . . . .	18
2.5	Two-photon Raman transitions . . . . .	21
2.5.1	Experimental measurements . . . . .	31
2.6	Resonant scattering interactions . . . . .	31
2.6.1	Scattering from a finite well potential . . . . .	33
2.6.2	Scattering amplitude and partial wave expansion . . . . .	38
2.6.3	Scattering cross-section . . . . .	40
2.6.4	Scattering of identical atoms . . . . .	42
2.6.5	Scattering in two-dimensions . . . . .	43
2.6.6	Feshbach Resonances . . . . .	43
2.6.7	Coupling of scattering channels . . . . .	45
2.7	Single particle imaging . . . . .	50
<b>3</b>	<b>Spin-balanced few-fermion systems</b>	<b>55</b>
3.1	Energy levels of a 2D harmonic oscillator . . . . .	56
3.2	Two particles in a harmonic trap . . . . .	58
3.3	Theoretical predictions for many-body behavior in a few-body system . . . . .	61
3.4	Precursor of a phase transition . . . . .	64
3.4.1	Preparing closed shell configurations . . . . .	64
3.4.2	Effect of interactions on shell structure . . . . .	66
3.4.3	Exciting the few-body system . . . . .	66

---

3.4.4	Excitation spectrum . . . . .	69
3.4.5	Coherent Driving . . . . .	72
3.5	Pauli Blocking . . . . .	74
3.5.1	Visualizing Pauli blocking . . . . .	76
3.5.2	"Melting" the Pauli Crystal . . . . .	78
3.6	Cooper Pairing . . . . .	80
3.6.1	Measuring in situ momenta in an interacting system . . . . .	81
3.6.2	Correlation measurements . . . . .	81
3.7	Conclusions . . . . .	85
<b>4</b>	<b>Matterwave Microscopy</b>	<b>87</b>
4.1	Introduction . . . . .	87
4.2	Concept of Matterwave Microscopy . . . . .	88
4.3	System length scales and requirements . . . . .	90
4.4	Implementation . . . . .	92
4.5	Trap parameters . . . . .	95
4.6	Characterizing the matterwave lens . . . . .	97
4.6.1	Magnification . . . . .	98
4.6.2	Anharmonicity . . . . .	98
4.6.3	Anisotropy . . . . .	101
4.6.4	Resolution . . . . .	101
4.7	Imaging pairs in a spin-balanced few-fermion system . . . . .	104
4.8	Conclusion . . . . .	109
<b>5</b>	<b>Impurity Physics</b>	<b>111</b>
5.1	Introduction . . . . .	111
5.2	Variational wavefunctions . . . . .	115
5.3	Preparing a spin-imbalanced few-fermion system in the ground state . . . . .	117
5.3.1	Preparing a spin-imbalanced system using differential magnetic moments . . . . .	117
5.3.2	RF transitions . . . . .	117
5.3.3	RF motional sideband transfer . . . . .	120
5.3.4	Landau-Zener transfer to dark motional ground state . . . . .	122
5.4	Experimental measurements . . . . .	122
5.4.1	Particle-hole excitations . . . . .	124
5.4.2	Second-order correlator . . . . .	124
5.4.3	Third-order correlator . . . . .	126
5.5	Repulsive interactions . . . . .	133
5.6	Tuning fermion number . . . . .	136
5.7	Finite impurity concentrations - Mismatched Fermi surfaces . . . . .	138
5.8	Conclusions . . . . .	141

---

<b>6 Conclusions and Outlook</b>	<b>145</b>
<b>Acknowledgements</b>	<b>149</b>
<b>References</b>	<b>152</b>

---



# List of Figures

2.1	Fine and hyperfine structure at zero magnetic field . . . . .	9
2.2	Energy of states in the $2^2S_{1/2}$ manifold . . . . .	12
2.3	Energy of states in the $2^2P_{1/2}$ manifold . . . . .	13
2.4	Energy of states in the $2^2P_{3/2}$ manifold . . . . .	15
2.5	Magnetic dipole transitions between states in the $2^2S_{1/2}$ manifold . . . . .	17
2.6	Electric Dipole transitions on the D1 line . . . . .	19
2.7	Electric Dipole transitions on the D2 line . . . . .	20
2.8	Two-photon stimulated Raman transitions . . . . .	22
2.9	Two-photon Rabi Coupling $\Omega_R = \Omega_1\Omega_2/4\Delta$ among states $ 1\rangle \dots  6\rangle$ . . . . .	25
2.10	Single photon scattering rate $\Gamma_{in}$ for states $ 1\rangle \dots  6\rangle$ . . . . .	26
2.11	Quality of two-photon transition $\beta$ between states $ 1\rangle \dots  6\rangle$ . . . . .	27
2.12	Summary of two-photon stimulated Raman transitions between states $ 1\rangle \dots  6\rangle$ . . . . .	29
2.13	Optimal two-photon detuning for strong transitions two-photon transition between $ 3\rangle -  4\rangle$ . . . . .	30
2.14	Experimental measurements of two-photon Raman transitions between states $ 3\rangle -  4\rangle$ . . . . .	32
2.15	Two particles interacting with a model potential . . . . .	34
2.16	Tuning the scattering length in a finite well potential for low collision energies . . . . .	36
2.17	Singlet and triplet scattering potentials for $^6\text{Li}_2$ dimer with the two atoms in the ground electronic state $2^2S_{1/2}$ . . . . .	44
2.18	Magnetically tuned Feshbach resonance . . . . .	47
2.19	Scattering lengths among the high-field seeking states $ 1\rangle,  2\rangle,  3\rangle$ . . . . .	48
2.20	Imaging sequence for two-state imaging . . . . .	51
2.21	Two state microscopy snapshots . . . . .	52
3.1	Eigenstates of the 2D harmonic oscillator . . . . .	57
3.2	Energy of two particles in a quasi-2D trap with $\eta = \omega_r/\omega_z = 1/7$ interacting via contact interactions . . . . .	59
3.3	Excitation spectrum of a finite few-body system consisting of $3+3$ and $6+6$ fermions in a 2D harmonic oscillator potential . . . . .	62
3.4	Preparation of closed shells of atoms in a quasi-2D harmonic trap . . . . .	65
3.5	Effect of interparticle interactions on the shell structure . . . . .	67
3.6	Experimental scheme to extract the collective excitation spectrum . . . . .	68
3.7	Excitation spectrum of a few-body system . . . . .	70

---

3.8	Comparison of the lowest monopole mode for N=6 and N=12 . . . . .	71
3.9	Coherently driving the monopole mode associated with pair excitations . . .	73
3.10	Configuration of fermions in a 2D harmonic oscillator potential with maximum likelihood . . . . .	75
3.11	Experimental observation and comparison to simulations for N=3, N=6 Pauli Crystal . . . . .	77
3.12	"Melting" the Pauli Crystal . . . . .	79
3.13	Momentum space correlations reminiscent of Cooper pairing . . . . .	82
3.14	Total number of opposite momentum pairs . . . . .	84
4.1	Concept of the Matterwave Microscope . . . . .	89
4.2	Effective imaging resolution . . . . .	91
4.3	Potentials of the first matterwave lens and the microtrap . . . . .	93
4.4	Trap frequency measurement . . . . .	96
4.5	Magnification of the Matterwave Microscope . . . . .	97
4.6	Anharmonicity and controlling matterwave aberrations . . . . .	99
4.7	Analysis of anisotropy of the matterwave microscope . . . . .	102
4.8	Resolution limit of the matterwave microscope at a magnification of 30 . . .	103
4.9	Snapshots of 6+6 particles in position and momentum space . . . . .	105
4.10	In situ position correlations . . . . .	107
4.11	Number of particles with short-range correlations . . . . .	108
5.1	Particle-hole excitations . . . . .	114
5.2	Preparation of a spin-imbalanced system . . . . .	118
5.3	Motional sidebands in a spin-polarized system . . . . .	119
5.4	Motional sideband transfer in an interacting system . . . . .	121
5.5	Motional ground state transfer with Landau-Zener sweep . . . . .	123
5.6	Effect of an impurity on majority atoms in momentum and real space for a system consisting of 1+3 atoms . . . . .	125
5.7	Second-order correlation of an impurity and a fermion for a 1+6 system . .	126
5.8	Second order correlation of an impurity and a fermion for a 1+3 system . .	128
5.9	Third-order correlator $C^{(3)}(r_1, r_2)$ for 1+6 particles . . . . .	130
5.10	Third-order correlator $C^{(3)}(r_1, r_2)$ for 1+3 particles . . . . .	132
5.11	Second-order correlator in a 1+3 mixture with repulsive interactions . . . .	133
5.12	Third-order correlator for a 1+3 system with repulsive interactions . . . . .	135
5.13	Preparation of a 1+N system . . . . .	137
5.14	Third-order correlator $C^{(3)}(r_1, r_2)$ for a single impurity and variable number of fermions . . . . .	138
5.15	Second-order correlator $C_c^{(2)}(p_{\text{COM}})$ in a 3+6 system compared to a balanced 6+6 system in momentum space . . . . .	140

---

# 1 Introduction

The description of interacting many-body systems is characterized by emergent degrees of freedom[1]. Without recourse to details of the microscopic Hamiltonian, the macroscopic properties and phases can be explained using these emergent degrees of freedom. All microscopic models which have the same symmetry lead to similar macroscopic behaviour near phase transitions and are described by the same universality class. While for an interacting system consisting of two particles an emergent description is futile, a system such as a piece of metal consisting of  $10^{24}$  particles is certainly amenable to such an approach. This begs the question, how many particles are needed before qualitative behaviours similar to many-body phases are observed?

Ultracold quantum gases have established themselves as versatile experimental platforms due to the level of control afforded by them. Along with in situ control of interactions[2] and single particle detection[3], they have been successfully used to emulate model Hamiltonians encompassing fields from condensed matter to high energy physics[4]. The high level of control present in the preparation of these systems and single particle detection capabilities are especially suited to the study of few-body interacting systems. Such systems abound in nature from atomic to nuclear length scales. What distinguishes such systems is that while they certainly are far from the many-body limit, their properties can nonetheless be explained using collective behaviour found in many-body systems[5], [6]. For example, a mesoscopic system of as little as 60  $^4\text{He}$  atoms has been found to possess rotational properties consistent with a superfluid[7].

A balanced system of two-component fermions features a rich phase diagram with a BEC-BCS crossover in the many-body limit[8]. The advent of atomic Fermi gases and the subsequent experiments[9]–[14] renewed an interest in this crossover which was predicted long ago[15], [16]. Depending on the two-body interactions, the scattering length  $a$  can be positive or negative. A positive scattering length is associated with repulsive interactions and possesses a two-body bound state. At  $T = 0$ , these molecules can Bose condense and form a superfluid. However for negative scattering lengths no two-body bound state is present and the system is characterized by attractive interactions. A Fermi sea leads to a frozen core and fermions of opposite spin interacting attractively can form a bound state at the Fermi surface[17]. It was then demonstrated by Bardeen, Cooper and Schrieffer[18] that such Cooper pairs could condense to form a superfluid at  $T = 0$ . Formation of these Cooper pairs and superfluidity is a truly many-body effect. The spin-imbalanced counterparts also possess a rich phase diagram in the many-body limit. At weak interactions in the extreme case of imbalance featuring a single impurity immersed in a Fermi sea, the impurity

is dressed by the surrounding Fermi sea and a new quasi-particle, the Fermi polaron, is formed. In the ground state, as attractive interactions are increased this polaron is expected to undergo a transition into a molecular state. Finite impurity concentrations lead to a situation with mismatched Fermi surfaces where a rich pairing phase diagram is expected. In this thesis, these systems are explored from the few-body limit. In addition to spectroscopic means, microscopy of in situ observables is used to extract correlation functions. The correlation functions are used to connect the few-body system to its many-body counterpart. A brief overview of the investigations followed by an outline is presented.

## 1.1 Spin-balanced few-fermion systems

A spin-balanced few-fermion system which consists of a minimal Fermi sea with a few occupied levels is an interesting system which is smoothly connected to the many-body limit. Do such systems possess collective modes and phase transitions reminiscent of many-body systems? Few-fermion systems have been successfully prepared at low entropies in 1-dimension(1D)[19] and many-body characteristics in the energy spectrum have been observed for very few particle numbers[20]. In higher dimensions, due to the presence of symmetries degeneracies appear which lead to non-uniform density of states. In this thesis we explore such few-fermion systems in quasi 2-dimensional(2D) harmonic traps where degeneracies lead to the formation of shells similar to that seen in atomic and nuclear systems. Experiments in the spin-balanced case are first summarized before exploring spin-imbalanced systems. Starting with the preparation of such systems, we demonstrate the formation of shells due to degeneracies in the system. By modulating interactions the few-body ground and excited states can be coupled causing a collective excitation of the system. The excitation spectrum as a function of interaction strength reveals a gap closing between the ground and excited states reminiscent of many-body gap closing at the normal-superfluid phase transition. Using the ability to tune particle number and adding an additional shell reveals a further reduction in the gap consistent with the trend towards larger particle numbers and the many-body limit. In such a mesoscopic system, the single particle gap given by the energy levels sets an additional energy scale preventing coupling to decay channels making the collective mode stable. The stability of the collective mode is demonstrated by driving coherent oscillations between the ground and excited states. This gap closing in the few-body system is a consequence of Pauli blocking and leads to the formation of Cooper pairs. Using single particle imaging techniques the effect of Pauli blocking is then explored. The anti-symmetrization of the many-body wavefunction leads to correlations which can be visualized as a Pauli crystal[21]. Using the ability to image multiple spin states, the correlations arising in interacting systems are summarized. Correlations in momentum space provide evidence supporting the formation of Cooper pairs at the Fermi surface for finite interaction strengths. Comparison to the many-body system is provided and qualitative similarities are pointed out.

## 1.2 Matterwave microscope

The ability to access single particle observables in these mesoscopic systems provides access to microscopic correlations. While Cooper pair correlations are presented in momentum space, access to in situ positions of the particles is challenging due to technical limitations. The size of the mesoscopic system is smaller than the effective imaging resolution and prevents a direct measurement of in situ positions. There have been techniques developed in other fields where such limits are overcome by expanding the system prior to imaging[22] and such expansion schemes have also been explored for quantum gases[23]. Expansion of a many-body system can be performed by a quench of interactions followed by matterwave transformations in harmonic traps. Implementation of such a matterwave expansion scheme is presented using a combination of nearly harmonic traps. The parameters of the trap compared to typical scales of the system under study is presented. The resulting matterwave microscope is characterized and used to study in situ position correlations of the spin-balanced mesoscopic system. In the many-body limit, an interacting Fermi gas features a BEC-BCS crossover with contrasting qualitative features on either side of the crossover. The BCS state is characterized by formation of zero center-of-mass(COM) momentum Cooper pairs which appear as correlations in momentum space. In the many-body limit the size of these Cooper pairs in position space are large compared to the inter-particle spacing. The BEC limit features molecules which also have zero COM momentum and appear as correlations in momentum space. However, in contrast to Cooper pairs these molecular pairs are smaller in size compared to the inter-particle spacing and feature correlations at short distances. Extending in situ single particle measurements to position space using the matterwave microscope, such complementary correlations in position space are explored. At large coupling strengths in the BEC limit of the crossover region, the two-body binding energy of the molecular pairs far exceeds the Fermi energy. In this regime correlations in position space reveal an enhancement of correlations at short distances indicating the formation of a molecular state. The number of close distance pairs is related to a universal quantity, the Tan Contact[24] and is evaluated as a function of interaction strength.

## 1.3 Spin-imbalanced few-fermion systems

The advent of atomic Fermi gases was responsible for the renewed interest in the BEC-BCS crossover. The situation was no different with spin-imbalanced systems and led to a flurry of theoretical activity with implications across many areas[25]–[30]. Theoretical predictions of the phase diagram of spin-imbalanced systems had not seen much activity since a long time[31]–[35]. Experiments on spin-imbalanced atomic Fermi gases were responsible for renewed interest in such systems[36]–[38]. These experiments studied the effect of spin-polarization on the superfluidity in the system. Since the imbalanced Fermi gas was confined in a trap, the inhomogeneous densities led to observation of a central superfluid

region, an outer polarized fluid in both experiments and an additional intermediate region with a partially polarized normal fluid in the MIT experiment[36]. Since the size of the three regions could not be explained by BCS theory, Chevy proposed a variational wave-function[39] to explain the experimental observations. The intermediate partially polarized region was modelled an impurity interacting with a Fermi sea. The impurity is then dressed by particle-hole excitations of the Fermi sea and forms a quasi-particle, the Fermi polaron. An impurity interacting with a bosonic environment consisting of phonons was studied long ago in the context of electron motion in a lattice[40], [41]. For an attractively interacting impurity in the ground state, a transition to a molecular phase was predicted with increasing interactions[42]. The spectroscopic signatures of the polaron and evidence for a transition into a molecular state were subsequently observed in 3D[43]. Further evidence in favor of the polaron was also found by measuring its quasi-particle mass[44] finding agreement with theoretical predictions[42]. This model of extreme imbalance featuring a impurity interacting with a Fermi sea and its realizations with cold atoms generated a lot of interest since it has relevance for the understanding of high- $T_c$  superconductivity[45]. Experiments were subsequently performed in the many-body limit in 2D where spectroscopic signatures of the polaron and evidence in favor of a transition were also found[46]. While the fate of the polaron-molecule transition in 2D was subject to some initial debate[47], consensus has developed from different approaches[48]–[51]. However, microscopic observations have only been restricted to lattice systems[52] and complementary observations in continuous systems are lacking.

Techniques to prepare low entropy spin-balanced few-fermion samples in quasi-2D are extended to prepare spin-imbalanced systems. The preparation of such ground state systems poses technical challenges. In interacting systems, radio frequency(RF) transitions can be used to introduce spin-motion coupling due to overlap between various many-body motional states. Exploiting this spin-motion coupling, a model system consisting of a single impurity in a minimal Fermi sea is prepared deterministically in the motional ground state. Using complementary microscopy in position and momentum space, evidence for particle-hole excitations and attractive binding is presented. Microscopic detection opens up possibilities to measure correlations functions and this is used to measure correlations of second and third order. Third order correlations among an impurity and two fermions points to the formation of an asymmetric paired state where the impurity binds to one of the fermions providing evidence for a transition to a molecular state. The parameter range where this transition happens is in line with theoretical predictions for quasi-2D trapped systems in the many-body limit[49]. The effect of this asymmetric pairing is explored as a function of fermion number yielding outcomes consistent with mean field expectations. The stability of excited metastable systems featuring a repulsively interacting impurity is also explored. The spin-imbalanced Fermi gas is connected on the one hand to this extreme case of imbalance featuring a single impurity interacting with a Fermi sea and on the other hand to a spin-balanced Fermi gas. While in the spin-balanced case an attractively interacting Fermi gas forms Cooper pairs which have zero COM momentum, the fate of these pairs are

strongly debated in the spin-imbalanced case where the Fermi surfaces of the two-species are mismatched[53], [54]. The ability to prepare finite impurity concentrations enables measurements to be performed in this regime in the few-body limit. The COM momentum distribution of the correlation function is obtained and compared with the spin-balanced case. While pairing is weaker compared to the balanced case, in certain interaction regimes the correlator peaks at finite COM momentum for the imbalanced case. Using the ability to perform microscopy in such interacting few-body systems, connections to phenomena and phases in the many-body limit are made.

## 1.4 Outline

Chapter 2 presents the basic technical details which are necessary for understanding the results presented in this thesis. An overview of internal structure of  ${}^6\text{Li}$  is provided followed by magnetic and electric dipole transitions. This is followed by a discussion of two-photon Raman transitions which are used for fast interaction switch-off enabling the measurement of in situ quantities. A discussion on resonant interactions follows which explains the choice of internal states to switch-off interactions. These combinations of internal state manipulations are then used to summarize a two-state imaging scheme used for the experiments presented in this thesis.

Chapter 3 then summarizes experiments in the spin-balanced few-body regime which sets the stage for subsequent experiments. A brief summary of single and two-particle physics in quasi-2D systems is presented, the results of which are used throughout the thesis. Using spectroscopic measurements, evidence for the emergence of a phase transition precursor is presented which is surprising given that these few-body systems are far from the many-body limit. The collective modes which are spectroscopically measured occur due to interactions and Pauli blocking. Microscopic measurements in momentum space are used to demonstrate correlations occurring in spin-polarized systems due to Pauli blocking. Microscopic measurements of interacting systems are then used to demonstrate correlations in momentum space reminiscent of Cooper pairing.

The size of the few-body system being smaller than the effective imaging resolution prevents direct imaging of in situ positions in such systems. In Chapter 4 experimental matterwave techniques are presented to magnify the many-body wavefunction of the system prior to imaging overcoming this limitation. Design considerations for the matterwave microscope are summarized and a complete characterization along with limits and regime of applicability is presented. The matterwave microscope is then used to perform in situ microscopy of the spin-balanced few-fermion system in position space and comparisons to in situ momentum measurements are presented. Correlation functions are extracted from the experimental data and indicate the formation of a pairs with short-distance correlations at large interaction strengths.

Chapter 5 lifts the equal spin-population constraint and extends experiments to the regime

of few-fermion systems with imbalanced spin populations. Since the ground states of these systems are host to a number of interesting phases in the many-body limit, their few-body analogs are studied. Preparation of such systems in the motional ground state is presented exploiting interaction induced spin-motion coupling. The extreme case of imbalance featuring a single impurity immersed in a minimal instance of a Fermi sea is explored where the ground state features a polaron-molecule transition in the many-body limit. Evidence for particle-hole excitations of the Fermi sea are followed by correlation measurements indicating the formation of a molecular state at large interaction strengths. The effect of fermion number is then studied followed by the stability of metastable excited states in such systems. The chapter concludes by changing impurity concentration thereby reaching the regime where the Fermi surfaces of the two species are mismatched. Comparisons to correlations in the spin-balanced case are provided.

Chapter 6 summarizes the conclusions from the experiments presented in the thesis. An outlook is presented with possible future directions.

## 2 Experimental Details

### 2.1 Introduction

The experiments performed in this thesis are related to the ground state properties of strongly interaction few-fermion systems. We use atomic quantum gases of fermionic  ${}^6\text{Li}$  to emulate model Hamiltonians associated with these systems[4]. In this chapter atomic properties and experimental details necessary to understand the experiments in this thesis are summarized. Internal state manipulations of  ${}^6\text{Li}$  are indispensable for interaction control, fluorescence detection and spin-resolved single particle imaging. Hence the internal structure of  ${}^6\text{Li}$  at finite magnetic fields is presented first. The internal states are elucidated in the uncoupled basis and these can be used to quickly identify optical and magnetic dipole transitions between these states. The magnetic and optical transitions are then presented in detail and the strengths of various transitions as a function of magnetic field and polarization are summarized. The optical dipole transitions are used for fluorescence imaging of single atoms and the summary helps identify which transitions are closed and which ones need repumping beam(s). Magnetic dipole transitions are used for internal state manipulations of the ground  $2^2\text{S}_{1/2}$  state to enable two-state single particle imaging so that correlations can be accessed. They are also used in Chapter 5 to prepare the system in the ground state exploiting interaction induced spin-motion coupling. These transitions are then summarized along with their strengths and polarization as a function of magnetic field. While some magnetic transitions can be made fast, to access in situ observables internal state manipulations an order of magnitude faster and at nearly all magnetic fields are needed necessitating the use of two-photon stimulated Raman transitions. These transitions within the ground state manifold and the associated qualities are then quantified, and all possible two-photon transitions summarized. The specific two-photon transition used in this thesis is then quantified in detail for various parameter possibilities. Such a detailed characterization of internal state manipulations has been summarized here since it has not been performed before.

A large part of the uniqueness of cold atomic gases is attributed to tunable interactions which enables the realization of model Hamiltonians in various regimes. These interactions arise due to resonant scattering processes which can be represented by a few universal quantities in the low-energy scattering limit. A summary of low-energy scattering in this universal limit is presented using a model potential where exact expressions for the scattering length can be obtained. The effect of changing the potential on the scattering length is then presented which is desired for tunable interactions. The scattering process is then

decomposed in terms of a partial wave expansion of waves with finite angular momentum. The total scattering amplitude and cross-section is then related to the amplitudes and cross section of these individual waves. The scattering problem of two  ${}^6\text{Li}$  atoms is different from this simplistic situation since the colliding particles have internal structure. In such a situation the interaction potential depends on the internal configuration of the atoms. The hyperfine interaction in such a situation causes coupling of various internal channels and this can lead to a resonant enhancement similar to the situation with a model potential where the potential was tuned. This leads to a Feshbach resonance in  ${}^6\text{Li}$  which can be magnetically tuned. A brief discussion of channel coupling is followed by a qualitative analysis for mixtures with large and weak interactions. The mixtures with strong interactions are used for studying model systems of interest while the weakly interacting states are used for switching-off interactions. Such an interaction switch-off gives access to the measurement of in situ properties of the system.

A large part of this thesis is concerned with extraction of correlation functions from single particle microscopy. An overview of single particle imaging and detection is presented. Since we work with two-component interacting fermions, the measurement of correlation functions require simultaneous imaging of both spin states. This requires a series of internal state manipulations using magnetic dipole and two-photon transitions. Internal state manipulations are followed by fluorescence detection using some of the optical dipole transitions presented.

In addition to experimental details presented above, standard experimental procedures like laser cooling, optical dipole trapping, tuning optical potentials are used for the experiments performed in this thesis. These details have already been summarized elsewhere[55], [56] and are not repeated.

## 2.2 Level structure

The atomic species used for the experiments presented in this thesis is  ${}^6\text{Li}$  which is a fermionic isotope. It is an alkali atom with one valance electron in the 2s shell. The electrons in the inner shell shield the nuclear charge and the central field approximation is used to obtain the level structure. The first correction to energy comes from the coupling of the intrinsic spin of the valance electron with the orbital motion. This can be obtained considering the coupling of the magnetic field caused due to the motion of the nucleus in the rest frame of the electron and the Thomas precession term which takes into account relativistic corrections[57]. The resulting correction to the Hamiltonian can be written as[58]

$$H'_{SO} = \frac{e}{2m^2c^2\hbar^2} \left( \frac{1}{r} \frac{\partial\phi}{\partial r} \right) \vec{\mathbf{L}} \cdot \vec{\mathbf{S}} \quad (2.1)$$

where  $\vec{\mathbf{L}}$  ( $\vec{\mathbf{S}}$ ) is the orbital(spinn) angular momentum,  $\vec{\mathbf{J}} = \vec{\mathbf{L}} + \vec{\mathbf{S}}$  is the total angular momentum and  $\phi$  is the electrostatic potential at point r due to the nucleus. This fine-structure

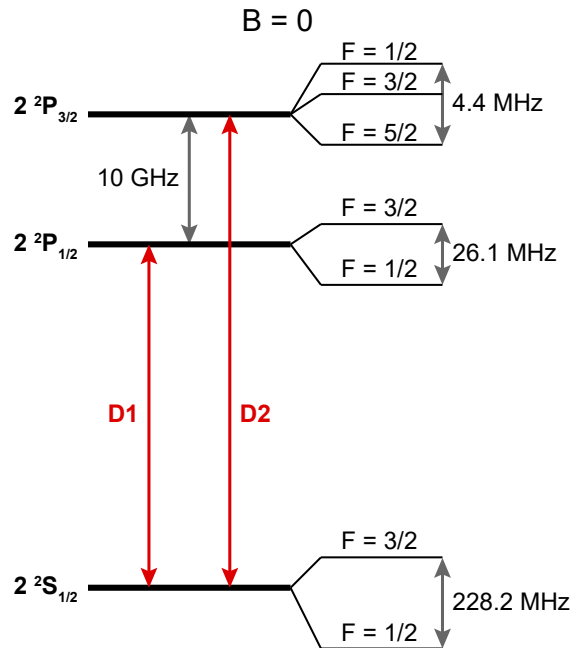


Figure 2.1: **Fine and hyperfine structure at zero magnetic field ( $B = 0$ ).** In the ground electronic state  $2s$ , there is no fine structure correction since  $L=0$ . However, the excited  $2p$  state splits into  $2^2P_{1/2}$  and  $2^2P_{3/2}$  states corresponding to  $J=1/2$  and  $J=3/2$  respectively with a splitting of approximately  $10\text{GHz}$ . The hyperfine correction leads to a coupling of the nuclear spin  $\vec{I}$  and total electron spin  $\vec{J}$  resulting in the Hamiltonian being diagonal in  $|F, m_F\rangle$  basis at  $B=0$ , where  $\vec{F} = \vec{J} + \vec{I}$ . This leads to a splitting of the  $2^2S_{1/2}$  and  $2^2P_{1/2}$  states into  $F=1/2$  and  $F=3/2$  manifolds. The  $2^2P_{3/2}$  state is split into  $F=1/2$ ,  $F=3/2$  and  $F=5/2$  manifolds. The energy splitting of the hyperfine manifolds are determined by the magnetic dipole and electric quadrupole hyperfine constants for each of the fine structure states. The splittings are only indicative and not to scale.

## 2. Experimental Details

---

correction does not affect the ground state since it has  $L=0$ . In spectroscopic notation the ground state is represented as  $2^2S_{1/2}$ . The first excited state has  $L=1$  and hence is split into  $J=3/2$  and  $J=1/2$  with a fine-structure splitting energy of 10 GHz. The optical transition from the  $2^2S_{1/2}$  to  $2^2P_{1/2}$  ( $2^2P_{3/2}$ ) is known as the D1(D2) transition.

In addition to this fine-structure correction, an additional correction to the energy occurs due to the coupling of the nuclear spin  $\vec{I}$  to  $\vec{J}$ . This leads to the hyperfine structure and the Hamiltonian for the correction is

$$H'_{HF} = -\mu \cdot \vec{B}(0) + \frac{1}{6} e \sum_{\alpha\beta} Q_{\alpha\beta} \frac{\partial^2 \phi}{\partial x_\alpha \partial y_\beta} \quad (2.2)$$

where  $\mu$  is the nuclear magnetic dipole moment,  $Q$  is the nuclear electric quadrupole moment,  $\vec{B}(0)$  is the magnetic field at the location of the nucleus. Using experimentally obtained magnetic dipole hyperfine constant  $A$  and electric quadrupole hyperfine constant  $B$  [59], the hyperfine energy corrections can be written as,

$$H'_{HF} = A \vec{J} \cdot \vec{I} + \frac{3}{2} B \frac{\vec{J} \cdot \vec{I} (\vec{J} \cdot \vec{I} + 1)}{I(2I-1)J(2J-1)} \quad (2.3)$$

This Hamiltonian is diagonal in  $|F, m_F\rangle$  basis where  $\vec{F} = \vec{J} + \vec{I}$  is total angular momentum. The hyperfine energy correction is much weaker than the fine-structure corrections by a factor of  $\alpha^2$  where  $\alpha$  is the fine-structure constant. Due to the hyperfine coupling, the ground state  $2^2S_{1/2}$  manifold splits into  $F=3/2$  and  $F=1/2$  manifolds separated by approximately 228 MHz. The excited states  $2^2P_{1/2}$  is split into  $F=3/2$  and  $F=1/2$  and  $2^2P_{3/2}$  is split into  $F=5/2$ ,  $F=3/2$ ,  $F=1/2$  states. The splittings and the states at  $B=0$  are shown in Figure 2.1.

All of the experiments in this thesis are performed at finite magnetic fields to make use of tunable interactions due to Feshbach resonances[2]. Under this circumstance the Zeeman corrections need to be added to the Hamiltonian consisting of fine and hyperfine corrections.

$$H_Z = \mu_B g_J \vec{J} \cdot \vec{B} - \mu_B g_I \vec{I} \cdot \vec{B} \quad (2.4)$$

where  $\mu_B$  is the Bohr magneton,  $g_J$  ( $g_I$ ) are the Landé g-factors for the spin-orbit coupled electron (nucleus). The energies and states of the resulting Hamiltonian  $H = H'_{SO} + H'_{HF} + H_Z$  can be obtained by solving the eigen value problem in the uncoupled basis. The energies of the states are shown in Figure 2.2 for  $2^2S_{1/2}$ , Figure 2.3 for  $2^2P_{1/2}$  and Figure 2.4 for  $2^2P_{3/2}$  states. The admixtures in the uncoupled basis and their relative strengths for various eigen states are enumerated below. These states will be especially necessary to list out all possible magnetic, optical and two-photon transitions at finite magnetic fields. At large magnetic fields, the electron and nuclear spin decouple and states split into a multiplet of different  $m_J$  levels containing different  $m_I$  projections  $-1, 0, 1$ .

### 2.2.1 Eigenstates of the $2^2S_{1/2}$ manifold

The eigen states of the  $2^2S_{1/2}$  manifold are denoted by  $|1\rangle \dots |6\rangle$  in the order of increasing energy. The states in the uncoupled basis are

$$\begin{aligned}
|1\rangle &= a_1 \left| 0, -\frac{1}{2}, 1 \right\rangle - a_2 \left| 0, \frac{1}{2}, 0 \right\rangle \\
|2\rangle &= a_3 \left| 0, -\frac{1}{2}, 0 \right\rangle - a_4 \left| 0, \frac{1}{2}, -1 \right\rangle \\
|3\rangle &= \left| 0, -\frac{1}{2}, -1 \right\rangle \\
|4\rangle &= a_4 \left| 0, -\frac{1}{2}, 0 \right\rangle + a_3 \left| 0, \frac{1}{2}, -1 \right\rangle \\
|5\rangle &= a_2 \left| 0, -\frac{1}{2}, 1 \right\rangle + a_1 \left| 0, \frac{1}{2}, 0 \right\rangle \\
|6\rangle &= \left| 0, \frac{1}{2}, 1 \right\rangle
\end{aligned} \tag{2.5}$$

The states are expanded in the  $|m_L, m_S, m_I\rangle$  basis. At large magnetic fields the co-efficients in black(red) tend to 1(0) resulting in states  $|1\rangle, |2\rangle, |3\rangle$  ( $|4\rangle, |5\rangle, |6\rangle$ ) constituting the  $m_J = -1/2$  ( $m_J = 1/2$ ) manifold with  $m_I$  projections 1,0,-1 (-1,0,1). It can also be seen immediately that the states  $|1\rangle \dots |6\rangle$  are orthogonal to each other. Expressing the states in the uncoupled  $|m_l, m_s, m_I\rangle$  basis also makes it easy to identify magnetic and electric dipole transitions between states.

### 2.2.2 Eigenstates of the $2^2P_{1/2}$ manifold

The eigen states of the  $2^2P_{1/2}$  manifold are denoted by  $|1'\rangle \dots |6'\rangle$  in the order of increasing energy as shown in Figure 2.3. The states can be expanded in the uncoupled basis

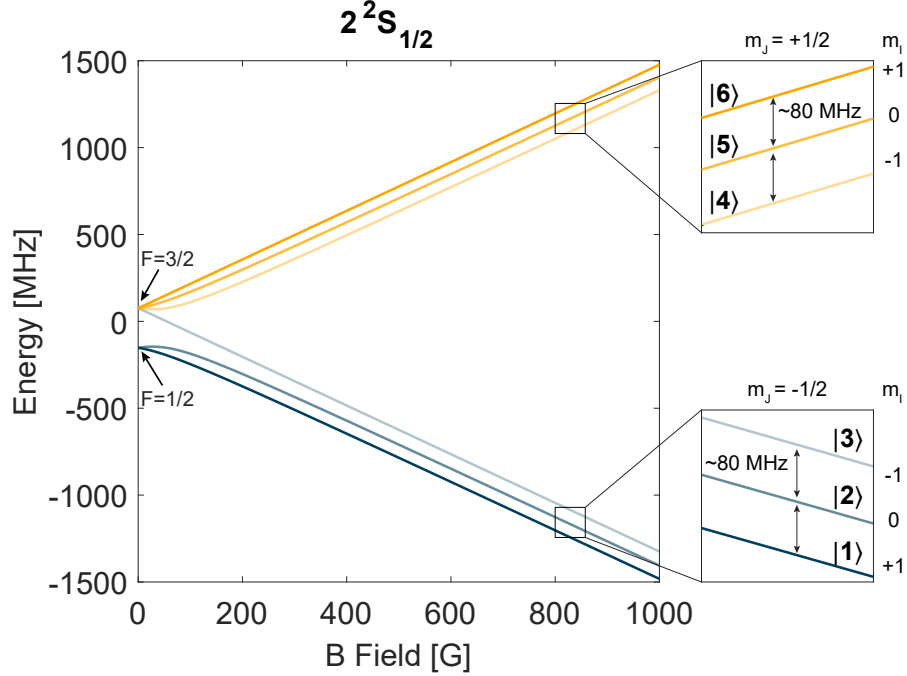


Figure 2.2: **Energy of states in the  $2^2S_{1/2}$  manifold as a function of magnetic field.**

At zero magnetic field, the Hamiltonian includes the hyperfine coupling term  $A_{hf}\vec{J}\cdot\vec{I}$  and the Hamiltonian is diagonal in  $|F, m_F\rangle$  basis where  $\vec{F} = \vec{J} + \vec{I}$ . This leads to a splitting of  $2^2S_{1/2}$  state into  $F=1/2$ (below) and  $F=3/2$ (above) manifolds with a spacing of 228.2 MHz. As the magnetic field is turned on, in addition to the hyperfine correction, the Zeeman term is added to the Hamiltonian. Due to this, the Hamiltonian is no longer diagonal in the  $|F, m_F\rangle$  basis. The  $F=1/2$  and  $F=3/2$  manifold splits into a total of six states labelled in order of increasing energy from  $|1\rangle \dots |6\rangle$ . The states  $|1\rangle \dots |6\rangle$  can be obtained as a superposition of the uncoupled basis states by solving the eigen value problem. As  $B \rightarrow \infty$ , high-field (low-field) seeking states  $|1\rangle, |2\rangle, |3\rangle$  ( $|4\rangle, |5\rangle, |6\rangle$ ) asymptotically tend to state  $|J = 1/2, m_J = -1/2\rangle$  ( $|J = 1/2, m_J = 1/2\rangle$ ) with nuclear spin projections  $m_I = 1, 0, -1$  ( $m_I = -1, 0, 1$ ). The splitting between adjacent states in the low and high-field seeking manifold is roughly 80MHz and is shown in the insets.

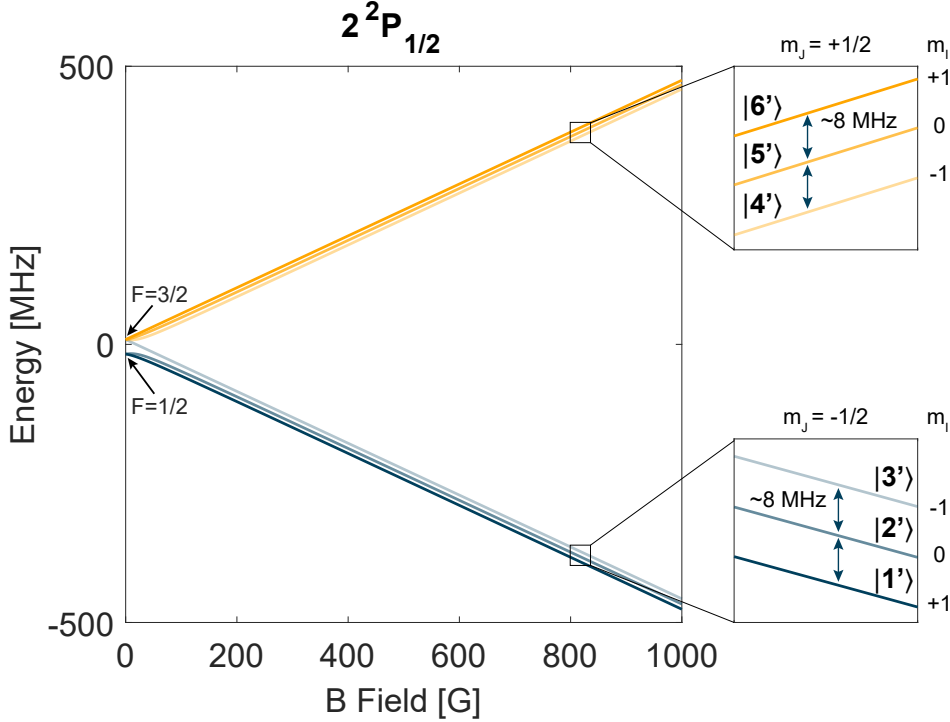


Figure 2.3: **Energy of states in the  $2^2P_{1/2}$  manifold as a function of magnetic field.** At zero magnetic field, the Hamiltonian is diagonal in  $|F, m_F\rangle$  basis where  $\vec{F} = \vec{J} + \vec{I}$ . This leads to a splitting of  $2^2P_{1/2}$  state into  $F=1/2$ (below) and  $F=3/2$ (above) manifolds with a spacing of 26.1 MHz. At non-zero magnetic fields, the Hamiltonian is no longer diagonal in the  $|F, m_F\rangle$  basis. The  $F=1/2$  and  $F=3/2$  manifold splits into a total of six states labelled in order of increasing energy from  $|1'\rangle \dots |6'\rangle$ . The states  $|1'\rangle \dots |6'\rangle$  can be obtained as a superposition of the uncoupled basis states by solving the eigen value problem. For large magnetic fields, high-field (low-field) seeking states  $|1'\rangle, |2'\rangle, |3'\rangle$  ( $|4'\rangle, |5'\rangle, |6'\rangle$ ) asymptotically tend to state  $|J = 1/2, m_J = -1/2\rangle$  ( $|J = 1/2, m_J = 1/2\rangle$ ) with nuclear spin projections  $m_I = 1, 0, -1$  ( $m_I = -1, 0, 1$ ). The splitting between adjacent states in the low and high-field seeking manifold is roughly 8MHz and is shown in the insets.

$|m_L, m_S, m_I\rangle$  as follows

$$\begin{aligned}
 |1'\rangle &= -b_1 \left| -1, \frac{1}{2}, 1 \right\rangle + b_2 \left| 0, -\frac{1}{2}, 1 \right\rangle + b_3 \left| 0, \frac{1}{2}, 0 \right\rangle - b_4 \left| 1, -\frac{1}{2}, 0 \right\rangle \\
 |2'\rangle &= b_5 \left| -1, \frac{1}{2}, 0 \right\rangle - b_6 \left| 0, -\frac{1}{2}, 0 \right\rangle - b_7 \left| 0, \frac{1}{2}, -1 \right\rangle + b_8 \left| 1, -\frac{1}{2}, -1 \right\rangle \\
 |3'\rangle &= -b_9 \left| -1, \frac{1}{2}, -1 \right\rangle + b_{10} \left| 0, -\frac{1}{2}, -1 \right\rangle \\
 |4'\rangle &= -b_8 \left| -1, \frac{1}{2}, 0 \right\rangle + b_7 \left| 0, -\frac{1}{2}, 0 \right\rangle - b_6 \left| 0, \frac{1}{2}, -1 \right\rangle + b_5 \left| 1, -\frac{1}{2}, -1 \right\rangle \\
 |5'\rangle &= b_4 \left| -1, \frac{1}{2}, 1 \right\rangle - b_3 \left| 0, -\frac{1}{2}, 1 \right\rangle + b_2 \left| 0, \frac{1}{2}, 0 \right\rangle - b_1 \left| 1, -\frac{1}{2}, 0 \right\rangle \\
 |6'\rangle &= -b_{10} \left| 0, \frac{1}{2}, 1 \right\rangle + b_9 \left| 1, -\frac{1}{2}, 1 \right\rangle
 \end{aligned} \tag{2.6}$$

At large magnetic fields the sum of squares of co-efficients in black(red) tend to 1(0) leading to states  $|1'\rangle \dots |3'\rangle$  ( $|4'\rangle \dots |6'\rangle$ ) constituting the  $m_J = -1/2$  ( $m_J = 1/2$ ) manifolds with  $m_I$  projections 1,0,-1 (-1,0,1).

### 2.2.3 Eigenstates of the $2^2P_{3/2}$ manifold

The eigenstates of the  $2^2P_{3/2}$  manifold are denoted by  $|1''\rangle \dots |12''\rangle$  in the order of increasing energy as shown in Figure 2.4. The states are expanded in the uncoupled basis  $|m_L, m_S, m_I\rangle$  basis as follows

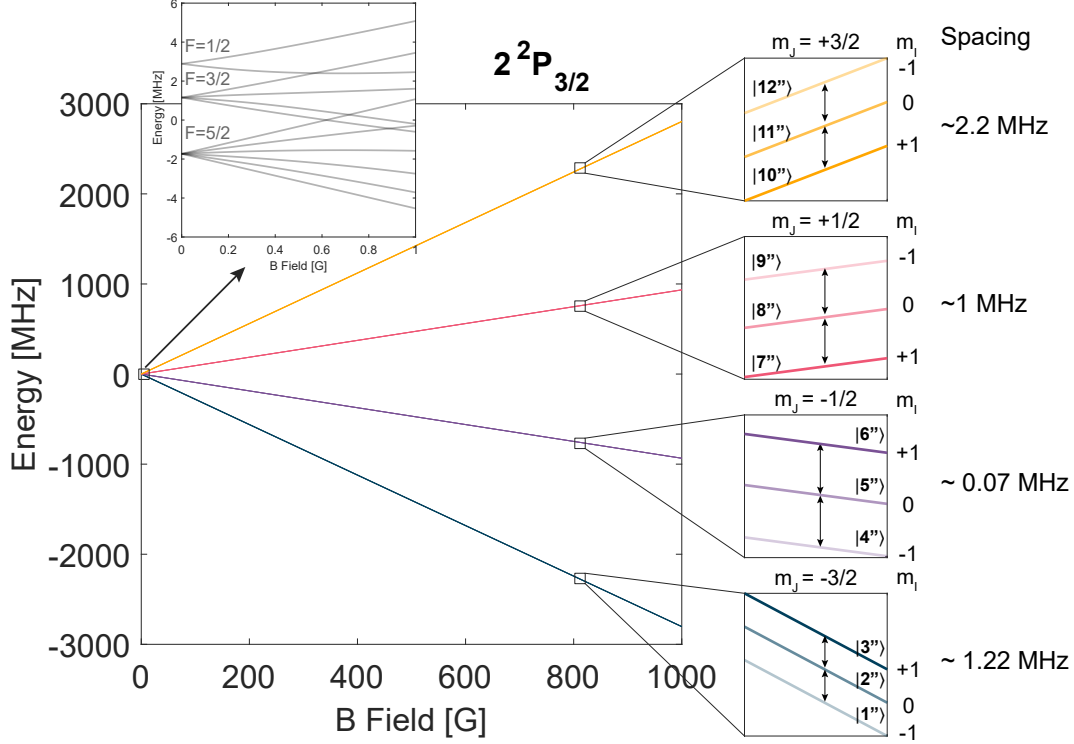


Figure 2.4: **Energy of states in the  $2^2P_{3/2}$  manifold as a function of magnetic field.** At zero magnetic field, the Hamiltonian is diagonal in  $|F, m_F\rangle$  basis where  $\vec{F} = \vec{J} + \vec{I}$ . This leads to a splitting of  $2^2P_{3/2}$  state into  $F=1/2$ ,  $F=3/2$  and  $F=5/2$  manifolds with a spacing of 1.65 MHz and 2.75 MHz (See inset at  $B=0$ ). At non-zero magnetic fields, the Hamiltonian is no longer diagonal in the  $|F, m_F\rangle$  basis. The  $F$  manifolds split into a total of twelve states labelled in order of increasing energy from  $|1''\rangle \dots |12''\rangle$ . The states  $|1''\rangle \dots |12''\rangle$  can be obtained as a superposition of the uncoupled basis states by solving the eigen value problem. For large magnetic fields, states  $|1''\rangle \dots |3''\rangle$ ,  $|4''\rangle \dots |6''\rangle$ ,  $|7''\rangle \dots |9''\rangle$  and  $|10''\rangle \dots |12''\rangle$  asymptotically tend to states  $m_J = -3/2$ ,  $m_J = -1/2$ ,  $m_J = 1/2$  and  $m_J = 3/2$  respectively with three nuclear spin projections  $-1, 0, +1$ . The splitting between each of these states at high field is shown in the insets.

$$\begin{aligned}
|1''\rangle &= \left| -1, -\frac{1}{2}, -1 \right\rangle \\
|2''\rangle &= -\square \left| -1, -\frac{1}{2}, 0 \right\rangle - \square \left| -1, \frac{1}{2}, -1 \right\rangle - \square \left| 0, -\frac{1}{2}, -1 \right\rangle \\
|3''\rangle &= -\square \left| -1, -\frac{1}{2}, 1 \right\rangle - \square \left| -1, \frac{1}{2}, 0 \right\rangle - \square \left| 0, -\frac{1}{2}, 0 \right\rangle - \square \left| 0, \frac{1}{2}, -1 \right\rangle - \square \left| 1, -\frac{1}{2}, -1 \right\rangle \\
|4''\rangle &= \square \left| -1, -\frac{1}{2}, 0 \right\rangle - \square \left| -1, \frac{1}{2}, -1 \right\rangle - \square \left| 0, -\frac{1}{2}, -1 \right\rangle \\
|5''\rangle &= \square \left| -1, -\frac{1}{2}, 1 \right\rangle - \square \left| -1, \frac{1}{2}, 0 \right\rangle - \square \left| 0, -\frac{1}{2}, 0 \right\rangle - \square \left| 0, \frac{1}{2}, -1 \right\rangle - \square \left| 1, -\frac{1}{2}, -1 \right\rangle \\
|6''\rangle &= -\square \left| -1, \frac{1}{2}, 1 \right\rangle - \square \left| 0, -\frac{1}{2}, 1 \right\rangle - \square \left| 0, \frac{1}{2}, 0 \right\rangle - \square \left| 1, -\frac{1}{2}, 0 \right\rangle - \square \left| 1, \frac{1}{2}, -1 \right\rangle \\
|7''\rangle &= \square \left| 0, \frac{1}{2}, 1 \right\rangle + \square \left| 1, -\frac{1}{2}, 1 \right\rangle + \square \left| 1, \frac{1}{2}, 0 \right\rangle \\
|8''\rangle &= -\square \left| -1, \frac{1}{2}, 1 \right\rangle - \square \left| 0, -\frac{1}{2}, 1 \right\rangle + \square \left| 0, \frac{1}{2}, 0 \right\rangle + \square \left| 1, -\frac{1}{2}, 0 \right\rangle + \square \left| 1, \frac{1}{2}, -1 \right\rangle \\
|9''\rangle &= \square \left| -1, -\frac{1}{2}, 1 \right\rangle - \square \left| -1, \frac{1}{2}, 0 \right\rangle - \square \left| 0, -\frac{1}{2}, 0 \right\rangle + \square \left| 0, \frac{1}{2}, -1 \right\rangle + \square \left| 1, -\frac{1}{2}, -1 \right\rangle \\
|10''\rangle &= \left| 1, \frac{1}{2}, 1 \right\rangle \\
|11''\rangle &= -\square \left| 0, \frac{1}{2}, 1 \right\rangle - \square \left| 1, -\frac{1}{2}, 1 \right\rangle + \square \left| 1, \frac{1}{2}, 0 \right\rangle \\
|12''\rangle &= \square \left| -1, \frac{1}{2}, 1 \right\rangle + \square \left| 0, -\frac{1}{2}, 1 \right\rangle - \square \left| 0, \frac{1}{2}, 0 \right\rangle - \square \left| 1, -\frac{1}{2}, 0 \right\rangle + \square \left| 1, \frac{1}{2}, -1 \right\rangle \quad (2.7)
\end{aligned}$$

Unlike for  $2^2S_{1/2}$  and  $2^2P_{1/2}$  the co-efficients do not repeat and are denoted as  $\square$  ( $\square$ ) if it tends to a finite value (zero) for large magnetic fields. States  $|1''\rangle \dots |3''\rangle$ ,  $|4''\rangle \dots |6''\rangle$ ,  $|7''\rangle \dots |9''\rangle$  and  $|10''\rangle \dots |12''\rangle$  are asymptotically states with  $m_J = -3/2$ ,  $m_J = -1/2$ ,  $m_J = 1/2$  and  $m_J = 3/2$  with different  $m_I$  projections respectively.

### 2.3 Magnetic dipole transitions

Transitions between states of the  $2^2S_{1/2}$  manifold  $|1\rangle \dots |6\rangle$  are very important for preparing the system, controlling interactions and imaging sequences and in this section the possible magnetic dipole transitions are elaborated. As seen in Figure 2.2, at large magnetic fields the energy differences between these states are in the MHz regime and the states can be coupled

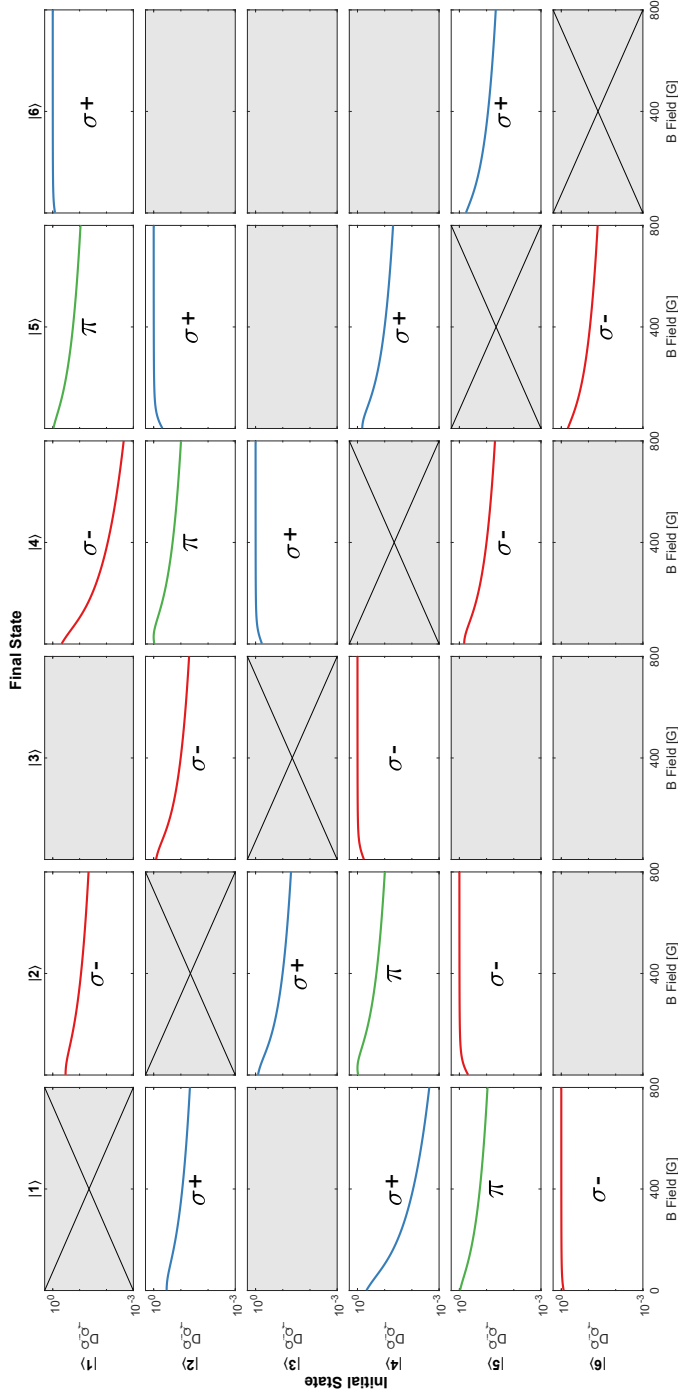


Figure 2.5: **Magnetic dipole transitions between states  $|1\rangle \dots |6\rangle$  as a function of magnetic field.** The magnetic dipole transition matrix elements  $D_Q^{Q'} = \langle Q|\mu|Q'\rangle$  in units of Bohr magneton  $\mu_B$ .  $\mu = \mu_e + \mu_n$  is the magnetic moment of the electron plus nucleus and state  $|Q'\rangle$  ( $|Q\rangle$ ) is the initial (final) state. The initial states are represented along the rows and the final states along the columns. The strongest transition matrix elements arise from coupling of states with mostly opposite electron spin but same nuclear spin. The annotations  $\sigma_\pm$  and  $\pi$  denote the kind of transitions. Since the nuclear magneton is 4 orders of magnitude smaller than the Bohr magneton, transitions among the high(low) field seekers occurs mainly due to the small admixtures of opposite electron spins. For the experiments described in this thesis, we mainly utilize transitions between states  $|1\rangle - |2\rangle$ ,  $|2\rangle - |3\rangle$  and  $|3\rangle - |4\rangle$ .

by magnetic dipole transitions in the radio frequency(RF) and microwave(MW) regimes. In addition to magnetic dipole transitions, two-photon optical dipole transitions are also possible between these states and are presented in Section 2.5. The coupling between states due to an oscillating magnetic field in the rotating wave approximation is[60]

$$H_{ij} = \langle Q | -\mu \cdot \vec{\mathbf{B}} | Q' \rangle \quad (2.8)$$

where  $\mu = \mu_e + \mu_n$  is the total magnetic moment and  $\vec{\mathbf{B}}$  is the amplitude of the magnetic field. This coupling operator can be re-written in terms of raising,lowering and z-projection operators as follows

$$\hat{\mathbf{H}} = \mu_B g_e \left( \frac{1}{2}(S_+ B_- + S_- B_+) + S_z B_z \right) + \mu_B g_I \left( \frac{1}{2}(I_+ B_- + I_- B_+) + I_z B_z \right) \quad (2.9)$$

where  $S_{\pm} = S_x \pm iS_y$  ( $I_{\pm} = I_x \pm iI_y$ ) are the raising/lowering operators for the electron (nuclear) spin;  $B_{\pm} = B_x \pm iB_y$  is the magnetic field amplitude in terms of the components x and y;  $S_z$  ( $I_z$ ) is the electron (nuclear) spin projections along the z axis;  $B_z$  is the magnetic field component along the quantization axis.

The  $S_{\pm}$  ( $I_{\pm}$ ) term couples an initial and final state whose electron (nuclear) spin projections are different by  $\mp 1$  and  $S_z$  ( $I_z$ ) term couples states with the same electron (nuclear) spin projections. These transitions are denoted  $\sigma_{\pm}$  and  $\pi$  respectively. It is important to note that  $g_I$  is four orders of magnitude smaller than  $g_e$  and hence nuclear spin states couple only very weakly. Thus the largest matrix elements are the ones where electronic spin states are coupled namely states  $|1\rangle - |6\rangle$ ,  $|2\rangle - |5\rangle$  and  $|3\rangle - |4\rangle$  through a  $\sigma_{\pm}$  transition. The states  $|1\rangle \dots |6\rangle$  have already been diagonalized in the uncoupled basis in Section 2.2 and matrix elements can be directly evaluated as a function of the magnetic field. The magnetic dipole matrix elements corresponding to  $\sigma_{\pm}$  transition  $\frac{1}{2}(\langle Q | g_e S_{\pm} + g_I I_{\pm} | Q' \rangle)$  and  $\pi$  transition  $\langle Q | (g_e S_z + g_I I_z) | Q' \rangle$  as a function of the magnetic field are plotted in Figure 2.5 for different initial and final states as a function of magnetic field. In the experiments we utilize mainly transitions between states  $|1\rangle - |2\rangle$ ,  $|2\rangle - |3\rangle$  for preparation, internal state manipulations to enable imaging and  $|3\rangle - |4\rangle$  for two-state single particle imaging sequence elaborated later in Section 2.7.

## 2.4 Electric dipole transitions

The  $2^2S_{1/2} - 2^2P_{1/2}$  and  $2^2S_{1/2} - 2^2P_{3/2}$  states can be coupled by optical dipole transitions and are denoted as the D1 and D2 lines. The optical dipole transition matrix element for polarization q between uncoupled states having quantum numbers  $|L, m_L; S, m_S; I, m_I\rangle$  (final state) and  $|L', m'_L; S', m'_S; I', m'_I\rangle$  (initial state) is

$$D_q = \langle L, m_L; S, m_S; I, m_I | e r_q | L', m'_L; S', m'_S; I', m'_I \rangle \quad (2.10)$$

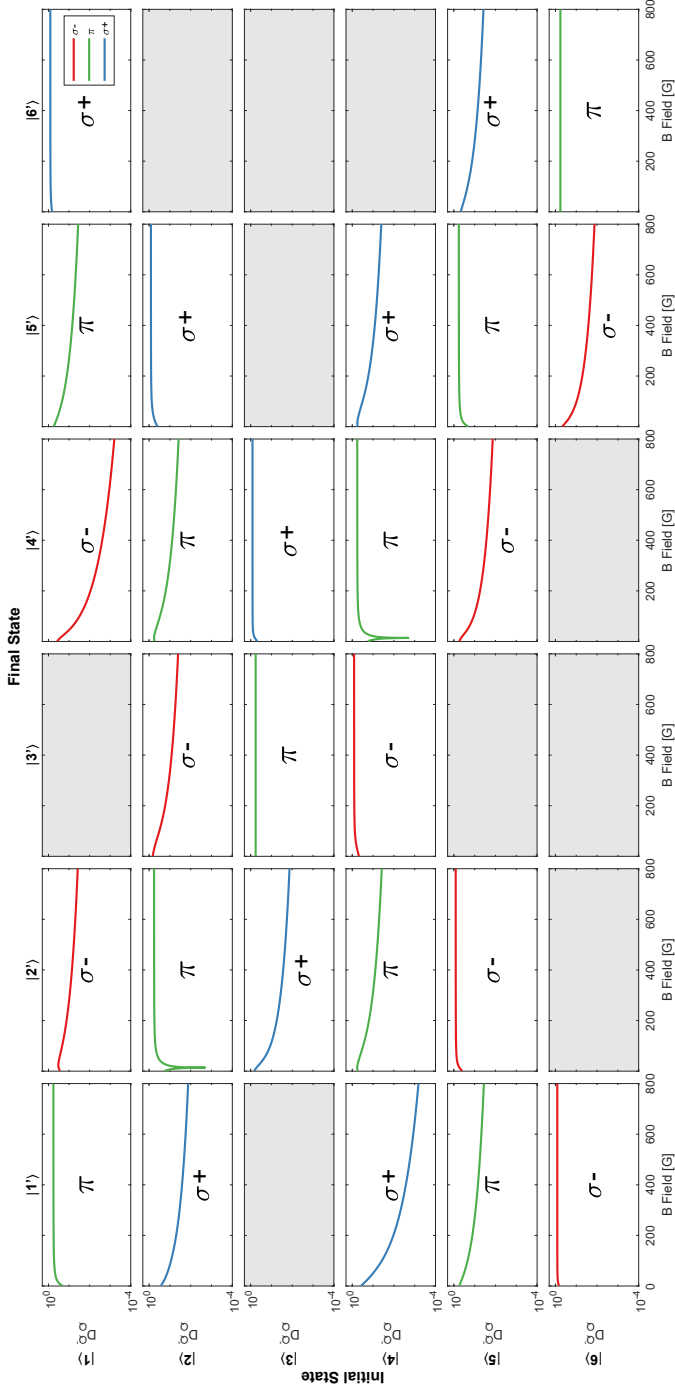


Figure 2.6: **Electric Dipole transitions on the D1 line.** The electric dipole transition matrix element  $D_Q^{Q'} = \langle Q|p|Q'\rangle$  in units of the reduced matrix element ( $L=1|p|L'=0$ ) as a function of magnetic field. Here  $Q'$  ( $Q$ ) are the initial(final) states and  $p$  the electric dipole operator. Annotations  $\sigma_{\pm}$  and  $\pi$  denote the kind of transition. The initial (final) states  $|Q'\rangle$  ( $|Q\rangle$ ) are depicted along rows (columns). For experiments carried out in this thesis, imaging is mainly done on the D2 line, however these matrix elements are used in the next sections to obtain two-photon transition matrix elements. Two-photon transitions are later used for flipping states and turning-off interactions faster than with magnetic dipole transitions.

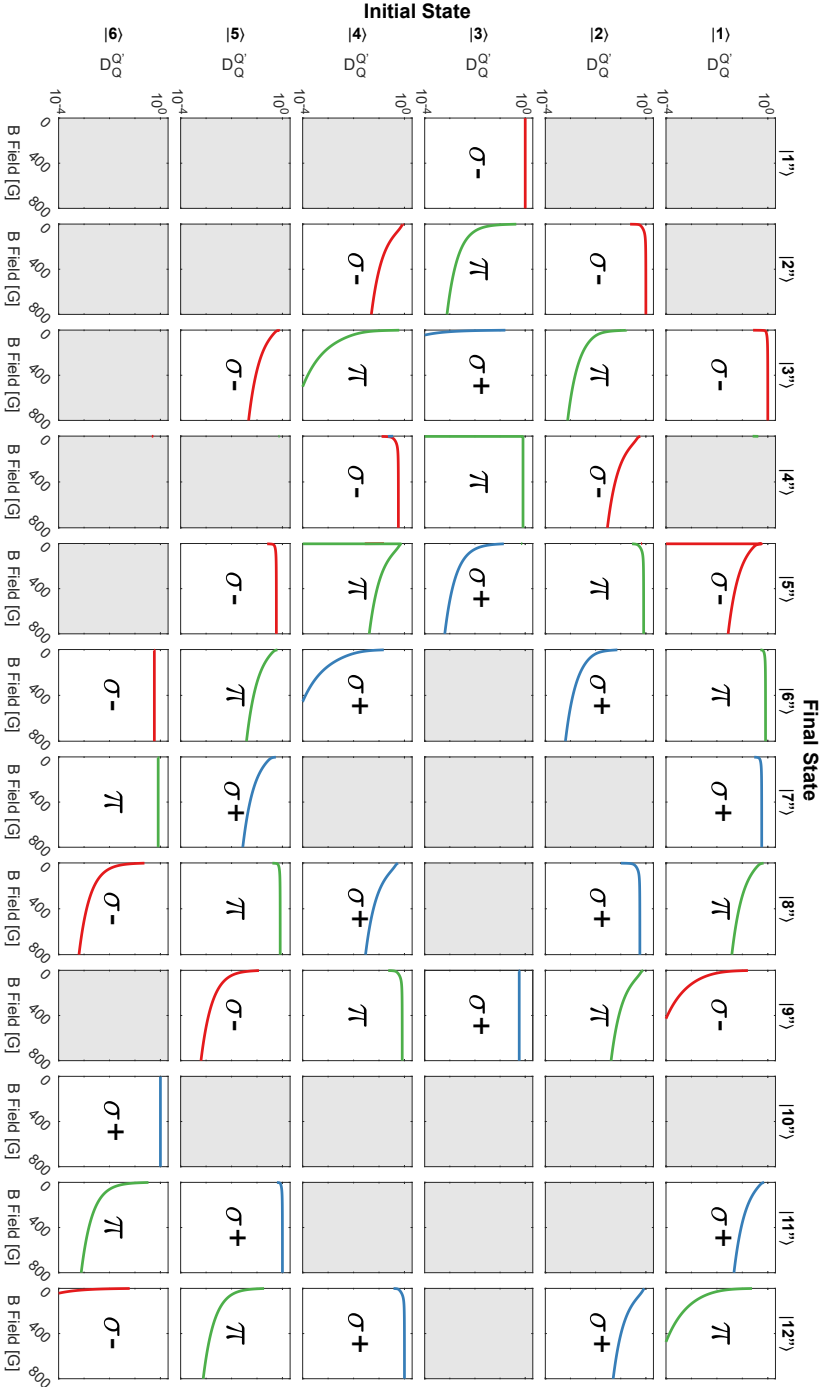


Figure 2.7: **Electric Dipole transitions on the D2 line.** The electric dipole transition matrix element  $D_Q^{Q'} = \langle Q|p|Q'\rangle$  in units of the reduced matrix element  $\langle L=1|p|L'=0\rangle$  as a function of magnetic field. Here  $Q'$  ( $Q$ ) are the initial(final) states and  $p$  the electric dipole operator.  $\sigma\pm$  and  $\pi$  denote the kind of transition. The initial (final) states  $|Q'\rangle$  ( $|Q\rangle$ ) are depicted along rows (columns). At large magnetic fields, the  $m_j$  excited state multiplets cannot be optically distinguished since the linewidth is larger than their spacing. From the table it is also clear that there are only two states with closed transitions, namely states  $|3\rangle$  and  $|6\rangle$  with  $\sigma-$  and  $\sigma+$  transitions respectively. This constrains multi-state imaging to determine correlations in few-body systems studied later.

Representing the position operator  $r_q$  as an irreducible tensor and using the Wigner-Eckart theorem[61], the matrix element can be simplified as

$$D_q = \delta_{m_S m'_S} \delta_{m_I m'_I} W_{m'_L q m_L}^{L'L} \langle L || er || L' \rangle \quad (2.11)$$

where  $\langle L || er || L' \rangle$  is the reduced matrix element independent of z-spin projections  $m_L, m_S, m_I$ . The co-efficient  $W_{m'_L q m_L}^{L'L}$  can be written in terms of the Wigner-3j symbol as follows

$$W_{m'_L q m_L}^{L'L} = (-1)^{L'-1+m_L} \sqrt{2L+1} \begin{pmatrix} L' & 1 & L \\ m'_L & q & -m_L \end{pmatrix} \quad (2.12)$$

The Wigner-3j symbol ensures that polarization  $q$  couples only states with  $q = m_L - m'_L$ . In the previous sections, we have already represented the states in terms of the uncoupled basis as follows,

$$|LQ\rangle = \sum_{m_L m_S m_I} C_{m_L m_S m_I}^Q |L, m_L; S, m_S; I, m_I\rangle \quad (2.13)$$

An additional label  $L$  is used to identify if the state belongs to the S or P state. Using this expansion, the transition matrix between initial state  $|L'Q'\rangle$  and final state  $|LQ\rangle$  is obtained from the sum[62]

$$D_{q, LQ}^{L'Q'} = \sum_{m_L m'_L m_S m_I} C_{m_L m_S m_I}^Q C_{m'_L m_S m_I}^{Q'} W_{m'_L q m_L}^{L'L} \langle L || er || L' \rangle \quad (2.14)$$

Using these expressions, the optical dipole transition matrix elements are obtained for transitions on the D1 and D2 lines and are shown in Figure 2.6 and 2.7 respectively. The D1 line does not support closed transitions at any field while the D2 line supports 2 closed transitions from the stretched initial states. For experiments presented in this thesis, optical transitions on the D2 line are used for laser cooling at zero magnetic field and transitions from state  $|3\rangle - |1\rangle$  on the D2 line are used for single particle imaging as detailed in the later sections. In addition two-photon Raman transitions are used for internal state manipulations and the optical dipole transition matrix elements calculated here are used to determine two-photon coupling in Section 2.5.

## 2.5 Two-photon Raman transitions

In the previous section, electric dipole transitions coupling two states were introduced. These transitions are mainly used for cooling and imaging. In addition transitions to manipulate internal states such as states in the  $2^2S_{1/2}$  manifold  $|1\rangle \dots |6\rangle$  are needed. This was previously addressed using magnetic dipole transitions in Section 2.3. However for certain internal state manipulations involving interaction switch-off, transitions faster than motional time-scales are desired. Electric dipole transitions between these states are for-

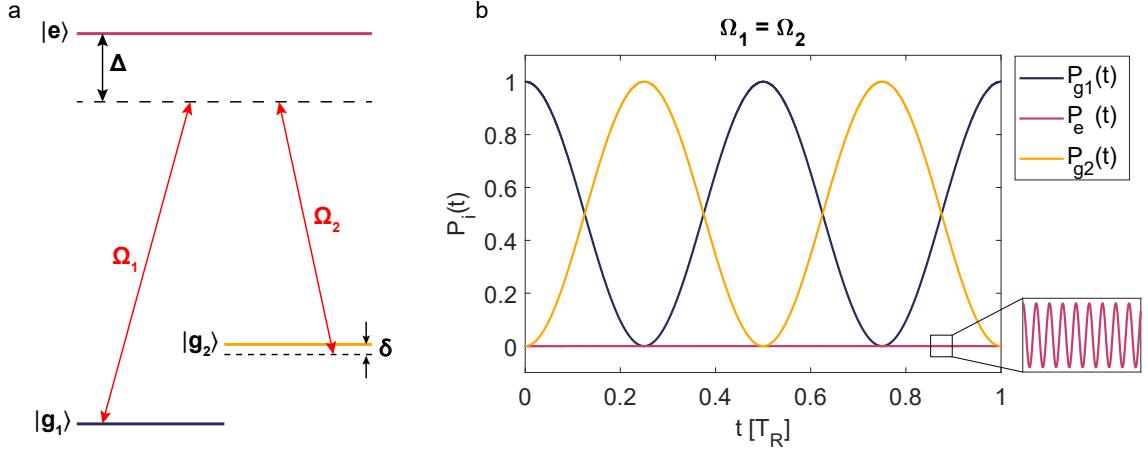


Figure 2.8: **Two-photon stimulated Raman transitions.** (a) Two ground states  $|g_1\rangle$  and  $|g_2\rangle$  are coupled to an excited state  $|e\rangle$  using two laser fields with a Rabi coupling given by  $\Omega_1$  and  $\Omega_2$  respectively. The two laser fields are far detuned from the ground-excited transition  $|g_i\rangle - |e\rangle$  by  $\Delta$ . The large detuning ensures that single-photon scattering due to  $|g_i\rangle - |e\rangle$  transition is kept low. The frequency detuning between the laser beams is given by the difference in energy between the ground states plus an additional detuning  $\delta$ . (b) Numerical solution of the resulting 3 state system. Though there is no electric dipole transition directly between states  $|g_i\rangle$ , the coupling with the excited state  $|e\rangle$  results in coherent population oscillations between states  $|g_i\rangle$ . Due to the large detuning the excited state is hardly populated (inset) justifying the adiabatic elimination used in the text. The numerical solution is plotted for an effective two-photon detuning  $\delta = 0$  and symmetrical coupling of the ground states to the excited state  $\Omega_1 = \Omega_2$ . The time is plotted in terms of the Rabi Coupling time  $T_R = 2\pi/\Omega_R$  where  $\Omega_R = \Omega_1\Omega_2/4\Delta$  is the effective two-photon Rabi coupling between the ground states.

bidden due to wavefunction symmetry of the initial and final states. However two-photon transitions involving an additional excited state are possible. The schematic describing the situation is depicted in Figure 2.8. Two states in the ground manifold  $|g_1\rangle, |g_2\rangle$  are coupled to each other through an intermediate excited state  $|e\rangle$ . State  $|g_1\rangle$  ( $|g_2\rangle$ ) is coupled to  $|e\rangle$  with a Rabi coupling  $\hbar\Omega_1 = \langle e | \vec{p} \cdot \vec{E}_1 | g_1 \rangle$  ( $\hbar\Omega_2 = \langle e | \vec{p} \cdot \vec{E}_2 | g_2 \rangle$ ). Each of these optical fields are detuned from the excited state by a detuning  $\Delta$  much larger than the excited state linewidth  $\gamma$ . While a large  $\Delta$  reduces the effective two-photon coupling, it ensures that detrimental single-photon scattering with excited state are avoided and the population from state  $|g_1\rangle$  to  $|g_2\rangle$  can be coherently transferred. For the experiments performed in this thesis, the two beams for the transition are phase-locked with respect to each other using an optical phase-lock loop from Toptica Photonics based on [63]. Under such a situation where the three states are coherently coupled, the state at any time can be represented as

$$|\psi(t)\rangle = \sum_{n=g_1, g_2, e} c_n(t) e^{-i\zeta_n t} |n\rangle \quad (2.15)$$

Using appropriate choice of the phase factors  $e^{-i\zeta_n t}$  and performing the rotating wave approximation one can get expressions for the coefficients  $c_n(t)$  which determine state populations as follows[60]

$$i\hbar \begin{bmatrix} \dot{c}_{g_1}(t) \\ \dot{c}_e(t) \\ \dot{c}_{g_2}(t) \end{bmatrix} = \frac{\hbar}{2} \begin{bmatrix} 0 & \Omega_1 & 0 \\ \Omega_1 & 2\Delta & \Omega_2 \\ 0 & \Omega_2 & 2\delta \end{bmatrix} \begin{bmatrix} c_{g_1}(t) \\ c_e(t) \\ c_{g_2}(t) \end{bmatrix} \quad (2.16)$$

here  $\delta$  is the two-photon detuning and is depicted in Figure 2.8.

When the  $\Delta$  is large, the excited state population hardly changes since the amplitude of this oscillation is  $\Omega_i / \sqrt{\Omega_i^2 + \Delta^2}$  is very small. In addition the population oscillates very fast with a frequency  $\sqrt{\Omega_i^2 + \Delta^2}$  which is orders of magnitude faster than  $\Omega_R$ . The result of numerically solving Equation 2.16 is shown in Figure 2.8(b). The populations in states  $|g_i\rangle$  undergo sinusoidal Rabi oscillations, while the population in the excited state hardly changes. Due to these reasons, it is reasonable to use adiabatic elimination to set  $\dot{c}_e(t) = 0$ [60]. This leads to the following equation

$$i\hbar \begin{bmatrix} \dot{c}_{g_1}(t) \\ \dot{c}_{g_2}(t) \end{bmatrix} = -\frac{1}{4} \begin{bmatrix} \frac{\Omega_1^2}{\Delta} & \frac{\Omega_1\Omega_2}{\Delta} \\ \frac{\Omega_1\Omega_2}{\Delta} & \frac{\Omega_2^2}{\Delta} - 4\delta \end{bmatrix} \begin{bmatrix} c_{g_1}(t) \\ c_{g_2}(t) \end{bmatrix} \quad (2.17)$$

Thus the states  $|g_1\rangle$  and  $|g_2\rangle$  are coupled with a two-photon coupling  $\Omega_R = \Omega_1\Omega_2/4\Delta$ . We use this natural coupling time-scale  $T_R = 2\pi/\Omega_R$  to plot oscillations of states in Figure 2.8(b).

In the simple model presented above, the excited state was depicted as a single state.

However from the analysis in the previous sections we know that at finite magnetic fields the excited state consists of a number of states. To obtain the total two-photon Raman coupling, the coupling of the ground states to all excited states has to be considered and is obtained as

$$\Omega_R = \sum_{\mu} \frac{\Omega_{1\mu}\Omega_{2\mu}}{4\Delta_{\mu}} + \sum_{\nu} \frac{\Omega_{1\nu}\Omega_{2\nu}}{4\Delta_{\nu}} \quad (2.18)$$

here  $\mu$  ( $\nu$ ) is used to index all states in the  $2^2P_{1/2}(2^2P_{3/2})$  manifold. In addition to this two photon coupling there is still a finite single photon scattering rate  $\Gamma_{in}$  from coupling of the ground to the excited states. Expression for  $\Gamma_{in}$  can be written by also taking the sum over all possible excited states in the D1 and D2 lines as follows

$$\Gamma_{in} = \gamma \left( \sum_{\mu} \frac{\Omega_{1\mu}^2 + \Omega_{2\mu}^2}{4\Delta_{\mu}^2} + \sum_{\nu} \frac{\Omega_{1\nu}^2 + \Omega_{2\nu}^2}{4\Delta_{\nu}^2} \right) \quad (2.19)$$

where  $\gamma$  is the excited state linewidth. Thus there are two competing processes namely, two-photon coherent coupling and single photon inelastic scattering. A quality factor  $\beta$  is introduced to quantitatively compare these rates.

$$\beta = \frac{\Omega_R}{\Gamma_{in}} \quad (2.20)$$

A few qualitative features of  $\beta$  can already be gleaned from an approximate analysis of the two rates. Using the fact that the ground state quadrupole matrix element is zero, and inserting a complete set of excited states one can obtain  $\sum_{\mu} \Omega_{1\mu}\Omega_{2\mu} + \sum_{\nu} \Omega_{1\nu}\Omega_{2\nu} = 0$ [62]. In addition, since the states  $\mu$  and  $\nu$  are separated by the fine-structure splitting  $A_f$  at  $B=0$ ,  $\Omega_R \sim A_f/\Delta^2$  for large detunings with  $\Delta$  being the detuning from the D2 line at zero field. The scattering rate on the contrary scales as  $\Gamma_{in} \sim \gamma/\Delta^2$ . This implies that  $\beta$  scales as  $\beta \sim A_f/\gamma$ . Thus a larger splitting between the D1,D2 lines or a smaller excited state linewidth leads to a better quality of the two-photon transition. Among the alkali atoms, Li has the smallest fine-structure splitting of the excited state and hence the worst two-photon transition quality[62].

The two-photon matrix element  $\Omega_R$  is calculated by summing over all excited states as in Equation 2.18.  $\Omega_R$  for all combinations of initial and final states at different magnetic fields is plotted in Figure 2.9. The two-photon transition matrix elements from the D1 and D2 lines have opposite signs which leads to a smaller  $\Omega_R$  if the transitions are simultaneously red/blue detuned from both the lines. More on this is presented in Figure 2.13 for a single two-photon transition between states  $|3\rangle$  and  $|4\rangle$  and will be elaborated later. Hence in Figure 2.9,  $\Omega_R$  is calculated when frequency of the beams is between D1 and D2 lines with a detuning of  $\Delta = A_f/2 = 5\text{GHz}$  at  $B=0$ . In Figure 2.9 three classes of transitions can be identified (i) strong transitions which occur due to coupling of majority-majority and majority-majority admixtures (ii) weak transitions which occur due to coupling of

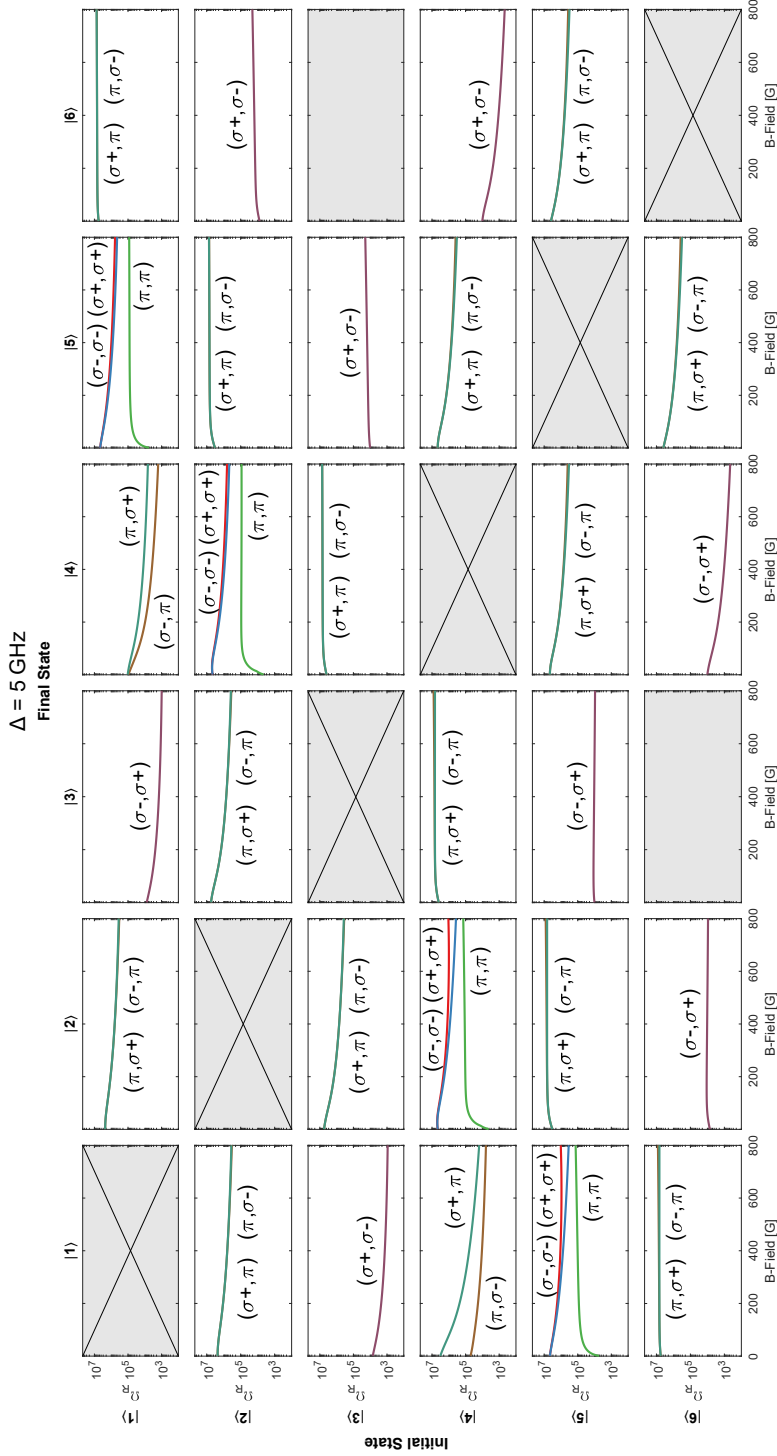


**Figure 2.9: Two-photon Rabi Coupling  $\Omega_R = \Omega_1\Omega_2/4\Delta$  as a function of magnetic field for different initial and final states.** The initial states are represented along the rows and the final states along the columns. In each of the plots,  $\Omega_R$  is in units of Hz and the magnetic field in units of Gauss.  $\sigma_{\pm}$  and  $\pi$  denote the kind of transition.  $\Omega_R$  is calculated for typical beam powers resulting in an electric field amplitude of 35 V/cm and with frequencies of the beams detuned from the D2 line at zero field by  $\Delta = 5\text{GHz}$ . The transitions in the upper triangular part of the array are opposite to the ones in the lower triangular part since the initial and final states are swapped. The strongest transitions are between states  $|1\rangle - |6\rangle$ ,  $|2\rangle - |5\rangle$  and  $|3\rangle - |4\rangle$  yielding  $\Omega_R/(2\pi)$  of a few MHz consistent with experiment. The weaker transitions are at least a few orders of magnitude slower than these transitions.

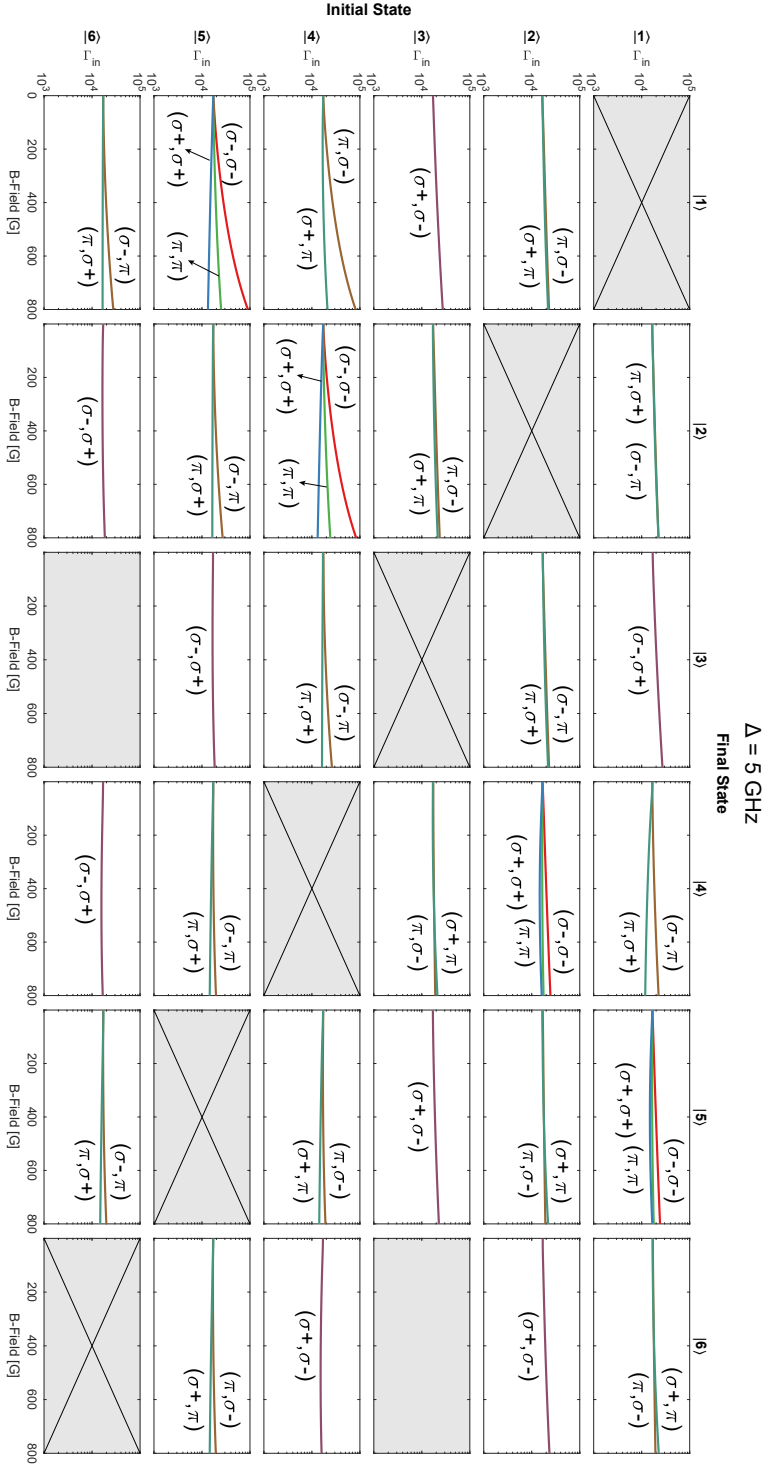


Figure 2.10: **Single photon scattering rate  $\Gamma_{in}$  due to coupling of the initial states to the excited states in the  $2^2\text{P}_{1/2}$  and  $2^2\text{P}_{3/2}$  manifolds.** The initial states for the two-photon transition are represented along the rows and the final states along the columns.  $\sigma_{\pm}$  and  $\pi$  denote the kind of transition. In each of the plots,  $\Gamma_{in}$  is in units of Hz and the magnetic field in units of Gauss. As for  $\Omega_R$ ,  $\Gamma_{in}$  is calculated for typical beam powers resulting in an electric field amplitude of 35 V/cm and with frequencies of the beams detuned from the D2 line at zero field by  $\Delta = 5 \text{ GHz}$ . The transitions in the upper triangular part of the array are opposite to the ones in the lower triangular part since the initial and final states are swapped.

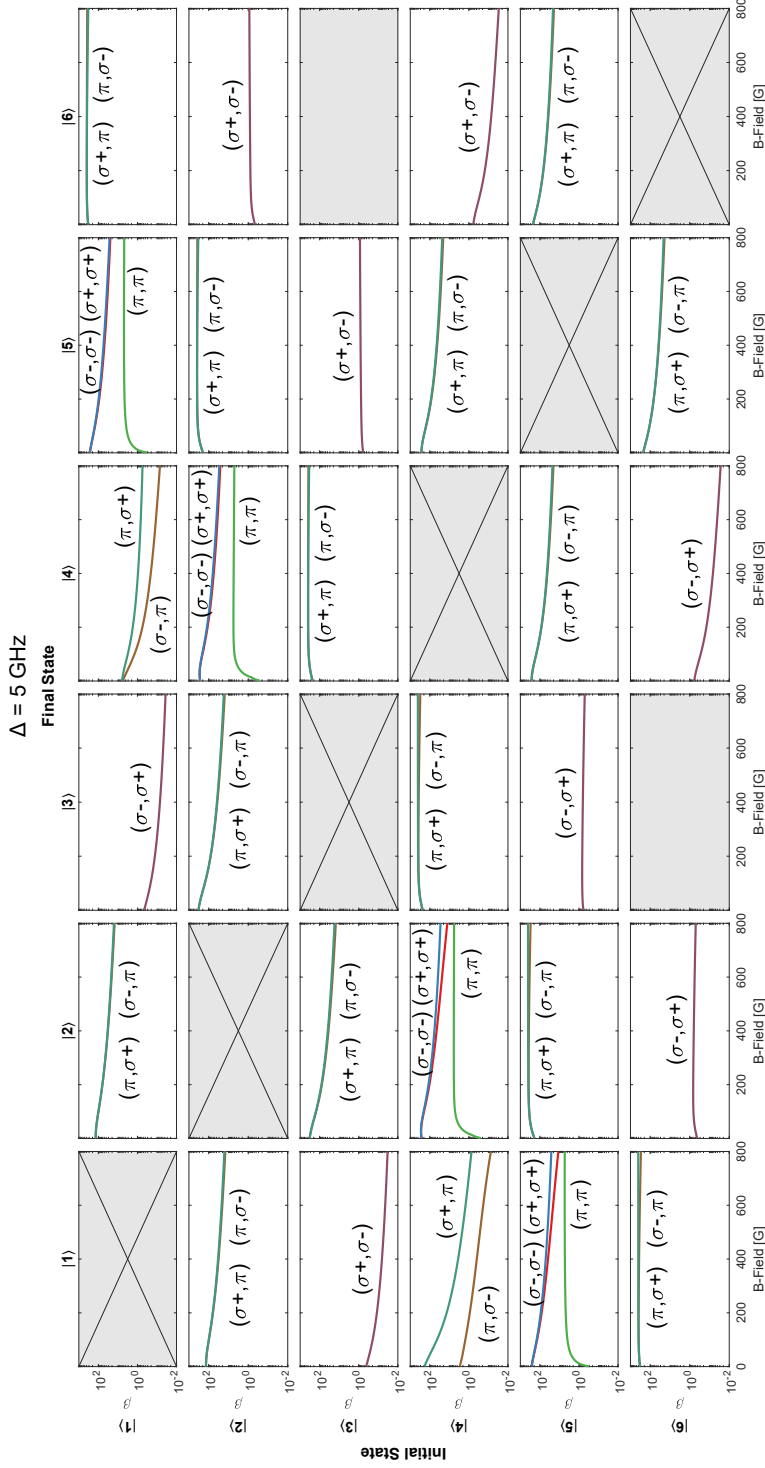


Figure 2.11: **Quality of two-photon transition**  $\beta = \Omega_R/\Gamma_{in}$  **between states**  $|1\rangle \dots |6\rangle$ . The initial states for the two-photon transition are represented along the rows and the final states along the columns. In each of the plots,  $\beta$  is dimensionless and the magnetic field is in units of Gauss.  $\beta$  is calculated for typical beam powers resulting in an electric field of 35 V/cm and with frequencies of the beams detuned from the D2 line at zero field by  $\Delta = 5\text{GHz}$ . The strong transitions involving  $|1\rangle - |6\rangle$ ,  $|2\rangle - |5\rangle$  and  $|3\rangle - |4\rangle$  have the largest  $\beta$  since  $\Gamma_{in}$  does not vary as much and  $\beta$  is mainly determined by how fast  $\Omega_R$  can get. For these transitions at large magnetic fields we get  $\beta$  of approximately 350. This is at least 20x better than for the weaker transitions between  $|1\rangle - |2\rangle$  and  $|2\rangle - |3\rangle$ [62]. For the experiments in this thesis, we utilize mainly transitions between states  $|3\rangle$  and  $|4\rangle$ .

majority-majority and majority-minority admixtures and (iii) extremely weak transitions which occur due to coupling of majority-minority and majority-minority admixtures of ground and excited states. Similar to magnetic dipole transitions between these states, the strongest transitions are between states  $|1\rangle - |6\rangle$ ,  $|2\rangle - |5\rangle$  and  $|3\rangle - |4\rangle$ .

As mentioned previously to determine the quality of these two-photon transitions, the single particle scattering rate  $\Gamma_{in}$  also has to be determined. This is obtained by summing over contributions from all the excited states in the D1 and D2 line as in Equation 2.19. These are calculated for all combinations of initial/final states and polarization combinations as a function of magnetic field with  $\Delta = 5$  GHz as for  $\Omega_R$ . The result is shown in Figure 2.10. Unlike  $\Omega_R$ , the variation in  $\Gamma_{in}$  is not as much between the possible two-photon transitions.

Having evaluated both  $\Omega_R$  and  $\Gamma_{in}$ ,  $\beta$  can be readily evaluated by taking their ratios. This is presented in Figure 2.11. Since  $\Gamma_{in}$  does not vary as much as  $\Omega_R$  among the two-photon transitions, it is the strength of  $\Omega_R$  which mostly determines the quality of the two-photon transition. The largest  $\beta$  factors are obtained for the strongest transitions involving states  $|1\rangle - |6\rangle$ ,  $|2\rangle - |5\rangle$  and  $|3\rangle - |4\rangle$ . At large magnetic fields of  $B \approx 750G$ , the strongest transitions are at least a factor of 20 better than the ones which are weaker. Previously  ${}^6\text{Li}$  was found to be not such a good candidate for these kind of two-photon transitions[62]. However, these studies had considered coupling of states  $|1\rangle - |2\rangle$  which we know from Figure 2.11 to be a factor of 20 worse than the strong transitions between  $|1\rangle - |6\rangle$ ,  $|2\rangle - |5\rangle$  and  $|3\rangle - |4\rangle$ . All possible strong and weak two-photon transitions are further summarized in Figure 2.12. For the experiments presented in this thesis, we utilize mainly strong transitions between states  $|3\rangle - |4\rangle$  to perform spin-flips on a time-scale orders of magnitude faster than the motional time-scales in the system. This enables us to effectively turn off interactions instantaneously and measure in situ properties of the system.

Having characterized two-photon Raman transitions between different initial and final states at fixed detuning, one of the strongly coupled transitions are characterized as a function of detuning at a fixed large magnetic field of  $B=750$  G. This is necessary to find the optimal detuning that produces the largest coupling  $\Omega_R$  while at the same time minimizing unwanted single photon scattering. The results for the transition between states  $|3\rangle - |4\rangle$  with polarization  $(\sigma+, \pi)$  are shown in Figure 2.13. The Raman coupling  $\Omega_R$  shows two peaks where each of the optical beams becomes closely detuned to states in either the  $2^2P_{1/2}$  or  $2^2P_{3/2}$  manifold. However, at these same detunings the single photon scattering rate from the excited states also increases resulting in low two-photon quality factor  $\beta$ . The largest  $\Omega_R$  while at the same time minimizing  $\Gamma_{in}$  resulting in a large  $\beta$  is obtained when the beams are red detuned from  $2^2P_{3/2}$  states and blue detuned from  $2^2P_{1/2}$  states. This is because the two-photon transition matrix elements from the D1/D2 lines have opposite signs and due to the opposite detunings add constructively. Large blue or red detunings from both the lines can still yield a good  $\beta$  factor. However these transitions are then orders of magnitude slower than when the frequency of the beams are in between the D1 and D2 lines. For the experiments performed in this thesis, we use optical fields with frequencies between the D1 and D2 lines to ensure large  $\Omega_R$  and  $\beta$ . While we only make use of coupling

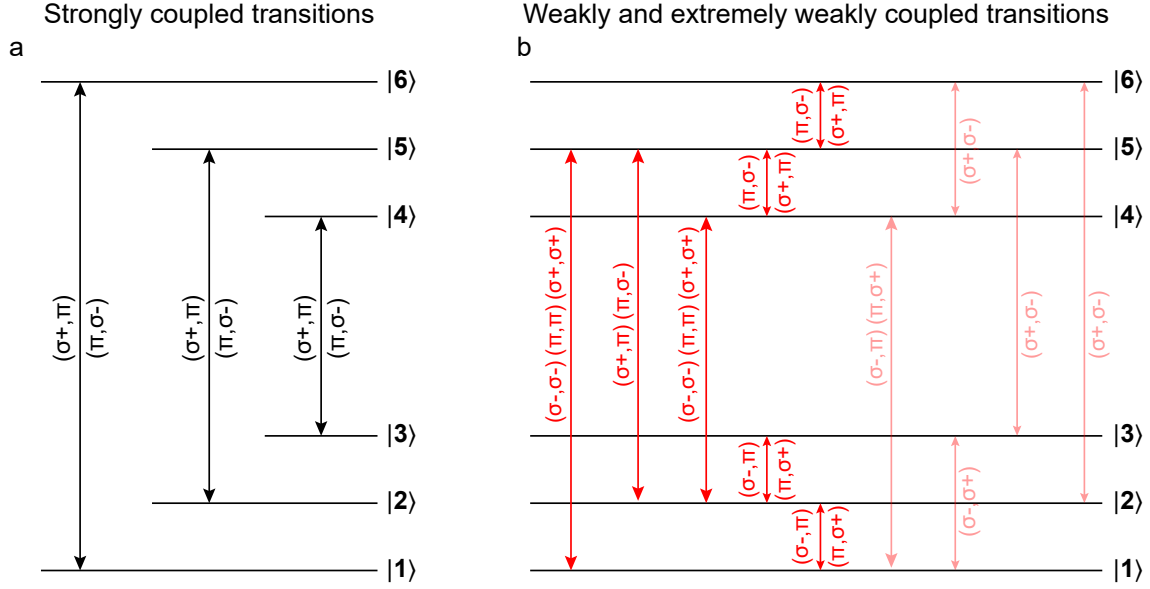


Figure 2.12: **Summary of two-photon stimulated Raman transitions between states  $|1\rangle \dots |6\rangle$ .** (a) Strongly coupled transitions are obtained between states  $|1\rangle - |6\rangle$ ,  $|2\rangle - |5\rangle$  and  $|3\rangle - |4\rangle$ . The polarization of the beams are indicated in brackets. For example in a  $(\sigma+, \pi)$  transition coupling state  $|1\rangle$  to state  $|6\rangle$ ,  $|1\rangle$  is coupled to excited states with  $\sigma+$  transition and state  $|6\rangle$  with a  $\pi$  transition. At large magnetic fields, these transitions are the strongest since they couple the largest admixtures of states effectively flipping the electron spin due to the spin-orbit coupling. (b) Weakly coupled transitions between states  $|1\rangle \dots |6\rangle$ . At large magnetic fields, these transitions occur either due to (i) coupling of the large-large + large-small admixtures. The small admixtures are due to the hyperfine interaction and set the energy scale for the effective two-photon coupling. Since the energy scale of the hyperfine interaction is orders of magnitude smaller than the spin-orbit interaction, these transitions are weaker (ii) coupling large-small + large-small admixtures. The coupling energy scale for these transitions are extremely small. While these are the possible transitions, the quality factor of a two-photon transition is quantified by  $\beta = \Omega_R/\Gamma_{in}$ . Comparison of these quantities is presented for all these transitions in the following sections.

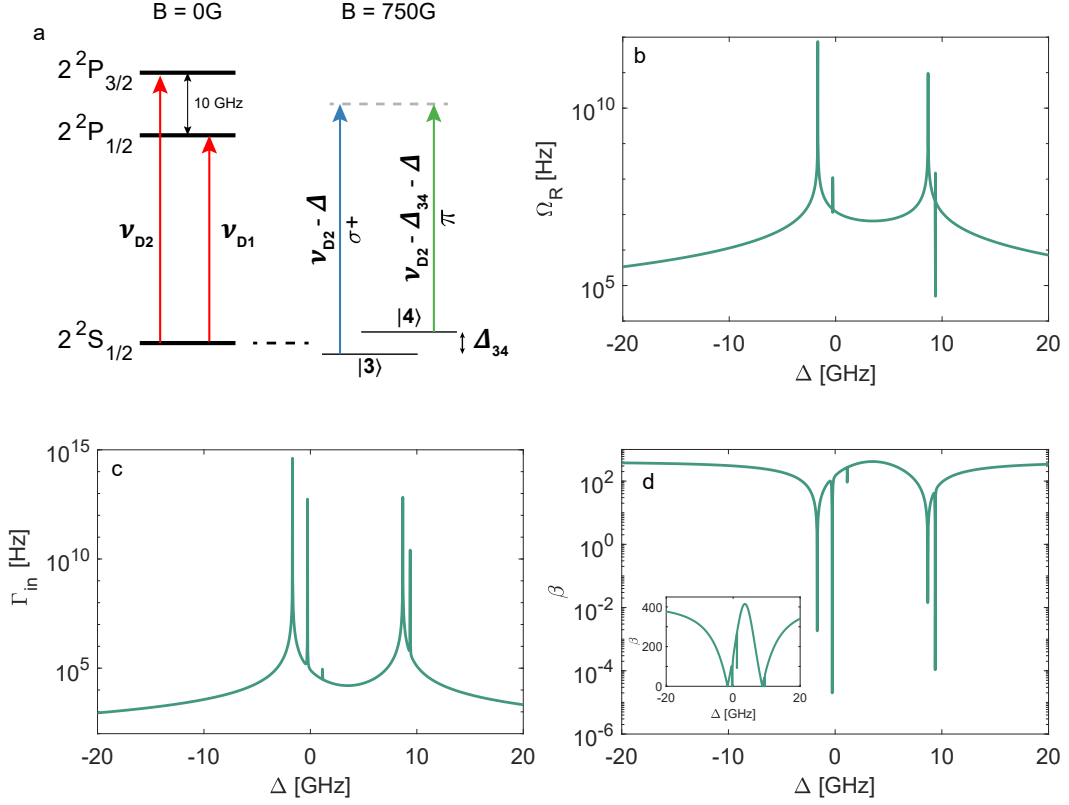


Figure 2.13: **Optimal two-photon detuning for strong transitions.** (a) Two-photon transitions between states  $|3\rangle$  and  $|4\rangle$ . State  $|3\rangle$  is coupled to the excited states with a  $\sigma+$  transition and state  $|4\rangle$  with a  $\pi$  transition. At large magnetic fields, here  $B=750\text{G}$ , the states  $|3\rangle$  and  $|4\rangle$  are split by  $\Delta_{34}$  which is around  $1951\text{ MHz}$ . The two beams are detuned by  $\Delta_{34}$  with respect to each other, but by  $\Delta$  from the D2 line at zero field. Depending on the value of  $\Delta$ , the beams can be either red or blue detuned from the excited states in the  $2^2P_{1/2}$  and  $2^2P_{3/2}$  manifolds. (b) Two-photon Rabi rate  $\Omega_R$ . (c) Single photon scattering rate  $\Gamma_{in}$  and (d) Quality factor  $\beta$  as a function of detuning  $\Delta$ . Inset shows  $\beta$  in linear scale.  $\Omega_R$  is largest when the frequency of the beams are closer to excited states in either  $2^2P_{1/2}$  or  $2^2P_{3/2}$  manifolds, but this also increases  $\Gamma_{in}$  and decreases  $\beta$ . The product of the single photon transition matrix elements  $\Omega_1\Omega_2$  has opposite signs for excited states in the  $2^2P_{1/2}$  and  $2^2P_{3/2}$  manifolds. Hence  $\Omega_R$  is the largest when  $\Delta$  is red detuned from the  $2^2P_{3/2}$  manifold and blue detuned from  $2^2P_{1/2}$ . For large red and blue detunings from both  $2^2P_{1/2}$  and  $2^2P_{3/2}$  manifolds, good  $\beta$  factors can also be obtained, but at a reduced  $\Omega_R$ . All values are calculated for typical beam powers resulting in electric field amplitudes of  $35\text{ V/cm}$ .

to the  $2^2P_{1/2}$  and  $2^2P_{3/2}$  states of  $^6\text{Li}$ , a further improvement in  $\beta$  by a factor of around 2 can be obtained by instead coupling to  $3^2P_{1/2}$  and  $3^2P_{3/2}$ . This excited state has a linewidth of 754 KHz which is approximately 7 times narrower than the 2P linewidth. This smaller linewidth transition has previously been used to obtain lower MOT temperatures[64]. The fine-structure splitting between 3P states is 3 GHz, which is lower than the 2P splitting of 10 GHz. Hence even though  $\Gamma_{in}$  can be reduced by a factor of 7,  $\Omega_R$  is smaller by a factor of approximately 3 resulting in a gain in  $\beta$  by a factor of only 2. In addition such a moderate increase of  $\beta$  would require UV lasers and optics as the transition is at 323 nm.

### 2.5.1 Experimental measurements

The fast two-photon transition between states  $|3\rangle$  and  $|4\rangle$  is characterized experimentally. Starting with a few-body system consisting of 6 atoms in state  $|3\rangle$ , a two-photon coupling is created to state  $|4\rangle$ . The two co-propagating beams for the Raman transition are phase locked with respect to each other[63] and their powers are actively stabilized. The co-propagating beams ensure that no momentum is transferred to the atoms. The detuning from the excited state  $\Delta$  corresponds to 5GHz from the D2 line at zero magnetic field. The resulting Rabi oscillations are shown in Figure 2.14. From the Rabi oscillations, a Raman coupling  $\Omega_R$  of approximately 750KHz is obtained. From the total populations in state  $|3\rangle$  and  $|4\rangle$ , the single photon scattering rate can be obtained which gives a quality factor  $\beta = 285.85 \pm 79.20$ . The measurements are performed at a high magnetic field of 750G. At these fields, the transition frequency between states  $|3\rangle$  and  $|4\rangle$  depends strongly on the magnetic field and tunes as  $2\mu_B = 2.8\text{MHz/G}$ . The magnetic fields in the experiments are stabilized to 40mG and this leads to a detuning noise of approximately 100KHz which is comparable to  $\Omega_R$ . This could explain the dephasing of the Rabi oscillations. In contrast, the magnetic dipole transitions between high(low) field seeking states are much more insensitive to magnetic fields and are susceptible to detuning noise of less than 2% of the Rabi rate. The large quality factor  $\beta$  is consistent with expectations presented previously. In experiments since a fast transfer of atoms from state  $|3\rangle$  to  $|4\rangle$  is desired, we use a  $\pi$  pulse to transfer atoms on a timescale of approximately 300ns.

## 2.6 Resonant scattering interactions

So far the possible optical and magnetic dipole transitions in  $^6\text{Li}$  were introduced. The optical dipole transition elements were combined to obtain two-photon matrix elements between the states in the ground state manifold where single-field electric dipole transitions are forbidden. One of the main aims of performing these internal state manipulations either through magnetic dipole or two-photon optical transitions is to instantaneously switch-off resonant interactions so that in situ properties of the system can be measured. The concept of resonant interactions has a long history in physics and was initially explored in the context of nuclear reactions by Feshbach[65] and atomic scattering by Fano[66].

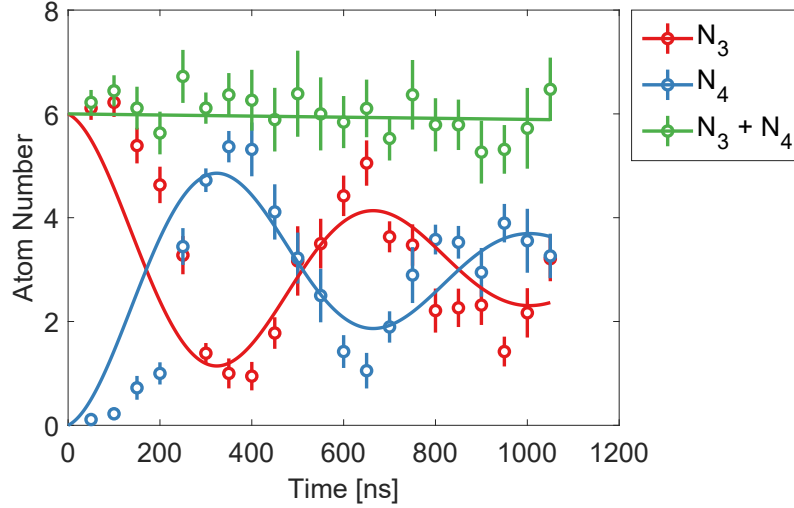


Figure 2.14: **Experimental measurements of two-photon Raman transitions between states  $|3\rangle - |4\rangle$ .** Starting with a few-body system with 6 atoms in state  $|3\rangle$ , a two-photon Raman transition is performed to state  $|4\rangle$ . The number of atoms in state  $|3\rangle(|4\rangle)$ ,  $N_3(N_4)$  is shown in red(blue). The total number of atoms ( $N_3 + N_4$ ) is plotted in green and does not indicate large losses. The circles with error bars denote experimental measurements and the solid lines are fits. We obtain a two-photon Rabi rate  $\Omega_R = 2\pi \times (734.25 \pm 224.66)$  KHz and a quality factor of  $\beta = 258.85 \pm 79.20$ . The dephasing of Rabi oscillations occurs mainly due to the fact that at high magnetic fields the energy difference between states  $|3\rangle$  and  $|4\rangle$  is sensitive to the magnetic field at a rate of 2.8 MHz/G. Since magnetic fields are stabilized to approximately 40mG, a detuning on the order of 100 KHz can result. This is unlike magnetic dipole transitions between high(low) field seeking states since their energies scale similarly with magnetic field and are much more insensitive to magnetic field noise. The error bars indicate standard error of the mean.

This section provides a summary of scattering theory necessary to understand experiments performed in this thesis and more details can be found elsewhere[2], [67]. The effect of a potential between two atoms, can only lead to phase shift  $\delta$  of the asymptotic wavefunction since the probability current should be conserved. The asymptotic phase shift is related to a new length scale the scattering length  $a(k) = -\delta/k$ . In the low energy limit of ultracold collisions, the range of the interaction potential  $r_0$  is orders of magnitude smaller than the de Broglie wavelength  $\lambda_{dB} = 2\pi/k$  ensuring that  $kr_0 \ll 1$ . In this regime the scattering properties do not depend on the exact details of the potential and are determined only by a so-called well parameter which encapsulates all details about the scattering potential. Thus, the scattering properties can be obtained by equivalent pseudo-potentials which are simpler to solve and result in the same scattering properties. This motivates an introduction of the scattering problem through simple model potentials which can be easily solved. This is followed by connecting the scattering length with scattering properties like collision cross-sections. The relation of the scattering length to the energetics of a quantum gas is also alluded to. This section concludes with the situation typically encountered in cold atoms where there isn't a single scattering potentials, but a multitude of different potentials in various channels - some open and others closed. In addition to being coupled at short distances, these channels usually possess a differential magnetic moment due to which a bound state in the closed channel can be made resonant with an open channel in which the atoms enter. This leads to a resonant enhancement in scattering similar to tuning the potential depth in scattering with only a single channel.

### 2.6.1 Scattering from a finite well potential

To demonstrate the emergence of an asymptotic phase shift, a scattering scenario using a radial potential well in 3D is presented. The radial potential well has a depth  $V_0$  and a range  $r_0$  as shown in Figure 2.15. The atomic density in cold gases is low and only binary collisions need to be considered. The Hamiltonian describing the situation where collision occurs between particles of equal mass  $m$  is

$$H = \frac{p_1^2}{2m} + \frac{p_2^2}{2m} + V(|\vec{r}_1 - \vec{r}_2|) \quad (2.21)$$

where  $\vec{r}_i$  ( $\vec{p}_i$ ) are the position (momentum) of the particles and a central interaction potential  $V(|\vec{r}_1 - \vec{r}_2|)$  has been considered. The Hamiltonian can be simplified into a center-of-mass (CM) part and a relative part (rel) as follows

$$\begin{aligned} H &= H_{CM} + H_{rel} \\ &= \left( \frac{P^2}{2M} \right) + \left( \frac{p^2}{2\mu} + V(r) \right) \end{aligned} \quad (2.22)$$

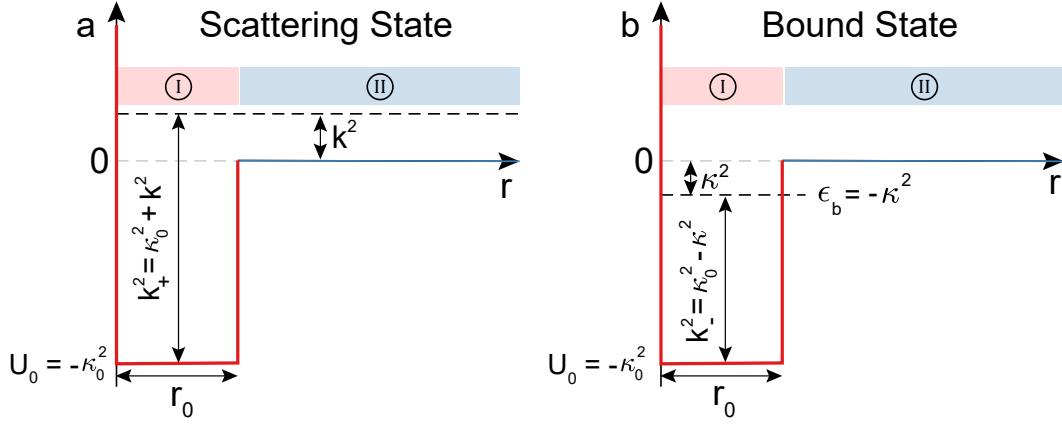


Figure 2.15: **Two particles interacting with a model potential.** Cold collisions occur in the universal regime where the interaction range  $r_0$  is small compared to de Broglie wavelength  $\lambda_{dB} = 2\pi/k$  such that  $kr_0 \ll 1$ . In such a situation the scattering properties depend only on the asymptotic phase shift of the scattering wavefunction at large separations and the physics of the scattering problem can be understood by studying the scattering from model potentials where the  $kr_0 \ll 1$ . The interaction potential is a finite well with range  $r_0$  and depth  $U_0 = -\kappa_0^2$  in units of  $\hbar^2/2\mu$ . (a) Scattering problem energies. The Schrödinger equation can be solved in regions I and II separately and boundary conditions matched. The scattering energy is  $k^2$  in region II and  $k_+^2 = \kappa_0^2 + k^2$  in region I in units of  $\hbar^2/2\mu$ . (b) Bound state problem energies. To find the condition for the bound state, the bound state energy is defined as  $-\kappa^2$  in units of  $\hbar^2/2\mu$ . Similar to the scattering problem, matching the boundary conditions of the wavefunction in the two regions gives the allowed bound state energies for a given well parameter  $\gamma = \kappa_0 r_0$ .

where  $\vec{R}$  ( $\vec{r}$ ) is the CM (rel) position and  $\vec{P}$  ( $\vec{p}$ ) is the CM (rel) momentum.  $M = 2m$  ( $\mu = m/2$ ) denotes the total (reduced) mass. Since the CM motion is unaffected by the potential, only the solution for the relative motion needs to be obtained. In 3D, the momentum operator can be written in terms of the radial momentum  $p_r$  and angular momentum operator  $L$  and the eigen value problem can be setup as follows

$$\left( \frac{p_r^2}{2\mu} + \frac{L^2}{2\mu r^2} + V(r) \right) \psi = E\psi \quad (2.23)$$

To find scattering solution, the following Ansatz for the wavefunction is used to split the wavefunction dependence into the radial and angular parts

$$\psi(r) = R_l(kr)Y_{lm}(\theta, \phi) \quad (2.24)$$

where  $Y_{lm}(\theta, \phi)$  are the spherical harmonic functions which are eigen functions of the  $L^2$  operator and  $R_k(r)$  gives the radial dependence. Since  $L^2 Y_{lm} = \hbar^2 l(l+1) Y_{lm}$  the following equation can be obtained,

$$R_l'' + \frac{2}{r}R_l' + \left( k^2 - U(r) - \frac{l(l+1)}{r^2} \right) R_l = 0 \quad (2.25)$$

where  $U(r) = \frac{2\mu}{\hbar^2}V(r)$  and  $E = \frac{\hbar^2}{2\mu}k^2$ . Solving the problem in this model potential amounts to applying this equation in different regions I,II of the potentials and ensuring the continuity of  $R_l(kr)$  and  $R_l'(kr)$  at the boundary  $r = r_0$ .

$$R_l(kr) = \begin{cases} Aj_l(k+r) & r \leq r_0 \\ c_l [\cos \eta_l j_l(kr) + \sin \eta_l n_l(kr)] & r > r_0 \end{cases} \quad (2.26)$$

where  $U(r) = -\kappa_0^2$  for  $r \leq r_0$ ;  $k_+^2 = \kappa_0^2 + k^2$ ;  $j_l(kr)$  are the spherical Bessel functions and  $n_l(kr)$  are the spherical Neumann functions. Asymptotically as  $r \rightarrow \infty$ ,  $j_l(kr) \sim \sin(kr - l\pi/2)/(kr)$  and  $n_l(kr) \sim \cos(kr - l\pi/2)/(kr)$ . Hence  $R_l(kr) \rightarrow \sin(kr - l\pi/2 + \eta_l)$ , and  $\eta_l$  represents the asymptotic phase shift of the scattered wave due to the interaction potential. The solution in region I contains only the spherical Bessel function, since  $|n_l(0)| \rightarrow \infty$ . Matching the wavefunctions and derivatives at the boundary gives,

$$\frac{j_l'(k+r_0)}{j_l(k+r_0)} = k \frac{\cos \eta_l j_l'(kr) + \sin \eta_l n_l'(kr)}{\cos \eta_l j_l(kr) + \sin \eta_l n_l(kr)} \quad (2.27)$$

In the ultracold regime a number of simplifications are in order. Firstly, the low temperatures mean that  $k \rightarrow 0$ . Secondly, the high centrifugal barrier prevents scattering in  $l \neq 0$ . For example, in  ${}^6\text{Li}$  the p-wave centrifugal barrier ( $l = 1$ ) is on the order of mK and at ultracold temperatures the wavepacket is unable to overcome this barrier and probe the

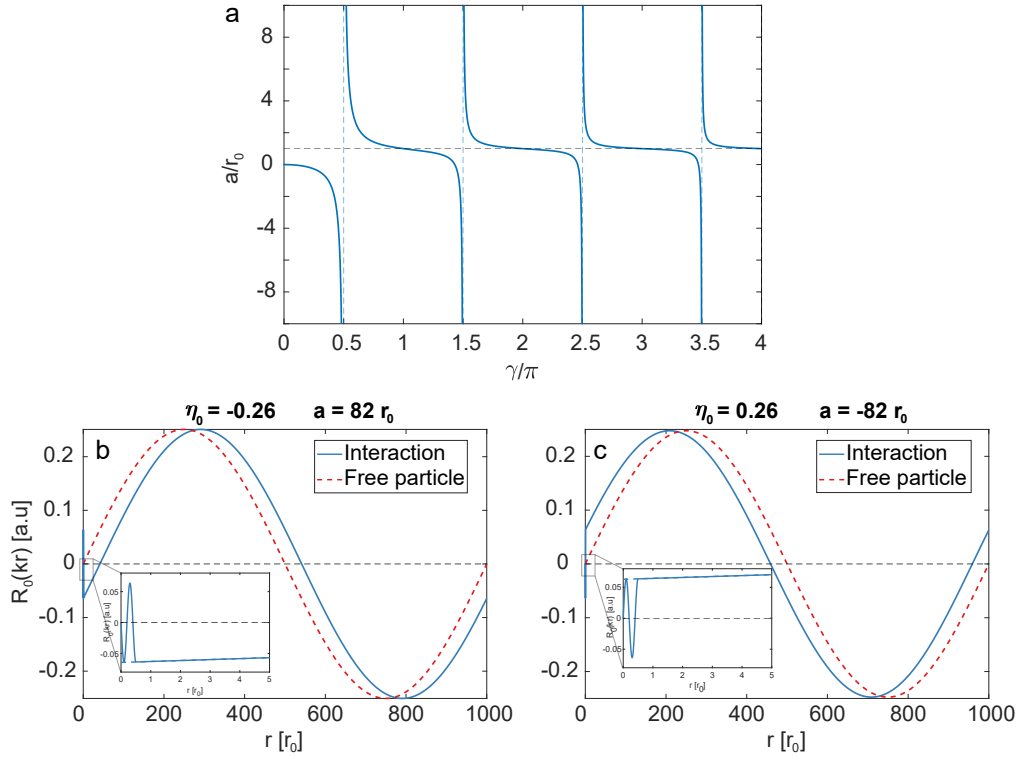


Figure 2.16: **Tuning the scattering length in a finite well potential for low collision energies**  $k \rightarrow 0$ . (a) The scattering length for scattering from a finite well depends only on the well parameter  $\gamma$ . As the well parameter is tuned additional bound states appear where the scattering length diverges. In this figure the range of  $\gamma$  values correspond to 0-4 bound states. (b,c) For an interaction potential with range  $r_0 = 0.5$ , the wavefunction is plotted for  $\gamma = 5\pi/2 \pm \epsilon$ . The blue (red) solid (dotted) lines indicate wavefunctions for the scattering (free particle) scenario. (b) When  $\gamma$  is slightly larger than the value required to support a bound state, the scattering length (phase shift) is positive (negative). In this situation the wavefunction is pushed away from the scattering center and corresponds to a repulsive energy in the mean field limit. (c) When  $\gamma$  is slightly smaller than the value required to support an additional bound state, the scattering length (phase shift) is negative (positive). The wavefunction is pulled towards the scattering center and corresponds to an attractive energy correction in the mean field limit. The insets in (b,c) show the scattering wavefunction in the region of the interaction potential. The scattering wavefunctions have three nodes since  $\gamma$  supports three bound states.

interaction region. Hence it is reasonable to consider only scattering in the s-wave ( $l = 0$ ) channel. In addition it makes sense to remove the  $k$ -dependence of the phase shift and define the scattering length as follows  $\eta_l = -ka(k)$ . Using these simplifications, the boundary condition yields

$$\kappa_0 r_0 \cot \kappa_0 r_0 \approx \frac{r_0}{r_0 - a} \quad (2.28)$$

Thus the scattering length  $a$  is a function of the well depth and range is,

$$\frac{a}{r_0} = \left( 1 - \frac{\tan \gamma}{\gamma} \right) \quad (2.29)$$

where  $\gamma = \kappa_0 r_0$  is the well parameter. A plot of the scattering length as a function of  $\gamma$  is shown in Figure 2.16. A few observations regarding the scattering scenario can be made. Firstly, by tuning the well parameter the scattering length can be changed over a large value spanning both positive and negative values. Secondly, there are divergences of the scattering length at certain values of  $\gamma$  and as will be shown below they are associated with the appearance of bound states.

Next we look at the bound state problem in this potential as depicted in Figure 2.15 for  $l = 0$ . Using the energy of the bound state as  $\epsilon_b = -\kappa^2$ , the wavefunctions in region I and II are

$$R_l(kr) = \begin{cases} \frac{A \sin k_- r}{r} & r \leq 0 \\ \frac{B e^{-\kappa r}}{r} & r > 0 \end{cases} \quad (2.30)$$

where  $k_-^2 = \kappa_0^2 - \kappa^2$ . Matching the  $R_l'(r = r_0)$  and  $R_l(r = r_0)$  for  $l = 0$  gives,

$$k_- \cot k_- r_0 = -\kappa \quad (2.31)$$

For a bound state at the threshold,  $\kappa \rightarrow 0$  and the well parameter takes on values,

$$\gamma_n = n \frac{\pi}{2} \quad (2.32)$$

When an expression for the scattering length was plotted as a function of the well parameter as in Figure 2.16 there were divergences in  $a$  observed for  $\gamma_n = n\pi/2$ . These occur when an additional bound state appears when the well is made deeper. The analysis above also leads to one important result which is related to the universality in s-wave scattering. A bound state appearing at the threshold and a scattering state with  $k \rightarrow 0$  are limiting cases of the same situation and Equations 2.28 and 2.31 are equivalent. In the case  $a \rightarrow +\infty$ , a relation between the bound state energy and  $a$  is obtained as follows,

$$\kappa = \frac{1}{a} \quad (2.33)$$

The wavefunction of this loosely bound state exists mostly outside the range of the potential

and is called a Halo state. The binding energy of the Halo state is given by the universal relation which depends only on the scattering length as follows,

$$E_B = -\frac{\hbar^2}{2\mu a^2} \quad (2.34)$$

In situations when the scattering momentum is comparable to  $1/r_0$ , the s-wave phase shift is no longer  $-ka$  and the phase shift is obtained by an effective-range expansion[68]. The asymptotic phase shift  $\eta_0$  depends on the scattering length( $a$ ) and a parameter called the effective range( $r_e$ ) which is determined by the wavefunction over the range of the potential. The expression for the phase shift then becomes,

$$k \cot \eta_0 = -\frac{1}{a} + \frac{1}{2}k^2 r_e + \dots \quad (2.35)$$

For the finite well potential considered here, this expression can be obtained from matching the boundary conditions and  $r_e$  depends on the range  $r_0$ [67]. This expression becomes important in situations where the effective range is large compared to  $1/k$  as is the case for collisions between  ${}^6\text{Li}$ - ${}^{40}\text{K}$  mixtures[69]. In the case of  ${}^6\text{Li}$ , the effective range is very small  $\approx 30a_0$ [2] and can be ignored unless large Fermi energies  $k_F$  are involved.

For low-energy scattering considered so far, the collisional properties of the system depend only on the asymptotic phase shift far away from the scattering center. Effectively, the same scattering properties can be obtained by replacing the actual potential by a pseudo-potential which produces the same asymptotic phase shift[70]. This is especially very useful for the case of universal scattering where  $kr_0 \ll 1$ . In such cases the scattering properties can be recovered by a zero-range potential such as a  $\delta(\vec{r})$  which is regularized as follows,

$$V(\vec{r}) = \frac{4\pi\hbar^2 a}{m} \delta(\vec{r}) \frac{\partial(r\Box)}{\partial r} \quad (2.36)$$

The scattering length enters into the expression for  $V(\vec{r})$  and is the only quantity which determines the asymptotic phase shift and scattering properties. This pseudo-potential is used in Chapter 3 to obtain the energies of two particles in a harmonic trap in two-dimensions(2D).

### 2.6.2 Scattering amplitude and partial wave expansion

Previously a binary scattering event involving a model potential was introduced. The scattering phase shift in the low energy limit  $k \rightarrow 0$  was related to the well parameter and the universal relation between scattering length and bound state energy was presented. Finally an expression for the s-wave scattering phase shift at finite  $k$  was presented through the effective range expansion. Here the relation of the scattering phase shift to the scattering amplitude and cross-section are summarized. Having obtained scattering eigen functions,

we setup a scattering problem to include an incoming and outgoing wave and expand these waves in terms of the eigen functions. This decomposition is termed the partial wave expansion and projects the incoming and outgoing waves onto different angular momentum channels. The total scattered amplitude is obtained as a sum of amplitudes of due to each of the partial waves. The scattering wavefunction is setup as,

$$\psi(\vec{r}) = \underbrace{e^{ikz}}_{\psi_{in}} + f(\theta) \underbrace{\frac{e^{ikr}}{r}}_{\psi_{sc}} \quad (2.37)$$

The wavefunction describes an incoming relative wave along the z-axis with a scattering center located at  $\vec{r} = 0$ . The scattering produces an outward travelling wave  $e^{ikr}/r$  where the  $1/r$  term encapsulates the fact that the probability amplitude reduces radially away from the scattering center. The scattering is axially symmetric and does not depend on the azimuthal angle  $\phi$ . The total wavefunction can be expanded in terms of the eigen states as follows,

$$\psi(\vec{r}) = \sum_{l,m} c_{l,m} R_l(kr) Y_{l,m}(\theta, \phi) \quad (2.38)$$

The azimuthal symmetry of  $\psi(\vec{r})$  should also be reflected in the basis states used for the expansion and hence only states with  $m = 0$  enter into the sum. By rewriting  $Y_{l,0}$  in terms of Legendre polynomials  $P_l(\cos \theta)$  the expansion becomes,

$$\psi(\vec{r}) = \sum_l (2l+1) i^l c_l R_l(kr) P_l(\cos \theta) \quad (2.39)$$

The incoming wave can be expanded in the free-particle basis given by the spherical Bessel function as follows,

$$e^{ikz} = \sum_l (2l+1) i^l j_l(kr) P_l(\cos \theta) \quad (2.40)$$

Using Equations 2.39 and 2.40, the expression for  $\psi_{sc}$  can be obtained as,

$$\underbrace{\psi_{sc}}_{\psi - \psi_{in}} = \sum_l (2l+1) i^l \underbrace{Q_l(kr)}_{c_l R_l(kr) - j_l(kr)} P_l(\cos \theta) \quad (2.41)$$

Using the asymptotic expressions for  $R_l(kr)$  and the fact that  $\psi_{sc}$  only contains the outward expanding wave  $e^{ikr}$ ,  $c_l$  is obtained to be  $e^{i\eta_l}$  resulting in the partial wave expansion as follows,

$$\psi_{sc} = \sum_l (2l+1) \frac{e^{ikr}}{2ikr} (e^{i2\eta_l} - 1) P_l(\cos \theta) \quad (2.42)$$

Comparing this expression to the scattered wave in Equation 2.39, the scattering amplitude  $f(\theta)$  can be obtained as

$$f(\theta) = \sum_l (2l + 1) \underbrace{\frac{e^{i2\eta_l - 1}}{2ik}}_{f_l} P_l(\cos \theta) \quad (2.43)$$

The expression for the scattering amplitude  $f_l$  of partial wave  $l$  depends only on the phase shift  $\eta_l$  and the scattering momentum  $k$ . The expression can be rewritten to make the dependence of the  $\eta_l$  on the magnitude of  $f_l$  clear

$$f_l = \frac{e^{i\eta_l}}{k} \sin \eta_l \quad (2.44)$$

Thus the total scattering amplitude is due to the sum of scattering amplitudes of all partial waves. The scattering amplitude for each partial wave  $f_l$  depends only on the phase shift for that partial wave. For situations like ultracold scattering there are contributions from only s-wave scattering amplitude.

$$f_0 = \frac{1}{k \cot \eta_0 - ik} \quad (2.45)$$

Using the effective range expansion in Equation 2.35, the  $f_0$  can be written in terms of the scattering length

$$f_0 \approx \frac{1}{-\frac{1}{a} + \frac{1}{2}k^2 r_e - ik} \quad (2.46)$$

In addition for  $k \rightarrow 0$ ,  $f_0$  simplifies as,

$$f_0 \approx -\frac{a}{1 + ika} \quad (2.47)$$

This brings us back to the importance of the scattering length and how it determines most of the collisional properties for low-energy scattering.

### 2.6.3 Scattering cross-section

Having determined the scattering amplitude, we relate this to the scattering cross-section in this subsection. Since the scattering cross-section determines the strength of elastic scattering, it is important for processes such as evaporative cooling. The scattering cross-section is closely related to the probability currents associated with the incoming and outgoing waves in the scattering problem. A wavefunction  $\psi$  and its density  $\rho = |\psi|^2$  is associated with a

probability current  $j$  given by,

$$\vec{j} = \frac{\hbar}{2mi} (\psi^* \nabla \psi - \psi \nabla \psi^*) \quad (2.48)$$

This probability current satisfies the continuity equation,

$$\nabla \cdot \vec{j} + \frac{\partial \rho}{\partial t} = 0 \quad (2.49)$$

The probability current for the incoming wave  $j_{in}$  and outgoing scattered wave  $j_{sc}$  are then

$$j_{in} = \frac{\hbar k}{m} \quad (2.50)$$

$$j_{sc} = \frac{\hbar k}{m} |f(\theta)|^2 \quad (2.51)$$

The differential scattering cross-section then relates the magnitude of the scattered wave probability current to the incoming wave probability current and is given by  $j_{sc}/j_{in}$  as follows,

$$\left( \frac{d\sigma}{d\Omega} \right) = |f(\theta)|^2 \quad (2.52)$$

The total cross-section  $\sigma$  can be obtained by integrating the differential cross-section around the solid angle  $\Omega$ . Using the expression for  $f(\theta)$  in Equation 2.43 and orthogonal properties of Legendre Polynomials, the total cross section can be obtained as

$$\sigma = 4\pi \sum_l (2l+1) |f_l|^2 \quad (2.53)$$

Thus the total cross section is given by contributions from the cross-sections of the different partial waves  $|f_l|^2$  and the factor  $(2l+1)$  accounts for the degeneracy of a certain  $l$  scattering channel. In the ultracold limit where only s-waves contribute, the scattering cross-section in terms of the s-wave scattering length using Equation 2.47 can be written as,

$$\sigma_0 = \frac{4\pi a^2}{1 + k^2 a^2} \quad (2.54)$$

The s-wave scattering cross-section  $\sigma_0$  depends only on the magnitude of the scattering length and not its sign. Even when the scattering length diverges at the unitary limit, the scattering cross-section is finite and reaches a maximum value given by

$$\sigma_0^{max} = \frac{4\pi}{k^2} \quad (2.55)$$

### 2.6.4 Scattering of identical atoms

In the previous subsection, a partial wave expansion of the scattering wavefunction was performed and expressions for the cross-section were obtained. The expression for the scattering wavefunction in Equation 2.37 considered the two scattering constituents as non-identical particles. The wavefunction needs to be symmetrized( $\psi_+$ ) or anti-symmetrized( $\psi_-$ ) when considering scattering of identical particles depending on whether they are bosons or fermions as follows,

$$\psi_{\pm} = \underbrace{e^{ikz} \pm e^{-ikz}}_{\psi_{in}} + \underbrace{\frac{f(\theta) \pm f(\pi - \theta)}{r}}_{\psi_{sc}} e^{ikr} \quad (2.56)$$

The partial wave expansion of this wavefunction can be performed similar to Equation 2.40. The incoming wave  $\psi_{in}$  and the scattered wave  $\psi_{sc}$  can now be expanded using the properties of  $P_l(\cos \theta)$  under transformation  $\theta \rightarrow \pi - \theta$  as follows

$$P_l(\cos(\pi - \theta)) = (-1)^l P_l(\cos \theta)$$

$$\psi_{in} = \sum_l (2l + 1) i^l j_l(kr) \left[ 1 + (-1)^l \right] P_l(\cos \theta) \quad (2.57)$$

$$\psi_{sc} = \sum_l (2l + 1) e^{im} \left[ 1 + (-1)^l \right] \sin \eta_l P_l(\cos \theta) \quad (2.58)$$

The scattering amplitude  $f_{\pm}(\theta)$  and the total cross-section obtained by integration over the solid angle can be obtained as follows,

$$f_{\pm}(\theta) = \frac{2}{k} \sum_{l = \text{Even/Odd}} (2l + 1) e^{im} \sin \eta_l P_l(\cos \theta) \quad (2.59)$$

$$\sigma_{\pm} = 8\pi \sum_{l = \text{Even/Odd}} (2l + 1) |f_l|^2 \quad (2.60)$$

For bosons (fermions) only the even  $l = 0, 2, 4, \dots$  (odd  $l = 1, 3, 5, \dots$ ) partial waves enter into the expansion. The even/oddness of the partial waves is a direct manifestation of the symmetry of the wavefunction under exchange. In the case of bosons, experiments have verified the presence of only even  $l$  waves by measuring the angular dependence of the scattering-amplitudes[71]. When the two colliding atoms are fermionic  ${}^6\text{Li}$  atoms in the same internal state, only odd-partial waves are allowed. At low temperatures since the centrifugal barrier is quite high ( $\sim mK$ ) and collisions are suppressed, evaporative cooling of spin-polarized fermions is not possible. The situation where the colliding atoms belong to two different hyperfine states of the same atom is different. Here even though the wavefunction of the scattering atoms has to be (anti-)symmetrized, effectively same expressions as for the case of non-identical particles are obtained and collisions in all  $l$

channels are possible. Thus two  ${}^6\text{Li}$  atoms in two different hyperfine states can undergo s-wave collision at low temperature thus enabling evaporative cooling of the mixture.

### 2.6.5 Scattering in two-dimensions

All the expressions for the scattering length, amplitude and cross-section were for scattering situations in 3D. Experiments in this thesis are mainly performed in the quasi-2D limit where the trap with azimuthal symmetry has a finite aspect ratio  $\eta = \omega_r/\omega_z$ .  $\omega_r$  ( $\omega_z$ ) is the trap frequency along the radial (axial) direction. Only the results for the scattering length and amplitude for such a situation are summarized here and more details can be found in [72]. In such a situation, when the axial motion of the system is frozen out and only radial levels are populated a 2D scattering length  $a_{2D}$  can be defined as follows,

$$a_{2D} = l_z \sqrt{\frac{\pi}{A}} \exp\left(-\sqrt{\frac{\pi}{2}} \frac{l_z}{a}\right) \quad (2.61)$$

where  $l_z$  is the harmonic oscillator length along the axial direction and  $A = 0.905$  is a constant. The s-wave scattering amplitude is different from the 3D case and is,

$$f_0(k) = \frac{-4}{\cot \delta_0(k) - i} \quad (2.62)$$

The s-wave scattering phase shift  $\delta_0$  is,

$$\cot \delta_0(k) = \frac{2}{\pi} \ln(ka_{2D}) \quad (2.63)$$

In the many-body limit, the term  $\ln(k_F a_{2D})$  is then used to quantify interactions in a Fermi gas.

### 2.6.6 Feshbach Resonances

In the scattering scenarios presented previously the internal structure of the scattering constituents was not considered. However in experiments consisting of multi-component quantum gases, the scattering potential depends on the internal structure of the atoms. For example consider two atoms with a single valance electron like  ${}^6\text{Li}$ . The atoms can approach the scattering region with their electron spins aligned (triplet channel) or anti-aligned (singlet channel). Since the spin-singlet is anti-symmetric, the motional wavefunction of these electrons should be symmetric. The motional wavefunction in this case is built from molecular orbitals and for symmetric combinations the electrons can be found in a region between the nuclei. This effectively screens the nuclei thereby reducing the repulsion. For the triplet potential since the motional wavefunction is anti-symmetric, the electrons are not found in the inter-nuclear region and hence cannot effectively screen the nuclear charge. Thus

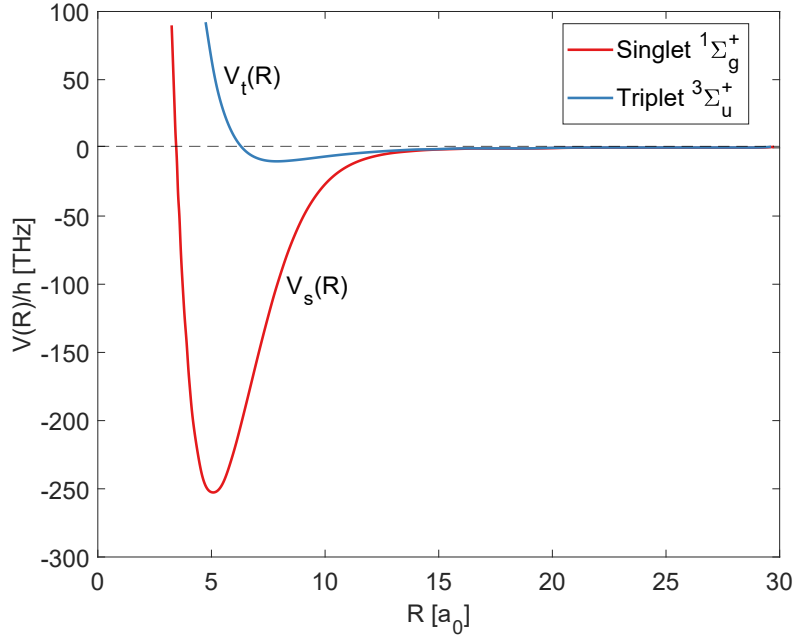


Figure 2.17: **Singlet and triplet scattering potentials for  ${}^6\text{Li}_2$  dimer with the two atoms in the ground electronic state  $2^2\text{S}_{1/2}$ .** The singlet ( $V_s(R)$ ) and triplet ( $V_t(R)$ ) potentials are plotted as a function of internuclear distance  $R$ . The singlet  ${}^1\Sigma_g^+$  potential (red) is quite deep since with an anti-symmetric spin wavefunction, the spatial wavefunction is symmetric and the two valence electrons find themselves between the two nuclei. This facilitates screening of the nuclear charge effectively reducing the repulsion between the nuclei. The potential supports 38 vibrational levels and the last bound state belongs to  $|\nu = 38, J\rangle$  rovibrational state and has an energy  $\approx 1.38$  GHz below the threshold. This leads to a relatively small singlet scattering length of  $a_s = 45.17a_0$  ( $a_0$  is the Bohr radius). On the contrary, the triplet  ${}^3\Sigma_u^+$  potential (blue) is rather shallow since due to the symmetric spin-state the motional wavefunction of the electrons is anti-symmetric and prevents the electrons from being present in the inter-nuclear region. Thus the nuclei are not as well screened by the electrons leading to higher repulsion. Unlike the singlet potential, the triplet potential supports only 9 bound states and the last bound state belongs to the rovibrational state  $|\nu = 9, J\rangle$  which is  $\approx 24$  GHz below the threshold. This leads to a large triplet scattering length of  $a_t = -2140a_0$ [2].

the singlet potential is much deeper than the triplet. The singlet ( $^1\Sigma_g^+$ ) and triplet ( $^3\Sigma_u^+$ ) potentials for two  $^6\text{Li}$  atoms in the ground state  $2^2S_{1/2}$  are shown in Figure 2.17. For the deep singlet channel, there are 38 vibrational states and the s-wave scattering length for the singlet channel is  $45.17a_0$ , where  $a_0$  is the Bohr radius. The shallower triplet state on the contrary has 9 vibrational levels and the potential depth is on the verge of supporting an additional bound state which leads to a large triplet scattering length of  $-2140a_0$ .

### 2.6.7 Coupling of scattering channels

With internal degrees of freedom present, the total Hamiltonian for the scattering problem can be written as,

$$H_{rel} = \underbrace{\frac{p_r^2}{2\mu} + \frac{\hbar^2 l(l+1)}{2\mu r^2} + \overbrace{V_D(r) + J(r)\vec{s}_1 \cdot \vec{s}_2}^{V(r)}}_{H_m} + \underbrace{g_e\mu_B\vec{S} \cdot \vec{B} - g_n\mu_B\vec{I} \cdot \vec{B}}_{H_Z} + \underbrace{A_{hf}(\vec{s}_1 \cdot \vec{i}_1 + \vec{s}_2 \cdot \vec{i}_2)}_{H_{hf}} \quad (2.64)$$

The Hamiltonian for relative motion ( $H_{rel}$ ) now includes a motional term ( $H_m$ ) as before and two additional terms due to internal degrees of freedom - Zeeman term ( $H_Z$ ) and Hyperfine term ( $H_{hf}$ ). Here  $\vec{s}_{1,2}$  ( $\vec{i}_{1,2}$ ) denotes the electron (nuclear) spin of the two atoms,  $\vec{S} = \vec{s}_1 + \vec{s}_2$  ( $\vec{I} = \vec{i}_1 + \vec{i}_2$ ) is the total electron (nuclear) spin of the atoms.  $V_D(r)$  is the direct contribution and  $J(r)$  is the exchange contribution and defined as follows,

$$V_D(r) = \frac{1}{4}V_s(r) + \frac{3}{4}V_t(r)$$

$$J(s) = V_t(r) - V_s(r)$$

This definition of  $V(r)$  makes it clear that the interaction potential is diagonal in the coupled electron spin basis and that the potential reduces to  $V_s(r)$  ( $V_t(r)$ ) for a singlet (triplet). The energy scales of each of these terms are known. The Zeeman and hyperfine energy scales were presented in Section 2.2 and is of the order of MHz/GHz. The potential energy curves for the singlet and triplet at short distances were shown in Figure 2.17 and are orders of magnitude larger at THz. At large internuclear separations the interaction potential goes to zero and the resulting electronic Hamiltonian is diagonal in states ( $|1\rangle \dots |6\rangle$ ) found in Section 2.2. However at short internuclear distances the Hamiltonian is diagonal in  $|SM_S\rangle$  basis. As particles in two different hyperfine states enter the scattering region, the total wavefunction needs to be anti-symmetric and hence the atoms find themselves in an

anti-symmetric spin state composed of the hyperfine states  $|1\rangle \dots |6\rangle$  as follows,

$$\chi_- = \frac{1}{\sqrt{2}} (|ij\rangle - |ji\rangle) \quad (2.65)$$

where  $|i\rangle, |j\rangle$  are the hyperfine states. However, at short distances these states need to be projected onto the coupled electron spin basis states  $|SM_S\rangle$ . Depending on the magnetic field and the hyperfine states involved in the collision, the interaction potential is a combination of singlet and triplet potential with different weights. The Zeeman term  $H_Z$  is diagonal in the total electron and nuclear spins and doesn't cause coupling of collision channels. All the coupling arises from the hyperfine interaction as will be elaborated below. The hyperfine term can be rewritten as

$$H_{hf} = \underbrace{\frac{A_{hf}}{2} (\vec{s}_1 + \vec{s}_2) \cdot (\vec{i}_1 + \vec{i}_2)}_{H_{hf}^+} + \underbrace{\frac{A_{hf}}{2} (\vec{s}_1 - \vec{s}_2) \cdot (\vec{i}_1 - \vec{i}_2)}_{H_{hf}^-} \quad (2.66)$$

The  $H_{hf}^+$  term couples only states within the singlet or triplet manifold. On the contrary the  $H_{hf}^-$  term couples the singlet and triplet manifolds and is responsible for the interesting Feshbach resonance arising in atomic collisions[67]. The channel that the incoming hyperfine states couple to has to then be projected back to the hyperfine states at large separations and effectively a collision in the  $|i\rangle, |j\rangle$  hyperfine channel can couple to a channel consisting of  $|i'\rangle, |j'\rangle$ . The hyperfine interaction term conserves  $M_F = m_f^i + m_f^j$  and hence only states with  $m_f^i + m_f^j = m_f^{i'} + m_f^{j'}$  are coupled by it. However, the channel  $|i'\rangle, |j'\rangle$  can be asymptotically larger or smaller in energy. If the coupled channel  $|i'\rangle, |j'\rangle$  is asymptotically higher in energy than the incoming channel  $|i\rangle, |j\rangle$ , it is denoted as a closed channel since atoms cannot leave the collision region in this channel. However, if a bound state in the closed channel is resonant with the incoming energy, the scattering length diverges as in the case where the potential depth was tuned in Figure 2.16 to have a bound state at the threshold. The scattering length in a situations with channel coupling can be obtained from a coupled channel calculation[73].

The hyperfine term  $H_{hf}^-$  which couples channels couples the following singlet and triplet channels  $|0, 0\rangle \longleftrightarrow |1, \pm 1\rangle$  and  $|1, 0\rangle \longleftrightarrow |0, 0\rangle$ [67]. States  $|0, 0\rangle$  and  $|1, 0\rangle$  do not tune with magnetic fields since their  $m_S$  projection is zero. On the contrary states  $|1, \pm 1\rangle$  tune with magnetic field since they have a non-zero  $m_S$  projection. This coupling among states  $|1, \pm 1\rangle \longleftrightarrow |0, 0\rangle$  combined with a differential magnetic moment between them is responsible for tunable magnetic Feshbach resonances. For example for a scattering scenario involving asymptotic states in the  $|1\rangle - |2\rangle$  channel, at large magnetic fields the incoming channel is mostly triplet dominated since both the states have electron spin projections  $m_s = -1/2$ . Using the conservation of  $M_F = m_f^1 + m_f^2$ , the only states that the  $|1\rangle - |2\rangle$  mixture couples to is  $|4\rangle - |5\rangle, |3\rangle - |6\rangle, |1\rangle - |4\rangle$  and  $|2\rangle - |5\rangle$ [2]. Since the last bound state

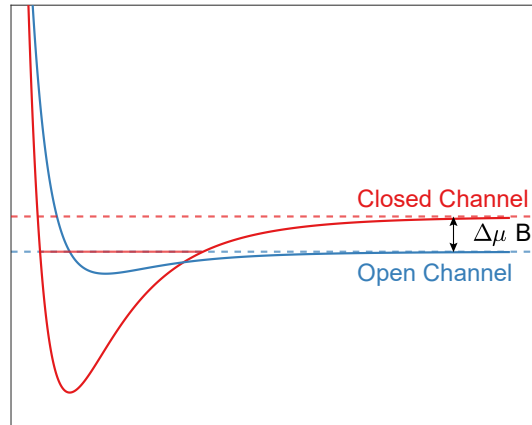


Figure 2.18: **Magnetically tuned Feshbach resonance.** A Feshbach resonance occurs when the scattering particles have internal structure and the interaction potential depends on this internal configuration. The atoms enter the scattering region in an open channel (blue) and can couple to a closed channel (red) which is higher in energy at large separations. The coupling occurs due to hyperfine interaction in the case of a magnetic Feshbach resonance. The atoms cannot leave in the closed channel since it is energetically higher in energy. The internal states associated with these potential channels have a differential magnetic moment and hence they can be tuned relative to each other. When the incoming energy in the open channel matches the energy of a bound state in the closed channel, the scattering length  $a$  diverges.

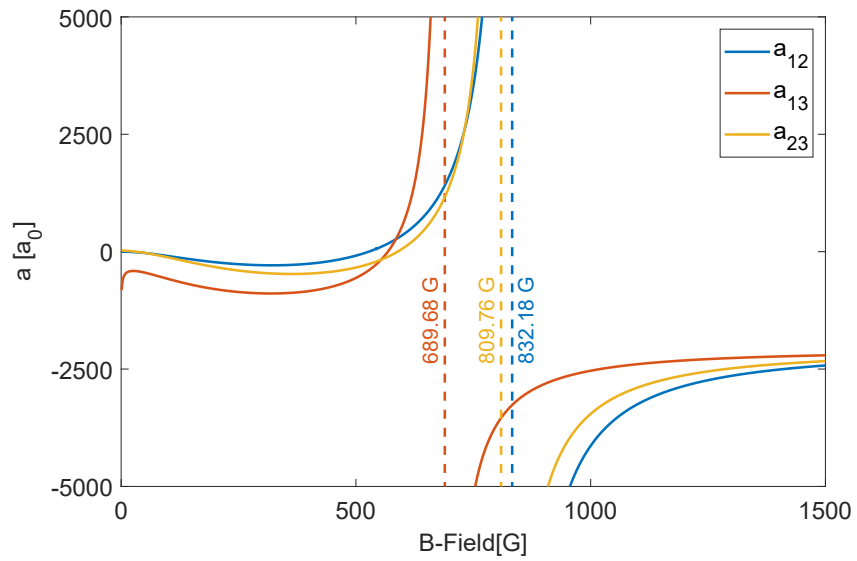


Figure 2.19: **Scattering lengths among the high-field seeking states  $|1\rangle, |2\rangle, |3\rangle$  of  ${}^6\text{Li}$ .** The positions of the resonances are indicated for each of the combinations. The resonances are broad, except for an additional very narrow resonance for the  $|1\rangle - |2\rangle$  mixture around 543G not shown. The resonance positions overlap for the three spin combinations and this is later used in Chapter 5 to prepare spin-imbalanced systems in the motional ground state.

of the singlet potential is  $\approx 1.35\text{GHz}$  below the singlet asymptote, by tuning the magnetic field the energy of the triplet channel can be pushed to lower values. Thus the triplet incoming channel of the former mixture can couple with singlet channels in the latter state combinations and a resonant enhancement as a function of magnetic field can be observed. The combinations of the three lowest hyperfine states  $|1\rangle, |2\rangle, |3\rangle$  are used for experiments in this thesis and a plot of the scattering lengths in this scenario as a function of the magnetic field is shown in Figure 2.19. The resonance in this case is broad and can be modelled by a dispersive relation between the scattering length and the magnetic field as follows

$$a = a_{bg} \left( 1 - \frac{\Delta}{B - B_0} \right) \quad (2.67)$$

where  $a_{bg}$  is the background scattering length;  $\Delta$  is the width of the resonance and;  $B_0$  is the position of the resonance.  $B_0, \Delta$  and  $a_{bg}$  for the spin mixtures of  $|1\rangle, |2\rangle, |3\rangle$  are known precisely[74].

In Section 2.5, two-photon transitions between the hyperfine states  $|1\rangle \dots |6\rangle$  were summarized. The reason for using these transitions was to perform very fast flips between these states, on a time-scale orders of magnitude faster than the motional time-scales in the system. If the final state has (close to) no interactions, this enables measurement of in situ quantities presented in Chapters 3,4 and 5. Since we are interested in the behaviour of interacting systems, we start with states consisting of  $|1\rangle - |3\rangle$  or  $|2\rangle - |3\rangle$  mixtures. At large magnetic fields of interest ( $> 500\text{G}$ ), the entrance collision channel for these mixtures is triplet ( $|1, -1\rangle$ ) dominated. For example as mentioned previously the  $|1\rangle - |2\rangle$  mixture couples to  $|4\rangle - |5\rangle, |3\rangle - |6\rangle, |1\rangle - |4\rangle$  and  $|2\rangle - |5\rangle$ . All of these coupled channels are asymptotically larger in energy. The  $H_{hf}^-$  term couples this triplet incoming channel  $|1, -1\rangle$  to a singlet  $|0, 0\rangle$  in these coupled channels. Since the singlet potential has a bound state  $\approx 1.38\text{ GHz}$  below the asymptote, and the triplet potential tunes with  $2\mu_B \approx 2.8\text{ MHz/G}$  the bound state can be made resonant with accessible magnetic fields. To turn off interactions we flip state  $|3\rangle$  to  $|4\rangle$  using the aforementioned two-photon transition resulting in a  $|1\rangle - |4\rangle$  mixture. At these magnetic fields, the incoming channel for the  $|1\rangle - |4\rangle$  mixture is a combination of singlet ( $|0, 0\rangle$ ) and triplet ( $|1, 0\rangle$ ) potentials and couples to triplet ( $|1, \pm 1\rangle$ ) and singlet ( $|0, 0\rangle$ ) potentials respectively in  $|1\rangle - |2\rangle, |3\rangle - |6\rangle, |4\rangle - |5\rangle$  and  $|2\rangle - |5\rangle$  collision channels. The singlet states in the closed channels do not have to be considered since they do not have a differential magnetic moment with the incoming triplet ( $|1, 0\rangle$ ) channel.  $|1\rangle - |2\rangle$  mixture does not have to be considered since it is lower in energy and being a triplet  $|1, -1\rangle$  coupling to a bound state is ruled out. The only closed channel combinations which matter are triplet states  $|1, \pm 1\rangle$  in channels  $|4\rangle - |5\rangle, |3\rangle - |6\rangle$  and  $|2\rangle - |5\rangle$ . The lowest bound state of the triplet potential is  $\approx 24\text{ GHz}$  below the triplet asymptote and hence in the magnetic field regions considered no bound state in these channels can be made resonant with the incoming energy since the triplet tunes with approximately  $\pm 2.8\text{ MHz/G}$  and only a range of  $\approx 2.8\text{ GHz}$  can be achieved. Thus the scattering in the  $|1\rangle - |4\rangle$  mixture

is determined by the open channel which is a combination of singlet and triplet potentials without any resonant enhancement due to closed channel coupling. Since the singlet potential is much deeper than the triplet, the effect of the triplet potential is a perturbative correction leading to the scattering length being mostly small as in the singlet case. We have measured the scattering length in this mixture by measuring two-particles energies in a harmonic trap using interaction modulation spectroscopy introduced in Chapter 3. We obtain an upper bound of  $|a| < 500a_0$  and hence the  $|1\rangle - |4\rangle$  mixture can be considered to be nearly non-interacting compared to the initial scattering length before turning off interactions.

### 2.7 Single particle imaging

In this section the relevant details associated with single particle imaging with spin resolution is summarized. Unlike quantum gas microscopes[3], imaging is performed in free space in absence of any confining potentials. Since only a small number of photons are scattered ( $\sim 200/\text{atom}$ ) and collected ( $\sim 20/\text{atom}$ ) elaborate Raman sideband cooling schemes during imaging are circumvented. The very small number of photons collected however requires an EMCCD camera which can operate in photon counting mode[76]. The EMCCD sensor in such cameras is cooled to low temperatures and have low background noise levels. In addition Clock Induced Charges(CICs), which are created when clock pulses are applied for pixel readout, are minimized. These low noise levels make it possible to detect single photons and with very few photons per atom, an atom can be reliably detected. A detailed description of the image analysis needed to obtain atom positions is presented in [77]. However, simultaneous imaging of two spin states is needed to extract correlation functions in interacting systems and an overview of how this is done is summarized here.

Two aspects determine the internal state manipulations which are needed. Firstly, the possible optical transitions determine which internal states are preferred for imaging. All possible optical dipole transitions along with their polarization and magnetic field dependence were presented in Section 2.4. We utilize only transitions on the D2 line and the possible transitions can be seen in Figure 2.7. Additionally, the imaging path has a polarization constraint since it is used for both MOT beams along top/down directions and fluorescence imaging. The polarization constraint requires that only  $\sigma-$  light can be collected. State  $|3\rangle$  has a completely closed  $\sigma-$  transition to the excited state  $|1''\rangle$  at high field and is preferred. States  $|1\rangle, |2\rangle$  on the contrary do not have a closed transition and require at least one repumping laser to efficiently collect photons and ensure that the atom does not end up in a dark state during imaging. Further, the repumping laser is  $\sigma+$  polarized and so would be the spontaneous emission light from this transition. Due to the polarization constraint this cannot be collected on the camera. Hence to image the two spin components, we always image state  $|3\rangle$  and perform internal state manipulations to transform the state prior to imaging. Secondly, interaction among the spin states determine

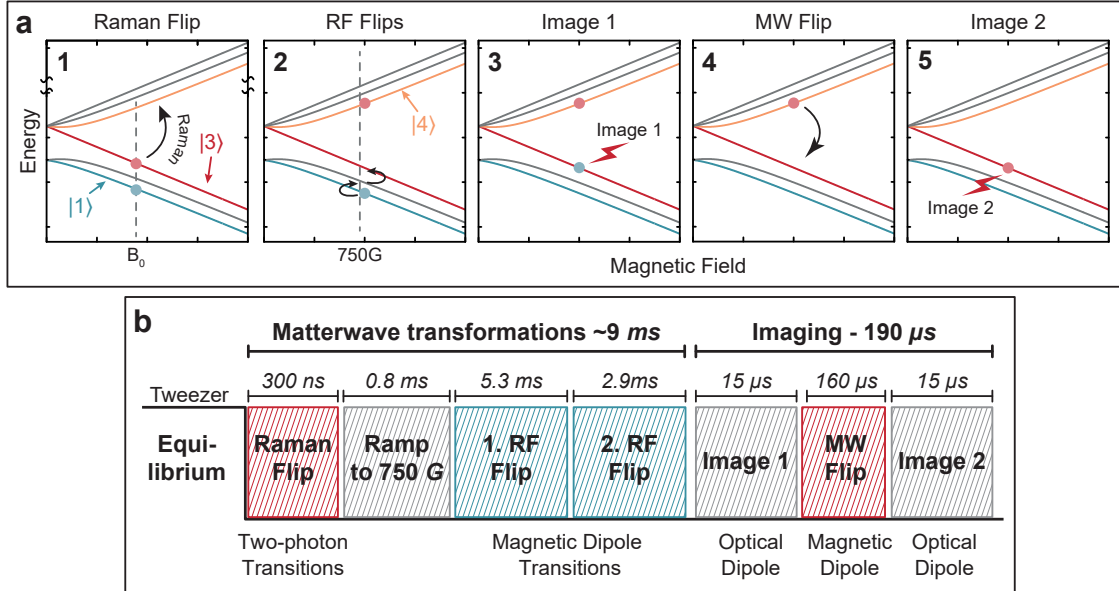


Figure 2.20: **Imaging sequence for two-state imaging.** (a) To perform two-state imaging, a number of internal state manipulations are required. (1) The manipulations start with a two-photon Raman transition to transfer atoms in state  $|3\rangle$  to  $|4\rangle$  using a coherent  $\pi$ -pulse. Simultaneously matterwave transformations (For example an expansion in a harmonic trap for a quarter time period  $T/4$ ) are started. For all initial interaction strengths, the matterwave transformation is performed at 750G. (2) During the matterwave transformations, rf Landau-Zener pulses are used to transfer atoms in state  $|1\rangle \rightarrow |2\rangle \rightarrow |3\rangle$ . These are completed before the matterwave transformations conclude. (3) Image of atoms in state  $|3\rangle$  is taken. (4) A microwave (MW) Landau-Zener passage transfers atoms in state  $|4\rangle$  back to state  $|3\rangle$ . (5) Atoms in state  $|3\rangle$  are imaged. Thus both spin components can be imaged and in situ quantities can be obtained. (b) Typical time-scales for each of the above mentioned transitions are shown. The kind of internal state manipulation is indicated below each transition. The size of the boxes corresponding to each transformation is not to scale. Figure adapted from [75]

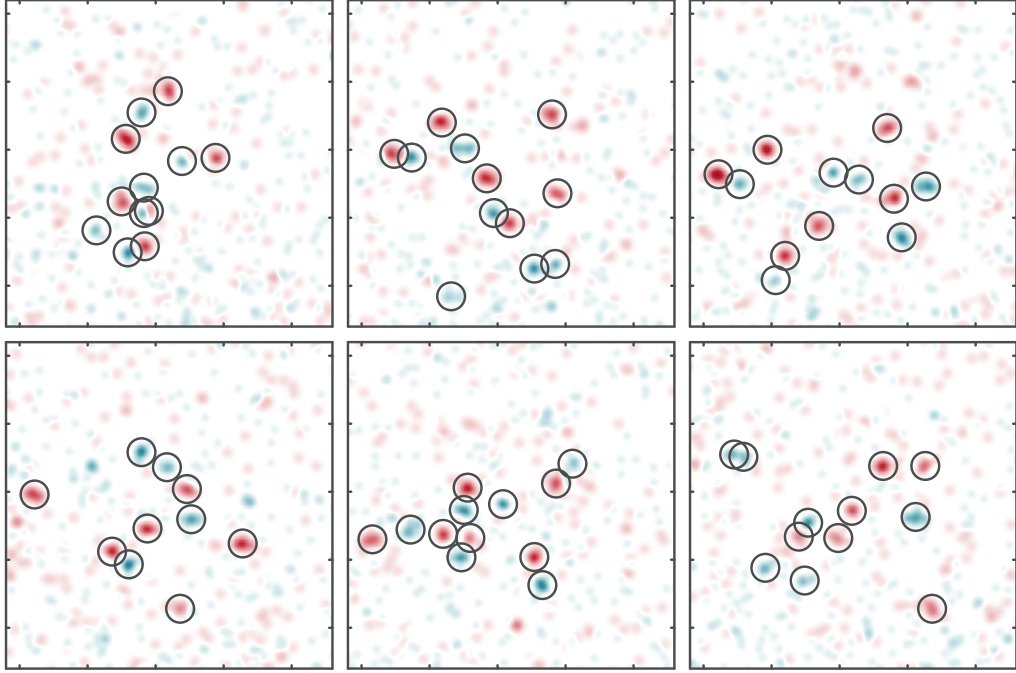


Figure 2.21: **Snapshots from two-state microscopy.** A few snapshots from the resulting imaging sequence is shown. The blue and red false color channels denote images for the two spin states. The blobs with circles around them are identified as atoms after processing the images[77]. The blobs without circles around them arise from CICs and background photons and are rejected based on a thresholding scheme. These snapshots were taken for a system of 6+6 atoms after a single matterwave transformation to obtain the in situ momentum. Figure adapted from[75]

further internal state manipulations. In order to measure in situ properties of the system, matterwave transformations involving the system is necessary. This would only work if during these matterwave transformations the system is (nearly) non-interacting. Starting with an interacting  $|1\rangle - |3\rangle$  mixture, flipping state  $|3\rangle$  to state  $|4\rangle$  would render the resulting  $|1\rangle - |4\rangle$  mixture nearly non-interacting. A transition from the interacting to the non-interacting mixture also needs to be performed orders of magnitude faster than the motional time-scales. Two-photon Raman transitions which make this possible were presented in Section 2.5. Transition between states  $|3\rangle - |4\rangle$  was found to have a large two-photon Rabi rate  $\Omega_R$  along with a large quality factor  $\beta$ . Further, the optimal detuning for this two-photon transition was also determined in Figure 2.13.

The complete imaging sequence is shown in Figure 2.20. The experiment begins by

preparing an interacting system in a  $|1\rangle - |3\rangle$  or  $|2\rangle - |3\rangle$  mixture and the sequence is presented here for the  $|1\rangle - |3\rangle$  mixture. The sequence for the  $|2\rangle - |3\rangle$  mixture is similar. The sequence starts by first switching-off interactions using a two-photon Raman transition. This Raman transition converts all atoms in state  $|3\rangle$  to  $|4\rangle$  using a coherent  $\pi$ -pulse 3 orders of magnitude faster than the motional time-scales in the system. The system now finds itself in a  $|1\rangle - |4\rangle$  mixture and one or more matterwave transformations ensue. During these matterwave transformations lasting  $\approx 9\text{ms}$ , the internal states of atoms in state  $|1\rangle$  are transformed first to  $|2\rangle$  then to  $|3\rangle$  using radio frequency (rf) magnetic dipole transitions. A Landau-Zener frequency sweep is performed to transfer all atoms in the initial state to the final state with high fidelities. The transition matrix elements for these transitions were summarized in Figure 2.5. Magnetic dipole  $|1\rangle - |2\rangle$  and  $|2\rangle - |3\rangle$  are weak and in total require  $\approx 8\text{ms}$  to perform. At the end of the matterwave transformation(s), the system is illuminated for approximately  $15\mu\text{s}$  and atoms in state  $|3\rangle$  (originally state  $|1\rangle$  atoms of the interacting mixture) are detected. This is followed by a microwave (MW) Landau-Zener passage to transfer all the atoms in state  $|4\rangle$  back to state  $|3\rangle$  for imaging. The magnetic dipole transition between states  $|3\rangle - |4\rangle$  (Figure 2.5) is approximately 50 times stronger than  $|1\rangle - |2\rangle$  and  $|2\rangle - |3\rangle$  transitions and takes approximately  $160\mu\text{s}$ . For this a two-photon Raman transition is not optimal since the sample has already expanded and the transition fidelities are much better with MW. The transition also does not have to be extremely fast and the additional expansion time though small can nonetheless be compensated for by taking this into account for the matterwave transformation and initial position/momentum lookup. A resulting image obtained at the end of these transformations is shown in Figure 2.21.



## 3 Spin-balanced few-fermion systems

In this chapter experiments with mesoscopic spin-balanced few-fermion systems in quasi-2D harmonic oscillator potentials are presented. The presence of symmetries in 2D results in degenerate motional orbitals grouped into shells. The prerequisites related to the single particle spectrum and the eigenstates are first presented. The properties of two-particles confined in such a harmonic trap interacting via contact interactions is then summarized. The energies of the ground and first excited states are particularly important since they are used to quantify the interaction strength for all experiments presented in this thesis.

The mesoscopic systems we experimentally study consist of a two-component mixture of resonantly interacting fermions with 2 to 3 occupied shells resulting in closed shell configurations of  $1 + 1$ ,  $3 + 3$  and  $6 + 6$  atoms. Such systems are far removed from the many-body limit and might at first seem incapable of explaining truly many-body properties like phase transitions and collective modes. In the many-body limit at  $T = 0$  a two-component mixture of fermions which are attractively interacting undergo transition to a superfluid state at arbitrarily weak attractions. At this point the excitation spectrum features a gap closing and as interactions are further increased, the amount of pairing in the system quantified by the order parameter  $\Delta$  increases. In this superfluid regime, there exists a collective amplitude mode associated with a modulation of  $|\Delta|$  called the Higgs mode[78]. Motivation for the experiments of few-fermion systems in 2D came from a numerical study where the authors predicted that already for such small systems a precursor of a phase transition could be observed[79]. Evidence for an asymptotic gap closing behaviour as a function of interaction was provided for a system as small as  $3 + 3$  atoms. A brief summary of key experimental observables from the proposal is provided.

An experiment observing such a phase transition precursor is then presented[80]. Starting with the preparation of spin-balanced few-fermion systems in closed shell configurations, the experimental protocol to extract the excitation spectrum is summarized and the measurements are presented. The nature of excitations of the resulting modulation scheme is pointed out and the effect of particle number is studied. Due to the finite size of the system, decay channels are strongly suppressed which make this precursor of the many-body Higgs mode long lived. The coherent properties of the precursor are then demonstrated by driving coherent oscillations between the few-body ground and excited states.

Since the precursor of the Higgs mode is associated with pair excitations only at the Fermi surface, Pauli blocking with a frozen fermion core plays an important role in the emergence of these collective modes. Using the ability to perform microscopy of the few-body system and extract correlation functions, experiments on microscopic observation of Pauli blocking

are presented[81]. Pauli blocking is a consequence of the anti-symmetrization of the total wavefunction under particle exchange and this results in fermionic anti-bunching. In a harmonic trap this leads to correlations which are termed Pauli Crystals[21]. The effect of temperature on the visibility of these correlated structures are then presented and show a continuous "melting" of the crystal with temperature.

Experiments on microscopy of an interacting system in momentum space[75] are then presented and correlation functions are evaluated. The second-order density-density correlator in momentum space indicates the formation of Cooper pairs at the Fermi surface for finite interaction strengths. As the interaction strength is increased, correlations appear even within the Fermi surface indicative of a molecular like state. Comparison to the many-body limit is discussed and the number of opposite momentum pairs having a zero center-of-mass(COM) momentum are evaluated. A brief discussion of the onset of pairing only at finite interaction strength in contrast to infinitesimally weak attractions in the many-body limit is provided.

### 3.1 Energy levels of a 2D harmonic oscillator

In this section we summarize the eigenstates of the 2D harmonic oscillator along with the associated eigen energies. The Hamiltonian  $\hat{\mathbf{H}}$  for the 2D Harmonic oscillator is

$$\hat{\mathbf{H}} = \frac{1}{2}\hat{\mathbf{p}}^2 + \frac{1}{2}\hat{\rho}^2 \quad (3.1)$$

where  $\hat{\mathbf{p}}$  is the momentum operator in units of the harmonic oscillator momentum  $p_0 = \sqrt{\hbar m\omega}$ ,  $\hat{\rho}$  is the position operator in units of the harmonic oscillator length scale  $l_0 = \sqrt{\frac{\hbar}{m\omega}}$  and  $\hat{\mathbf{H}}$  is in units of the harmonic oscillator energy  $\hbar\omega$ . To get the spatial representation of the eigenstates, the position representation for the operators  $\hat{\mathbf{p}} \rightarrow -i\nabla$  and  $\hat{\rho} \rightarrow \rho$  are introduced. This leads to the following differential equation to get the eigenvalues and eigenstates

$$-\frac{1}{2\rho} \frac{\partial}{\partial \rho} \left( \rho \frac{\partial \Phi_n^{|m|}(\rho, \phi)}{\partial \rho} \right) - \frac{1}{2\rho^2} \frac{\partial \Phi_n^{|m|}(\rho, \phi)}{\partial \phi} + \frac{1}{2}\rho^2 \Phi_n^{|m|}(\rho, \phi) = E_n^{|m|} \Phi_n^{|m|}(\rho, \phi) \quad (3.2)$$

Using the Ansatz that the radial and angular part can be separated as follows,

$$\Phi_n^{|m|} = R_n^{|m|}(\rho) T_m(\phi) \quad (3.3)$$

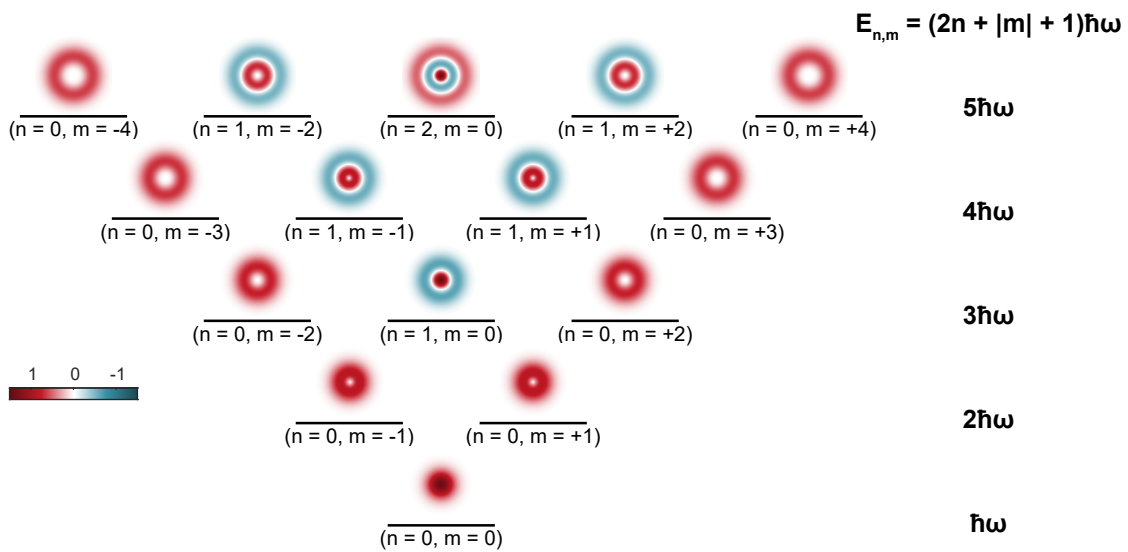


Figure 3.1: **Eigenstates of the 2D harmonic oscillator.** A shell structure appears due to the degeneracy of states in a 2D harmonic oscillator potential. There are  $N$  states of energy  $N\hbar\omega$  and the associated radial part of the wavefunctions  $R_n^{|m|}$  are shown for each of the orbitals. The angular part of the wavefunction only introduces a complex phase modulation of angular periodicity  $2\pi m$  and is not shown here.

and solving this differential equation gives the following eigenvalues and eigenstates,

$$E_n^{|m|} = 2n + |m| + 1 \quad (3.4)$$

$$\Phi_n^{|m|}(\rho, \phi) = \sqrt{\frac{2n!}{(n + |m|)!}} \rho^{|m|} L_n^{|m|}(\rho^2) e^{-\rho^2/2} \frac{e^{im\phi}}{\sqrt{2\pi}} \quad (3.5)$$

where  $n(m)$  denotes the radial translational (angular rotational) quantum number and  $L_n^{|m|}$  is the generalized Laguerre polynomial. The first few eigenstates, their energies and the associated degeneracies for a particle in a 2D harmonic oscillator potential are depicted in Figure 3.1. Unlike in the 1D case, additional symmetries in 2D result in the appearance of a shell structure. The  $N^{\text{th}}$  shell has an energy  $N\hbar\omega$  and possesses  $N$  degenerate motional orbitals.

### 3.2 Two particles in a harmonic trap

The previous section introduced the single particle eigenstates for a 2D-harmonic oscillator potential. Here we summarize how the energies of two interacting particles in a harmonic trap change due to a contact interaction between them. An analytical solution for two atoms of equal mass in an isotropic 3D trap have been solved[82] and recent analytical methods have extended this to the case of anisotropic traps[83]. We are more interested in the case of a quasi-2D trap which accurately describes the experimental system we have. Analytical solutions are also available for this situation[84]. The Hamiltonian for such a system can be described as

$$\hat{\mathbf{H}} = \frac{\hat{\mathbf{p}}_1^2}{2m} + \frac{\hat{\mathbf{p}}_2^2}{2m} + \frac{1}{2}m\omega_r^2\hat{\rho}_1^2 + \frac{1}{2}m\omega_r^2\hat{\rho}_2^2 + \frac{1}{2}m\omega_z^2\hat{\mathbf{z}}_1^2 + \frac{1}{2}m\omega_z^2\hat{\mathbf{z}}_2^2 + \hat{\mathbf{V}}_{\text{int}}(\vec{\mathbf{r}}_1 - \vec{\mathbf{r}}_2) \quad (3.6)$$

Using the center of mass(COM)  $\vec{\mathbf{R}} = (\vec{\mathbf{r}}_1 + \vec{\mathbf{r}}_2)/2$  and relative(rel) co-ordinates  $\vec{\mathbf{r}} = \vec{\mathbf{r}}_1 - \vec{\mathbf{r}}_2$ , the Hamiltonian can be decomposed into the COM and rel parts as follows

$$\hat{\mathbf{H}} = \underbrace{\frac{\hat{\mathbf{P}}^2}{2M} + \frac{1}{2}m\omega_r^2\hat{\mathbf{R}}^2 + \frac{1}{2}m\omega_z^2\hat{\mathbf{Z}}^2}_{\hat{\mathbf{H}}_{\text{COM}}} + \underbrace{\frac{\hat{\mathbf{p}}^2}{2\mu} + \frac{1}{2}\mu\omega_r^2\hat{\rho}^2 + \frac{1}{2}\mu\omega_z^2\hat{\mathbf{z}}^2 + \hat{\mathbf{V}}_{\text{int}}(\vec{\mathbf{r}})}_{\hat{\mathbf{H}}_{\text{rel}}} \quad (3.7)$$

where  $M = 2m$  is the total mass,  $\mu = m/2$  is the reduced mass.  $\hat{\mathbf{H}}_{\text{COM}}$  is not affected by interactions since the interactions only depend on the relative separation of the atoms.  $\hat{\mathbf{H}}_{\text{rel}}$  can be rewritten in position representation with lengths in units of  $\sqrt{\hbar/(\mu\omega_z)}$ , momentum in units of  $\sqrt{\hbar\mu\omega_z}$ , energies in units of  $\hbar\omega_z$  and  $\eta = \omega_r/\omega_z$  as follows

$$\mathbf{H}_{\text{rel}} = -\frac{\nabla^2}{2} + \frac{1}{2}(\eta^2\rho^2 + z^2) + 2\pi a \delta^{(3)} \frac{\partial}{\partial r} \quad (3.8)$$

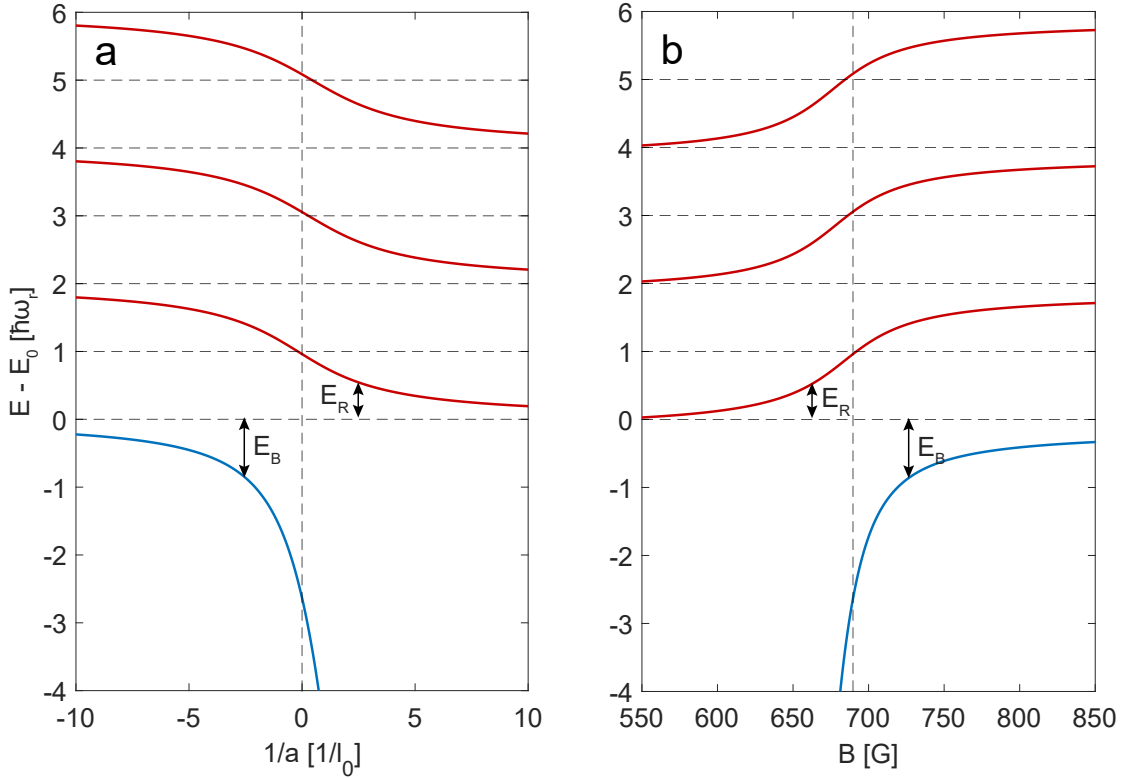


Figure 3.2: **Energy of two particles in a quasi-2D trap with  $\eta = \omega_r/\omega_z = 1/7$  interacting via contact interactions.** For a harmonic potential the Hamiltonian separates into the COM and rel parts and only the rel motion is affected by interactions. (a) Energies of relative motion for zero COM excitations. The energies relative to the zero-point energy ( $E_0$ ) versus interaction ( $1/a$ ). The energy  $E - E_0$  is in units of  $\hbar\omega_r$  and  $a$  is in units of the harmonic oscillator length  $l_0 = \sqrt{\hbar/(m\omega_r)}$ . (b) For two  ${}^6\text{Li}$  atoms in states  $|1\rangle, |3\rangle$  the scattering length is tuned by changing the magnetic field  $B$ . The energy levels are now shown as a function of  $B$ . The vertical dashed line indicates the position of the Feshbach resonance and the horizontal dashed lines indicate the unperturbed energy levels. For the other mixture of states namely  $|1\rangle, |2\rangle$  and  $|2\rangle, |3\rangle$  the states are horizontally shifted to their resonance position. The attractive branch is denoted in blue and the repulsive branches in red. The energy of the ground (excited) state relative to the zero-point energy  $E_0$  is the two-body binding (repulsion) energy  $E_B$  ( $E_R$ ) and is depicted in both (a) and (b) at different values of the scattering length.

Here the contact interaction term has been replaced by the Fermi pseudo-potential for s-wave scattering and  $a$  is the scattering length in the aforementioned length units. An Ansatz is introduced to build the eigenstates from the non-interacting basis states of the 2D-harmonic oscillator.

$$\psi(r) = \sum_{n,k} \Phi_{n,0}(\rho, \phi) \Theta_k(z) \quad (3.9)$$

Here only the basis states with  $m = 0$  are used for building the interacting eigenstates as the interaction potential being a  $\delta^{(3)}$  function couples only those basis states which have a non-vanishing value at  $r = 0$  (See Figure 3.1 for wavefunctions).  $\Phi_{n,m}(\rho, \phi)$  is the eigenstate along the radial+angular direction and was introduced in Section 3.1.  $\Theta_k(z)$  is the 1D harmonic oscillator wavefunction along the  $z$  direction and is

$$\Theta_k(z) = \frac{1}{\sqrt[4]{\pi}} \frac{1}{\sqrt{2^k k!}} e^{-z^2/2} H_k(z) \quad (3.10)$$

where  $H_k(z)$  is the Hermite polynomial of order  $k$ . Using the Ansatz Equation 3.9 in 3.8 and projecting on the non-interacting eigenstates with quantum numbers  $(n, 0, k)$  gives the following expression for the coefficients  $c_{n,k}$

$$c_{n,k} = C \frac{\Phi_{n,0}^*(0, \phi) \Theta_k^*(0)}{E_{n,k} - E} \quad (3.11)$$

where  $E_{n,k} = 2n\eta + k + \eta + 1/2$  is the energy of the non-interacting state with quantum numbers  $(n, 0, k)$ ,  $E$  is the energy of the interacting eigenstate and  $C$  is a constant which evaluates to

$$C = -2\pi a \frac{\partial}{\partial r} \left[ \sum_{n',k'} c_{n',k'} \left( r \Phi_{n',0}(\rho, \phi) \Theta_{k'}(z) \right) \right]_{r=0}$$

Since  $c_{n,k}$  is defined in terms of all the other coefficients  $c_{n',k'}$ , this is used to express the energy of the state in terms of the 3D scattering length  $a$  as follows

$$\frac{-1}{2\pi a} = \frac{\partial}{\partial r} (r\psi_\varepsilon(r))_{r=0} \quad (3.12)$$

where  $\psi_\varepsilon(r)$  evaluates to

$$\psi_\varepsilon(r) = \sum_{n,k} \frac{\Phi_{n,0}^*(0, \phi) \Theta_k^*(0) \Phi_{n,0}(\rho, \phi) \Theta_k(z)}{2\eta n + k - \varepsilon}$$

where  $\varepsilon = E - \eta - 1/2$  is the energy of the interacting eigenstate with respect to the zero-point energy. Using the generating functions for the Laguerre and the Hermite polynomials

one can simplify Equation 3.12 as

$$-\frac{\sqrt{\pi}}{a} = F(-\varepsilon/2) \quad (3.13)$$

where  $F(x)$  is defined as follows

$$F(x) = \int_0^\infty dt \left[ \frac{\eta e^{-xt}}{\sqrt{1 - e^{-t}}(1 - e^{-\eta t})} - \frac{1}{t^{3/2}} \right] \quad (3.14)$$

For a quasi-2D trap of aspect ratio  $\eta = 1/n$ , where  $n$  is an integer,  $F(x)$  can be further simplified yielding the following equation relating the scattering length  $a$  to the energy

$$\frac{n}{2a} = \sum_{l=0}^{n-1} \frac{\Gamma(-\frac{\varepsilon}{2} + \frac{l}{n})}{\Gamma(-\frac{\varepsilon}{2} - \frac{1}{2} + \frac{l}{n})} \quad (3.15)$$

The lowest energy level is usually denoted in literature as the attractive branch while the first(and higher) energy level(s) are denoted as the repulsive branch(es). The attractive branch always features a bound state whose energy becomes larger as the 3D resonance position is reached from negative scattering lengths and then increases further beyond the 3D resonance position. The variation of eigen state energies as a function of inverse scattering length  $1/a$  for an aspect ratio of  $\eta = 1/7$ , typically used in experiments, is shown in Figure 3.2(a). With Feshbach resonances, we can modify the scattering length  $a$  by changing the magnetic field. A plot of the energy levels as a function of the magnetic field for a mixture of  ${}^6\text{Li}$  atoms in states  $|1\rangle, |3\rangle$  is shown in Figure 3.2(b). Even for such moderate aspect ratios, the energies are close to the 2D values and more details on this comparison to the exact 2D case can be found in [55]. When studying few-body systems in the ground state, the two-body binding energy( $E_B$ ) can be used as a parameter to quantify the interaction strength in the system[79], [85] and is used through the thesis. For a system prepared in the first repulsive branch, the repulsive two-body energy( $E_R$ ) can also be used to quantify interactions and this is used in Chapter 5.

### 3.3 Theoretical predictions for many-body behavior in a few-body system

Emergent degrees of freedom at different length scales[1] have been used to understand the behavior of many-body systems encompassing disparate areas of scientific endeavor[86]. This approach has been used to understand emergent macroscopic phenomena such as phase transitions which cannot be explained from a simple extrapolation of two-body physics[87]. However this approach sidesteps the question of how many is many? Nature is abound with systems where there are countably finite number of constituents such as atoms, nuclei

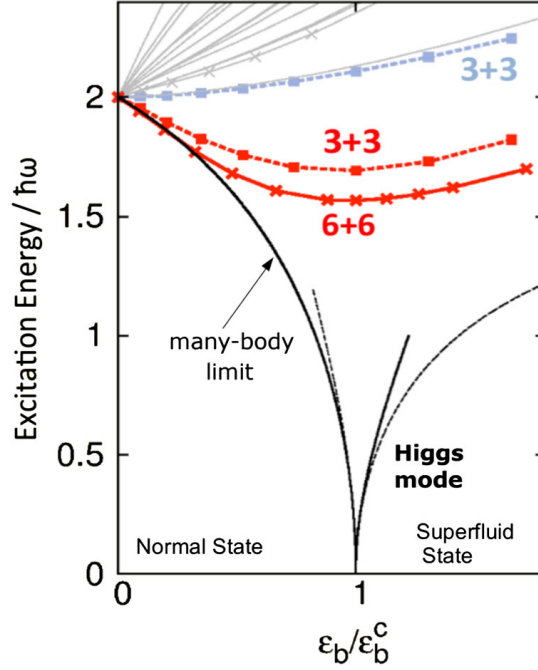


Figure 3.3: **Excitation spectrum of a finite few-body system consisting of 3 + 3 and 6 + 6 fermions in a 2D harmonic oscillator potential.** Excitation energy (in units of  $\hbar\omega_r$ ) versus two-body binding energy per particle  $\epsilon_b$ . At zero two-body binding energy, modulating the system can cause excitation of a single particle two shells up or a pair one shell up. Both of these excitations cost the same amount of energy  $2\hbar\omega$  given by the trap energy scale. At finite interaction strengths, there is a mode which increases with interactions and can be reconciled from the increased mean field energy. However, a lower energy mode appears which has a non-monotonic dependence on the interaction energy. As one more shell of atoms are filled (6 + 6) the gap in the excitation spectrum closes further. In the many-body limit the gap completely closes and is associated with the Higgs mode. Reprinted with permission from [79]

and other mesoscopic systems. Notwithstanding the fact that such systems are far from the thermodynamic limit, they exhibit collective effects reminiscent of systems in the many-body limit[5]–[7]. With the advent of cold atoms with tunable interactions[4], one can emulate such systems since they are not easily amenable to numerical or analytical approaches.

Such a finite few-body trapped system was recently studied numerically[79]. A system consisting of few-fermions with attractive interactions trapped in a 2D harmonic oscillator potential was considered. Due to symmetries in 2D, the single particle orbitals arrange in shells of equal energies as was shown in Figure 3.1. Adding more fermions in the trap leads to the formation of a Fermi sea and the authors considered two component fermions with 3 + 3 and 6 + 6 atoms. Such a system consists of fully filled 2 or 3 shells respectively. The Hamiltonian for such a system is

$$\hat{\mathbf{H}} = \sum_{i=1}^N \left( \frac{\hat{\mathbf{p}}_i^2}{2m} + \frac{1}{2}m\omega^2\hat{\mathbf{x}}_i^2 \right) + g \sum_{k,l} \delta(\hat{\mathbf{r}}_k - \hat{\mathbf{r}}_l) \quad (3.16)$$

$i$  is used to index the particles in the system and the contact interaction between particles is modelled by a regularized  $\delta$  function potential with strength  $g$ . They then performed an exact diagonalization of the Hamiltonian using a large number of non-interacting basis states and found the energy spectrum of such a system. A many-body system is usually characterized in terms of its response to perturbation and such an excitation spectrum can shed light on the phase or phase transitions in a system. This system in the many-body limit undergoes a quantum phase transition at  $T = 0$  for infinitesimally small attractive interactions from a normal to a superfluid phase. The complex scalar order parameter  $\Delta$ , which describes the extent to which symmetry is broken in the system, is zero in the normal phase while it takes up a finite value in the superfluid phase. Moreover in the superfluid phase the order parameter spontaneously breaks symmetry and picks up a phase. In the superfluid phase, perturbing the system can lead to either changing the amplitude or phase of the order parameter. Amplitude modulation costs energy and is called the Anderson-Higgs mode while the phase modulation costs no energy and is called the Goldstone mode[78]. Also importantly, the excitation energy for amplitude modulation at the phase transition goes to zero. While certainly a system of 3 + 3 or 6 + 6 fermions is definitely far from the thermodynamic limit, the excitation spectrum of this finite system was explored.

The excitation spectrum from the study is shown in Figure 3.3. The interaction strength in the system is quantified in terms of the two-body binding energy per particle  $\varepsilon_b$ .<sup>1</sup> Only monopole excitations were considered which can be excited by either modulating the interaction strength, which couples strongly, or by modulating the trap, which couples weakly. At zero interactions, periodic driving of the system can cause excitation of a single particle two shells up or a pair of particles one shell up. Both these excitations cost  $2\hbar\omega$  which is set by the trap energy scale. However, the situation changes dramatically as interactions are

---

<sup>1</sup>In experiments we quantify the interaction strength in terms of the two-body binding energy  $E_B = 2\varepsilon_b$

introduced. Single particle excitations cost energy larger than  $2\hbar\omega$  simply due to the mean field shift while excitation of pairs costs energy lesser than  $2\hbar\omega$  since the pairs can occupy multiple excited orbitals which are empty thereby increasing their overlap and reducing the energy due to attractive interactions. Starting with a non-interacting system and tuning interactions results in this monopole mode having a non-monotonic behaviour. Increasing the particle number by an additional shell makes the mode deeper and the energy gap between the ground/excited state asymptotically goes to zero. The Figure 3.3 shows the binding energy per particle  $\varepsilon_b$  in terms of the critical binding energy  $\varepsilon_b^c$  to enable comparison of different particle numbers. However, in absolute terms the critical binding energy  $\varepsilon_b^c$  also decreases since with each shell the density of states increases leading to more possibilities and more empty orbitals to excite pairs. And finally due to the discrete energy levels in the system decay channels are largely suppressed and the mode can be long-lived unlike in the many-body limit[88]. The study predicted that this mode is then associated with excitations of pairs and is the few-body analog of the Higgs mode featuring a modulation of  $|\Delta|$ . The asymptotic gap closing with increasing particle number is then interpreted as a few-body precursor of a phase transition in the many-body limit. In the following sections we detail how we measure the excitation spectrum in such a deterministically prepared model system.

## 3.4 Precursor of a phase transition

### 3.4.1 Preparing closed shell configurations

The first step to experimentally measure collective excitations in a few-body system involves the preparation of closed shells of atoms in a 2D harmonic oscillator potential. Technical details of experiment can be found in [55], [56] and only an overview is provided here. Using standard methods from laser cooling we cool a sample of  $^6\text{Li}$  atoms using a Zeeman slower and a MOT and then load the atoms in an ODT. Using a sequence of RF pulses the atoms are prepared in a mixture of states  $|1\rangle, |3\rangle$ . A tightly focused tweezer is then superimposed on the ODT and the sample is evaporatively cooled in this combined trapping potential for approximately 20ms resulting in around 300 cold atoms. The ODT is switched-off at the end of this evaporation ramp. The tweezer is tightly focused in the radial direction and weakly along the axial. A spilling procedure is performed[19] to create a low entropy sample of around 30 atoms in this trap. Subsequently the size of the tweezer in the radial direction is made larger (thereby reducing the radial trap frequency) with a spatial light modulator(SLM) and simultaneously a single layer of an optical lattice trap with tight axial and weak radial confinement is turned on. The combination of the tweezer trap and the single layer optical lattice trap results in a 2D microtrap with trapping frequencies  $\omega_z \approx 2\pi \times 7340$  Hz and  $\omega_r \approx 2\pi \times 1000$  Hz. This results in a quasi-2D geometry with an aspect ratio of  $\eta = \omega_r/\omega_z \approx 1/7$ . We perform spilling of the atoms transferred to this 2D microtrap by lowering the power in the tweezer beam and applying a magnetic field

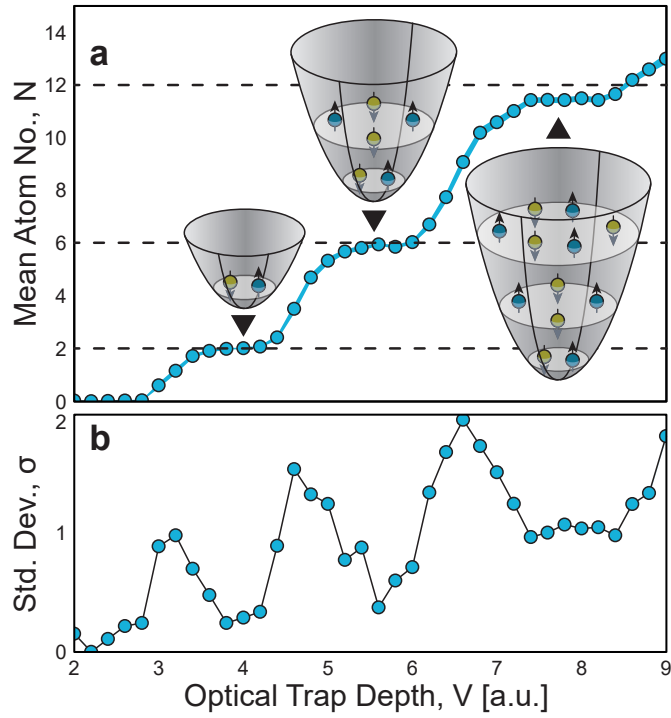


Figure 3.4: **Preparation of closed shells of atoms in a quasi-2D harmonic trap.** (a) Plot of mean atom number versus spill depth. As the final spill depth is varied, the system shows discrete steps corresponding to 1 + 1, 3 + 3 and 6 + 6 atoms. These correspond to closed shell configurations of the 2D-harmonic oscillator potential. The mean atom numbers corresponding to closed shell configurations are also indicated by dashed lines. The spilling is performed at a weak interactions of  $E_B = 0.6\hbar\omega_r$ . (b) Plot of standard deviation of atom number vs spill depth. The fluctuations of atom numbers shows that for closed shell configurations the fluctuations are significantly reduced. Figure adapted from [80]

gradient of approximately 70 G/cm. The spilling procedure works better when performed with moderate interactions and is done at either at 300G or 750G depending on the final interactions desired.

A plot of the number of atoms remaining in the trap as a function of the final spill depth is shown in Figure 3.4. As the final trap depth for spilling is tuned, stable plateaus consisting of 1 + 1, 3 + 3 and 6 + 6 atoms emerge signalling the preparation of closed shell configuration of atoms in a quasi-2D harmonic oscillator potential. Since the atoms are close to the motional ground state and the trap has an aspect ratio of  $\eta \approx 1/7$ , the axial motion is frozen out. Fluctuations of the prepared atom number also confirm that the closed shell configurations correspond to states which have suppressed fluctuations. We achieve preparation fidelities of  $97 \pm 2$ ,  $93 \pm 3$  and  $76 \pm 2$  for 1 + 1, 3 + 3 and 6 + 6 atoms respectively. For 6 + 6 atoms we achieve an entropy of  $0.1k_B$  per particle.

#### 3.4.2 Effect of interactions on shell structure

The plots of mean atom number versus depth of the optical trap were used to infer the preparation of closed shell configurations in Figure 3.4. It is also interesting to explore the effect of interactions on the shell structure. To this end we perform the spilling procedure at various interaction strengths. The results are shown in Figure 3.5. The strength of interactions is quantified by the two-body binding energy (repulsion energy)  $E_B$  ( $E_R$ ) for attractive (repulsive) interactions. At zero interactions  $E_B = 0\hbar\omega_r$ , the shell structure is visible with stable plateaus at 2,6 and 12 atoms. As the attractive interactions are increased, for weak attractions the shell structure persists albeit shifting to smaller values of spill depths to get the same atom numbers. This can be understood due to the attractive mean field interactions providing additional trapping thereby reducing the required confinement from the optical trapping potential. In contrast, the repulsive case needs a larger confinement to achieve the same number of atoms since the repulsion between the atoms has to be overcome. A histogram of the atom numbers for weak and strong attractive interactions further attest to the fact that the shell structure vanishes with increasing attractions. At weak interactions,  $E_B = 0.6\hbar\omega_r$ , the shell structure is still present as seen from the histogram peaks corresponding to 2,6,12 atoms. In contrast for strong interactions,  $E_B = 4.3\hbar\omega_r$ , the system predominantly favours an even atom number as this increases the total binding energy per particle. This can be compared to the stability of nuclei with even protons and (or) neutrons[89].

#### 3.4.3 Exciting the few-body system

The scheme to determine the excitation spectrum is shown in Figure 3.6. The system is first prepared in a closed shell configuration at weak attractive interactions where the shell structure is still present. The magnetic field is then adiabatically ramped to get a system with the desired two-body binding energy  $E_B$ . Excitation of the system can be performed

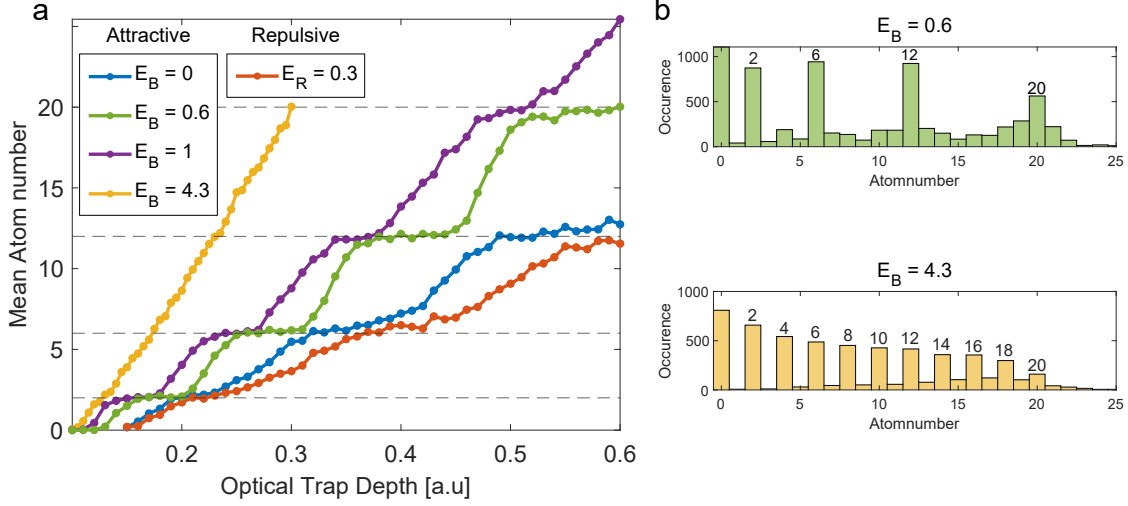


Figure 3.5: **Effect of interparticle interactions on the shell structure.** (a) Plot of mean atom number versus optical trap depth at different interaction strengths. The shell structure present for a non-interacting system,  $E_B = 0\hbar\omega_r$ , persists for weak interactions. The effect of attractive interactions is to shift the required trap depth for a given atom number to lower trap depth values. This can be understood from a mean field attraction which provides an additional confinement potential. On the contrary the effect of repulsive interactions is to shift the trap depth for a given atom number to higher values since the confinement potential has to now overcome repulsive interparticle forces. At large attractive interactions  $E_B = 4.3\hbar\omega_r$ , the shell structure completely vanishes. The horizontal dashed lines indicate closed shell configurations. (b) A histogram of atom numbers at weak  $E_B = 0.6\hbar\omega_r$  and strong  $E_B = 4.3\hbar\omega_r$  attractive interactions accumulated for all trap depths. At large binding energies  $E_B$ , the shell structure vanishes and even atom numbers are stable since this can lower the overall binding energy of the system.  $E_B$  and  $E_R$  are in units of  $\hbar\omega_r$ .

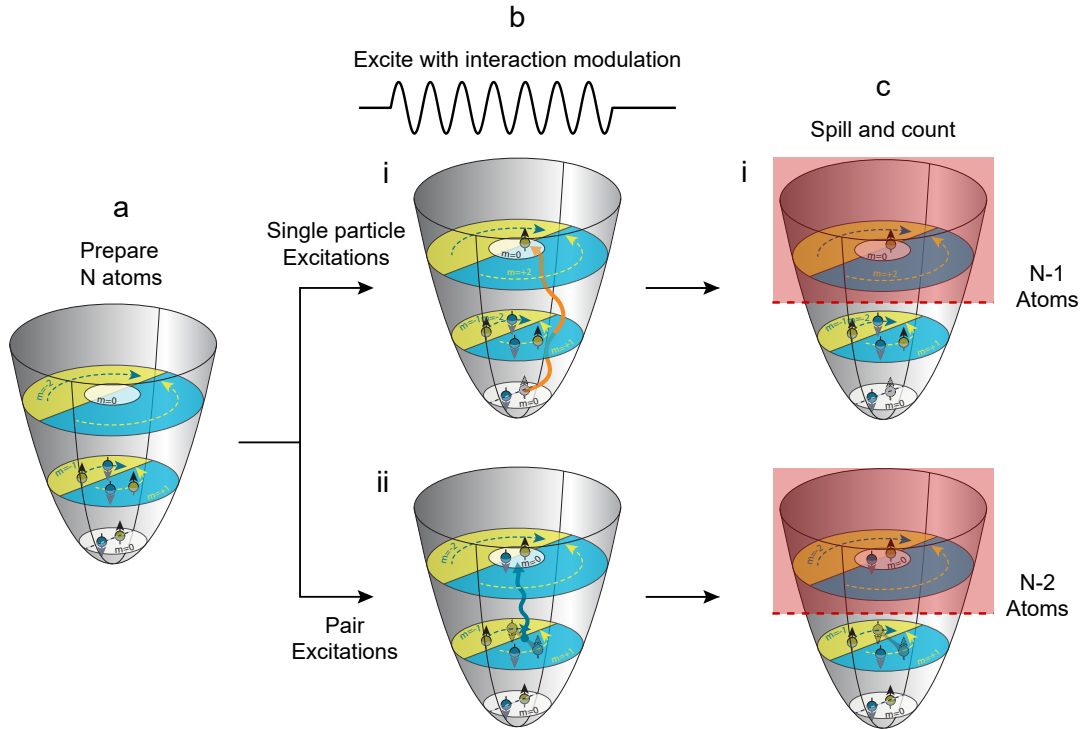


Figure 3.6: **Experimental scheme to extract the collective excitation spectrum.** (a) The system is prepared deterministically at weak attractive interactions. The magnetic field is then adiabatically tuned to initialize the system with a desired interaction strength. (b) Excitation of the system is performed by modulating the interaction strength since this couples strongly to pair excitations. Since no angular momentum is added to the system, only two possible excitations are possible. (i) Excitation of a single particle two shells up or (ii) Excitation of a pair of particles a single shell up such that  $\Delta m = 0$ . (c) The system is adiabatically returned to weak attractive interactions where the spill levels are known. Subsequent spilling to the same level as the prepared system results in (i)  $N-1$  particles for a single particle excitation, (ii)  $N-2$  particles for a pair excitation. The probabilities are then used to determine the excitation spectra and identify the resulting modes.

either by modulating the trap or interactions. Interaction modulation couples to the mode associated mainly with pair excitations much stronger than modulating the trap[79]. This mode with pair excitation is the precursor of the Higgs mode in the many-body limit. The Higgs mode is due to the modulation of the amplitude of the superfluid order parameter  $|\Delta|$  and is a modulation of the amount of pairing in the system. Interaction modulation has also been proposed to excite the Higgs mode[90]. In a system with perfect radial symmetry such an modulation can either excite a single particle two shells up or a pair single shell up with no change in the angular momentum  $\Delta m = 0$ . For the non-interacting case, both these possibilities cost  $2\hbar\omega$  in energy. Once the system has been excited for a finite duration, the system is returned adiabatically to the interaction strength at which it was prepared where the spill levels are known. Subsequent spilling to the ground state results in a loss of (at least) one particle for single particle excitations and two for pair excitations. Thus these probabilities are then used to determine the excitation spectrum.

### 3.4.4 Excitation spectrum

The 2D scattering length  $a_{2D}$  determines the interactions and depends on both the 3D scattering length  $a$  and the harmonic oscillator length  $l_z$  along the  $z$ -direction as in Equation 2.61. The interactions are modulated by modulating the power of the single layer optical lattice trap which changes  $\omega_z$  and hence  $l_z$ . This modulates the trap frequency along the radial direction  $\omega_r$  only weakly since the radial confinement is mostly created by the tweezer. To excite the system interactions are modulated for  $\approx 400$  ms. The resulting excitation spectrum for a system with  $N=6$  particles and a binding energy  $E_B = 0.33\hbar\omega_r$  is shown in Figure 3.7(a). It shows the probability of finding various atom numbers as a function of modulation frequency. The spectrum has two frequencies at which particle excitations happen. One of these is above  $2f_r$  and shows an enhanced probability to find  $N=5$  particles indicating single particle excitations. This is consistent with the mean field shift in energy which is larger for the denser ground state than the more dilute excited states. However, the mode below  $2f_r$  shows an enhanced probability to find  $N=4$  particles indicative of pair excitations. As will be shown later from correlation measurements in Section 3.6, in this case  $E_B < \hbar\omega_r$  and the ground state is hardly paired. In this regime where the binding energy is less than the single particle gap, pairing is mostly between time reversed pairs in the same shell[85], [91]. Contrary to open shell configurations where the system is paired for weak attraction due to the presence of empty orbitals[79], for closed shells the combination of Pauli blocking and weak attraction prevents the system from being paired. The excited state on the contrary is paired due to empty orbitals enabling the pairs to occupy all these states and increase the pairing energy. Hence the transition occurs at an energy lower than  $2f_r$ .

The complete spectrum for different interaction strengths is shown in Figure 3.7(b,c) for  $N=6$  and  $N=12$  particles respectively. Here only the pair excitations are tracked by plotting a normalized probability given by the ratio of pair excitations to no excitations  $P_{N-2}/P_N$ .

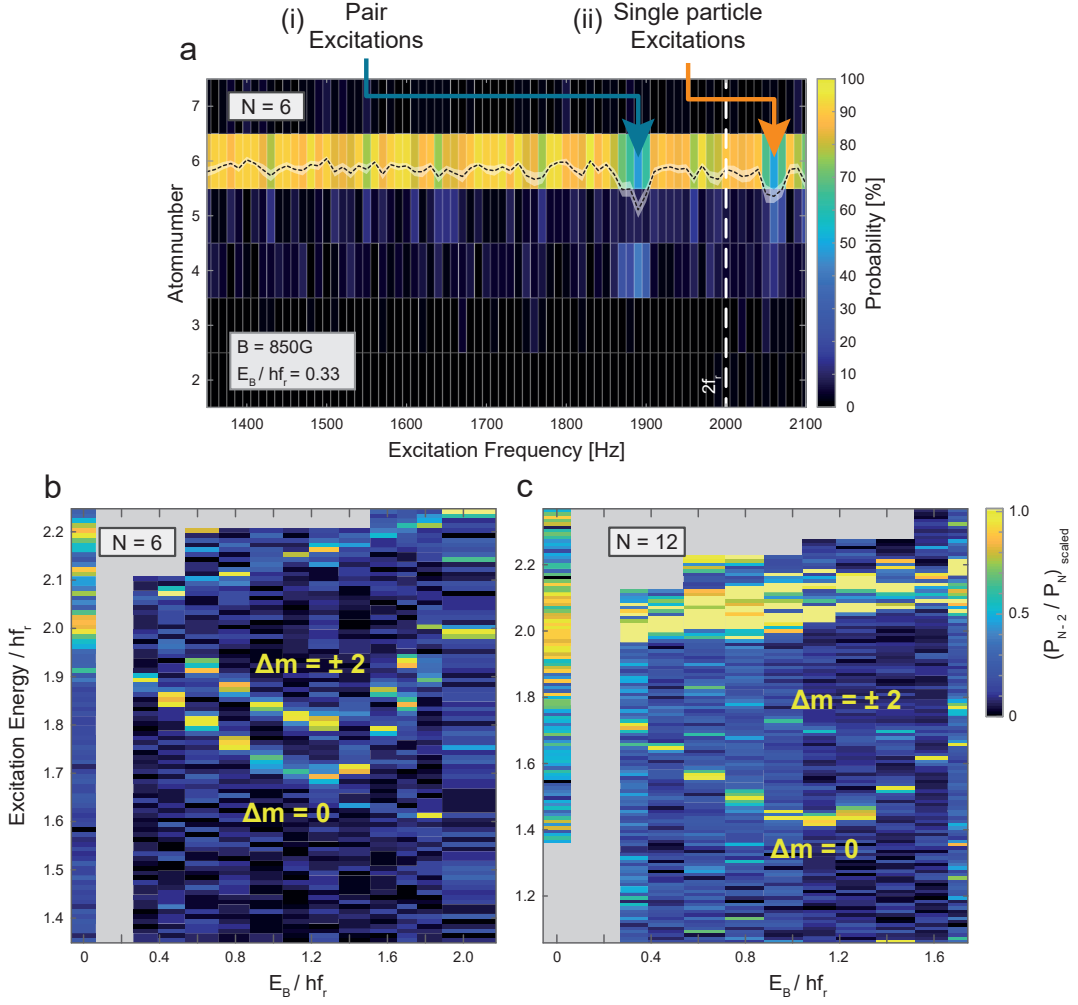


Figure 3.7: **Excitation spectrum of a few-body system.** (a) Plot of probabilities of finding various atom numbers as a function of modulation frequency for an interaction strength of  $E_B = 0.33\hbar\omega_r$  and  $N=6$ . There are two excitations (i) Pair excitations occur at a frequency less than  $2f_r$  while (ii) Single particle excitations occur at a frequency greater than  $2f_r$ . (b) Normalized probability of a pair excitation compared to probability of having no excitations  $P_{N-2}/P_N$  for  $N=6$  atoms at different interaction strengths. The mode with non-monotonic features now splits into two, one with  $\Delta m = 0$  and the other with  $\Delta m = \pm 2$ . This splitting is due to the fact that the trap has an anisotropy of 2% which couples ground and excited states with different angular momentum. The mode which induces a transition of  $\Delta m = \pm 2$  has a higher energy since the rotational energy has to be provided by the drive. (c) Similar plots of normalized probability for  $N=12$ . Figure adapted from [80]

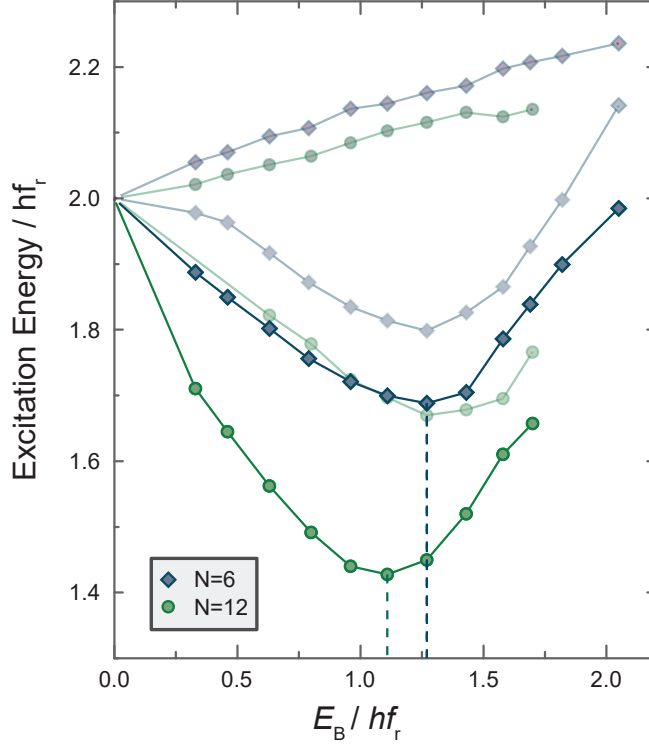


Figure 3.8: **Comparison of the lowest monopole mode for  $N=6$  and  $N=12$ .** At each interaction strength the excitation frequency for the various modes are obtained by fitting a Gaussian function to ascertain the peak position. The resulting plot of excitation frequency versus interaction strength is shown for both particle numbers  $N=6$  (blue, diamonds) and  $N=12$  (green, circles). The lowest excitation frequency for the monopole mode  $\Delta m = 0$  decreases with increasing particle number and shifts to lower values of  $E_B$ . This is consistent with the approach to the many-body limit  $N \rightarrow \infty$  where the gap closes and the normal-superfluid transition occurs at infinitesimal attractions for closed shell configurations. Modes corresponding to single particle excitations and  $m = \pm 2$  pair excitation modes are shown in the background. Figure adapted from [80].

The excitation spectrum shows two modes featuring a non-monotonic behavior and modes which monotonically increase in frequency with interactions. The non-monotonic modes which consist mainly of pair excitations and are the precursors of the Higgs mode in the many-body limit are now split into two. This can be understood from the fact that the slight anisotropy of around 2% is sufficient to couple the ground state with no angular momentum with an excited state with a finite angular momentum resulting in  $\Delta m \neq 0$ . This anisotropy in the trapping potential has been taken into account in a numerical evaluation which confirms this hypothesis[80]. The non-monotonic mode with a higher energy corresponds to  $\Delta m = \pm 2$  since additional rotational energy needs to be supplied.

A comparison of the excitation frequencies as a function of interaction strength and particle number is summarized in Figure 3.8. Two key features concerning the lowest monopole mode,  $\Delta m = 0$  which is associated with pair excitations, predicted by numerical studies are verified[79]. Firstly, the lowest frequency of the pair excitation mode corresponding to  $\Delta m = 0$  decreases with increasing particle numbers. This is due to the fact that addition of each shell should asymptotically recover the gap closing in the thermodynamic limit  $N \rightarrow \infty$ . Secondly, the critical binding energy  $E_B^c$  at which the minimum of the mode occurs shifts to lower values. In the thermodynamic limit, the transition from a normal to a superfluid occurs at infinitesimal attractions at  $T = 0$  for closed shell configurations. There is one other prediction from numerical calculations which is concerned with the stability of this precursor of the Higgs mode and will be presented in the next section.

#### 3.4.5 Coherent Driving

The discrete energy levels in our system introduce a single particle energy gap of  $\hbar\omega_r$ . This restricts the number of decay channels for the pair excitation mode and is expected to make it long-lived[79]. This hypothesis is explored by driving a 3 + 3 system with an interaction strength  $E_B = 0.6\hbar\omega_r$  at the frequency of the lowest pair excitation mode ( $\Delta m = 0$ , monopole mode) for varying driving times. Subsequently the number of atoms in the ground state is counted and the results are plotted in Figure 3.9. As the modulation time for the drive is varied, the system coherently oscillates between a system with pair excitations(N=4) and a system with no-pair excitations(N=6). During this time there are hardly any single particle excitations(N=5). The probability to find the system in either N=6 or N=4 remains constant indicating that pair excitation and de-excitation can be treated as a two-level system. A damped Rabi oscillation for a two-level system is fit to the probabilities resulting in an oscillation period of  $T_{\text{Rabi}} = (126.037 \pm 1.627)\text{ms}$  and a decay time of  $T_{\text{decay}} = (231.810 \pm 29.552)\text{ms}$ . With the observation of coherent oscillations, the stability of the precursor of the many-body Higgs mode is confirmed.

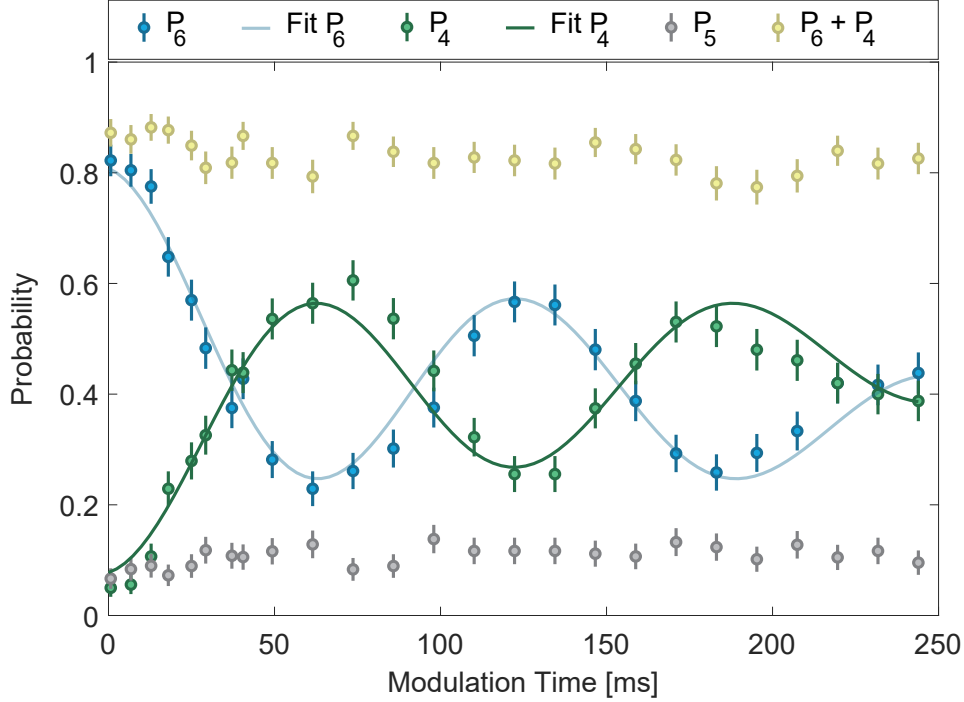


Figure 3.9: **Coherently driving the monopole mode associated with pair excitations.** At an interaction strength of  $E_B = 0.6\hbar\omega_r$  for 3 + 3 atoms, the lowest monopole mode is driven for different modulation times. The atoms in the ground state at the end of the drive are counted and the probabilities for 6,4,5 atoms ( $P_6, P_4, P_5$ ) are plotted versus modulation time. The system coherently oscillates between excitation(4 atoms) and de-excitation(6 atoms) of a pair. During this period there is hardly any probability to excite a single particle (5 atoms). The coherent nature of this mode is also confirmed by from the plot of  $P_6 + P_4$ . The probabilities  $P_6$  and  $P_4$  are fit with a damped Rabi oscillation which gives an oscillation time of  $T_{\text{Rabi}} = (126.037 \pm 1.627)\text{ms}$  and a decay time of  $T_{\text{decay}} = (231.810 \pm 29.552)\text{ms}$ . Figure adapted from [80]

### 3.5 Pauli Blocking

Fermions and bosons are distinguished from one another based on two features namely their spin and exchange symmetry. The exchange symmetry for fermions requires that the many-body wavefunction of a system of identical fermions under exchange be anti-symmetric. The many-body ground state of a system of  $N$ -identical fermions is then described by the Slater determinant as follows

$$\Psi(\mathbf{x}_1, \mathbf{x}_2, \dots, \mathbf{x}_N) = \begin{vmatrix} \psi_1(\mathbf{x}_1) & \psi_2(\mathbf{x}_1) & \dots & \psi_N(\mathbf{x}_1) \\ \psi_1(\mathbf{x}_2) & \psi_2(\mathbf{x}_2) & \dots & \psi_N(\mathbf{x}_2) \\ \vdots & \vdots & \ddots & \vdots \\ \psi_1(\mathbf{x}_N) & \psi_2(\mathbf{x}_N) & \dots & \psi_N(\mathbf{x}_N) \end{vmatrix} \quad (3.17)$$

where  $\psi_i$  are the single particle orbitals and  $\mathbf{x}_i$  are the co-ordinates of the particles. Anti-symmetrization also requires that no two particles occupy the same orbital ultimately ensuring that the particles avoid each other in position space[92]. While this property termed Pauli blocking is responsible for far reaching consequences such as atomic structure, it also has important consequences for the system studied previously. The formation of pairs at the Fermi surface is due to this blocking effect which renders the core of a many-body system frozen. We saw in Section 3.4 how Pauli blocking was responsible for excitations to have non-trivial characteristics. A frozen core also means that low energy excitations are mainly determined by particles at the Fermi surface which has been a paradigm to solve problems in condensed matter physics[93]. So far the effect of Pauli blocking in cold gases has been observed through the suppression of collisions[94], [95], Fermi pressure[96], anti-bunching of fermions[97], noise correlations[98], suppression of density fluctuations[99], [100] and quantum gas microscopy of a band insulator[101].

For a system of fermions the overall wavefunction comprises of spin and motional degrees of freedom. The combined wavefunction should be anti-symmetric under exchange of these particles - a symmetric spatial wavefunction can only be combined with an anti-symmetric spin state and vice versa[102]. For a system of interacting fermions, like spin-1/2 electrons, due to interactions either the symmetric or the anti-symmetric motional state has a lower energy. This constrains the symmetry of the spin state to ensure anti-symmetrization of the overall wavefunction. Thus there is a correlation between the particles due to this "Exchange interaction". It is important to note that this exchange interaction is no more than a certain wavefunction having lower energy due to interactions. This phenomena is responsible for explaining the ground state of a hydrogen molecule as a spin singlet[103] and the emergence of quantum magnetism[104]. In other words, the interactions between particles is responsible for causing spin-correlations between particles.

In contrast for a system of identical non-interacting fermions even though the particles don't interact, Pauli blocking ensures that the overall motional wavefunction is anti-symmetric under particle exchange. Thus, even though there is absolutely no interactions

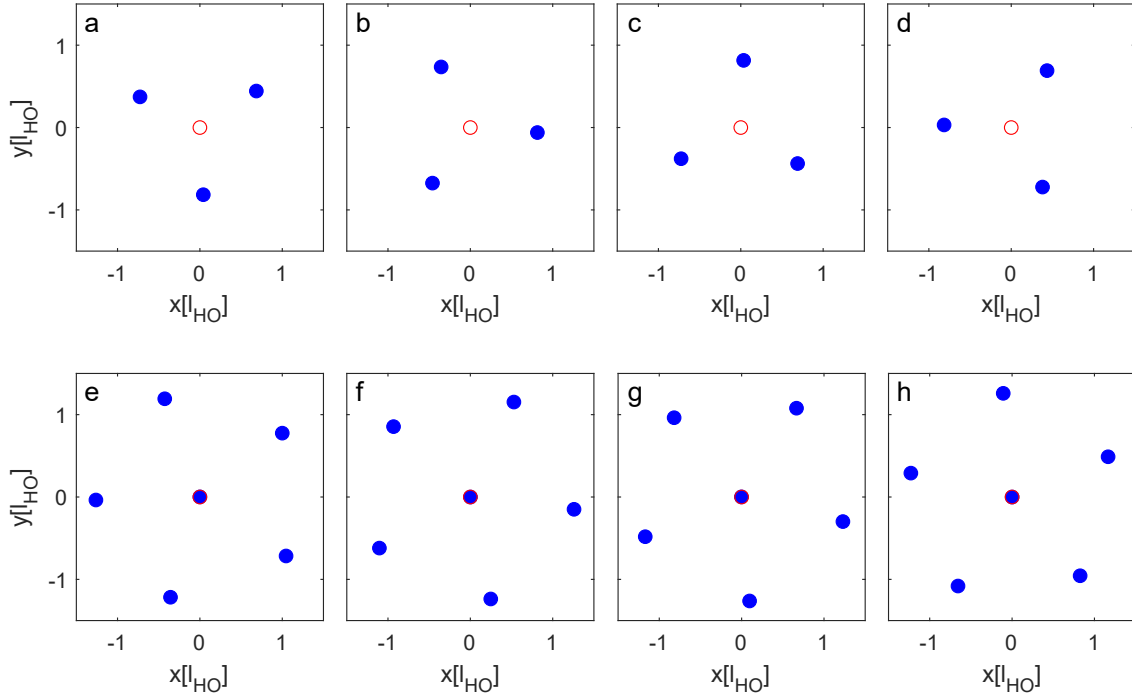


Figure 3.10: **Configuration of fermions in a 2D harmonic oscillator potential with maximum likelihood.** Using the many-body wavefunction from the Slater determinant, a probability density for different configurations is obtained. Using a Metropolis Monte-Carlo sampling scheme, different configurations are sampled until the most likely configuration is reached with  $10^5$  repetitions. Once a configuration is obtained, the whole set of co-ordinates are centered on the center of mass (COM) of the max likelihood positions. The blue dots indicate particle positions which result with maximum probability and the red circles indicate the COM position. (a-d)  $N=3$ , (e-h)  $N=6$  max likelihood for randomly chosen initial co-ordinates of the Markov Chain. Due to the azimuthal rotational symmetry in the 2D system, the maximum likelihoods from different starting co-ordinates chosen randomly differ only by a rotation angle. For  $N=3$  this results in a 3-fold rotation symmetry and for  $N=6$ , due to a single particle at the COM position, a 5-fold rotation symmetry. This feature is used to visualize correlations in the few-body system.

between the particles, the resulting state is highly entangled and correlated[105]. One way to quantify this correlation would be in terms of correlation functions. However, for a system of 6 particles (12 co-ordinates in 2D) the correlation function is 12 dimensional and hard to visualize. There have instead been proposals which suggest that this higher-order correlation function can be visualized by looking at the symmetries of the many-body wavefunction[21], [106]. The proposals are based on the idea that the many-body wavefunction gives a probability distribution for N-particles of the system. In these studies, a 2D harmonically trapped few-body system introduced in the previous sections was considered. In contrast to a two-component interacting fermionic system, a spin polarized system was considered. Metropolis Monte-Carlo sampling methods[107] were then used to determine the most probable configuration of this system of trapped fermions. The outcome for 2 filled shells(N=3) and 3-filled shells(N=6) are shown in Figure 3.10. The maximum likelihood positions are obtained from a Markov chain sampling scheme as follows.

```

 $\vec{x}_{\text{old}} \leftarrow \text{random sample } (\mathbf{x}_1, \mathbf{x}_2, \dots, \mathbf{x}_N)$ 
for i = 1 to  $N_{\text{rep}}$  do
     $\vec{x}_{\text{new}} \leftarrow \vec{x}_{\text{old}} + \vec{\epsilon}$ 
     $P_{\text{old}} = |\Psi(\vec{x}_{\text{old}})|^2$ 
     $P_{\text{new}} = |\Psi(\vec{x}_{\text{new}})|^2$ 
    if  $P_{\text{new}} > P_{\text{old}}$  then
         $\vec{x}_{\text{old}} = \vec{x}_{\text{new}}$ 
    end if
end for

```

The maximum likelihood positions reveal a kind of self-organization where the particles avoid each other as expected from Pauli blocking. The positions also reveal a symmetry present in the each likelihood outcome due to the azimuthal symmetry in the system. It is this 3-fold for N=3(5-fold for N=6) symmetry which is then used to visualize correlations in the system.

### 3.5.1 Visualizing Pauli blocking

With single particle imaging as described in Section 2.7, the in situ momentum of the individual particles can be obtained. In a harmonic trap both the position and momentum operator enter into the Hamiltonian quadratically. Due to this equal footing of both operators, the eigenfunctions are the same in both position and momentum representation. The eigenstates are Hermite(Laguerre) polynomials with a Gaussian envelope when the eigenstates are represented in Cartesian(cylindrical) co-ordinates. At the time of the experiment, only in situ momentum was accessible and this isomorphism was used to visualize Pauli blocking in momentum space. Each experimental snapshot of the system was used to sample the many-body wavefunction. Using the symmetry from the maximum likelihood positions, the images were analyzed in the following way[106]. From each snapshot of the experiment, the COM of the particles was determined and then subtracted from the parti-

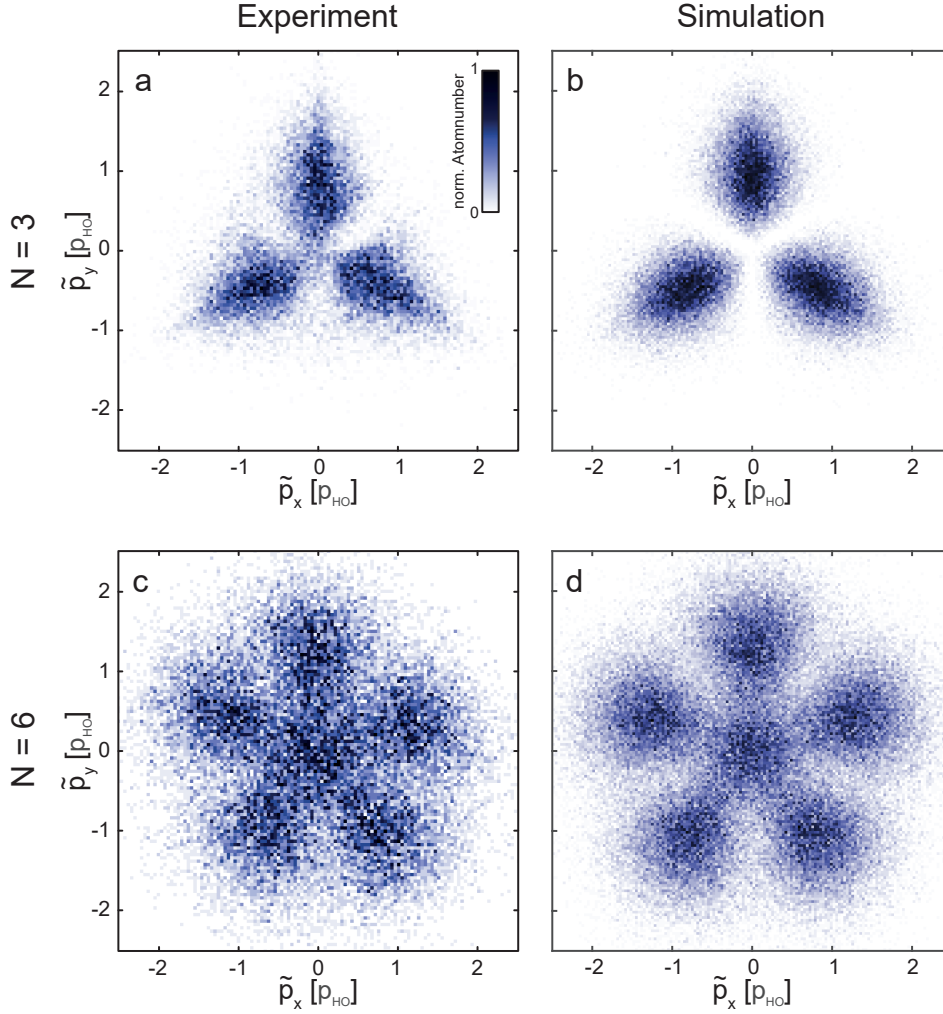


Figure 3.11: **Experimental observation and comparison to simulations for  $N=3$ ,  $N=6$  Pauli Crystal.** A heatmap of the particle positions after subtracting the COM and performing rotations depending on the  $n$ -fold symmetry present in the most probable configurations of the system. (a,b) Experiment and simulation for  $N=3$ . Experimental Pauli Crystal is obtained from a collection of approximately 10000 snapshots. The simulations are obtained by sampling the many-body wavefunction using a Monte-Carlo Metropolis[107] algorithm. (c,d) Experiment and simulation for  $N=6$ . Experimental results are obtained from approximately 20000 snapshots. All the transformed momenta are represented in harmonic oscillator momentum units  $\sqrt{\hbar m \omega_r}$ . The experimental system has very low, however finite entropies. This leads to a slight decrease in the contrast along the azimuthal angles. Figure adapted from [81].

cle positions. The existence of an  $n$ -fold symmetry is known from the maximum likelihood positions. For  $N=3$ , a 3-fold symmetry with the particles at the vertices of an equilateral triangle is present. Ordering the particles by their angles, the rotation angles for the particles to be at  $(0^\circ, 120^\circ, 240^\circ)$  are determined. An average of these rotation angles is determined and all the particle angles are rotated by this value. For  $N=6$ , a 5-fold symmetry is present with one particle at the COM. The co-ordinates are sorted to get the 5 particles which are farthest from the COM. Sorting these particles by their angles and using the 5-fold symmetry, the rotation angles for the particles to be at angles  $(0^\circ, 72^\circ, 144^\circ, 216^\circ, 288^\circ)$  are determined. The mean of these rotation angles was then used to rotate the co-ordinates of all the particles. More details can be found in [56]. The momenta of the particles after these transformations are denoted as  $(\tilde{p}_x, \tilde{p}_y)$ .

The system is prepared with closed shells of  $N=3$  and  $N=6$  particles (actually  $3+3$  and  $6+6$  but with the scattering length and hence interactions set to 0) with lowest possible entropy. A time-of-flight technique is then used to obtain the in situ momenta of all the particles[77]. The obtained particle positions are then processed according to the scheme summarized above. Approximately 10000(20000) snapshots of the many-body system for  $N=3(N=6)$  particles are obtained. The results for  $N=3$  and  $N=6$  is shown in Figure 3.11. The experiments are compared with simulations obtained by similar Monte-Carlo Metropolis sampling scheme to sample the many-body wavefunction. The outcome of the sampling is a list of particle positions which are drawn with a probability obtained from the Slater determinant. These positions are then subject to the same processing as for the experimental data. The resulting probability distributions of these post-processed co-ordinates show a striking regular geometric structure and have been termed Pauli Crystals[21], [106]. However, these are not crystals in the traditional sense where there is a spontaneous breaking of translation symmetry due to interactions like in condensed matter[93] or Coulomb crystals[108]. Firstly, there are no interactions between the atoms whatsoever. And secondly, there is no breaking of any symmetry - translational or otherwise. The act of measurement collapses the wavefunction and results in particles being found stochastically depending on the probability density. It is a crystal in the sense of the positions being highly correlated, not in the sense of spontaneous symmetry breaking.

#### 3.5.2 "Melting" the Pauli Crystal

The wavefunction given by the Slater determinant is for a particle in the ground state at zero temperature. When the system is heated, the many-body wavefunction can no longer be described by this coherent combination of single particle orbitals. As the temperature is increased, the statistics of the system transform from a Fermi-Dirac to a classical Boltzmann distribution. As the classical regime is reached, the correlations between particles are washed away and the Pauli crystal "melts". In order to probe this behavior the system is heated by modulating the trap power at a frequency of  $2\hbar\omega_r$  for a period of 50ms. Trap imperfections such as anharmonicity, anisotropy and potential drifts are responsible for dephasing on time

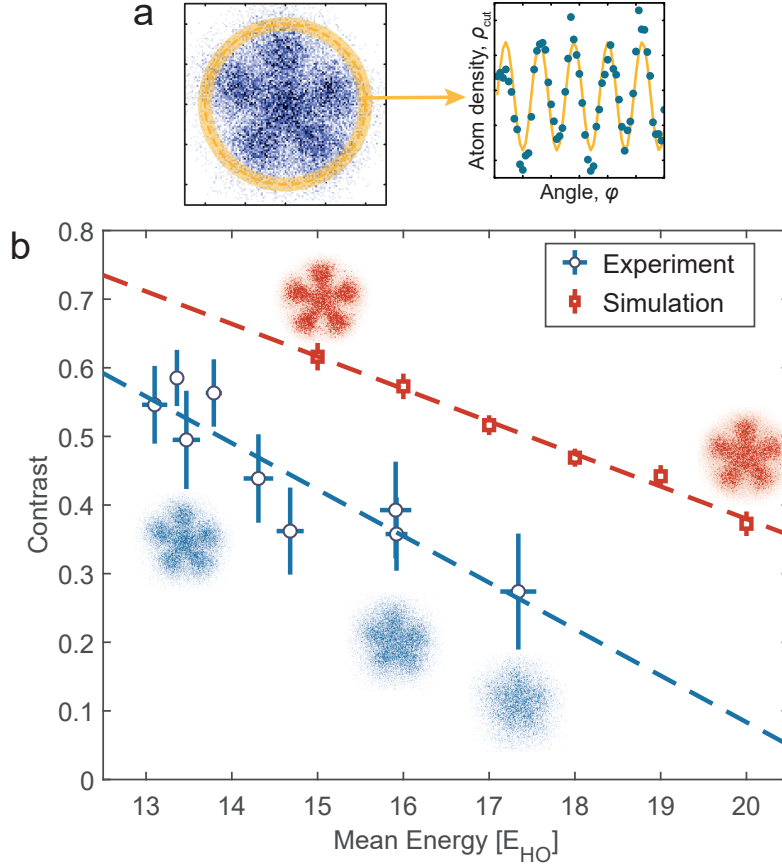


Figure 3.12: **"Melting" the Pauli Crystal.** The system is heated by modulating the trap. The total energy of the system is then quantified by measuring the total kinetic energy of the particles. (a) The effect of this heating on the correlations is quantified by extracting the contrast of azimuthal cuts of the Pauli Crystal images at a momentum of  $p = 2p_{HO}$ . The azimuthal cuts are fitted with a sine function to obtain the contrast. Shown here is the Pauli Crystal with no heating. (b) As more energy is put into the system, the contrast reduces monotonically. The observed contrast is compared with a Monte-Carlo simulation where heating is introduced by sampling the particle co-ordinates from a thermal N-body density matrix[106]. Only excitations with energies up to  $6\hbar\omega_r$  are included to reduce computational cost. Dashed lines for both experiment and simulation indicate linear fits to data. The linear fits give a slope for the contrast of  $(dC/dE)_{exp} = (-0.075 \pm 0.0013)/\hbar\omega_r$  for the experimental results and  $(dC/dE)_{sim} = (-0.048 \pm 0.0003)/\hbar\omega_r$  for simulation. Figure adapted from [81].

scales much faster than the modulation time. Thus the modulation does not coherently drive the system but instead creates a thermal state. In order to quantify the amount of correlations, the azimuthal periodicity of the Pauli crystal is used as shown in Figure 3.12(a). For  $N=6$ , an azimuthal cut of the Pauli crystal at a momentum of  $p = 2p_{HO}$  is performed and fit with a sine function. The contrast is then used as a metric to quantify correlations. The heating caused by trap modulation is quantified by measuring the mean energy of the system obtained from twice the kinetic energy. With no modulation an energy of  $13.1\hbar\omega_r$  is measured which is approximately 5% below the expected value of  $14\hbar\omega_r$  for  $N=6$  particles at  $T=0$ . This deviation can be explained due to the anharmonicity of the trapping potential and the uncertainty in the trap frequency measurement.

The contrast as a function of the energy of the system is shown in Figure 3.12. As the energy is increased, the contrast of the Pauli crystal decreases monotonically as would be qualitatively expected. A simulation of heating was performed by sampling states from a thermal  $N$ -body density matrix[106] to obtain the Pauli crystal at different temperatures. The simulation includes only states with excitation energies up to  $6\hbar\omega_r$  to reduce computational cost. The rate at which the contrast reduces is obtained from a linear fit to both experimental  $(dC/dE)_{exp} = (-0.075 \pm 0.0013)/\hbar\omega_r$  and simulation  $(dC/dE)_{sim} = (-0.048 \pm 0.0003)/\hbar\omega_r$  results. The slower rate of contrast reduction for the simulation could be as a result of inclusion of only states up to excitation energies of  $6\hbar\omega_r$ .

## 3.6 Cooper Pairing

The previous sections considered how pairing, which arises as a result of Pauli blocking, affects the excitation spectrum of a few-body system in a non-trivial way. Using microscopy of single particles in momentum space, Pauli blocking was visualized in such a trapped 2D harmonic oscillator potential. In this section results are presented on the microscopy of an interacting system where previously only the excitation spectrum was measured. An interacting system in the many-body limit is characterized by the formation of Cooper pairs at infinitesimally small attractive interactions. The formation of these pairs cannot be explained from an extrapolation of two-body physics alone. This pairing has been attributed to a many-body effect where due to the presence of a frozen Fermi sea, only particles at the Fermi surface can undergo scattering and form pairs with opposite momentum[17], [18]. These pairs are then bosonic in nature and can undergo condensation leading to superfluidity. In our finite system, the confinement potential introduces an energy scale in the system given by  $\hbar\omega_r$  which introduces a gap in the single-particle spectrum. The interaction energy in the system quantified by  $E_B$  has to now compete with this trap energy scale. As was seen in Section 3.4, such a minimal instance of a Fermi sea is already sufficient to possess qualitative features of a many-body system. In this section we utilize correlation measurements obtained from microscopy of individual atoms to study the formation of pairs and their characteristics.

### 3.6.1 Measuring in situ momenta in an interacting system

In Section 3.5, the in situ momentum of individual particles was measured in a non-interacting system. An interacting system would continue to interact during expansion and prevent the extraction of in situ momenta. On the contrary if interactions are switched-off prior to expansion, the atoms would undergo ballistic expansion and this would enable the extraction of in situ momenta. However, this would only be possible if the interactions are switched-off on a timescale orders of magnitude faster than the motional time scales in the system. This would prevent thermalization during switch-off, and the sudden quench would retain the in situ momenta. The motional timescales in the system are determined by the Fermi energy and for a 6+6 system under the experimental conditions this is around  $300\mu s$ . The interactions can be turned off by changing the scattering length. The possibility of using the magnetic field to turn-off the interactions would be untenable since changing it would take approximately  $200\mu s$  and would not be fast enough. The other option is to flip the spin to one of the other hyperfine states which would render the system (nearly)non-interacting. For a system in state  $|1\rangle, |3\rangle$  the only possibility would be to flip the state of one of the atoms to the low-field seeking states ( $|4\rangle, |5\rangle, |6\rangle$ ). In section 2.5, two-photon transitions between the various hyperfine states were presented. It was found that transitions between  $|3\rangle - |4\rangle$  have a large two-photon transition matrix element along with a good quality factor  $\beta$ . It was further pointed out in section 2.6.6 that in the magnetic field regime where experiments are performed, there is no Feshbach resonance between states  $|1\rangle - |4\rangle$  and that the scattering length is negligible.

We flip atoms in state  $|3\rangle$  to  $|4\rangle$  using a coherent  $\pi$ -pulse with a two-photon stimulated Raman transition. The duration of the  $\pi$ -pulse is approximately 300ns and is 3 orders of magnitude faster than the motional time-scales in the system. Thus the interaction switch-off can be considered instantaneous and a ballistic expansion of the resulting non-interacting particles can provide access to the in situ momenta of each particle. Using the two-state single particle imaging presented in section 2.7, the in situ momenta of all particles in the system can be obtained.

### 3.6.2 Correlation measurements

To obtain the emergence of interaction induced correlation, a second order density-density correlation function  $C^{(2)}$  of particle momenta can be defined as

$$C_c^{(2)}(\vec{p}_\uparrow, \vec{p}_\downarrow) = \langle n(\vec{p}_\uparrow)n(\vec{p}_\downarrow) \rangle - \langle n(\vec{p}_\uparrow) \rangle \langle n(\vec{p}_\downarrow) \rangle \quad (3.18)$$

where  $n(\vec{p}_{\uparrow(\downarrow)})$  is the number of spin- $\uparrow$  ( $\downarrow$ ) particles with momentum  $\vec{p}_\uparrow$  ( $\vec{p}_\downarrow$ ). The average is taken over multiple realizations of the experiment. Since the momenta are 2D quantities, the correlation function  $C_c^{(2)}$  is four-dimensional making it hard to visualize. To reduce the dimension, we integrate over a number of variables and redefine some co-ordinates.

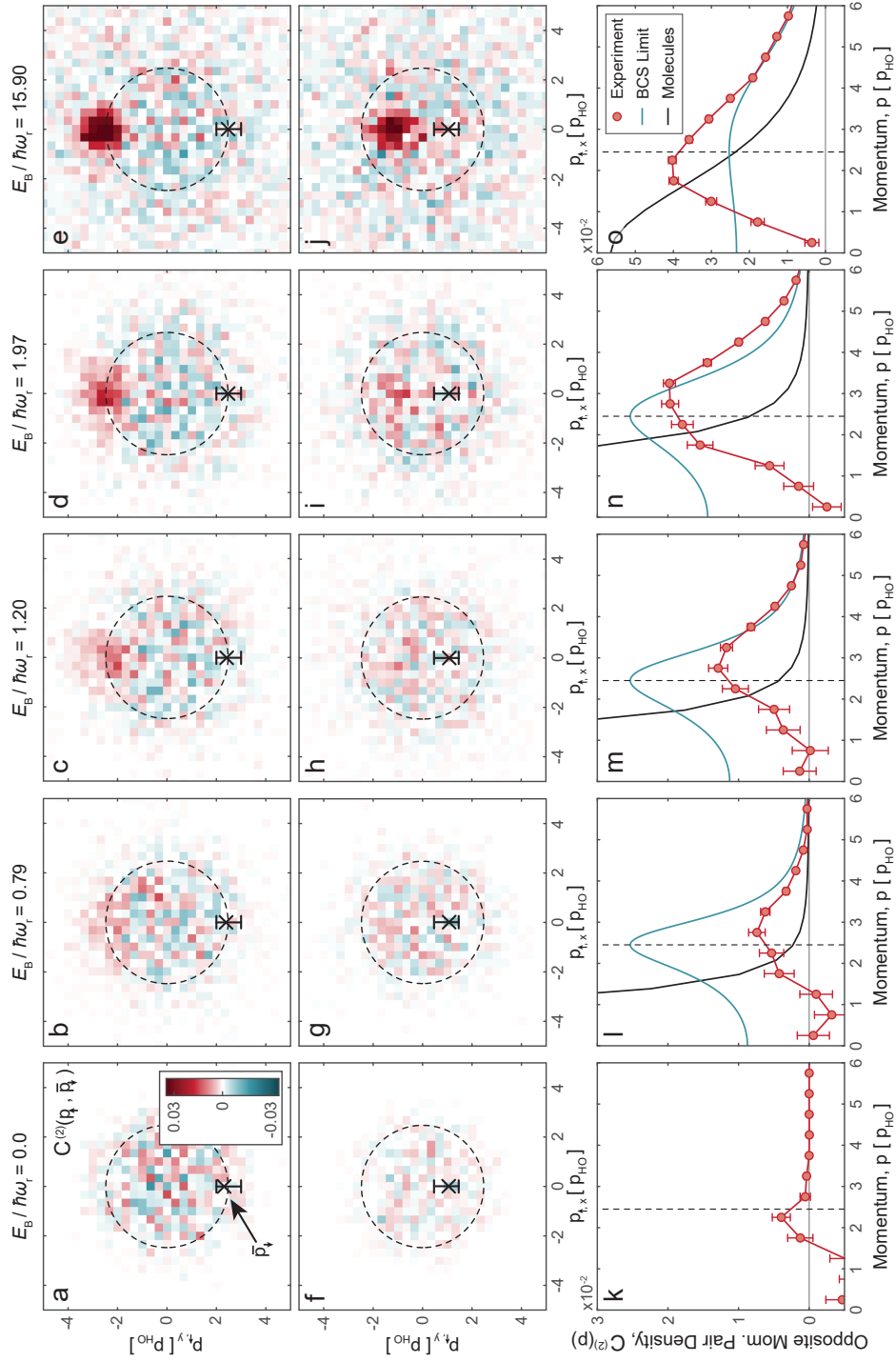
This results in a two-dimensional correlator  $C_{\bar{p}_\downarrow}^{(2)}(p_\uparrow, \Delta\phi)$ . The momenta of  $\bar{p}_\downarrow$  is integrated around a shell between momentum magnitude  $p_1$  and  $p_2$  and the angles are integrated to pick out only a certain relative angle  $\Delta\phi$  between the spins. The integrated values of  $p_\downarrow$  have an average value of  $\bar{p}_\downarrow$ . The momentum limits  $p_1$  and  $p_2$  are separated by  $p_{HO}$ .

$$C_{\bar{p}_\downarrow}^{(2)}(p_\uparrow, \Delta\phi) = \int_{p_1}^{p_2} \int_0^{2\pi} \int_0^{2\pi} C^{(2)}(p_\uparrow, \phi'_\uparrow, p'_\downarrow, \phi'_\downarrow) \delta(\Delta\phi - (\phi'_\uparrow - \phi'_\downarrow)) p'_\downarrow dp'_\downarrow d\phi'_\downarrow d\phi'_\uparrow \quad (3.19)$$

The new reduced correlator now gives an indication of the momentum magnitude and relative angle where particles of spin- $\uparrow$  would be found if the spin- $\downarrow$  particles are fixed around a mean momentum of  $\bar{p}_\downarrow$ . A plot of this correlator  $C_{\bar{p}_\downarrow}^{(2)}(p_\uparrow, \Delta\phi)$  as a function of interaction strength is shown in figure 3.13. For a non-interacting system, irrespective of the momentum of the spin- $\downarrow$  particle there is no structure to the density-density correlator. However, as interactions are increased the following qualitative features emerge. A spin- $\uparrow$

---

Figure 3.13 (*following page*): **Momentum space correlations reminiscent of Cooper pairing.** For a system of 6 + 6 fermions in a closed shell configuration, the second order density-density correlator  $C_{\bar{p}_\downarrow}^{(2)}(p_\uparrow, \Delta\phi)$  is plotted in (a-j). (a-e)  $C_{\bar{p}_\downarrow}^{(2)}(p_\uparrow, \Delta\phi)$  with  $\bar{p}_\downarrow$  at the Fermi surface. The interaction strength quantified by the two-body binding energy  $E_B$  is increased from 0 to  $15.90\hbar\omega_r$ . The dotted circle indicates the Fermi energy  $E_F = \sqrt{6\hbar\omega_r}$  for 6+6 non-interacting particles. The mean position of the spin- $\downarrow$  particle is indicated by a cross and the error bars around it indicate the range of  $p_\downarrow$  values for integration of the 4D correlator in equation 3.19. While there are no enhanced correlations at  $E_B = 0$  at any particular value of  $(p_\uparrow, \Delta\phi)$ , as  $E_B$  increases it is more probable to find spin- $\uparrow$  particles with opposite momentum at the other end of the Fermi surface. (f-j) For a spin- $\downarrow$  particle having a momentum  $\bar{p}_\downarrow$  within the Fermi surface. For weak interactions, the enhancement in the correlations within the Fermi surface is weak. However at the largest interaction strength accessible  $E_B = 15.90\hbar\omega_r$ , there is an increased probability to find spin- $\uparrow$  particles also inside the Fermi sea. This occurs since  $E_B > E_F$  and  $E_B$  is the largest energy scale in the system making the system molecular in character. (k-o) Opposite momentum pair density  $C^{(2)}(p)$  for these different interaction strengths. Comparison to molecular and BCS expectations for the respective  $E_B$  is shown. Adapted from [75]



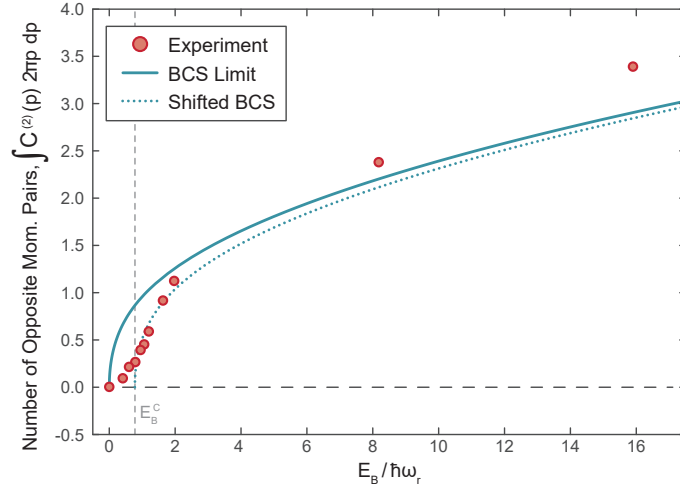


Figure 3.14: **Total number of opposite momentum pairs.** The total number of opposite momentum pairs is obtained by integrating  $C^{(2)}(p)$  over all pairs with opposite momentum. The total number of opposite momentum pairs increases monotonically with interaction energy as expected from an estimate of the BCS limit. In the many-body limit, Cooper pairs start forming with infinitesimally weak attraction. On the contrary, with  $6 + 6$  particles the few-body system is finite and this introduces an additional single particle gap  $\hbar\omega_r$  in the system. This gap prevents formation of pairs for arbitrarily weak attraction and requires a finite critical binding energy  $E_B^c$  to form pairs in the system. A plot of expectations from the BCS limit shifted by  $E_B^c$  agrees reasonably well with the experimental findings. Figure adapted from [75].

particle is more likely to be found at a relative angle of  $\pi$  if the spin- $\downarrow$  particle is fixed around the Fermi surface. However if the spin- $\downarrow$  particle is located within the Fermi surface this is no longer the case. This is reminiscent of Cooper-pairing at the Fermi surface where due to Pauli blocking only particles at the Fermi surface can pair-up leading to correlations. On the contrary the situation is remarkably different when the interaction energy is the largest energy scale in the system. For  $E_B = 15.9\hbar\omega_r$ ,  $E_B$  exceeds even the Fermi energy  $E_F$ . In this case the system possesses correlations not only at the Fermi surface but at nearly all momenta. Such a correlation is indicative of molecular character in the system.

In addition, the number of correlated particles at opposite momenta can be calculated by integrating the 1D correlator  $C^{(2)}(p, -p)$  and the results are shown in Figure 3.14. With increasing interaction strength, more pairs with opposite momenta are found. A few key points of departure compared to the many-body system can be observed. In a many-body system, Cooper pairs form already for infinitesimally weak attraction. On the contrary in a trapped few-body system the trap energy scale  $\hbar\omega_r$  is comparable to the Fermi energy.

This single particle energy gap is an additional energy scale that the interactions have to compete with. As a result, the number of correlated pairs hardly increases until a certain critical  $E_B$  is reached. Beyond this point the number of pairs increasing significantly with interactions. The number of pairs compares well with a BCS prediction which is shifted by a certain critical binding energy  $E_B^c$ .

### 3.7 Conclusions

Experiments concerning spin-balanced few-fermion systems in quasi-2D harmonic oscillator potentials were summarized. A summary of single particle and two-body physics in such potentials was presented. Theoretical predictions concerning such mesoscopic systems were presented and key experimental observables summarized. Evidence for the emergence of shell structure was presented and collective excitations in systems with closed shell configurations were studied. While these mesoscopic systems are far from the many-body limit, nonetheless the excitation spectrum showed features reminiscent of a phase transition in the many-body limit. The effect of additional shells on asymptotically reaching the many-body limit was studied and coherence properties of the collective excitations demonstrated. The microscopic origin for the qualitative many-body behaviour is Pauli blocking and the formation of Cooper pairs at the Fermi surface. Pauli blocking was visualized using higher order correlations encapsulated in the anti-symmetrized many-body wavefunction of a single spin-component. The effect of temperature on these correlations termed Pauli crystals were studied. Using the ability to simultaneously image two spin states, correlation measurements of an interacting system was presented. Using these second order density-density correlators of in situ momenta, evidence for the formation of Cooper pairs at the Fermi surface were presented supplementing the understanding for the emergence of collective behaviour in these mesoscopic systems.

The size of these systems is smaller than the effective imaging resolution. While this does not prevent measurement of in situ momenta demonstrated previously, it prohibits a direct measurement of in situ positions. In the next Chapter, this is circumvented by magnifying the system prior to imaging using matterwave techniques. The resulting matterwave microscope is characterized and its performance is demonstrated using the same spin-balanced system consisting of  $6 + 6$  fermions. In Chapter 5, using this additional observable spin-imbalanced systems are explored. The few-body limit of a model system which also possess a transition in the many-body limit is studied.



## 4 Matterwave Microscopy

The previous chapter presented experiments on few-fermion systems in 2D harmonic oscillator potentials. These systems have only a few shells occupied and are far from the many-body limit. However, already in such systems evidence for the emergence of collective modes were presented. These spectroscopic measurements were connected to phase transitions in the many-body limit. Imaging techniques presented in Chapter 2 were then used to perform single particle imaging in a non-interacting system to obtain in situ momenta. Anti-symmetrization of the total wavefunction leads to fermionic anti-bunching resulting in spatial correlations among the particles. Evidence for the presence of these spatial correlations dubbed Pauli crystals were presented. Microscopy was then performed in momentum space on a balanced interacting system of 6+6 fermions. Similar to spectroscopic measurements where many-body collective properties emerge already in these few-body systems, correlation functions in momentum space were used to demonstrate the formation of Cooper pairs which is a many-body phenomena. While single particle spin resolved imaging provided access to correlation functions, these measurements were restricted to in situ momenta. Direct access to in situ position measurements were inaccessible since the effective imaging resolution was larger than the size of the system. In this chapter, we circumvent this limitation by using matterwave techniques to magnify the system before imaging. This gives access to in situ positions of the particles and hence complementary correlations in position space.

### 4.1 Introduction

Recent advances in the microscopy of single ultracold atoms have enabled measurements beyond macroscopic observables in interacting quantum many-body systems. Microscopic detection schemes are varied and based on the following schemes - optical detection through fluorescence, ion detection subsequent to ionization and physical detection with microchannel plates(MCP). Current fluorescence approaches are based on quantum gas microscopes for lattice systems[3] and free space microscopy for continuous systems[77], [109]. Light scattering during fluorescence imaging leads to diffusion and heating of the atoms which limits resolution. Quantum gas microscopes circumvent this problem by pinning down the atoms and performing Raman sideband cooling during the imaging sequence. Free space imaging in contrast collects very few photons making use of EMCCD cameras in photon counting mode thereby minimizing diffusion during imaging. Schemes based on ion detection are scanning techniques where an electron beam is scanned across the atomic sample leading

to impact ionization. The resulting ions can be collected by ion optics and resolutions are determined by the size of the ion beams used for scanning across the sample[110]. However since this is a scanning technique, better resolution comes at the cost of duration needed for imaging. Physical detection is suitable for atomic species with a metastable state since this internal energy of the atoms can be converted for electronic detection using a MCP[111]. The resolution is determined by the size to which the atomic cloud is expanded and the size of the individual pixels of the MCP. However, detection fidelities are lower with this approach.

The insights which microscopic detection of many-body states has enabled have been far reaching. Quantum gas microscopes have been instrumental in microscopic observation of many-body phenomena such as the superfluid-Mott insulator transition[112], [113], emergence of anti-ferromagnetic ordering[114], [115] and observation of magnetic polarons[116] to name a few. Free space microscopy of in situ momenta with spin resolution has enabled demonstration of entanglement of two atoms in a double well potential[117] and extending this technique to the microscopy of mesoscopic 2D fermionic systems has led to the observation of fermionic anti-bunching in a trap dubbed Pauli crystals[81], [118] and the observation of Cooper pairs at finite interaction strengths[75]. However, direct free space microscopy of in situ positions has not been possible since the size of the system is smaller than the effective imaging resolution. Imaging in such a regime has been performed for biological samples by expanding the sample in a polymer network prior to imaging[22]. Such an approach of expanding the system prior to imaging has also been demonstrated recently for quantum gases in a lattice[23] using techniques from matterwave optics[119]–[121] achieving sub-lattice resolutions. Here the application of such a matterwave expansion technique to continuous few-body systems is demonstrated enabling microscopy of in situ particle positions with single atom resolution. This is done in a regime where the size of the system is smaller than the effective imaging resolution thereby prohibiting direct imaging. In what follows, the combination of expansion of the system using matterwave techniques followed by fluorescence imaging is referred to as matterwave microscopy.

## 4.2 Concept of Matterwave Microscopy

Fluorescence detection of atoms always detects atomic positions. In time-of-flight(TOF) imaging used frequently in atomic gases, the measured atomic positions after TOF expansion is connected to the in situ momentum of the particles in the trap. Such a TOF expansion can be viewed as a special case of a matterwave transformation in a harmonic trap. The phase space dynamics of a particle evolving in a harmonic oscillator trap with frequency  $\omega$  is,

$$\begin{bmatrix} x(t) \\ p(t) \end{bmatrix} = \begin{bmatrix} \cos \omega t & \frac{1}{m\omega} \sin \omega t \\ -m\omega \sin \omega t & \cos \omega t \end{bmatrix} \begin{bmatrix} x(0) \\ p(0) \end{bmatrix} \quad (4.1)$$

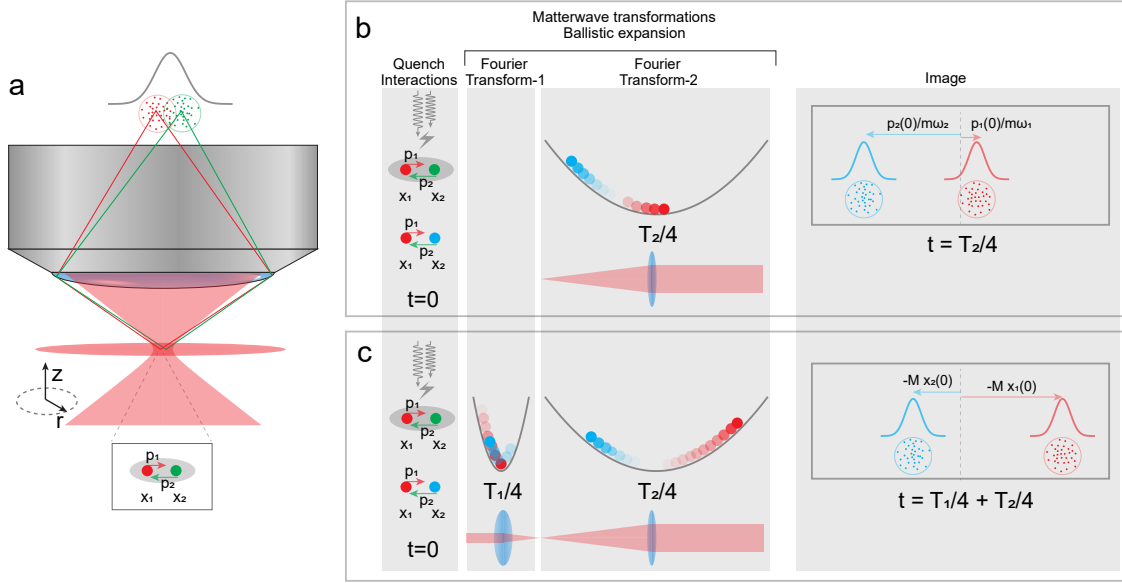


Figure 4.1: **Concept of the matterwave microscope (a)** Each atom in the trap has a position  $x_i$  and momentum  $p_i$  either of which we would like to measure. With a direct fluorescence measurement, in situ atom positions cannot be obtained since the effective imaging resolution is larger than the system size. The spread of the fluorescence photons on the image plane for atoms depicted as red and green are shown with dots of respective colors. **(b)** In situ momentum measurement. The system initially finds itself in a tweezer trap in which it is prepared. A ballistic expansion in a weak trap after switching-off interactions (thunderbolt symbol) and the tweezer is performed. Evolution for a quarter trap period ( $T_2/4$ ) in this trap performs a Fourier transform of the many-particle wave function. The trap frequency of the matterwave trap is chosen to ensure that measurement of final atom positions is no longer limited by the effective imaging resolution. However, such a measurement provides the in situ momentum distribution of the atoms which is the Fourier transform of the position distribution. **(c)** In situ position measurement with matterwave magnification. After switching-off interactions, when the system is expanded for a quarter trap period in a tight trap ( $T_1/4$ ) followed by a weak trap ( $T_2/4$ ), the final particle positions are magnified versions of the initial in situ particle positions. The magnification factor is given by the ratio of the tight trap frequency ( $\omega_1$ ) to the weak trap frequency ( $\omega_2$ ). The analogy to optics is depicted below for each of the matterwave transformations using lenses.

The position  $x(t)$  and momentum  $p(t)$  at any point of time  $t$  is a linear combination of the initial position  $x(0)$  and momentum  $p(0)$ . The phase-space dynamics has a periodicity  $T = 2\pi/\omega$  and depends only on the trap frequency  $\omega$  of the harmonic trap in which the particle evolves. For a particle subjected to an evolution for a quarter time period  $T/4$  in the harmonic trap, the final position(momentum) depends only on the initial momentum(position). Thus by taking an image of the particle positions after switching-off interactions followed by a  $T/4$  evolution in a harmonic trap, one obtains a final position which is proportional to the initial in situ momentum. The scaling factor is inversely proportional to  $\omega$  which implies that by performing an expansion in a weak trap the particles can be well separated as shown in Figure 4.1(b).

Post interaction switch-off, by performing an evolution in two traps for a quarter time period in each ( $T_1/4 + T_2/4$  where  $T_{1(2)} = 2\pi/\omega_{1(2)}$  is the time period of the first(second) trap), the final position of the particle at the end of the evolution is given by Equation 4.2. It indicates that the final position is proportional to the initial in situ position with the constant of proportionality  $M$  determined by a ratio of the trap frequencies. Thus by choosing  $\omega_1 > \omega_2$ , a magnification  $M$  can be obtained. This is shown in Figure 4.1(c) where the final particle positions can be well resolved and are proportional to the initial positions.

$$x(T_2/4 + T_1/4) = - \underbrace{\left(\frac{\omega_1}{\omega_2}\right)}_M \times x(0) \quad (4.2)$$

The linear transformation in Equation 4.1 is also valid when position and momentum are treated as quantum operators[121]. These linear transformations also require that the particles do not interact during this ballistic expansion in the harmonic trap. Thus to perform matterwave magnification the interactions in the system have to be switched off on a time scale orders of magnitude faster than the motional time scales.

### 4.3 System length scales and requirements

The design requirements of the matterwave magnifier are determined by the length and energy scales of the system one would like to study. It is also limited by the effective imaging resolution for single particles. Our system consists of a mesoscopic two-component Fermi gas of  ${}^6\text{Li}$  atoms in a quasi-2D Harmonic oscillator potential. The trap frequencies are  $\omega_r = 2\pi \times (1101 \pm 2)\text{Hz}$  along the radial and  $\omega_z = 2\pi \times (7432 \pm 3)\text{Hz}$  along the axial directions of the trap. This gives an aspect ratio of  $\eta \approx 1 : 7$  ensuring that the system is quasi-2D for small particle numbers. Only spin-balanced systems will be considered in this Chapter and details concerning the preparation of such a system were presented in Chapter 3. In Chapter 5, we will go beyond and study spin-imbanced systems from the extreme limit of a single impurity immersed in a Fermi sea to a scenario of mismatched

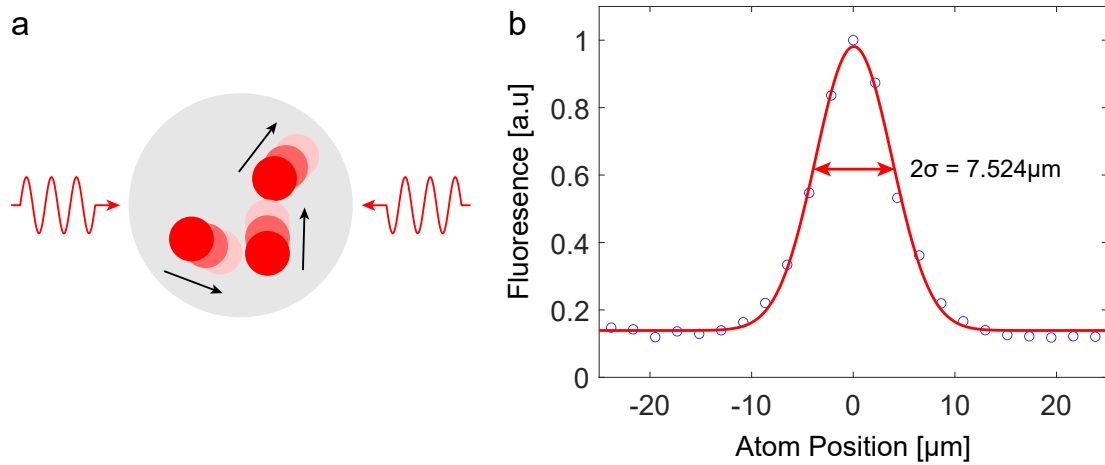


Figure 4.2: **Effective imaging resolution for single atoms.** (a) For microscopy of continuous few-body systems, the sample is illuminated with counter propagating resonant light fields. An atom is detected by collecting nearly 10% of the approximately 200 scattered photons. The light scattering causes diffusion of the atoms and is the dominant factor which determines the imaging resolution. (b) Effective imaging resolution. The effective imaging resolution is obtained by finding the distribution of atom fluorescence around its central position. We obtain an effective resolution of  $2\sigma = 7.524\mu\text{m}$ .

Fermi surfaces. The spatial extent of such a mesoscopic system is on the order of the harmonic oscillator length of  $1.23\mu\text{m}$  and scales only as the square root of the number of occupied shells. The effective imaging resolution on the other hand is influenced by a combination of optical system parameters and the spatial extent over which atoms diffuse during fluorescence imaging[77]. Taking into account all these factors gives an effective imaging resolution of approximately  $7.5\mu\text{m}$  and is shown in Figure 4.2. Since the effective imaging resolution is larger than the system size, a direct measurement of in situ positions of the atoms is precluded. Hence measurements presented in Chapter 3 have been done in momentum space with a time-of-flight(TOF) expansion. However, using matterwave optics the initial many-body wavefunction can be magnified before the atoms are imaged enabling in situ microscopy in position space.

The magnification of the matterwave microscope is one of the factors which determines the resolution. A larger magnification separates the initial in situ positions by a larger final distance enabling a better resolution. Typically the magnification that is chosen depends on the system and its smallest length scales that one would like to probe. Magnetic traps are good candidates for matterwave transformations since they can be made smooth over large distances and the potential produced can be very harmonic as was demonstrated[23]. However, in many cases they might not be very suitable due to the range of trap frequencies they can implement. In such cases, Gaussian beam optical dipole traps with the right combination of trap depth and waist can be rather harmonic for a chosen system energy scale. Phase-space evolution in a harmonic trap is analogous to transformation of optical beams using thin or graded-index lenses[121]. For a given trap frequency, the depth of the trap determines which initial momenta can be collected and is analogous to the numerical aperture. Larger trap depths correspond to larger numerical apertures leading to better resolution. The extent of the trap is analogous to the aperture of the lens. A larger trap would produce a more harmonic potential at the center compared to a smaller trap. This deviation from harmonicity also leads to aberrations similar to spherical aberrations in lenses. Thus typically Gaussian trap depth(waist) at least an order of magnitude larger than energy(length) scales in the system should be used to implement traps for the matterwave magnifier.

## 4.4 Implementation

The trap parameters for the two matterwave lenses can be chosen as follows. The field of view of the imaging system determines the desired magnification  $M$  as well as the waist of the second matterwave lens  $w_2$ . The energy scales of the system set the order of the trap depths  $U_2$ . The combination of trap depth and waist then completely determine the trap frequency  $\omega_2$  as follows[122]

$$\tilde{U}_i = \frac{1}{4}\tilde{\omega}_i^2\tilde{w}_i^2 \quad (4.3)$$

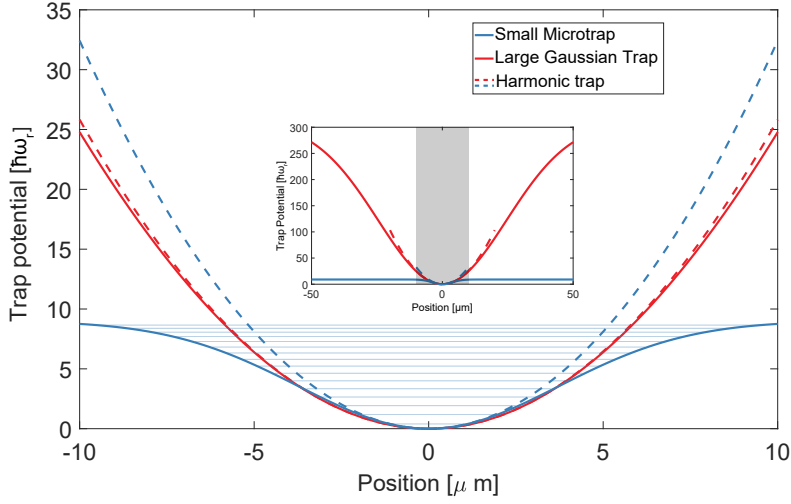


Figure 4.3: **Potentials of the first matterwave lens and the microtrap in which the system is prepared.** The first matterwave lens for  $T_1/4$  expansion is implemented using an optical Gaussian trap. The microtrap in which the system is prepared has a trap depth  $U_0 \approx 9.1\hbar\omega_r$  and waist  $w_0 \approx 7.45\mu m$ . On the contrary the first matterwave lens is larger and deeper with a  $U_1 \approx 310\hbar\omega_r$  for magnification 40 and  $w_1 \approx 49.5\mu m$ . This ensures that the potential of the first matterwave lens is nearly harmonic over the spatial extent of the system wavefunction. The completely harmonic trap for comparison is shown for each of these traps as dashed lines of the respective colors.

where indices  $i = 1, 2$  are for the first and second matterwave lens respectively and  $\{\tilde{U}_i, \tilde{w}_i, \tilde{\omega}_i\}$  is  $\{U_i, w_i, \omega_i\}$  in units of  $\{\hbar\omega, \sqrt{\frac{\hbar}{m\omega}}, \omega\}$  with  $\omega$  being the trap frequency of the microtrap in which the system is prepared. Defining energies, lengths and frequencies in harmonic oscillator units makes comparison to system scales easier. Since the trap frequency of the second matterwave lens is determined, the trap frequency  $\omega_1$  of the first matterwave lens is then fixed. Using the system size (energy) as a guide, the waist of the first matterwave lens  $w_1$  (depth  $U_1$ ) can then be appropriately chosen and using the relation between  $U_1$ ,  $w_1$  and  $\omega_1$ , the depth of the first matterwave lens  $U_1$  (waist  $w_1$ ) is determined. The trap parameters for the matterwave lenses can also be determined in the opposite order starting with the first lens followed by the second.

Due to the limited range of trap frequencies achievable in the experiment, optical dipole traps were used to implement matterwave lenses. The optical microtrap used for preparing the system has a trap frequency of  $\omega_r \approx 2\pi \times 1100\text{Hz}$ , a waist of  $w \approx 7.45\mu\text{m}$  and trap depth  $U_0 \approx 9\hbar\omega_r$ . Close to its center a Gaussian beam can be approximated with a harmonic and a quartic term. The quartic term gets larger as the distance from the center of the trap increases and the harmonic approximation fails. The waist (trap depth) is only approximately 3 times the length(energy) scales of the system and this is a very bad approximation to a harmonic potential. To circumvent this issue an additional beam with a waist  $w_1 = (49.45 \pm 0.7)\mu\text{m}$  and trap depths  $U_1$  ranging from 190 to  $310\hbar\omega_r$  was used to implement the first matterwave lens. The optical power in the beam is regulated since the power affects the trap frequency and hence the  $T_1/4$  time in the first matterwave lens. The range of trap depths accessible results in trap frequencies ranging from 763 to 977Hz. A sketch of the optical potentials of the microtrap and the first matterwave lens for comparison is shown in Figure 4.3. Section 4.5 details how the trap parameters were obtained accurately from experimental measurements.

For the second expansion, a combination of a single layer of an optical lattice and a magnetic trap is used. The optical lattice provides tight axial(weak radial) confinement with radial trap frequencies  $\omega_{\perp} \approx 2\pi \times 20\text{Hz}$  with a waist of  $w \approx 600\mu\text{m}$  and trap depth of  $U_2 \approx 1000\hbar\omega_r$ . The tight axial confinement ensures that the atoms are restricted to a single plane for imaging. The magnetic trapping potential has a trap frequency of  $\omega \approx 2\pi \times 10\text{Hz}$  and provides a confining(deconfining) harmonic potential for high(low) field seeking spin states. The resulting combined trap frequency is  $\omega_2 \approx 2\pi \times 23\text{Hz}$  ( $\omega_2 \approx 2\pi \times 17\text{Hz}$ ) for high(low) field seeking spin states.

The size of the system we have is smaller than the effective optical resolution. In such a situation even when the second matterwave lens is not harmonic, the initial momentum  $p(T_1/4)$  before the second expansion can be obtained by a lookup table. Such a look up table takes into account the characteristics of the potential such as  $\omega_2$ ,  $w_2$  and  $U_2$  and more details can be found in [75]. The first matterwave lens on the other hand needs to be as harmonic as possible and in such a situation momentum  $p(T_1/4)$  and in situ position  $x(0)$

are related as follows,

$$x(0) \approx -\frac{1}{m\omega_1} p(T_1/4) \quad (4.4)$$

Thus through a measurement of the final atom positions  $x(T_1/4 + T_2/4)$  one can obtain  $p(T_1/4)$  and eventually the initial in situ positions  $x(0)$  of the particles.

## 4.5 Trap parameters

In Section 4.4, trap parameters for the matterwave lenses were specified. Accurate determination of trap parameters is essential to estimate effects of matterwave aberrations. In this Section, a summary of how these parameters are extracted from experimental measurements is presented. There are three quantities which characterize a Gaussian trap - waist  $w_i$ , trap frequency  $\omega_i$  and trap depth  $U_i$ . The subscript  $i = 1, 2$  is used to index the two matterwave lenses.  $w_i$  can be calculated from Gaussian beam focusing using a lens, but for an imperfect Gaussian beam this has free parameters determined by the beam quality given by  $M^2$ . One way to experimentally determine  $w_i$  is to measure the beam profile at the position of the atoms. However since this is technically not practical, a parameter free scheme using actual measurements of trap frequency  $\omega_i$  was sought to determine both  $w_i$  and  $U_i$  without any free parameters.

From a classical analysis of optical dipole traps(ODT)[122] one can determine  $U_i$  as in Equation 4.5.

$$U_i = \frac{3\pi c^2}{2\omega_0^3} \left( \frac{\Gamma}{\omega_0 - \omega} + \frac{\Gamma}{\omega_0 + \omega} \right) \frac{2P}{\pi w_i^2} \quad (4.5)$$

where  $c$  is the speed of light in vacuum,  $\omega_0$  is the angular frequency of the resonant transition,  $\Gamma$  is the resonant transition linewidth,  $\omega$  is the angular frequency of the light used to create the dipole trap and  $P$  is the total beam power. The trap frequency  $\omega_i$  in the ODT is also related to the trap depth  $U_i$  and waist  $w_i$  as in Equation 4.6 where  $m$  is the particle mass.

$$w_i = \sqrt{\frac{4U_i}{m\omega_i^2}} \quad (4.6)$$

Thus by measuring  $P$  and  $\omega_i$ , both  $w_i$  and  $U_i$  can be estimated without any free parameters. The trap frequency is obtained by exciting collective modes in this trap with a few non-interacting atoms. This is achieved through a quench of the trapping potential by switching from the tweezer in which the system is prepared to the matterwave lens trap. Depending on the position of this trap with respect to the position of the tweezer containing the atoms different modes such as dipole, breathing, quadrupole and higher order modes can be excited. A Principal Component Analysis(PCA) of the images is then used to decompose the observed excitations of the few-body cloud of atoms in terms of these collective modes[123]. The trap frequency obtained from the dipole mode, which has the same frequency as the

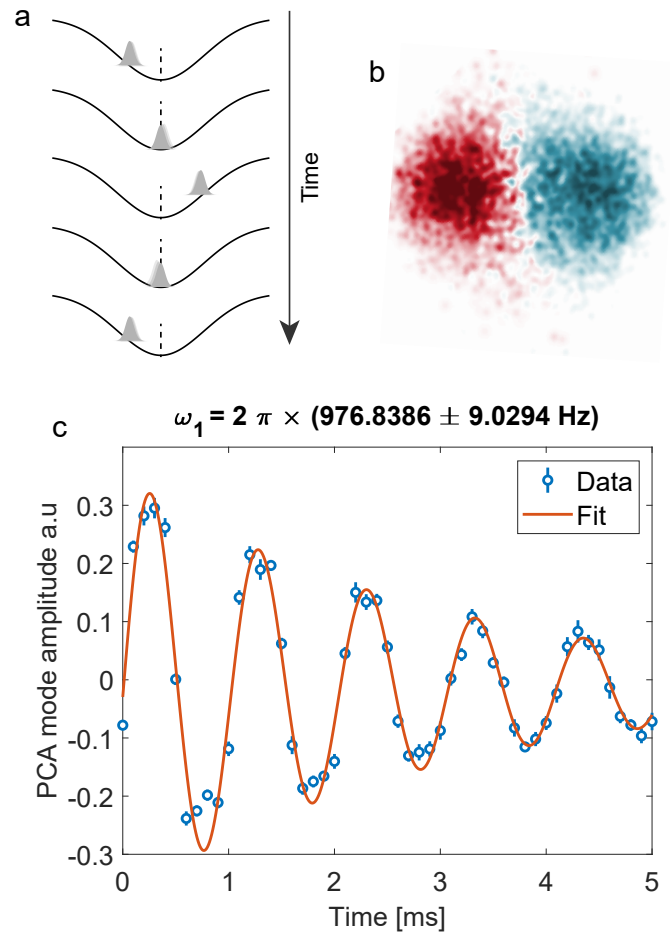


Figure 4.4: **Trap frequency measurement to determine trap parameters and  $T_1/4$  duration.** (a) Trap frequencies are measured by quenching the trap and exciting collective modes - monopole, dipole, quadrupole, etc. Depicted here is the dipole mode which oscillates at the trap frequency. (b) The various modes excited are obtained from a Principle Component Analysis (PCA). The principle component for the dipole mode is shown here. (c) Principle component amplitude oscillates as a function of time and is used to extract the frequency of the dipole mode for the first matterwave lens. Since the frequency of oscillation of the dipole mode is equal to the trap frequency,  $\omega_1 = 2\pi \times (977.2972 \pm 9.8458) \text{ Hz}$  is obtained. The error bars indicate standard error of the mean.

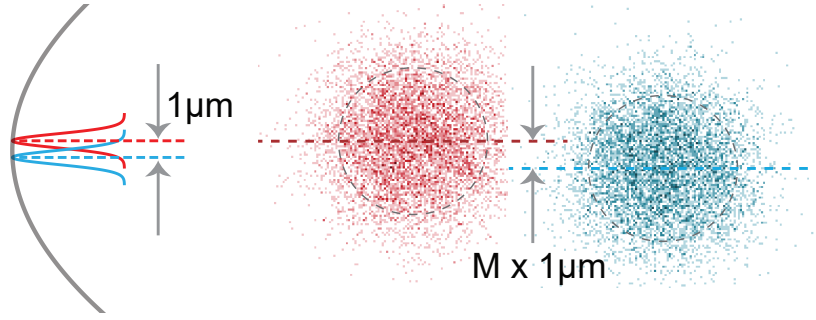


Figure 4.5: **Magnification of the Matterwave Microscope.** The position of the tweezer in the radial plane is displaced by  $1\mu m$  (relative to the matterwave lens shown in grey) followed by Matterwave expansion with  $T_1/4+TOF$ . By aggregating many images, the single atom density in position space is obtained. By comparing the center of the density distribution of the shifted and unshifted initial trap, the magnification is obtained. Depending on the trap frequency of the first trap used for expansion ( $\omega_1 \approx 2\pi \times 763$  to  $977\text{Hz}$ ) magnifications of (30 to 42) are obtained

trap, is shown in Figure 4.4. Anisotropy from such a scheme is hard to extract since the dipole mode amplitude depends on the displacement between the trap and the tweezer containing the atoms and can potentially couple only along one direction. Hence to determine anisotropy, a scheme based on imaging a single Feshbach molecule is used in Section 4.6.3.

## 4.6 Characterizing the matterwave lens

The characteristic energy scales and length scales in the system that one would like to probe determines the design parameters for the matterwave lenses. Based on these requirements, a combination of matterwave lenses was chosen. The key parameters of the matterwave lenses were determined through experimental measurements. Here we utilize these matterwave lenses to implement a matterwave microscope and use experimental measurements to characterize it. The magnification obtained with the combination of matterwave lenses is first characterized. Since Gaussian traps are used to implement harmonic potentials, aberrations due to anharmonicity arise. The effect of anharmonicity on matterwave transformations is estimated and experimentally measured. The system which we probe is confined to 2D and hence anisotropy of the matterwave microscope needs to be characterized. A characterization is performed by imaging a single s-wave Feshbach molecule. Finally the effective resolution that one can expect with the matterwave microscope is presented.

### 4.6.1 Magnification

Ideally the magnification can be obtained by imaging a tight tweezer array when the initial spacing is known. Atoms in a tight tweezer have large momentum and when subjected to matterwave transformations would probe the anharmonic parts of the potential. This leads to matterwave aberrations and hence is not appropriate to characterize the magnification. To circumvent this eventuality, a few atoms in a tweezer are loaded with trap frequencies in the regime where measurements are desired. Using a spatial light modulator (SLM), the tweezer location is translated by a known value with respect to the matterwave lens and the system is imaged following matterwave transformations for  $T_1/4 + \text{TOF}$ . The displacement of the tweezer center in the final image compared to the unshifted tweezer after matterwave transformations gives the magnification. This is shown in Figure 4.5. To obtain different magnifications  $M$ , the trap frequency of the first matterwave lens  $\omega_1$  is tuned while keeping the trap frequency of second matterwave lens  $\omega_2$  fixed. Magnifications of (30 to 42) for  $\omega_1 \approx 2\pi \times (763 \text{ to } 977)\text{Hz}$  are obtained.

### 4.6.2 Anharmonicity

As mentioned in the Section 4.4, the first matterwave lens has a large waist  $w_1 = (49.45 \pm 0.7)\mu\text{m}$  and trap depth  $U_1 = 190 \text{ to } 310\hbar\omega_r$ . On the contrary the microtrap in which the system is prepared is small and has a waist  $w = (7.485 \pm 0.017)\mu\text{m}$  and trap depth  $U = (9.1032 \pm 0.007)\hbar\omega_r$ . A comparison of these traps was shown in Figure 4.3. The central region of the first matterwave lens, where the system wavefunction is confined, is very harmonic. The largest deviation from harmonicity is on the order of 3% over the largest extent of the wavefunction. Due to the small deviation from harmonicity, the momentum that the particles have after the first expansion is  $p(T_1/4) \approx -m\omega_1 x(0)$ .

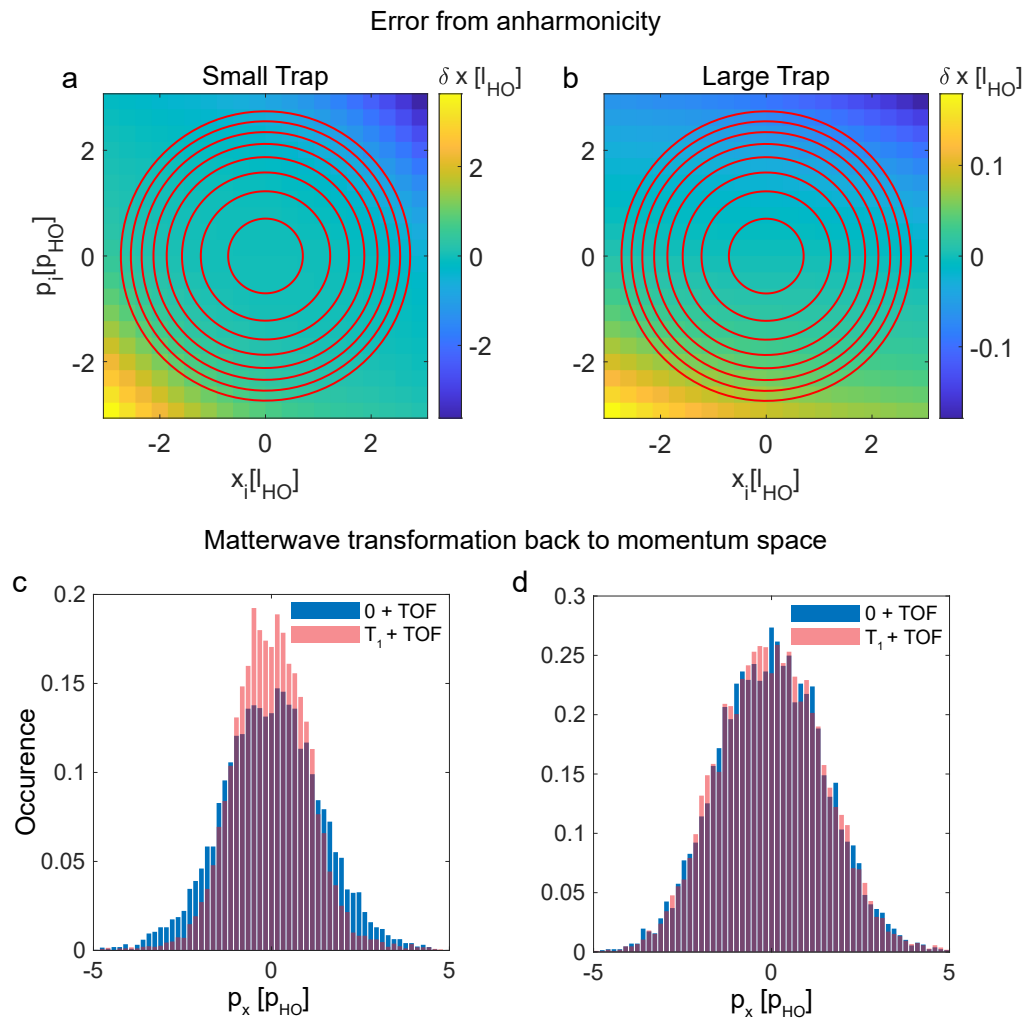
From the trap parameters of the first matterwave lens, the error due to anharmonicity is estimated as follows. Initial phase space co-ordinates  $(x_i, p_i)$  are randomly chosen and evolved in two matterwave lenses for  $T_1/4 + \text{TOF}$ . After the time evolution, using the trap parameters for the second matterwave lens a lookup of the momentum  $p(T_1/4)$  is performed. The final positions  $x(T_1/4 + \text{TOF})$  which is obtained by time evolution of  $(x_i, p_i)$  through the matterwave lenses is used to look up momentum  $p(T_1/4)$ . Assuming nearly harmonic evolution in the first matterwave lens, the initial in situ position  $x(0) = (-1/m\omega_1)p(T_1/4)$  is obtained. This value is compared to the actual initial position  $x_i$  and the difference  $\delta x = x(0) - x_i$  gives an estimate of the error due to anharmonicity of the first matterwave lens. The results are shown in Figure 4.6(a,b). To contrast how the anharmonicity affects the measured in situ position, the errors are compared for a small microtrap with  $w_1 \approx 7.45\mu\text{m}$ ,  $U_1 \approx 9\hbar\omega_r$  and a comparatively large trap with  $w_1 \approx 49.45\mu\text{m}$ ,  $U_1 \approx 190\hbar\omega_r$  as the first matterwave lens. For the large trap the largest deviations are small compared to the natural length scale given by the harmonic oscillator length.

In addition to estimating the anharmonicity and the extent to which it affects measured

in situ positions, its effect on matterwave transformations needs to be experimentally determined. To do this a  $T_1$ +TOF expansion is performed using the matterwave lenses. A time evolution for  $T_1$  in the first matterwave lens should have no effect and be equivalent to directly measuring the in situ momentum distribution of the sample[23], [124]. This scheme is used to compare the in situ momentum distributions of a small sample of atoms for both the small microtrap and the large trap as the first matterwave lens and is shown in Figure 4.6(c,d). For a small trap, significant deviations in the momentum distribution are

---

Figure 4.6 (following page): **Anharmonicity and controlling matterwave aberrations.** (a,b) Estimate of matterwave aberrations by simulation. Various initial phase space co-ordinates of a particle are evolved for  $T_1/4$ +TOF. To compare the effect of anharmonicity, the evolution is performed in a first matterwave lens with parameters corresponding to the small microtrap( $U_1 \approx 9\hbar\omega_r$ ,  $w_1 \approx 7.45\mu m$ ) or a large trap( $U_1 \approx 190\hbar\omega_r$ ,  $w_1 \approx 49.5\mu m$ ). A random diffusion distance sampled from a normal distribution is added to the final evolved position. From these final positions, a lookup of the momentum  $p(T_1/4)$  is performed from which the in situ position is obtained as  $x(0) = (-1/m\omega_1)p(T_1/4)$ . The deviation in atom lookup positions  $\delta x = x(0) - x_i$  compared to the actual initial position  $x_i$  is plotted as a heatmap for the (a)the small microtrap and the (b)large trap used as the first matterwave lens. The red contour lines correspond to the classical phase space limits for the first 8 harmonic oscillator shells which corresponds approximately to the quasi-2D limit. The small microtrap shows significantly large deviations from actual positions. (c-d) Experimentally measuring the effect of matterwave aberrations. To ensure that errors due to matterwave aberrations are not significant, a  $T_1$ +TOF expansion is performed and compared with a 0+TOF expansion. A first  $T_1$  expansion should not alter the measured in situ momentum and should be equivalent to no expansion in the first matterwave lens. When a small microtrap is used as the first matterwave lens, a histogram of measured particle momenta show significant deviations for  $T_1$ +TOF compared to 0+TOF for already 3+3 atoms with strong interactions. However, using a large Gaussian trap for the first matterwave lens mitigates the issue and no significant deviations are seen for 6+6 atoms with strong interactions.



present when an evolution in the first trap for  $T_1$  is performed compared to the large trap where the distributions are nearly identical. Hence from the above considerations, the trap can be considered as harmonic and the aberrations arising from the matterwave expansion are minimal. The total uncertainty arising from all sources including anharmonicity which determines the resolution of the matterwave microscope is discussed below in Section 4.6.4

### 4.6.3 Anisotropy

The main source of anisotropy for the matterwave microscope comes from the first matterwave lens. The trap used for the second matterwave lens has been characterized previously and has anisotropy of approximately 0.57% [125]. For the  $T/4$  evolution in the first matterwave lens, it is of paramount importance that the trap anisotropy be kept as low as possible otherwise the  $T/4$  duration would be different along different directions. Implementation of the first matterwave lens with a crossed beam trap instead of a single focused beam trap can potentially cause a large anisotropy since the trap frequencies along two directions then depend on the powers in the individual beams and the angle between them. To avoid this eventuality, we had to use a single focused beam trap.

To quantify the anisotropy, the evolution time  $t_1$  in the first matterwave lens is scanned around  $T_1/4$  and a single Feshbach molecule at  $E_B = 8.2\hbar\omega_r$  is imaged. The second order correlation function  $C^{(2)}(p_x^{rel}, p_y^{rel}) = \int d^2\vec{p}'_{\uparrow} \langle \mathbf{n}_{\uparrow}(\vec{p}'_{\uparrow}) \mathbf{n}_{\downarrow}(\vec{p}'_{\uparrow} + \vec{p}^{rel}) \rangle$  is extracted where  $\vec{p}'_{\uparrow}$  is momentum of the spin  $\uparrow$  and  $\vec{p}^{rel} = (p_x^{rel}, p_y^{rel})$  is the difference in momentum between the spin  $\uparrow$  and  $\downarrow$  particle at  $t_1$ . The slight difference in the focusing time along two orthogonal directions then gives the anisotropy of around 3.92% as shown in Figure 4.7.

### 4.6.4 Resolution

An important metric for the matterwave microscope is the smallest features it can resolve. There are two factors that influence the resolution - atom diffusion during fluorescence imaging and aberrations during matterwave transformations. During the fluorescence imaging process the atoms continuously scatter photons and are not confined in any potential. This leads to a diffusion of the atoms which results in an uncertainty in the final measured position of around  $2\sigma \approx 7.54\mu m$  and was shown in Figure 4.2. This uncertainty in the final measured position affects the lookup of the initial in situ positions. Anharmonicity in the trapping potential used for the first matterwave lens can lead to particle trajectory deviations from the harmonic case leading to matterwave aberrations. An estimate of these uncertainties for the trap parameters we have was shown in Figure 4.6(b).

To estimate the combined uncertainty which gives the resolution, two non-interacting particles in a trap at varying trap frequencies (initial sizes) are prepared and imaged with the matterwave microscope. Fitting a Gaussian density distribution to the system, the width  $\sigma$  of the in situ distribution is obtained. The size of the in situ cloud as a function of the initial size of the system is shown in Figure 4.8. As the trap frequency increases,

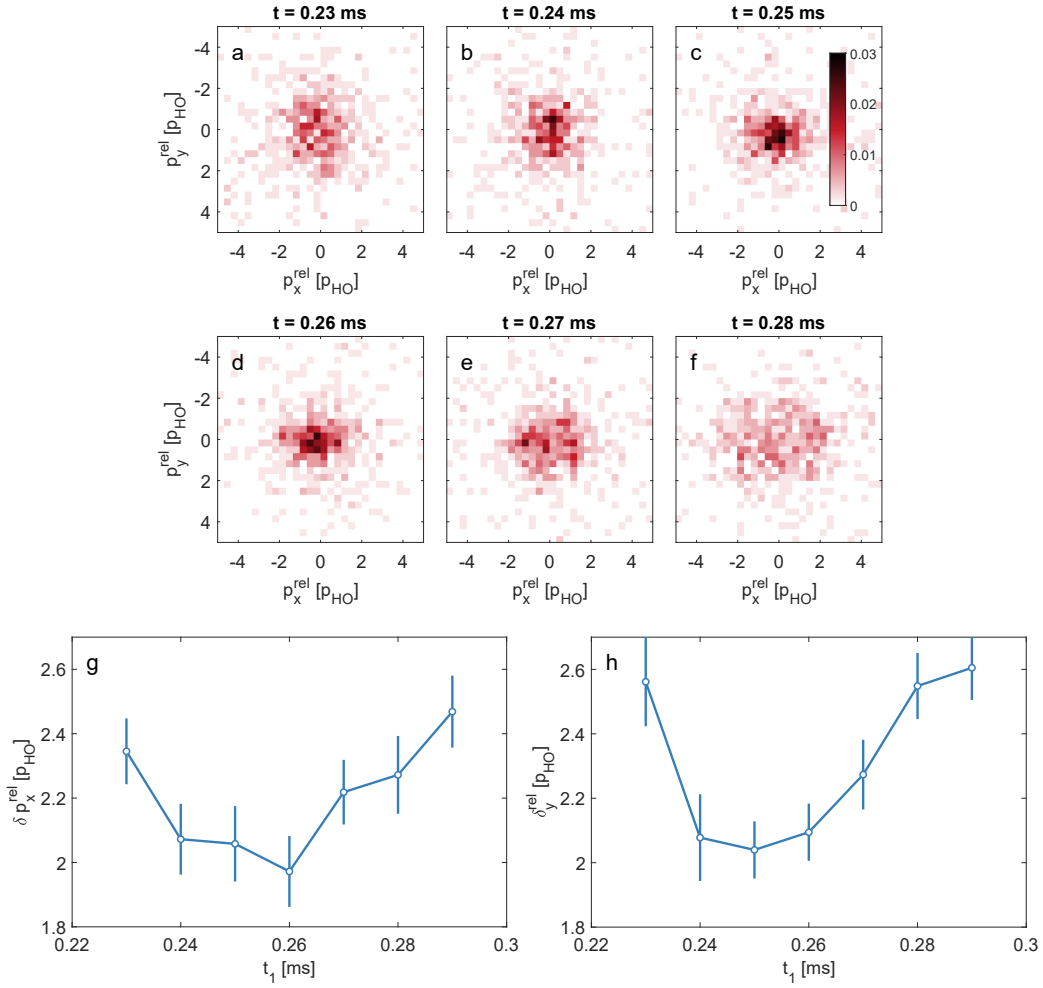


Figure 4.7: **Analysis of anisotropy of the matterwave microscope.** Anisotropy of the matterwave microscope is quantified by imaging a single Feshbach molecule at a binding energy  $E_B$  of  $8.2\hbar\omega_r$  after two matterwave transformations with times  $t_1$  and TOF respectively. The time in the first trap  $t_1$  is scanned around  $T_1/4$  and anisotropy is inferred from the slightly different focusing duration along two orthogonal axes. After the final positions of the atoms are imaged, the initial momentum at the end of the first expansion  $p(t_1)$  is extracted. The plots (a-f) show histograms of the relative momentum  $C^{(2)}(p_x^{\text{rel}}, p_y^{\text{rel}})$  with the two axes denoting the x and y relative momentum. This gives an anisotropy of  $\approx 3.92\%$ . (g,h) The root mean square (rms) widths of the relative momentum in the x and y directions as a function of the first matterwave lens time  $t_1$ . A large anisotropy would manifest itself as significantly different times at which the rms widths reach a minimum as a function of  $t_1$ . The error bars indicate standard error of the mean.

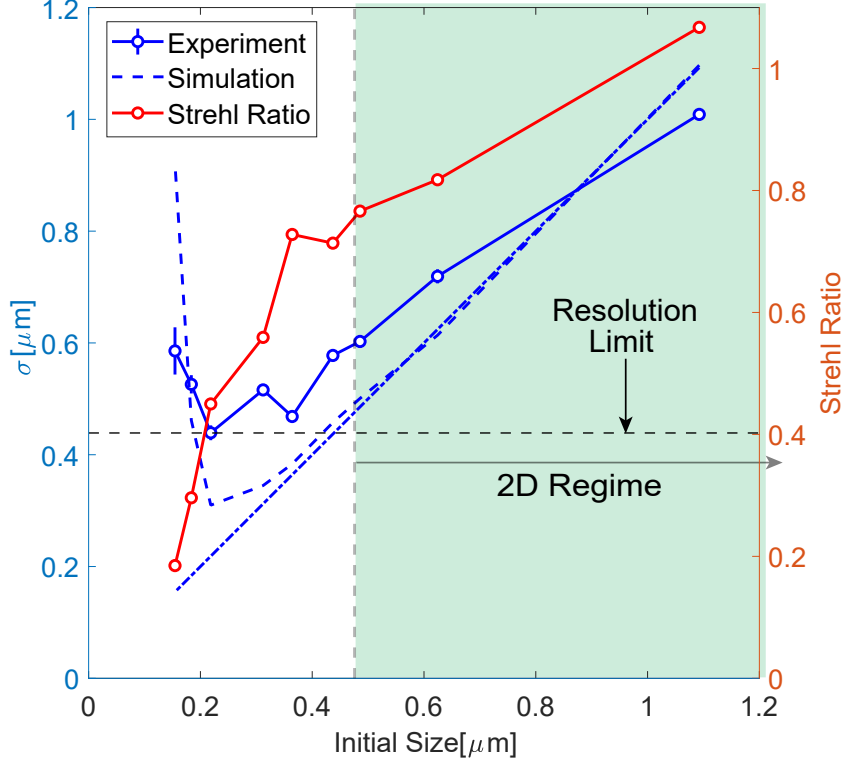


Figure 4.8: **Resolution of the matterwave microscope at a magnification of 30.**

The in situ density of a single atom in a trap is imaged after the magnification procedure for different initial sizes of the system (achieved by tuning system trap frequency) and then the width of the distribution  $\sigma$  is extracted by fitting a Gaussian function. The obtained  $\sigma$  is compared to the theoretical expectation value of  $\sqrt{\frac{\hbar}{2m\omega}}$  (dot-dashed line) and a simulation of particle trajectories (dashed line, blue) in the sequence of two traps followed by diffusion during imaging. The error bars indicate 95% confidence intervals for the Gaussian fit. The resolution limit of  $0.44\mu\text{m}$  is the smallest width of the Gaussian distribution which is obtained as the initial size of the system is reduced. The Strehl ratio, which gives a measure of aberrations, is plotted in red.

the atoms get more tightly confined and the measured size shrinks accordingly until the resolution limit is reached which is found to be at  $0.44\mu m$  for a magnification of 30. For the 2D systems that are imaged, the largest energy scale should be less than approximately 7KHz (corresponding to a length scale of  $0.477\mu m$ ) set by the axial trapping frequency. This length scale can also be reconciled from the fact that for the 2D scattering process, the effective range is given by the harmonic oscillator length of the strong trapping axis in contrast to the interaction range  $r_0$  in 3D[126]. To ensure the 2D-ness of the system, the largest absolute binding energies studied are 2.87KHz where the pair size is expected to be  $l_B \approx 0.765\mu m$ . For these binding energies the microtrap frequency is reduced to  $\omega_r = 2\pi \times 350\text{Hz}$  so that  $E_B = 8.2\hbar\omega_r$  is dominant energy scale in the system. This ensures that for the systems experimentally explored, the resolution of the matterwave microscope is not a limiting factor. To further quantify the extent of aberrations on the final image, a Gaussian density profile is fit to the image and its amplitude is compared to an unaberrated image. This gives the Strehl ratio which is a good indicator of the imaging performance of the system.

The resolution should also be compared to the effective resolution of our imaging system. While the smallest features that can be measured by our objective at imaging wavelengths (671nm) is given by its Point Spread Function  $\text{PSF} \approx 0.86\mu m$ , the smallest features that can be resolved with the imaging system taking into account the final magnification of the image and camera pixel size is  $2.165\mu m$ . Thus even with an upper bound of  $0.44\mu m$  from the resolution of the matterwave microscope, we still gain by at least a factor of 4 when imaging a single atom which is tightly pinned and does not diffuse during imaging. Under standard imaging conditions where the atom is not pinned the extent to which the atoms diffuse during fluorescence imaging sets the imaging resolution scale (which includes  $\text{PSF} +$  magnification of imaging system) of  $2\sigma \approx 7.54\mu m$  and compared to this the resolution of the matterwave microscope is 17 times smaller.

## 4.7 Imaging pairs in a spin-balanced few-fermion system

A spin-balanced few-fermion system in the BEC-BCS crossover is now imaged with the matterwave microscope. The system consists of a two component Fermi gas of  ${}^6\text{Li}$  atoms with tunable interactions in a 2D Harmonic oscillator potential. The system was presented in Chapter 3. The atoms are laser cooled and trapped in the ground state of a 2D harmonic oscillator trap with trapping frequencies  $\omega_r = 2\pi \times (1101 \pm 2)\text{Hz}$  in the radial ( $\omega_r = 2\pi \times 350\text{Hz}$  only for  $E_B = 8.2\hbar\omega_r$ ) and  $\omega_z = 2\pi \times (7342 \pm 3)\text{Hz}$  in the axial directions leading to an aspect ratio of  $\eta \approx 1 : 7$ . For small atom numbers the system is in the axial ground state and has a visible shell structure for the radial levels[80]. The interaction strength in the system is characterized by the two-body binding energy  $E_B$ [79] and the properties of the system are determined by the magnitude of  $E_B$  relative to the single particle gap given by  $\hbar\omega_r$  and the Fermi Energy  $E_F$ . Tuning interactions and measuring correlations

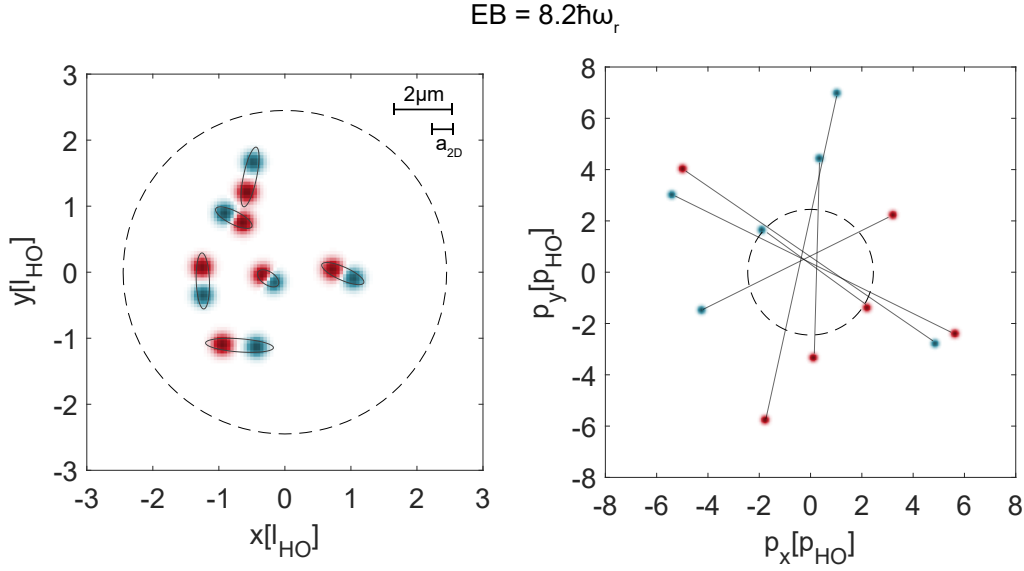


Figure 4.9: **Snapshots of 6 spin  $\uparrow$ (blue) and 6 spin  $\downarrow$ (red) particles in position and momentum space.** The binding energy characterizing the attraction between the particles is  $E_B = 8.2\hbar\omega_r$ . The binding energy is the largest energy scale in the system since it is larger than the Fermi energy  $E_F = 3\hbar\omega_r$  (a) In situ Positions. In position space images the system shows a tendency to form pairs whose size is smaller than the intraspin inter-particle spacing. In this case the axes denote position co-ordinates in terms of the harmonic oscillator units  $[l_{HO}]$ . (b) In situ momenta. On the contrary in momentum space, the pairs have opposite momenta and are large since position and momentum are Fourier pairs. The axes in this case are x and y co-ordinates of momentum in harmonic oscillator units  $[p_{HO}]$ . The dotted lines in both cases denote  $\sqrt{2E_F}$  with  $E_F$  in units of harmonic oscillator energy  $\hbar\omega_r$ . This also indicates that the system size in position space gets smaller compared to the non-interacting system due to attractive interactions.

in the system in momentum space have revealed Cooper pairing at the Fermi surface[75] for moderate interactions and were summarized in Section 3.6. Using the matterwave microscope such a system is imaged in the molecular limit  $E_B > E_F$  of the BEC-BCS crossover and compared with snapshots of the in situ momenta of the system.

At binding energies which are the largest energy scales in the system, a tendency to form pairs whose size is small compared to the inter-particle spacing of each spin component is expected[127]. As the largest binding energies of  $8.2\hbar\omega_r$  are accessed, the trap frequency is reduced to  $\omega_r = 2\pi \times 350$  Hz to ensure that the system remains in the quasi-2D regime. In absolute terms the binding energy is 2.87 KHz which is less than the axial confinement of 7.340 KHz. This also ensures that matterwave aberrations from anharmonicity are minimal even at large binding energies. A comparison of snapshots of two realizations of the system at the same  $E_B = 8.2\hbar\omega_r$ , one in position space and the other in momentum space is shown in Figure 4.9. In momentum space the particles with opposite spin tend to have opposite momenta while in position space they tend to form a short distance pair. At a binding energy of  $8.2\hbar\omega_r$ , the 2D scattering length  $a_{2D}$  is approximately  $0.76\mu\text{m}$  which sets the length scale of the pairs.

To quantify pairs at close distances the second-order density-density Correlator  $C_c^{(2)}(\vec{\mathbf{r}}_\uparrow, \vec{\mathbf{r}}_\downarrow)$  is calculated as

$$C_c^{(2)}(\vec{\mathbf{r}}_\uparrow, \vec{\mathbf{r}}_\downarrow) = \langle \mathbf{n}_\uparrow(\vec{\mathbf{r}}_\uparrow) \mathbf{n}_\downarrow(\vec{\mathbf{r}}_\downarrow) \rangle - \langle \mathbf{n}_\uparrow(\vec{\mathbf{r}}_\uparrow) \rangle \langle \mathbf{n}_\downarrow(\vec{\mathbf{r}}_\downarrow) \rangle \quad (4.7)$$

where  $\mathbf{n}_{\uparrow(\downarrow)}(\vec{\mathbf{r}}_{\uparrow(\downarrow)})$  is the density of spin  $\uparrow$  ( $\downarrow$ ) particles at  $\vec{\mathbf{r}}_{\uparrow(\downarrow)}$  and the averaging  $\langle \dots \rangle$  is over many realizations of the experiment. Like in Section 3.6, this correlator is four dimensional and integrating out the co-ordinates of the spin- $\uparrow$  particle and introducing relative co-ordinates between the spin- $\uparrow, \downarrow$  particles yields a 2D correlator which can be plotted

$$C_c^{(2)}(x_{rel}, y_{rel}) = \int \int dx dy \langle \mathbf{n}_\uparrow(x, y) \mathbf{n}_\downarrow(x+x_{rel}, y+y_{rel}) \rangle - \langle \mathbf{n}_\uparrow(x, y) \rangle \langle \mathbf{n}_\downarrow(x+x_{rel}, y+y_{rel}) \rangle \quad (4.8)$$

where  $(x, y)$  is the co-ordinate of the spin- $\uparrow$  particle,  $(x_{rel}, y_{rel})$  is the relative co-ordinate of the spin- $\downarrow$  particle with respect to the spin- $\uparrow$  particle. This correlator is plotted in Figure 4.10(a-e) for different interaction strengths from  $E_B = 0$  to  $8.2\hbar\omega_r$ . The relative radial angles of this correlator can be integrated to obtain a  $C_c^{(2)}(r_{rel})$  as follows

$$C_c^{(2)}(r_{rel}) = \frac{1}{2\pi} \int d\phi_{rel} C_c^{(2)}(x_{rel}, y_{rel}) \quad (4.9)$$

Here  $\vec{\mathbf{r}}_{rel} = (x_{rel}, y_{rel})$ ,  $r_{rel}$  is the relative distance and  $\phi_{rel}$  the relative angle of the spin- $\downarrow$  particle with respect to the spin- $\uparrow$  particle. This is also plotted in Figure 4.10(f-j). The Correlators show that with increasing interaction strength, the signal from short distance pairs increases monotonically. The number of short range pairs as a function of  $E_B$  is

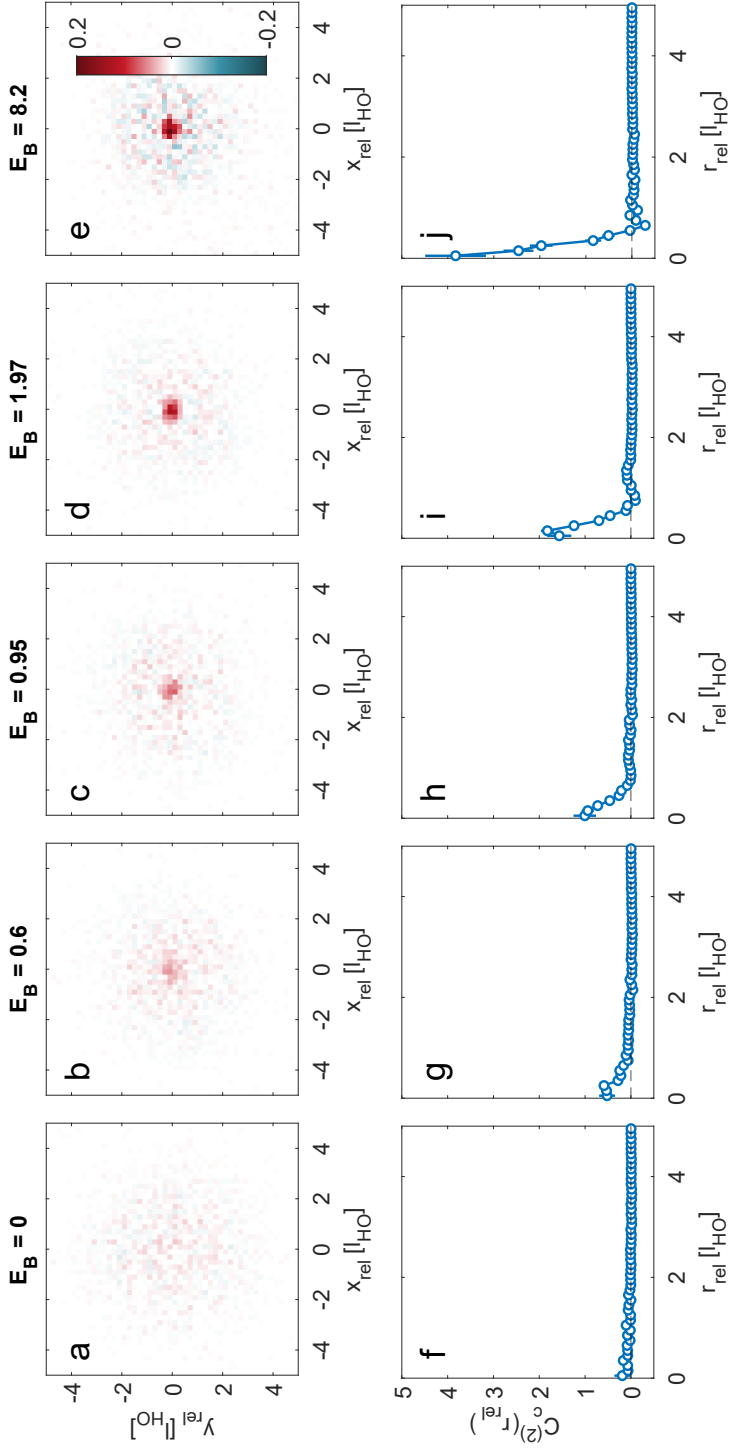


Figure 4.10: **Correlations of in situ positions for a system consisting of 6+6 fermions.** (a-e) Second-order correlator between spin  $\uparrow$  and  $\downarrow$  particles in terms of their relative co-ordinates  $C_c^{(2)}(x_{rel}, y_{rel})$ . The axes  $x_{rel}$  and  $y_{rel}$  both are in units of harmonic oscillator length units  $l_{HO}$ . As the two-body binding energy  $E_B$  is increased from 0 to  $8.2\hbar\omega_r$ , the correlations at short distances increase implying the presence of more correlated particles or pairs. (f-j) Second-order correlator  $C_c^{(2)}(r_{rel})$  as a function of relative distance between spin- $\uparrow, \downarrow$  particles. The relative distance is expressed in units of harmonic oscillator length  $l_{HO}$ . The error bars indicate standard error of mean. As  $E_B$  is increased from 0 to  $8.2\hbar\omega_r$  in (f-j) the correlations at short relative distances increase.

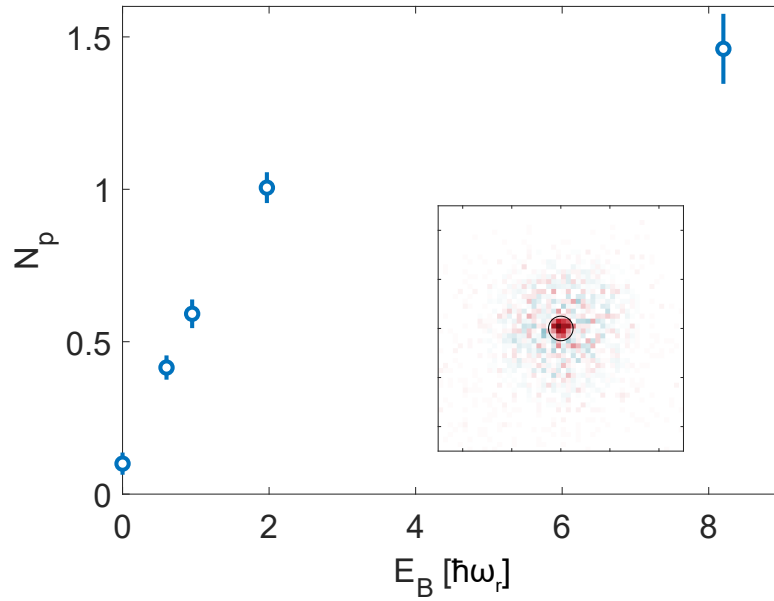


Figure 4.11: **Number of particles with short-range correlations for an interacting system comprising of 6+6 fermions.** Increasing the two-body binding energy  $E_B$  between the spin  $\uparrow$  and  $\downarrow$  particles leads to more particles  $N_p$  having short-range correlations. The number of such particles are calculated by summing the second order correlator within a relative distance cutoff radius of  $0.5l_{HO}$  as shown in the inset for  $E_B = 8.2\hbar\omega_r$ . The error bars indicate standard error of the mean.

obtained by integrating  $C_c^{(2)}$  as,

$$N = \int_0^{dr} \int dx_{rel} dy_{rel} C_c^{(2)}(x_{rel}, y_{rel}) \quad (4.10)$$

The integration is performed over a short distance window given by the cutoff radius  $dr = 0.5\sqrt{\hbar/m\omega_r}$ . The plot in Figure 4.11 summarizes the number of short distance pairs as a function of  $E_B$ .

Correlations at short length scales in a many-body system determine a quantity called Tan Contact[24]. This microscopic quantity has implications beyond what happens at short length scales and determines thermodynamic properties of the many-body system. The Contact determines the distribution of atoms at large momentum[128], the total energy[129] and the pressure in a Fermi gas[130]. The Contact has so far only been determined by the measurement of macroscopic observables[131]–[133]. Access to these correlations could in the future be used to obtain this universal quantity from microscopic measurements.

## 4.8 Conclusion

In Chapter 3, experiments concerning the microscopy of interacting mesoscopic systems in momentum space were presented. Such a measurement of single particle observables provided access to microscopic correlations which were used to infer the formation of Cooper pairs. Direct measurement of in situ positions of the particles were intractable since the spatial extent of the system was smaller than the effective imaging resolution. In this chapter, ways to circumvent this problem and obtain access to in situ positions of the particles were presented. The ability of harmonic traps to perform phase-space matterwave transformations was pointed out. Evolution of particles in a combination of harmonic traps was used to magnify the in situ position-space wavefunction of a many-body system. The requirements for such a matterwave magnification scheme were pointed out and technical challenges in the implementation were presented. An implementation using Gaussian optical dipole traps to approximate harmonic confinement needed for matterwave transformations was presented. The parameters of these matterwave lenses were precisely determined using experimental measurements. The characteristics of the resulting matterwave microscope - namely magnification, anharmonicity, anisotropy and resolution - were then presented. By a suitable choice of the trap frequency for the first matterwave lens magnifications of 30-42 were achieved. Since Gaussian traps were used to implement harmonic confinements, an estimate of the effect of anharmonicity was presented. Using experimental measurements it was made sure that the anharmonicity was sufficiently low. The net anisotropy of the matterwave microscope was experimentally quantified and ensured to be low. The effective resolution of the matterwave microscope was experimentally obtained and found to be smaller than the interesting length scales of the interacting system. The matterwave microscope was then used to study an interacting mesoscopic system consisting of 6+6 fermions

presented in the previous chapter. Snapshots of the system for  $E_B > E_F$  indicated the formation of closed distance pairs while the same system shows pairs with zero center-of-mass momentum in momentum space measurements. The second order density-density correlator was used to quantify the interaction dependence of correlations and the formation of short distance pairs as the interaction strength was increased. The number of closed distance pairs as a function of interaction strength was also quantified.

In the future each of the characteristics of the matterwave microscope can be improved. The magnification can be increased by increasing the trap frequency of the first matterwave lens. Since the trap frequency depends on the square root of power, it can be increased by increasing the optical power. Another option would be to implement the first matterwave lens with a wavelength closer to the D1 or D2 lines. Since the trap depth is inversely proportional to the detuning, this increases the trap frequency at the same optical power. Since small detunings from the D1/D2 lines lead to photon scattering, the amount of scattering during matterwave time might have to be considered. The anharmonicity can be further improved by making traps deeper and larger resulting in even smaller anharmonic corrections. Using adaptive optical components, closer approximations to harmonic traps can be obtained. Such methods could be additionally used to correct for optical aberrations which could improve the performance of the matterwave microscope. To reduce the drift of the matterwave lenses with respect to the mesoscopic system, active stabilization of the beam positions can be performed. The uncertainty in atom position due to diffusion during imaging can be reduced by using a pinning lattice or a heavier atomic species resulting in improved resolution.

Having demonstrated the performance of a matterwave microscope on a mesoscopic spin-balanced system, spin-imbalanced systems are explored in the next chapter. The extreme case of spin-imbalance featuring a single impurity immersed in a Fermi sea is particularly interesting to study in situ position correlations. The ground state of such a system is predicted to feature a Polaron-Molaron transition[48] in the many-body limit and the few-body counterpart of such a system will be explored.

## 5 Impurity Physics

In Chapter 4, a technique to access in situ particle positions was introduced. This technique was demonstrated on a spin-balanced system consisting of up to 6+6 fermions. In this chapter systems with unequal number of spin components are studied and microscopy of in situ quantities is used to access correlations in the system. A brief motivation for exploring such systems is first presented. Most of the interest surrounding such spin-imbalanced systems concerns their ground state[54]. A preparation scheme to reach the motional ground state of such a system is then presented followed by correlation measurements. Previously correlation functions up to second order were obtained to extract information about pairing in the system. Correlations in systems of extreme imbalance namely a single impurity immersed in a minimal few-body Fermi sea are first studied. Going beyond second order correlations, third order correlations are used to throw light on the few-body precursor of the many-body polaron-molecule transition in a 2D Fermi gas. The number of fermions are varied and its effect on the impurity studied. Repulsive mixtures of an impurity, which is an excited metastable state, are then studied. Using these correlation functions the region of stability before decay to lower lying ground state is explored. The interesting regime with finite impurity concentration is then explored where unlike Cooper pairs, pairs with finite center-of-mass(COM) momentum are speculated.

### 5.1 Introduction

In Chapter 3, experiments on a two-component few-fermion system in 2D were presented. Such a mesoscopic system features characteristics traditionally associated with a many-body system such as a phase transition and the formation of Cooper pairs. Direct evidence for Pauli blocking, which is responsible for the formation of Cooper pairs at finite interaction strength, was presented through the microscopy of a spin-polarized few-fermion system. Due to Pauli blocking, particles in such a system self-organize in the form of a Pauli crystal[81]. Introducing two spin components with finite interactions then revealed the formation of Cooper pairs in momentum space at the Fermi surface. Subsequently the extension of the single atom spin-resolved imaging to in situ positions was presented in Chapter 4 which made possible the complementary measurement of correlations in position space. At large binding energies  $E_B$  snapshots and correlations of such a system revealed the formation of short-distance pairs whose size was small compared the inter-particle spacing of each spin component. With such complementary microscopy in momentum and position space, the BEC-BCS crossover in a few-body system was demonstrated. While so far only systems with

equal number of spin components were studied, with the advent of ultracold gases there has been a growing interest in the physics of spin-imbalanced fermionic systems. Most notable directions of research have focused on the fate of pairing in systems with mismatched Fermi surfaces and the paradigmatic model of a single impurity immersed in a Fermi sea.

While for a spin-balanced system at weak attraction Cooper pairs at zero COM momentum are energetically favored at low temperatures, the fate of pairing in spin-imbalanced systems with mismatched Fermi surfaces is strongly debated with various possibilities[54]. The problem was first addressed independently by Clogston[32] and Chandrasekar[31] who predicted that Type-II superconductors subjected to a magnetic field would undergo transition from a BCS to a Normal phase. The applied magnetic field couples the spin with the motion of the particles thereby creating a chemical potential mismatch( $\delta\mu$ ) between spin components which competes with the superfluid gap  $\Delta$ . It was then predicted that when  $\delta\mu > \Delta/\sqrt{2}$  superfluidity would be destroyed. However, Fulde-Ferrell[34] and Larkin-Ovchinnikov[35] (FFLO) predicted a phase where pairs would form at finite COM momentum due to the mismatch in Fermi surfaces. This was expected to lead to a spatial modulation of the order parameter. While the FFLO phase is expected to occupy a smaller region of the phase diagram in 3D[53], it is postulated to occupy a discernible portion of the phase diagram in lower dimensions[134], [135] including the few-body limit[136], [137]. In addition, there have also been proposals where a superfluid region is formed in the interior of the majority Fermi surface around the minority Fermi surface leading to a breach in the majority spin component[26], [33]. This phase is named after Sarma and also called breached-pair or interior gap superfluidity descriptively.

The other instance of a spin-imbalanced system is one of extreme imbalance. It consists of a single impurity interacting with a fermionic environment and is a paradigmatic model in many-body physics. The notion of a polaron quasi-particle was introduced by Landau and Pekar to describe the motion of an electron in a crystal lattice. The electron motion in such a situation could be described as the motion of the bare electron with the surrounding cloud of lattice polarization. The lattice polarization causes an attractive binding resulting in deviation from the free particle dispersion relation of the electron. This free electron dressed by the surrounding lattice polarization was described as a new quasi-particle, the polaron, having an effective mass different from the electron[40]. Fröhlich introduced a variational wavefunction of an electron interacting with a bath of lattice phonons to describe such a system[41]. The advent of ultracold atomic Fermi gases with tunable interactions has created a renewed interest in spin-imbalanced systems[25]–[30]. Some of these experiments have also been responsible for renewing interest in the problem of a single impurity immersed in a Fermi sea - The Fermi polaron problem. It was found that at unitarity the ground state of an imbalanced two-component harmonically trapped Fermi gas phase separates into three regions - a central superfluid, an intermediate Normal partially polarized fluid and a fully polarized outer core[36]. Since the wide Normal region could not be explained by BCS theory, Chevy introduced a variational wavefunction to describe the Normal partially polarized fluid as a single impurity interacting with a Fermi sea - the Fermi polaron[39].

Such a variational wavefunction could then predict the radius of the regions of these different phases. Subsequently it was predicted that as the strength of the interactions is increased the polaron undergoes a transition into a molecular state[42]. Subsequent experiments in 3D with radio frequency(RF) ejection spectroscopy have found evidence for the Fermi polaron and also a transition to a molecular state at larger coupling strengths[43]. The quasi-particle mass of the Fermi polaron has also been measured at unitarity using collective excitations and found to be in agreement with theoretical predictions[44]. These Fermi polarons have also been observed in the repulsive regime where they are not the ground state[69], [138]. The effect of finite temperature and impurity concentration on the nature of the polaron-molecule transition has also been studied experimentally using Raman spectroscopy[139].

The fate of the ground state of a 2D attractive Fermi gas has also been subject to its fair share of debate. Theoretical studies have used a variational wavefunction approach to describe a polaron and a molecule and have found no evidence for a transition[47]. However in a realistic system, one cannot ignore the effect of interactions of the molecule with the Fermi Sea and particle-hole dressing of the molecule, the "molaron" should also be considered. Including such a particle-hole dressing of the molecule has indeed provided theoretical evidence for a polaron-molaron transition in a 2D[48] system as well as trapped quasi-2D systems[49]. These studies also correctly recover the energy of an infinitely heavy impurity, unlike [47]. Further evidence in favor of a polaron-molaron transition in 2D is provided by Diagrammatic Monte Carlo studies [50], [51]. Experiment in a quasi-2D regime using RF photoemission spectroscopy has provided evidence for the attractive and repulsive polaron and found evidence in favor of a polaron-molecule transition[46].

While all these experiments involving an impurity interacting with a Fermi sea have been performed in the many-body limit accessing spectral functions, microscopic studies in regimes with only few particles accessing correlation functions have only been performed in lattice systems[52], [140], [141]. In this Chapter, the simplest instance of a single impurity attractively interacting with a few-body Fermi sea in the ground state is studied. We perform microscopy on this system with single particle and spin resolution enabling us to access correlation functions beyond second-order which we use to interpret a transition into a molecular state. Since the preparation of such a few-body 1+N system is non-trivial, the preparation is presented first and then results of microscopic observables are presented concluding with how this relates to the many-body limit. In addition we also present a study of a single repulsive impurity interacting with the Fermi sea which is related to the repulsive polaron in the many-body limit. A system with finite impurity concentration should be smoothly related to a system with mismatched Fermi surfaces[134], [142] and we try to explore this connection by presenting momentum correlations of the COM motion of pairs to conclude this chapter.

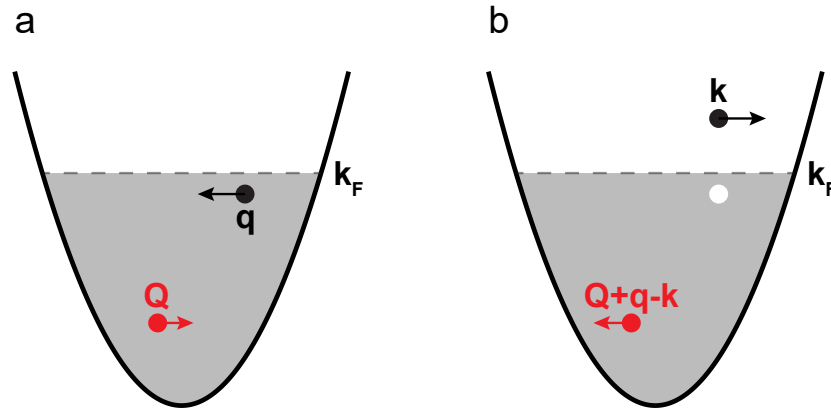


Figure 5.1: **An illustration of particle-hole excitations of the Fermi sea due to interaction with an impurity.** The impurity can be a particle or a molecule (composed of a fermion and an impurity). (a) Before the interaction between a fermion (black) and an impurity (red) they have momenta  $q < k_F$  and  $Q$  respectively. The total momentum of this impurity and fermion before the collision is  $Q + q$ . (b) After the collision, the fermion is excited out of the Fermi sea and has a momentum  $k > k_F$  leaving behind a hole (white). The impurity gets a recoil and now has a momentum  $Q + q - k$  so that the total momentum is conserved. This particle-hole excitation of the Fermi sea is a striking feature of a dressed impurity interacting with the bath. The net effect of such an interaction is broadening of the momentum distribution of the fermions compared to the non-interacting case. If the impurity interacts attractively (repulsively) with the fermions, the position distribution of the fermions becomes narrower (broader) due to the attraction (repulsion) provided by the impurity.

## 5.2 Variational wavefunctions

As was pointed out in Section 5.1, a variational wavefunction can capture the essential features of a single impurity immersed in a Fermi sea. Here we consider the case where the impurity and fermion are different internal states of the same particle. The impurity and fermion are denoted respectively by labels  $\downarrow$  and  $\uparrow$ . The Hamiltonian for such a system with no confinement in second quantization can be written as[39],

$$\hat{\mathbf{H}} = \underbrace{\sum_{k,\sigma} \epsilon_{k,\sigma} c_{k,\sigma}^\dagger c_{k,\sigma}}_{\text{Kinetic term}} + \underbrace{\frac{g}{V} \sum_{k,k',q} c_{k,\uparrow}^\dagger c_{k',\downarrow}^\dagger c_{k'+q,\downarrow} c_{k-q,\uparrow}}_{\text{Interaction term}} \quad (5.1)$$

The kinetic term includes the single particle energy  $\epsilon_{k,\sigma} = \frac{\hbar^2 k^2}{2m}$  of spin state  $\sigma$  and creation (annihilation)  $c_{k,\sigma}^\dagger$  ( $c_{k,\sigma}$ ) operator which creates (annihilates) a particle with momentum  $p = \hbar k$ . The interaction term accounts for the scattering of a spin- $\uparrow$  and  $\downarrow$  particle and conserves momentum before and after the interaction  $k + k'$ .  $g$  is the strength of interaction which is related to the scattering length and  $V$  the volume of the system. Chevy constructed a variational wavefunction to minimize the energy computed from this Hamiltonian as[143]

$$|P_3(Q)\rangle = \underbrace{\alpha^{(Q)} c_{Q,\downarrow}^\dagger |FS\rangle}_{\substack{\text{Free impurity} \\ + \text{Fermi sea}}} + \underbrace{\sum_q \beta_{k,q}^{(Q)} c_{Q+q-k,\downarrow}^\dagger c_{k,\uparrow}^\dagger c_{q,\uparrow} |FS\rangle}_q}_{\substack{\text{Impurity recoil} \\ + \text{Particle-hole excitations of Fermi sea}}} \quad (5.2)$$

The impurity is then considered as a free particle dressed with particle-hole excitations of the Fermi sea and is called a polaron.  $|P_3(Q)\rangle$  is the wavefunction of the polaron with momentum  $Q$  and the subscript 3 indicates that the particle-hole excitation term has 3 operators. The impurity with momentum  $Q$  scatters off a fermion in the Fermi sea with momentum  $q < k_F$  ( $c_{q,\uparrow}$ ) and changes its momentum to  $k > k_F$  ( $c_{k,\uparrow}^\dagger$ ). This leads to the impurity acquiring a momentum  $q - k$  in order to conserve momentum during the scattering event ( $c_{Q+q-k,\downarrow}^\dagger$ ). The terms  $\alpha^{(Q)}$  and  $\beta_{k,q}^{(Q)}$  are variational parameters which are obtained by minimizing the energy.  $|FS\rangle$  represents the state of the Fermi sea at  $T = 0$ . The situation is illustrated schematically in Figure 5.1.

As interactions in the system are increased a competing molecular phase emerges[43] where the impurity binds to a single fermion forming a molecule. The molecule then can also scatter off the Fermi sea and form a dressed particle, the molaron. In most cold atom experiments, the Feshbach dimer has a finite scattering length which is a constant times the atom-atom scattering length  $a_{ad} = 1.2a$ [144]. Hence is it not realistic[48] to consider molecules which do not interact with the Fermi sea and such models[47] do not realistically reproduce experimental observations in the many-body limit[43], [46]. A similar

wavefunction for the molaron can be written

$$|M_4(Q)\rangle = \underbrace{\sum_k \gamma_k^{(Q)} c_{Q-k,\downarrow}^\dagger c_{k,\uparrow}^\dagger |FS\rangle}_{\text{Molecule} \\ + \text{Fermi Sea}} + \underbrace{\sum_{k,k',q} \delta_{k,k',q}^{(Q)} c_{Q-k+q-k',\downarrow}^\dagger c_{k,\uparrow}^\dagger c_{k',\uparrow}^\dagger c_{q,\uparrow} |FS\rangle}_{\text{Molecule recoil} \\ + \text{Particle-hole excitation of Fermi sea}} \quad (5.3)$$

$|M_4(Q)\rangle$  is the molaron wavefunction with the dressed molecule having a momentum  $Q$  and the subscript 4 indicates the number of creation/annihilation operators in the particle hole excitation term. In this case a molecule with momentum  $Q$  scatters off a fermion in the Fermi sea with momentum  $q < k_F$  ( $c_{q,\uparrow}$ ) and excites the fermion beyond the Fermi sea with momentum  $k' > k_F$  ( $c_{k',\uparrow}^\dagger$ ). Conservation of momentum requires that the molecule then acquires an additional momentum  $q - k'$  ( $c_{Q-k+q-k',\downarrow}^\dagger c_{k,\uparrow}^\dagger$ ). The terms  $\gamma_k^{(Q)}$  and  $\delta_{k,k',q}^{(Q)}$  are variational parameters which are obtained by minimizing the energy.

Having introduced the different variational wavefunctions that could describe the system in different interaction regimes, qualitative features of these regimes can be summarized. The net effect of particle-hole excitations whether in the polaron or molaron phase is to promote fermions within the Fermi sea to a momentum larger than  $k_F$ . This results in a broadening of the momentum distribution of the fermions. Due to momentum conservation it has a similar effect on the impurity as well. In the attractive ground state branch of interest, where this polaron-molaron transition is expected, the net effect of the attraction is to cause the position distribution of the fermions to shrink. The impurity acts as a glue and brings the fermions closer which reflects on the position distributions. On the contrary repulsive interactions lead to broadening of the position distribution of the fermions.

The distribution of position or momenta are densities and in our experiments we have access to correlation functions of second order and beyond. In terms of these observables, the net effect on the second-order density-density correlator  $C^{(2)}$  would be to cause an accumulation of fermions around the impurity in position space. However, such an enhancement is not indicative if this is a result of all fermions moving closer to the impurity or if one of them binds to the impurity forming a molecule like object. A third-order correlator  $C^{(3)}$  would be a sensitive observable to detect this qualitative change[145] since a situation with two fermions being equally close to an impurity would be distinguishable from a situation with one fermion being closer and the other being farther away. The former has all the qualitative features of a polaronic state where the impurity is dressed by the fermions and the latter is the molaron state where the impurity forms a dimer with a fermion and is dressed by the surrounding Fermi sea. As was seen in Chapter 3, interacting few-fermion systems with just a few filled shells possess many of the qualitative features of a many-body system. An example of a precursor of such a phase transition was presented both with spectroscopic as well as microscopic measurements. In this chapter, we explore if this can also be extended to a situation with unequal number of spin states and if microscopic measurements could indicate a precursor of a polaron-molaron transition in a few-body system.

## 5.3 Preparing a spin-imbalanced few-fermion system in the ground state

Deterministic preparation of balanced few-fermion systems has been performed in quasi-1D[19] and quasi-2D trapped systems[80]. Spin-imbalanced few-body systems on the repulsive branch(excited state) have been prepared in quasi-1D and RF spectroscopy has been performed on them[20]. However, there have been no experiments so far where a few-body system with spin-imbalance has been prepared in the ground state on the attractive branch where a polaron-molaron transition is expected.

### 5.3.1 Preparing a spin-imbalanced system using differential magnetic moments

Deterministic preparation of imbalanced few-body systems is similar to balanced systems. Bound states with a higher energy are made to tunnel out of the potential by applying a magnetic field gradient while at the same time lowering the optical tweezer depth. If the states involved in preparation have the same magnetic moment and the same optical polarizability, they are subject to the same potential and equal number of atoms in the two spin states are prepared. Thus to prepare spin-imbalanced systems states possessing either a differential magnetic moment or optical polarizability are needed. Using far detuned optical dipole traps, it is not possible to obtain a differential polarizability. A differential polarizability can be obtained by using blue-detuned near-resonant beam for one spin state and red-detuned for the other. However using near-resonant beams leads to unwanted photon scattering and heating. Thus we use states which have a differential magnetic moment to perform spilling of the atoms. We prepare such states in a Fermi gas consisting of  ${}^6\text{Li}$  atoms in the ground electronic state  $2S_{1/2}$  which has six hyperfine states labelled  $|1\rangle - |6\rangle$  in the increasing order of energy. The energies of these states and their representation in terms of uncoupled basis states was summarized in Section 2.2. The energy of each of these states varies as a function of the magnetic field as shown in Fig 5.2(a). The resulting variation of the magnetic moment as a function of magnetic field is shown in Fig 5.2(b). At large magnetic fields where there exists a Feshbach resonance between the spin states  $|1\rangle \dots |3\rangle$  the differential magnetic moment vanishes. However by performing the spilling at low magnetic fields (28-50G) different combinations of the two spin states can be obtained as shown in Fig 5.2(c).

### 5.3.2 RF transitions

Radio frequency magnetic dipole transitions between states  $|1\rangle \dots |6\rangle$  were introduced in Section 2.3. The coupling between two spin states including their motional wavefunction can be written as,

$$\hbar\Omega = -\langle i | \vec{\mu} \cdot \vec{\mathbf{B}} | f \rangle \langle \phi_i | \phi_j \rangle \quad (5.4)$$

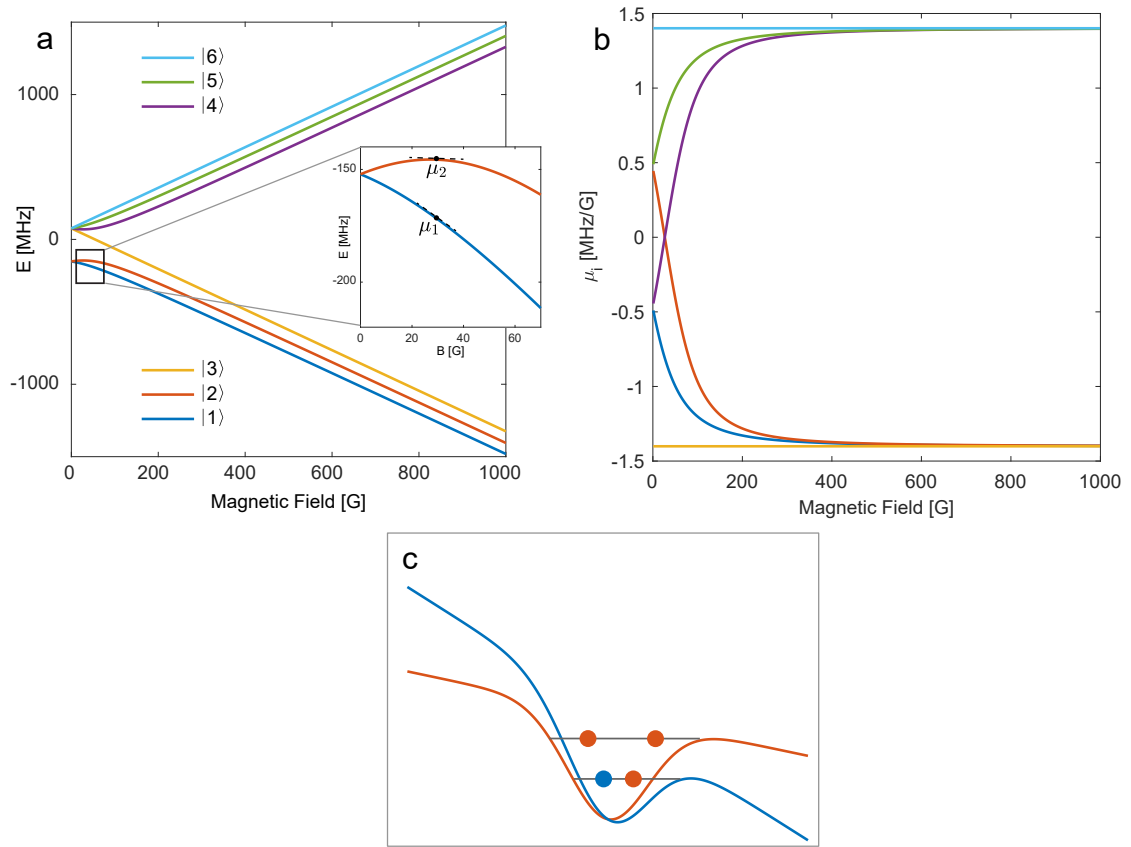


Figure 5.2: **Preparation of a spin-imbalanced system.** (a) The energy ( $E$  in MHz) of hyperfine states  $|1\rangle$ - $|6\rangle$  of the ground electronic state  $2S_{1/2}$  of  ${}^6\text{Li}$  as a function of the magnetic field  $B$  (in Gauss). When working with states  $|1\rangle$  -  $|3\rangle$ , at low fields there is a differential magnetic moment between states  $|1\rangle$ ,  $|2\rangle$  (shown in inset) and states  $|2\rangle$ ,  $|3\rangle$ . (b) The magnetic moment of hyperfine states  $|1\rangle \dots |6\rangle$  as a function of magnetic field. At large magnetic fields a differential magnetic moment between states  $|1\rangle \dots |3\rangle$  ( $|4\rangle \dots |6\rangle$ ) cannot be obtained. However, at low magnetic fields for moderate gradients (along radial directions) of 1.4 G/cm a differential shift of approximately 140 Hz over the extent of the wavefunction, which is comparable to the motional energy scales during spilling, can be obtained. (c) For a few-particle system at low entropy in a tweezer trap, an applied magnetic field gradient would result in different energy shifts ( $-\mu \cdot B$ ) and hence different potentials for states  $|1\rangle$ ,  $|2\rangle$ . This can be used to prepare an unequal number of pseudo spin  $\uparrow$  and  $\downarrow$  particles in the ground state.

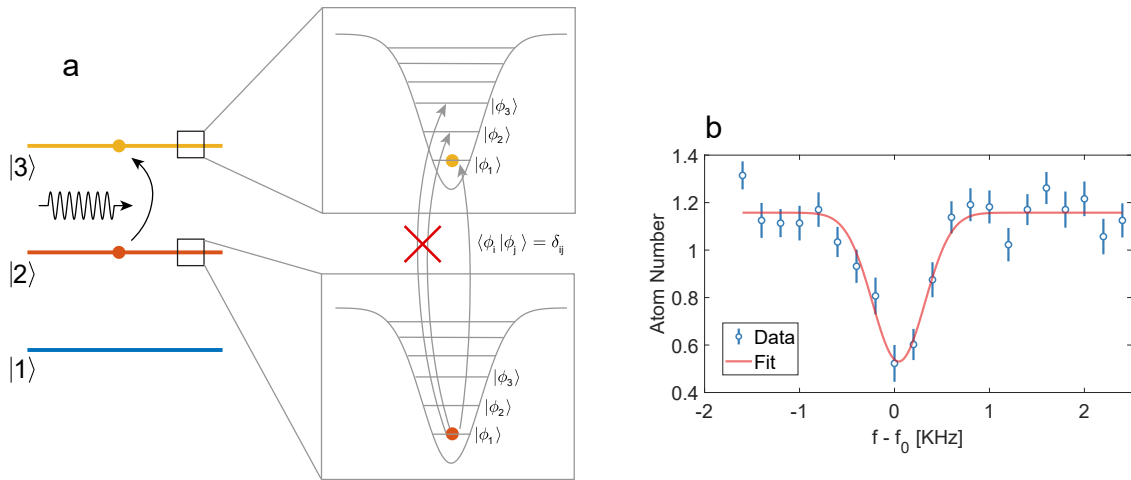


Figure 5.3: **Motional sidebands in a spin-polarized system.** (a) For a single particle in state  $|2\rangle$ , a radio frequency (RF) field can drive transitions from state  $|2\rangle$  to  $|3\rangle$ . Even with sufficient RF resolution, the final motional state is the same as the initial state and cannot be changed since  $\langle \phi_i | \phi_j \rangle = \delta_{ij}$ . (b) This is also confirmed by the RF spectrum which shows a single frequency at which the transition can be driven.  $f - f_0$  is the RF drive frequency with respect to the bare transition frequency  $f_0$ . The error bars in (b) depict standard error of the mean.

where  $\Omega$  is the Rabi rate and  $|i\rangle(|j\rangle)$  is the initial(final) electronic state,  $|\phi_i\rangle(|\phi_j\rangle)$  is the initial(final) motional state,  $\vec{\mu}$  is the magnetic moment of the electron and  $B$  is the amplitude of magnetic field due to RF radiation at the position of the atoms. The inner product of the initial and final states is like a Franck-Condon factor for these motional states. A situation where the magnetic field amplitude does not vary over the extent of the motional wavepacket is considered here. The RF photon frequency is approximately 80 MHz while motional energy scales  $\omega_r/(2\pi)$  are 3 orders of magnitude lower,  $\sim$  KHz. Driving the transition at a Rabi rate  $\Omega \ll \omega_r$  and with sufficient RF resolution can in principle result in transitions between (discrete) motional states. However for a single atom in a trap this is not possible since the motional overlap between the initial and final states is zero unless the initial and final motional states are the same as shown in Fig. 5.3(a). This is also reflected in the RF spectrum shown in Fig. 5.3(b) which shows a dip at the bare transition frequency. Transitions between these motional states can be engineered if a finite motional overlap can be introduced between the initial and final states. For a single particle in a trap this has been performed using large magnetic field gradients which cause spin-motion coupling in ion-traps[146], [147]. On the contrary, in the following subsection a scheme to perform motional sideband transfers in an interaction system is presented.

### 5.3.3 RF motional sideband transfer

Having prepared a spin-imbalanced system, the magnetic field needs to be adiabatically tuned to reach the required interaction strength. Doing so would prepare the system in an excited state known as the repulsive branch. This can be understood by looking at the Energies of two particles interacting with contact interactions in a quasi-2D Harmonic trap in their ground COM motional state[84](See Fig. 5.4a above for two atoms in states  $|1\rangle, |3\rangle$  and below in states  $|1\rangle, |2\rangle$ ). This system was also introduced in Section 3.2. The two particle energies are now modified due to interactions and feature an attractive ground state and multiple excited repulsive branches. After having performed spilling at low fields, adiabatically changing the magnetic field moves the system on this upper energy state initializing the system in the excited state.

As was seen in the previous subsection, an RF transition can change the motional state provided sufficient motional overlap exists between the initial and final states. Here we describe how this spin-motion coupling resulting in finite overlap between the initial and final motional states can be achieved using interactions in the system. To illustrate this we consider two-particles resonantly interacting in a harmonic trap where one spin state is subjected to an RF transition as shown in Figure 5.4. The location of the Feshbach resonance for states  $|1\rangle, |2\rangle$  and states  $|1\rangle, |3\rangle$  are separated by  $\sim 143G$  [74] and this results in different motional states at the same magnetic field depending on the mixture as shown in Fig. 5.4(a). In such a situation two atoms in states  $|1\rangle, |2\rangle$  on the repulsive branch have a finite motional overlap with the repulsive and ground-attractive branches of the  $|1\rangle, |3\rangle$  mixture. Evidence of this overlap can be found by performing RF spectroscopy under similar

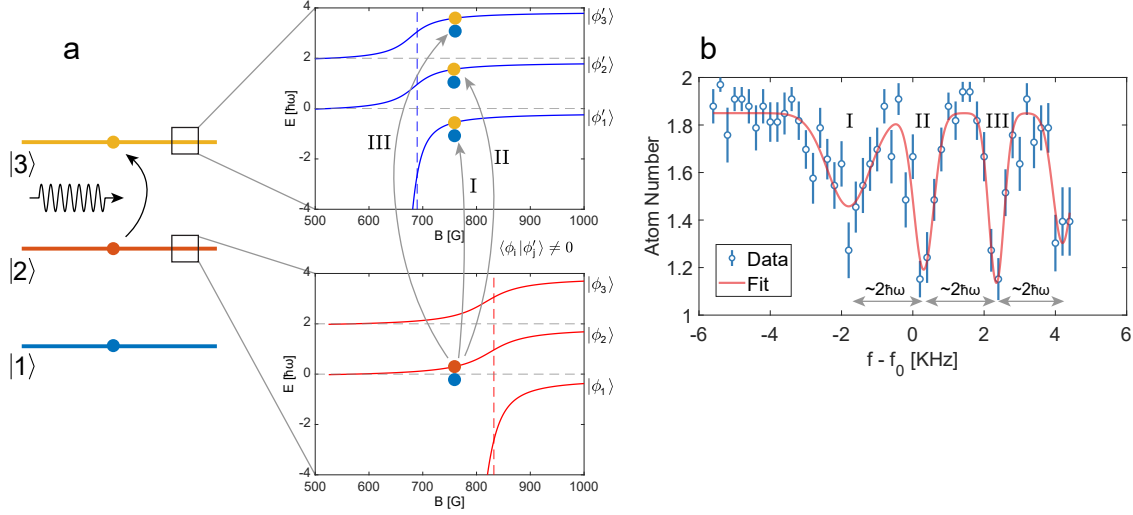


Figure 5.4: **Motional sideband transfer in an interacting system.** (a) For a two-particle system ( $|1\rangle - |2\rangle$ ) interacting through contact interactions, the energy spectrum (pictured for the 2D case, for  $|1\rangle - |2\rangle$  below and  $|1\rangle - |3\rangle$  above) depends on the magnetic field which determines the strength of the interactions through a Feshbach resonance. The spectrum features an attractive branch (lowest one with a bound state), a repulsive branch (the next one) and other excited states. In this scenario driving an RF transition from  $|2\rangle$  to  $|3\rangle$  results in final state interactions which are different from the initial state. With sufficient resolution of the RF drive and with a Rabi rate which is slow compared to motional time scales, it is possible to drive transitions between motional states since  $\langle \phi_i | \phi'_j \rangle \neq 0$ . (b) A scan of the RF drive frequency shows peaks corresponding to the transitions marked I, II, III. The spacing between the peaks is approximately  $2\hbar\omega$  since the initial and final motional states should have the same parity. Error bars indicate standard error of the mean

conditions as above namely  $\Omega \ll \omega_r$  and is shown in Fig. 5.4(b). Multiple RF transitions labelled I, II and III appear which are separated by  $\sim 2\hbar\omega$  as expected[84]. The transition labelled I occurs at a lower frequency compared to the bare transition frequency  $f_0$  and corresponds to a transition to the attractive ground state while the other transitions II and III correspond to transitions to the repulsive manifold. Similar shifts in RF frequencies have been explored in the many-body limit not only for balanced[14], [148] but also imbalanced systems to identify the polaron[43], [69], [149].

### 5.3.4 Landau-Zener transfer to dark motional ground state

Once the motional sidebands are resolvable with RF transitions, a spin-imbalanced system prepared in the repulsive manifold can be deterministically transferred to the attractive ground state as follows (See Figure 5.5). We start with a mixture of atoms in states  $|1\rangle, |2\rangle$  and with the RF power set such that  $\Omega \ll \omega_r$  we sweep the drive frequency from  $f_0 - \Delta$  to  $f_0 + \Delta$  at a rate  $\dot{\Delta}$  slow compared to  $\Omega$ . This results in a Landau-Zener adiabatic passage to a  $|1\rangle, |3\rangle$  mixture. Here  $f_0$  is the bare RF transition frequency for the  $|2\rangle - |3\rangle$  transition. It is of paramount importance to start from low frequencies and drive towards high frequencies ( $\Delta > 0$ ) in order to transfer the system to the ground state with this Landau-Zener passage. Starting with low frequencies ensures that the system first encounters the attractive ground state of the  $|1\rangle, |3\rangle$  mixture and is transferred there. Continued RF frequency sweeps don't affect this state as all transitions back to the repulsive manifolds of  $|1\rangle, |2\rangle$  mixture happen at lower frequencies. Transitions back to the attractive manifold of the  $|1\rangle, |2\rangle$  mixture are also avoided, even though they happen at higher frequencies, by a judicious choice of the magnetic field at which we drive the transition and the Landau-Zener detuning  $\Delta$ . Hence, atoms once transferred to the attractive ground state of  $|1\rangle, |3\rangle$  mixture are dark to subsequent RF photons and an attractively interacting spin-imbalanced few-fermion system in the ground state is prepared. With this scheme we can prepare different configurations of 1+3, 1+6 and 3+6 atoms. These correspond to closed shell configurations in 2D for each of the spin states. We ensure that the system thus prepared is indeed in the ground state by spilling once more and obtain fidelities of  $\sim 86\%$  for a 1+3 system. We also verify that frequency sweeps in the opposite direction (high to low) do not result in deterministic preparation of the system in the ground state.

## 5.4 Experimental measurements

Using this ability to prepare spin-imbalanced systems in the motional ground state, we explore the problem of a single impurity immersed in a minimal Fermi sea. We prepare a system consisting of 1+N particles with N up to 7 and thereby also explore closed shell configurations of 1+3 and 1+6 atoms. A similar system in the few-body limit consisting of 1+2 particles has been explored numerically at various mass ratios and interaction strengths demonstrating a trimer-dimer transition in a regime far away from the polaron-molaron

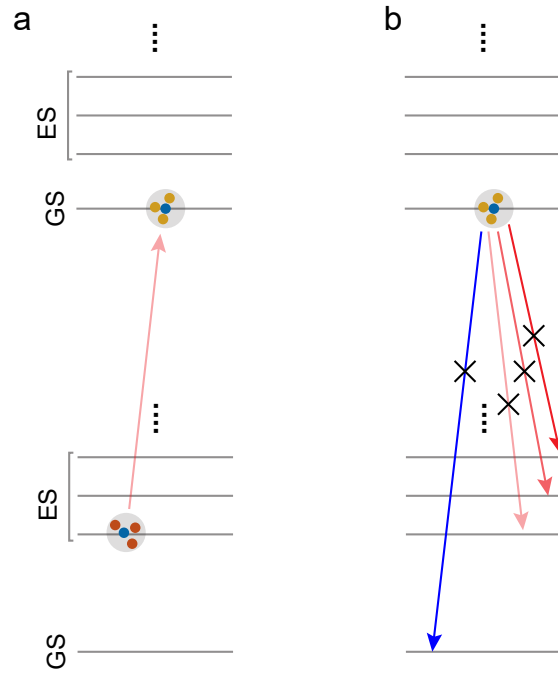


Figure 5.5: **Preparation of a ground state system by a Landau-Zener sweep of RF frequency.** The frequency is swept from  $f_0 - \Delta$  to  $f_0 + \Delta$ . (a) The system is initially prepared in the repulsive excited state (ES) and the Landau-Zener sweep transfers atoms in a  $|1\rangle - |2\rangle$  mixture to a  $|1\rangle - |3\rangle$  mixture in the motional ground state (GS). (b) Once the system finds itself in the GS of the  $|1\rangle - |3\rangle$  mixture it is dark to subsequent RF radiation from the frequency sweep since transitions to ES of the  $|1\rangle - |2\rangle$  mixture happen at lower frequencies while transfer to GS happens at much larger frequency compared to  $f_0 + \Delta$ . Thus a spin-imbalanced system can be deterministically prepared in the motional ground state

transition[145]. Here we perform microscopy of such a system in real and momentum space and demonstrate how a combination of density measurements and higher-order correlations can be used to infer a transition from a state where the impurity mainly scatters off the majority atoms to a state where it seems to form a molaron-like state. The interaction strength between the impurity and bath particles is quantified in terms of the two-body binding energy ( $E_B$ ) as was also done in Chapter 3.

### 5.4.1 Particle-hole excitations

The effect of an impurity on the Fermi sea has been described by variational wavefunctions both in the cases when the impurity is not bound to a fermion and when it is bound as a molecule[48], [49] and was summarized in Section 5.2. In either case the impurity and molecule scatter off the Fermi sea and can cause particle-hole excitations of the fermions. This leads to a broadening of momenta of the bath particles while at the same time making the cloud of fermions smaller in position space due to the attractive binding mediated by the impurity. These fermion density measurements in momentum and position space are shown in Fig 5.6 for a 1+3 system. The momenta of individual fermions are obtained using a time-of-flight measurement technique[75]. Many repetitions of the experiment are performed to construct the momentum densities and these are shown in Fig 5.6a. In momentum space with increasing interactions, the effect of the impurity is to cause more fermions to appear at larger momentum compared to the non-interacting state. This could be attributed to scattering between the free particle or molecule with the fermions which causes excitations of fermions beyond the Fermi surface in the many-body limit as was illustrated in Figure 5.1. Using techniques from matterwave optics[23] we image the system in position space and more details were presented in Chapter 4. Contrary to momentum space, in real space the size of the fermion bath shrinks with increasing interaction signalling binding of the bath to the impurity due to attractive interactions. However these complementary measurements in real and momentum space are densities and do not give access to correlations in the system which is necessary to infer the nature of the state as interactions are increased.

### 5.4.2 Second-order correlator

A second order correlation function was introduced in Section 3.6 to demonstrate the formation of Cooper pairs in momentum space. A similar second order correlation function was also defined in position space in Chapter 4. Here we use such a correlation function to demonstrate correlations around an impurity in position space. The connected part of the correlation function  $C_c^{(2)}$  can be defined as,

$$C_c^{(2)}(\vec{\mathbf{r}}_i, \vec{\mathbf{r}}_i + \vec{\mathbf{r}}) = \langle \mathbf{n}_i(\vec{\mathbf{r}}_i) \mathbf{n}_1(\vec{\mathbf{r}}_i + \vec{\mathbf{r}}) \rangle - \langle \mathbf{n}_i(\vec{\mathbf{r}}_i) \rangle \langle \mathbf{n}_1(\vec{\mathbf{r}}_i + \vec{\mathbf{r}}) \rangle \quad (5.5)$$

where  $\vec{\mathbf{r}}_i$  ( $\vec{\mathbf{r}}_i + \vec{\mathbf{r}}$ ) is the location of the impurity(fermion) and  $\mathbf{n}_i(\vec{\mathbf{r}}_i)$  ( $\mathbf{n}_1(\vec{\mathbf{r}}_i + \vec{\mathbf{r}})$ ) is the density of the impurity(fermion) at  $\vec{\mathbf{r}}_i$  ( $\vec{\mathbf{r}}_i + \vec{\mathbf{r}}$ ).  $C_c^{(2)}(\vec{\mathbf{r}}_i, \vec{\mathbf{r}}_i + \vec{\mathbf{r}})$  thus represents the connected

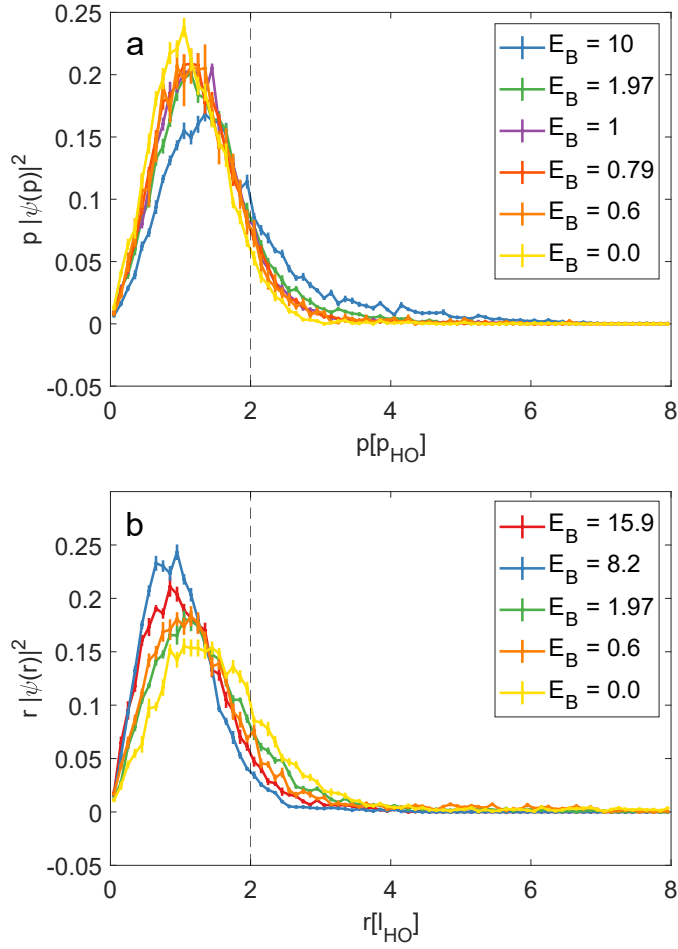


Figure 5.6: **Effect of an impurity on majority atoms in momentum and real space for a system consisting of 1+3 atoms.**(a) Density in momentum space for different interaction strengths. The density of majority atoms at different momenta are obtained by reconstructing densities from many realizations of an experimental run for 1+3 atoms. The error bars indicate standard error of the mean. In momentum space as interactions are increased more atoms can be found at higher momentum reminiscent of particle-hole excitations of the Fermi sea in a variational wavefunction. (b) Density in real space is obtained in a similar way and indicates that with increasing interactions, the majority cloud becomes smaller. This indicates some form of binding which is mediated by the single impurity. The vertical dotted line in both cases denotes  $\sqrt{2}E_F$ .

part of the second order correlation function where the disconnected part of the correlation function  $\langle n_i \rangle \langle n_1 \rangle$  has been subtracted from the total correlator  $\langle n_i n_1 \rangle$ .  $C_c^{(2)}(\vec{\mathbf{r}}_i, \vec{\mathbf{r}}_i + \vec{\mathbf{r}})$  is four dimensional and hard to visualize. Integrating out the location of the impurity gives access to a distribution of fermion positions relative to the impurity while at the same time reducing its dimension to 2.

$$C_c^{(2)}(\vec{\mathbf{r}}) = C_c^{(2)}(x, y) = \int d^2 \vec{\mathbf{r}}_i C_c^{(2)}(\vec{\mathbf{r}}_i, \vec{\mathbf{r}}_i + \vec{\mathbf{r}}) \quad (5.6)$$

The interaction strength quantified by  $E_B$  is tuned from  $E_B = 0$  to  $15.9\hbar\omega_r$  and the result is plotted in Figure 5.7(a-f) for 1+6 particles and Figure 5.8(a-e) for 1+3 particles. Further integrating out the relative angle  $\phi$  gives access to a 1D correlation function of distribution of relative positions of the fermions with respect to the impurity.

$$C_c^{(2)}(r) = \frac{1}{2\pi} \int d\phi C_c^{(2)}(\vec{\mathbf{r}})$$

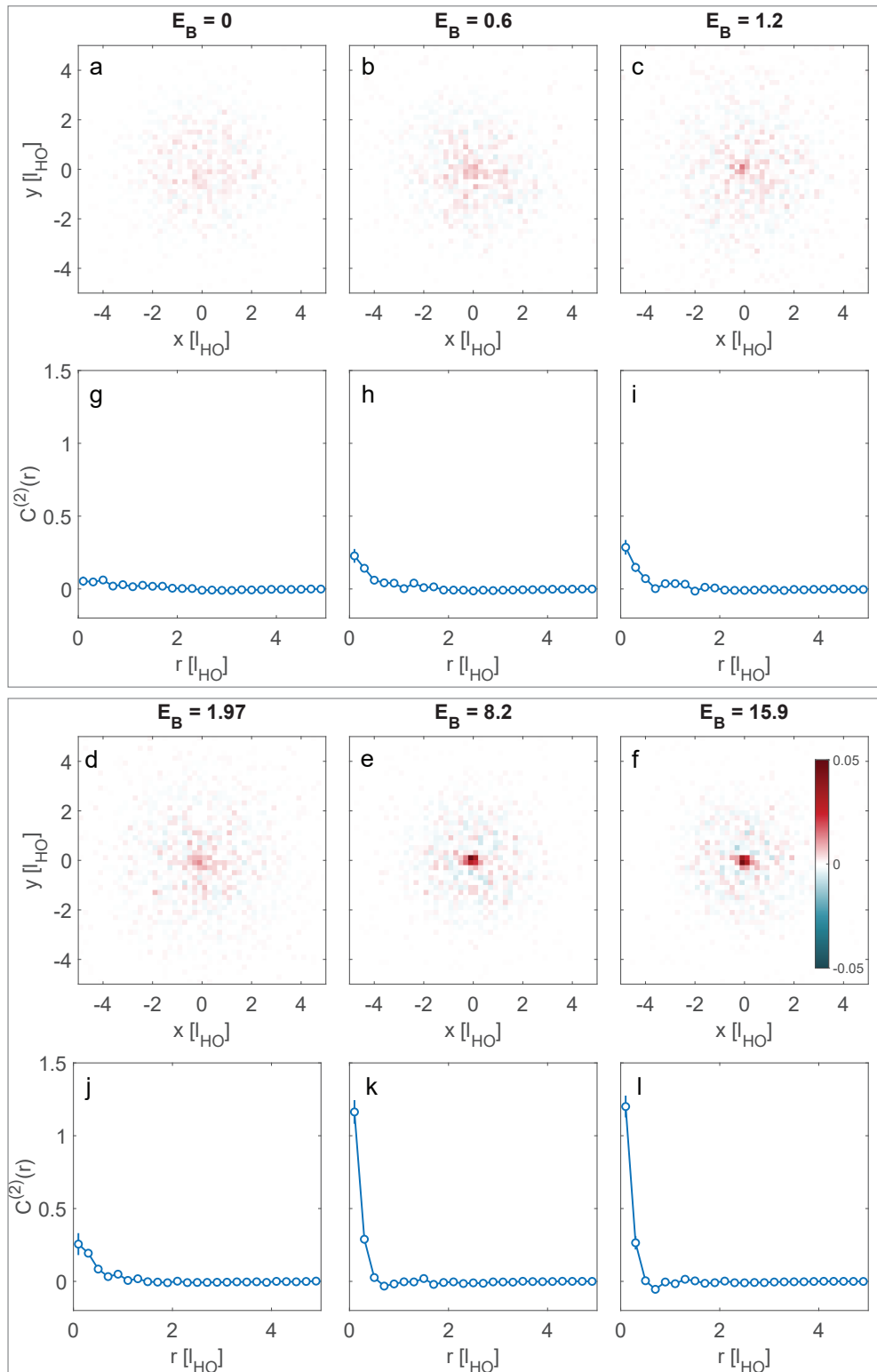
These are plotted in Figure 5.7(g-l) for a 1+6 system and in Figure 5.8(f-j) for a 1+3 system. Increasing the interaction strength results in a larger probability to find fermions around the impurity and molecule like correlations appear at large binding energies where  $E_B \gg E_F$ . Such a scenario could be because all the fermions are brought closer to the impurity or form a molecular like state where an impurity preferentially binds to a fermion. Hence, a higher order correlator  $C^{(3)}(r_1, r_2)$  involving 3 particles(impurity + 2 fermions) is necessary to highlight the asymmetry in how the impurity binds to one of these 2 fermions.

### 5.4.3 Third-order correlator

While a second-order correlator was useful to infer how the positions of two particles (impurity + fermion) were related to each other, a third-order correlator is necessary to explore

---

Figure 5.7 (following page): **Second-order correlator of an impurity and a fermion for a 1+6 system.** The interaction energy  $E_B$  is tuned from 0 to 15.9 in (a-f) and (g-l). (a-f) Two dimensional correlator  $C_c^{(2)}(\vec{\mathbf{r}})$  where  $\vec{\mathbf{r}} = (x, y)$  is the relative location of the fermion with respect to the impurity.  $(x, y)$  are in units of harmonic oscillator length  $l_{\text{HO}}$  and the interaction energy is in units of the harmonic oscillator energy scale  $\hbar\omega_r$ . (g-l) correlator  $C_c^{(2)}(r)$  obtained by integrating the relative angle  $d\phi$  of  $C_c^{(2)}(\vec{\mathbf{r}})$ . The vertical error bars indicate standard error of the mean. The second order correlator indicates that the fermions tend to cluster around the impurity with increasing  $E_B$



correlations among three particles (impurity + 2 fermions). With this we would obtain access to how the location of an impurity relates to the location of two other fermions and such higher order correlations have been used to demonstrate a transition from a trimer to a dimer state in a few-body system[145] and to detect magnetic polarons in lattice systems[52]. Such a metric would be sensitive to a situation where the impurity binds to one of the fermions indicative of a molecular state. A third order correlation function can be defined as

$$C^{(3)}(\vec{\mathbf{r}}_i; \vec{\mathbf{r}}_i + \vec{\mathbf{r}}_1, \vec{\mathbf{r}}_i + \vec{\mathbf{r}}_2) = \langle \mathbf{n}_i(\vec{\mathbf{r}}_i) \mathbf{n}_1(\vec{\mathbf{r}}_i + \vec{\mathbf{r}}_1) \mathbf{n}_2(\vec{\mathbf{r}}_i + \vec{\mathbf{r}}_2) \rangle \quad (5.7)$$

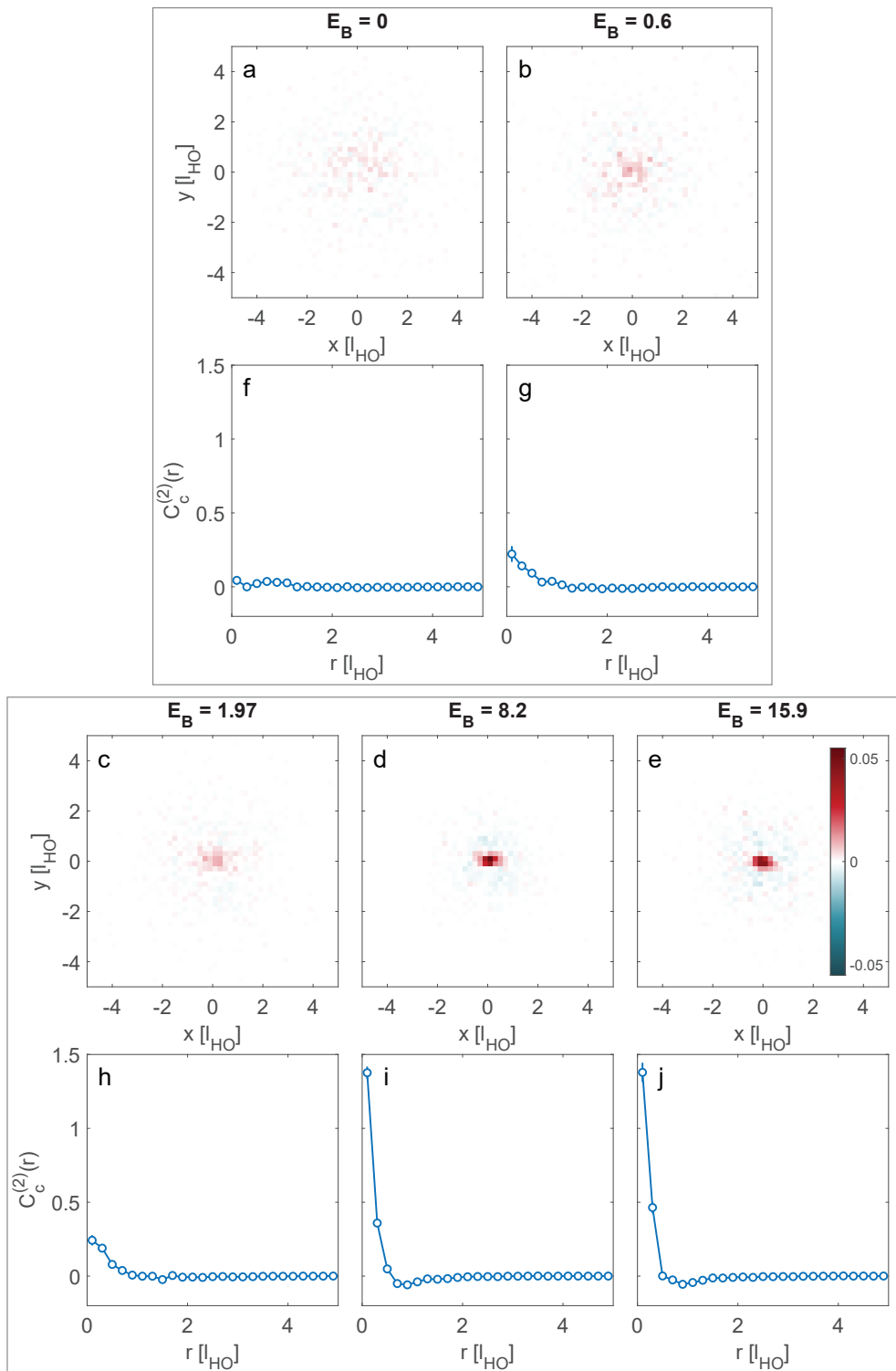
Here  $\vec{\mathbf{r}}_i$  ( $\vec{\mathbf{r}}_i + \vec{\mathbf{r}}_1, \vec{\mathbf{r}}_i + \vec{\mathbf{r}}_2$ ) are the co-ordinates of the impurity (fermions) and  $\mathbf{n}_i(\vec{\mathbf{r}}_i)$  ( $\mathbf{n}_1(\vec{\mathbf{r}}_i + \vec{\mathbf{r}}_1), \mathbf{n}_2(\vec{\mathbf{r}}_i + \vec{\mathbf{r}}_2)$ ) is the impurity (fermion) density at  $\vec{\mathbf{r}}_i$  ( $\vec{\mathbf{r}}_i + \vec{\mathbf{r}}_1, \vec{\mathbf{r}}_i + \vec{\mathbf{r}}_2$ ). The  $C^{(3)}$  correlator thus gives us the density of finding the impurity at  $\vec{\mathbf{r}}_i$  and the fermions at a relative distance of  $\vec{\mathbf{r}}_1$  and  $\vec{\mathbf{r}}_2$  with respect to the impurity. Integrating out the position of the impurity and the relative angles  $\phi_1, \phi_2$  gives us a correlator  $C^{(3)}(r_1, r_2)$  that indicates the probability to find two fermions at relative distances  $r_1$  and  $r_2$  from the impurity.

$$C^{(3)}(r_1, r_2) = \frac{1}{(2\pi)^2} \int d^2\vec{\mathbf{r}}_i d\phi_1 d\phi_2 C^{(3)}(\vec{\mathbf{r}}_i, \vec{\mathbf{r}}_i + \vec{\mathbf{r}}_1, \vec{\mathbf{r}}_i + \vec{\mathbf{r}}_2) \quad (5.8)$$

These probabilities  $C^{(3)}(r_1, r_2)$  as a function of interaction strength are shown in Fig 5.9(a-f) for 1+6 and in Figure 5.10(a-e) for 1+3 particles. The interaction energy is tuned from  $E_B = 0$  to  $15.9\hbar\omega_r$  reaching a regime where  $E_B \gg E_F$  is the largest energy scale in the system. At low binding energies, there is no tendency for one of the distances to be smaller compared to the other while at larger  $E_B$  the system tends to favor a configuration where the distance of the impurity to one of the fermions is smaller than the other. This kind of

---

Figure 5.8 (following page): **Second order correlation of an impurity and a fermion for a 1+3 system.** The interaction energy  $E_B$  is tuned from 0 to 15.9 in (a-e) and (f-j). (a-e) 2D correlator  $C_c^{(2)}(\vec{\mathbf{r}})$  where  $\vec{\mathbf{r}} = (x, y)$  is the relative location of the fermion with respect to the impurity.  $(x, y)$  are in units of harmonic oscillator length  $l_{\text{HO}}$  and the interaction energy is in units of the harmonic oscillator energy scale  $\hbar\omega_r$ . (f-j) correlator  $C_c^{(2)}(r)$  obtained by integrating the relative angle  $d\phi$  of  $C_c^{(2)}(\vec{\mathbf{r}})$ . The vertical error bars indicate the standard error of the mean. The second order correlator indicates that the fermions tend to cluster around the impurity with increasing  $E_B$ . This however does not distinguish if one or more of the fermions are close to the impurity and hence a higher-order correlator is needed to resolve this question.



asymmetry was previously also used to demonstrate the spatial characteristics of a dimer state in a few-body system[145].

To further demonstrate the qualitative features of this probability distribution we define an asymmetry parameter  $\chi(r_1, r_2)$  and plot its occurrence for different interaction strengths.

$$\chi(r_1, r_2) = 1 - \frac{\text{atan}(r_1/r_2)}{\pi/4} \quad (5.9)$$

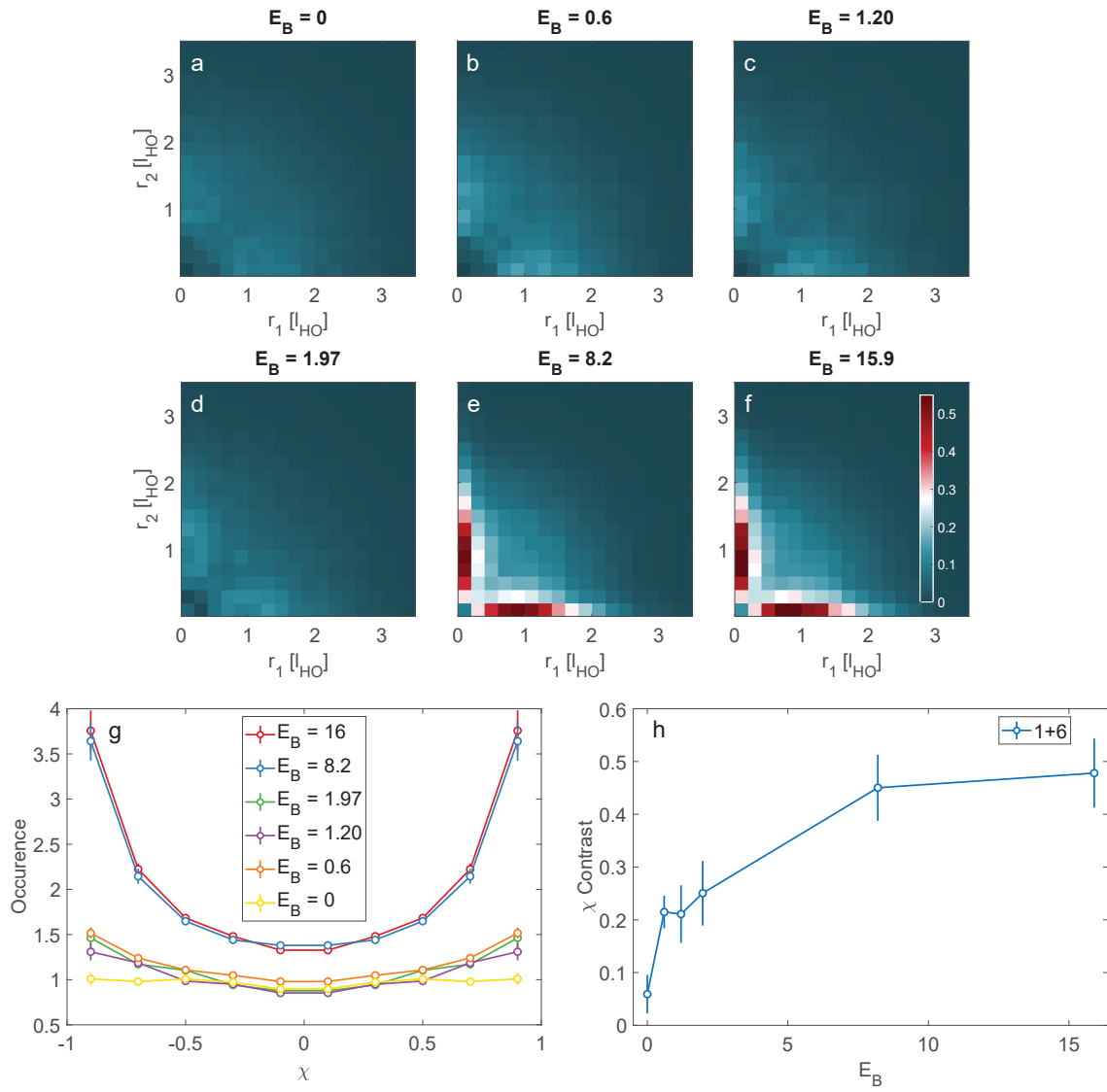
$\chi(r_1, r_2)$  quantifies the asymmetry involved when comparing the distances of two fermions to the impurity. A value of  $\pm 1$  indicates that the impurity is closer to one of the fermions than the other while a value of 0 indicates nearly equal distances to the impurity. A histogram of the occurrence of various values  $\chi$  can be obtained by taking into account the probability distribution for each combination of  $(r_1, r_2)$  given by  $C^{(3)}(r_1, r_2)$  as follows

$$n(\chi_0) = \int dr_1 dr_2 C^{(3)}(r_1, r_2) \delta(\chi_0 - \chi(r_1, r_2)). \quad (5.10)$$

The histogram  $n(\chi_0)$  for different interactions strengths is shown in Fig 5.9(g) for 1+6 particles and in Figure 5.10(f) for 1+3 particles. A histogram of values of  $\chi$  shows an enhanced occurrence at higher asymmetry values for systems in which  $E_B$  is the dominant energy scale compared to the Fermi Energy  $E_F$ . The contrast in the histogram distribution  $n(\chi_0)$  then gives a qualitative insight into how flat or skewed the distribution of asymmetry parameters are. These are shown in Figure 5.9(h) for a 1+6 system and Figure 5.10(g)

---

Figure 5.9 (following page): **Third-order correlator  $C^{(3)}(r_1, r_2)$  for 1+6 particles.** (a-f) Plots of correlation function  $C^{(3)}(r_1, r_2)$  for different interaction strengths from  $E_B = 0$  to 15.9 in units of  $\hbar\omega_r$ .  $r_1$  and  $r_2$  are the distances of the fermions to the impurity atom in units of harmonic oscillator length  $l_{\text{HO}}$ . The distance labels  $r_1$  and  $r_2$  are just to distinguish the two distances and the plot is completely symmetrical along the diagonal since the fermions are indistinguishable. (g) Histogram of asymmetry parameter  $\chi = 1 - \frac{\text{atan}(r_1/r_2)}{\pi/4}$  for different interaction strengths  $E_B$ . An asymmetry of  $\pm 1$  indicates a state consisting of an impurity and two fermions where the impurity is closer to one of the fermions. (h) Contrast in histogram of  $\chi$  as a function of  $E_B$ . An increasing contrast with  $E_B$  is indicative of formation of a state where the binding of the impurity is asymmetrical with respect to the fermions. The error bars in (g,h) indicate standard error of the mean.



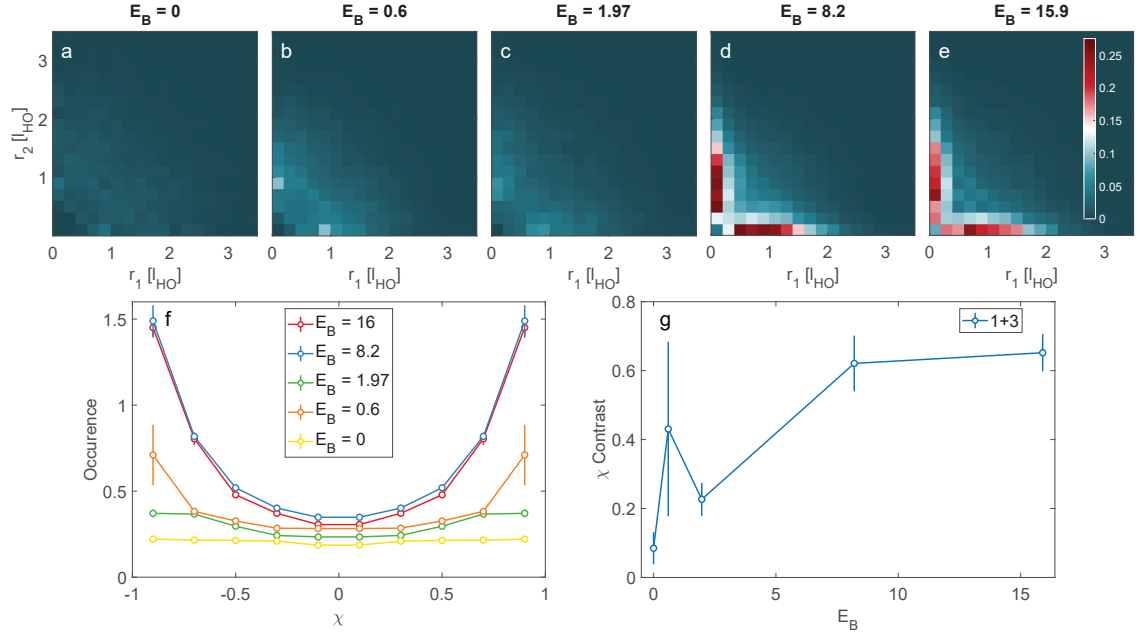


Figure 5.10: **Third-order correlator  $C^{(3)}(r_1, r_2)$  for  $1+3$  particles.** (a-e) Plots of correlation function  $C^{(3)}(r_1, r_2)$  for different interaction strengths from  $E_B = 0$  to 15.9 in units of  $\hbar\omega_r$ .  $r_1$  and  $r_2$  are the distances of the fermions to the impurity atom in units of harmonic oscillator length  $l_{\text{HO}}$ . The distance labels  $r_1$  and  $r_2$  are just to distinguish the two distances and the plot is completely symmetrical along the diagonal since the fermions are indistinguishable. (f) Histogram of asymmetry parameter  $\chi = 1 - \frac{\text{atan}(r_1/r_2)}{\pi/4}$  for different interaction strengths  $E_B$ . (g) Contrast in histogram of  $\chi$  as a function of  $E_B$ . The error bars in (f,g) indicate standard error of the mean.

for a 1+3 system as a function of interaction strength. At weak binding energies where particle-hole excitations are still visible, the contrast is smaller since nearly all asymmetry parameters are equally probable. There are as many situations where the impurity finds itself closer to one of the fermions as it finds itself equally close to both fermions. However for  $E_B \gg E_F$ , it is much more probable to find a situation where the impurity is closer to one of the fermions than it is to find the impurity equally close to both.

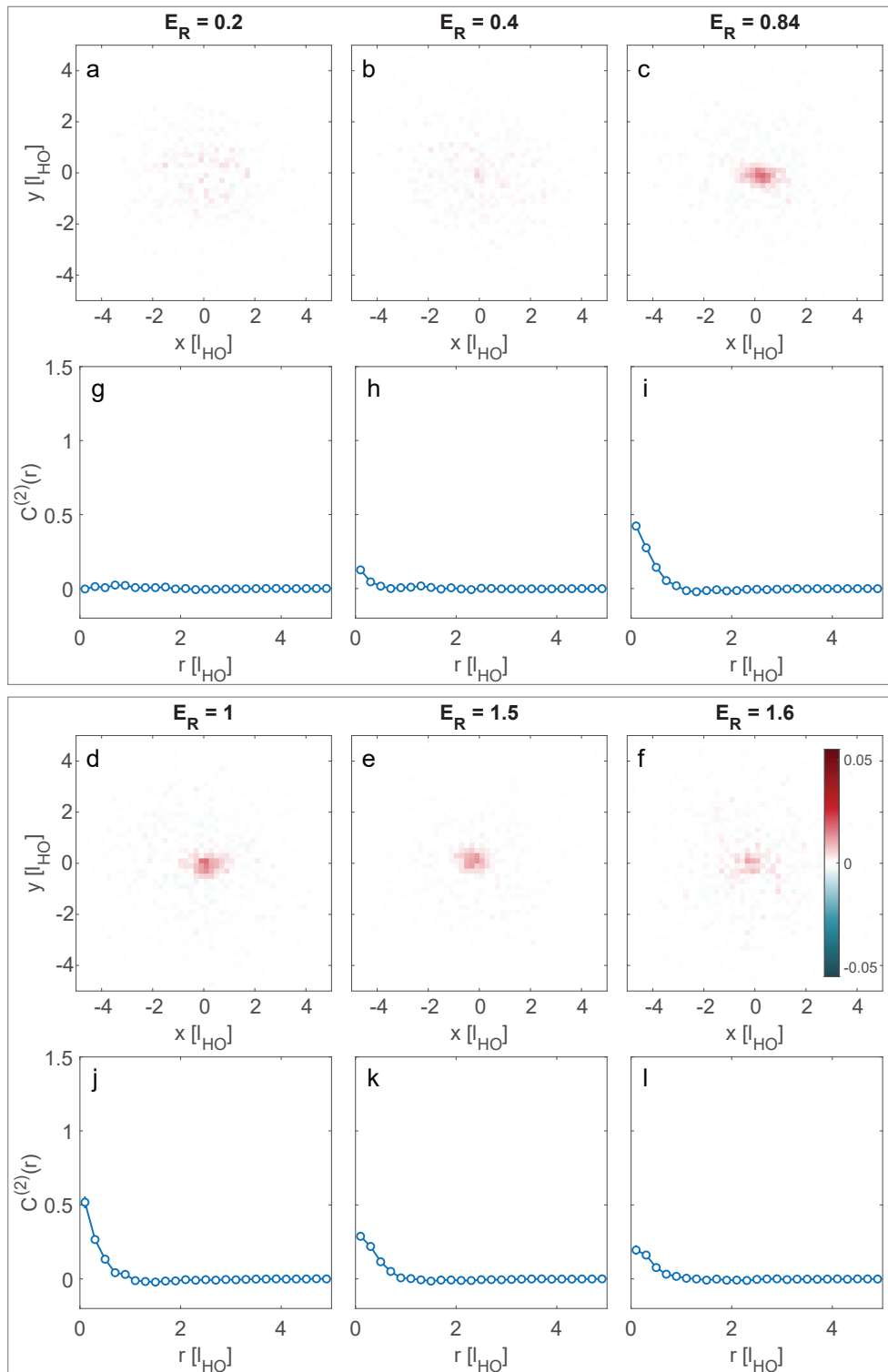
## 5.5 Repulsive interactions

So far only the ground state of an impurity immersed in a Fermi sea was considered. This state is characterized by attractive interactions and features an attractive quasi-particle called the attractive polaron at weak coupling in the many-body limit. However, there also exists a metastable excited state with repulsive interactions. This repulsive state has attracted a lot of interest due to its relevance to itinerant Ferromagnetism[150]. This state features a quasi-particle, the repulsive polaron, at weak coupling in the many-body limit. The stability of this state has been found to vary depending on the regime of scattering interactions. The dependence of the scattering phase shift on the scattering length and scattering energy was presented in Section 2.6. In the non-universal regime, the range of interaction is comparable to the inter-particle spacing  $r_0 \sim 1/k$ . The effective range  $r_{\text{eff}}$  which is proportional to  $r_0$  is then also comparable  $1/k$  and the second term in the effective range expansion Equation 2.35 has to be considered. In contrast, the universal regime is characterized by  $r_0 \ll 1/k$  due to which the scattering phase shift depends only on the scattering length. In the non-universal regime, this repulsive polaron state is found to be metastable and has been measured by RF injection spectroscopy[69]. In the universal regime, which is the case for  ${}^6\text{Li}$ , the repulsive polaron state has been found to be unstable and decays into the molecule-hole continuum[138].

To explore this repulsive excited state, we prepare such a system of 1+3 atoms at low field and then adiabatically tune the magnetic field to obtain the required interaction strength

---

Figure 5.11 (*following page*): **Second-order correlator in a 1+3 mixture with repulsive interactions.** (a-f) Two dimensional  $C_c^{(2)}(\vec{r})$  with  $\vec{r} = (x, y)$  in units of harmonic oscillator length  $l_{\text{HO}}$ . (g-l) One dimensional correlator  $C_c^{(2)}(r)$ . The interaction energy quantified by the two-body repulsive energy  $E_R$  is tuned from 0.2 to 1.6 in units of  $\hbar\omega_r$  in (a-f) and (g-l). Despite increasing repulsive interactions fermion(s) appear closer to the impurity reflecting decay into a molecular state. The decay reduces beyond the resonance even with increasing repulsive interactions as the overlap with the molecular state decreases.



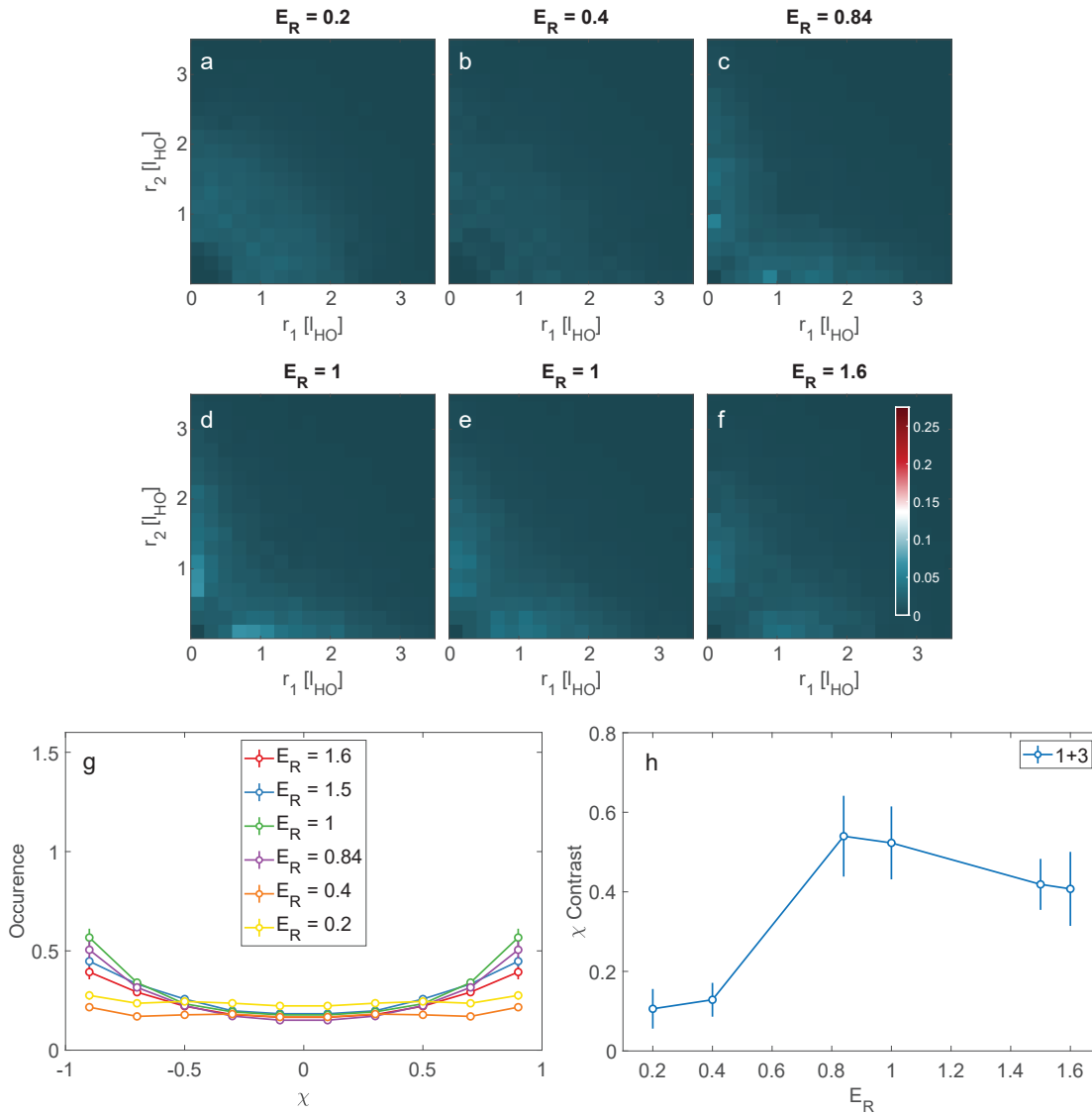


Figure 5.12: **Third-order correlator for a 1+3 system with repulsive interactions.**

(a-f) correlator  $C^{(3)}(r_1, r_2)$  as the repulsive energy  $E_R$  is increased from 0.2 to 1.6 in units of  $\hbar\omega_\tau$ . The colormap is same as plots for the 1+3 attractive case to enable comparison. (g) Distribution of the asymmetry parameter  $\chi$  shows some indication of increasing molecular correlations close to  $E_R \approx 1$ . (h) This molecular correlation is characterized by the contrast in distribution of  $\chi$ . While the contrast is smaller initially for small repulsive interactions, as the repulsive interactions are increased, the molecular correlations peak around  $E_R \approx 1$  before reducing with further increase in repulsive interactions. The error bars in (g,h) indicate standard error of the mean.

without performing additional motional ground state transfers. This moves the system adiabatically on the excited branch before it becomes unstable towards decay into the molecule-hole continuum. We find that the decay into lower molecule like state is enhanced close to the Feshbach resonance position where the two-body repulsive energy  $E_R \approx 1\hbar\omega_r$ . This can be seen in the increase in second order correlations signalling more fermion(s) around the impurity as shown in Figure 5.11 where both  $C_c^{(2)}(\vec{\mathbf{r}})$  and  $C_c^{(2)}(r)$  reflect this. The third-order correlator  $C^{(3)}(r_1, r_2)$  shown in Figure 5.12 also confirms this since the asymmetry increases closer to  $E_R \approx 1$ . With these microscopic measurements of repulsive few-body mixtures we recover observations in the many-body limit that the excited state is metastable and decays to the molecule-hole continuum. This decay is found to be larger close to the 3D resonance position due to the larger coupling of the repulsive excited state with the molecule-hole continuum.

## 5.6 Tuning fermion number

So far only closed shell configurations of the Fermi sea were considered resulting in system sizes consisting of either 1+3 or 1+6 atoms. To study the effect of fermion number, we first prepare open shells with varying fermion number as illustrated in Figure 5.13. Starting with an 2D isotropic harmonic trap at very low entropies, the trap is adiabatically deformed into an anisotropic trap. The adiabatic transformation smoothly connects the two motional states and does not create excitations. The degeneracies of the anisotropic trap are different from the isotropic trap. Spilling is done in this anisotropic trap at a magnetic field where a differential magnetic moment is present between the spin states as before. Spilling is done to closed shell configurations in this anisotropic potential and then the trap is adiabatically transformed back into an isotropic trap. This transformation does not create holes in the system but connects to a state which is open shell in the isotropic trap. Thus, effectively open shell configurations in the isotropic trap are created. By varying the aspect ratio of the anisotropic trap, different numbers of fermions  $N$  can be created. After preparing the 1+N system, RF frequency sweeps are used to transfer the system to the motional ground state as before.

To study the effect of fermion number on the correlations, we extract correlations in a 1+N system in a regime where  $E_B = 8.2\hbar\omega_r$  is the dominant energy scale compared to the Fermi energy. Here the correlator  $C^{(3)}(r_1, r_2)$  and distribution of asymmetry  $n(\chi)$  shows correlations consistent with appearance of a molecule like state where the impurity tends to preferentially bind to one fermion and is shown in Figure 5.14(a-f) and (g) respectively. The contrast in this asymmetry distribution is shown in Figure 5.14(h) and indicates a drop in molecular pairing asymmetry with increasing fermion number. Increasing the particle number increases the density and hence the local Fermi energy. The formation of the molecular state is influenced by competition of the interaction energy  $E_B$  with the Fermi energy  $E_F$ . Since  $E_B$  is kept constant while  $E_F$  increases with fermion number,  $E_B/E_F$

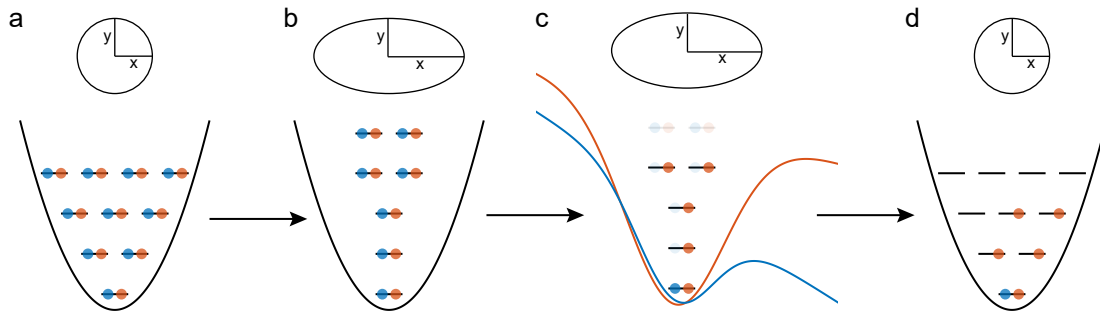


Figure 5.13: **Preparation of a single impurity with varying number of fermions in open shell configurations.** (a) We start with a few-fermion system in a 2D isotropic harmonic trap. (b) The trap is adiabatically deformed to create an anisotropic trap with aspect ratio  $\omega_x : \omega_y$ . The motional states in the isotropic and anisotropic trap are adiabatically connected and hence no holes are created in the process. (c) Spilling is performed at a magnetic field where a differential magnetic moment exists between the spin states. This creates a  $1+N$  system. (d) The anisotropic trap is adiabatically transformed back into an isotropic trap. An RF motional ground state transfer as explained earlier is performed to create a  $1+N$  system in the motional ground state. By changing the aspect ratio of the anisotropic trap, different number of fermions can be obtained.

decreases marginally which is reflected in the asymmetry and its contrast. Hence at the same  $E_B$  increasing the particle number makes it harder to form such a molecular state.

## 5.7 Finite impurity concentrations - Mismatched Fermi surfaces

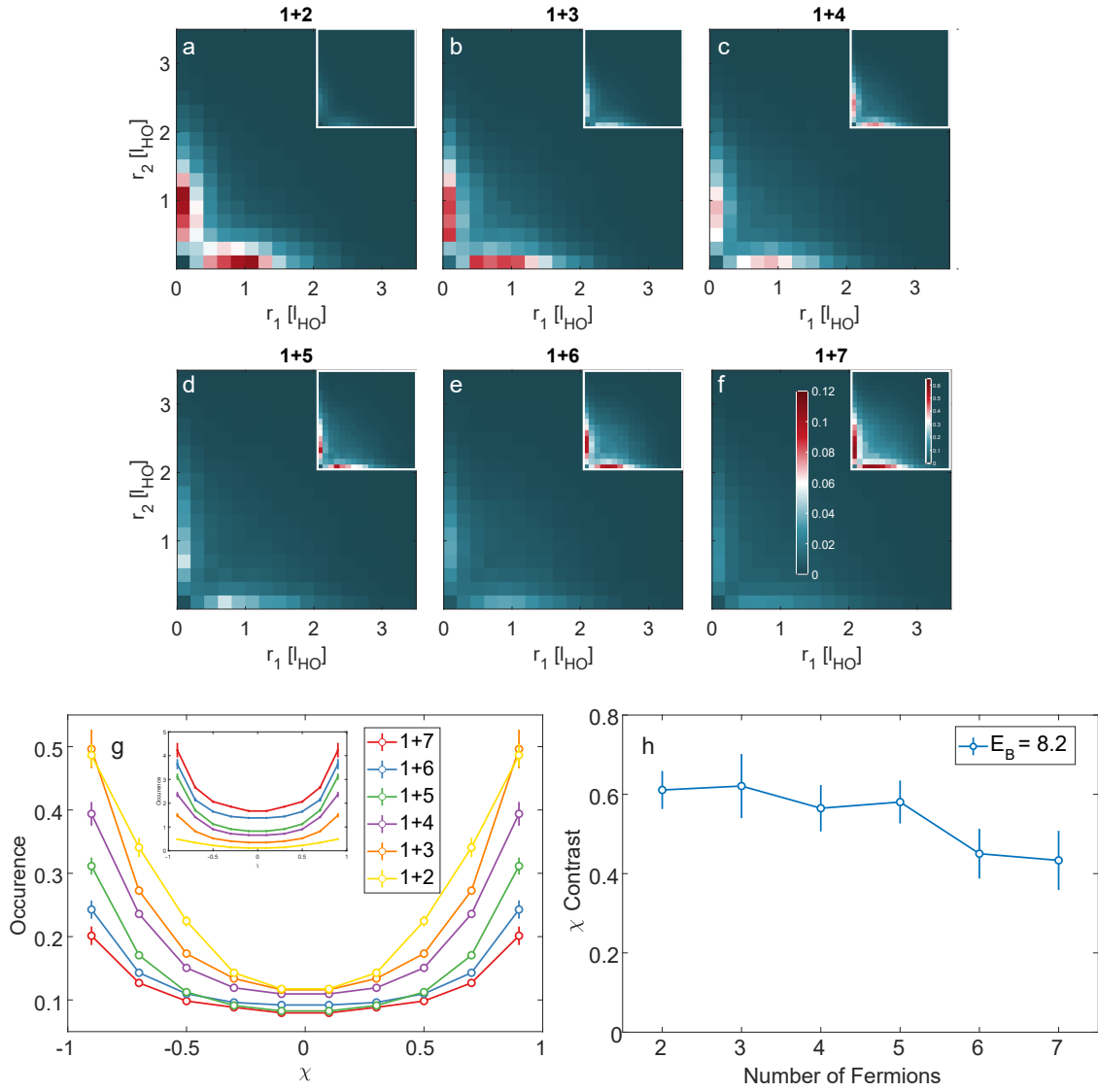
So far only the case of a single impurity with varying number of fermions was considered. At finite impurity concentrations, the Fermi surfaces of the impurity and the majority atoms are mismatched. The case when the Fermi surfaces are completely matched results in the formation of Cooper pairs with zero COM momentum and was summarized in Chapter 3. As was mentioned in Section 5.1, the fate of Cooper pairs in the case of mismatched Fermi surfaces has been a subject of ongoing debate with various phases predicted [54].

We utilize the possibility to prepare closed shells of 3+6 atoms in the ground state to study momentum space correlations. In a balanced system at weak coupling Cooper pairs with zero COM momentum are observed [75]. The effect of mismatched Fermi surfaces leads to a competition between the Fermi energy mismatch and the interaction energy. The Fermi energy mismatch has a pair breaking effect on the zero COM pairs while the interaction energy counteracts this tendency. Fulde-Ferrell and Larkin-Ovchinnikov (FFLO) proposed a phase where a state with Cooper pairs at finite COM momentum is the ground state in the many-body limit [34], [35]. This phase in the many-body limit is associated with a spatially modulated order parameter and has only recently been observed in a condensed matter system [151].

Exploring the possibility to measure COM momentum distribution of pairs, we perform

---

Figure 5.14 (*following page*): **Third-order correlator  $C^{(3)}(r_1, r_2)$  for a single impurity and variable number of fermions** (a-f) at an interaction strength  $E_B = 8.2$  in units of  $\hbar\omega_r$  in a regime where  $E_B \gg E_F$  and the system has molecular characteristics. All the plots are normalized to the number of 3-particle combinations that one can obtain for evaluation of the  $C^{(3)}$  for a 1+N system. The insets are without this normalization and indicate that a molecular state appears more asymmetrical just because of larger number of 3-particle combinations with increasing N. (g) The asymmetry distribution  $\chi$  and (h) its contrast. The error bars indicate standard error of the mean. The drop in contrast with increasing fermion number is a reflection of the fact that increasing fermion number increases density and makes it harder to find a molecular state since the local Fermi Energy against which  $E_B$  competes increases.



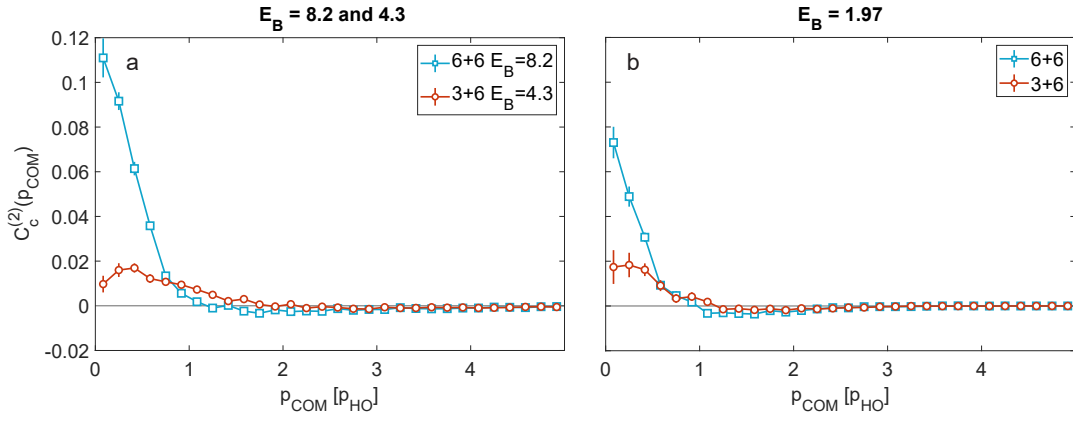


Figure 5.15: **Second-order correlator  $C_c^{(2)}(p_{\text{COM}})$  in a 3+6 system compared to a balanced 6+6 system in momentum space.**  $p_{\text{COM}}$  is the magnitude of COM momentum of a pair (a)  $C_c^{(2)}(p_{\text{COM}})$  in a regime where  $E_B > E_F$ . The square/blue(circle/red) data points correspond to 6+6(3+6) system and the error bars represent standard error of the mean. The solid lines are guides to the eye. Compared to a balanced system, the 3+6 system shows appearance of peak at finite COM momentum. (b)  $C_c^{(2)}(p_{\text{COM}})$  for  $E_B < E_F$ . Energies  $E_B$  are in units of  $\hbar\omega_r$  and  $p_{\text{COM}}$  is in units of harmonic oscillator momentum  $p_{\text{HO}}$ .

microscopy of a system with 3+6 atoms and extract a noise correlation function involving all possible pairs and defined as follows.

$$C_c^{(2)}(\vec{\mathbf{p}}_1, \vec{\mathbf{p}}_{\text{COM}} - \vec{\mathbf{p}}_1) = \langle \mathbf{n}_1(\vec{\mathbf{p}}_1) \mathbf{n}_2(\vec{\mathbf{p}}_{\text{COM}} - \vec{\mathbf{p}}_1) \rangle - \langle \mathbf{n}_1(\vec{\mathbf{p}}_1) \rangle \langle \mathbf{n}_2(\vec{\mathbf{p}}_{\text{COM}} - \vec{\mathbf{p}}_1) \rangle \quad (5.11)$$

This is a reformulation of the correlation function used in Equation 3.18 where the momentum of spin- $\downarrow$  is expressed in terms of momentum of the spin- $\uparrow$  particle and the COM momentum of the pair. Here  $\mathbf{n}_1(\vec{\mathbf{p}}_1)$  ( $\mathbf{n}_2(\vec{\mathbf{p}}_{\text{COM}} - \vec{\mathbf{p}}_1)$ ) is the density of spin- $\uparrow$  ( $\downarrow$ ) at  $\vec{\mathbf{p}}_1$  ( $\vec{\mathbf{p}}_{\text{COM}} - \vec{\mathbf{p}}_1$ ),  $\vec{\mathbf{p}}_{\text{COM}}$  is the COM momentum of the spin- $\uparrow, \downarrow$  pair. This can be further simplified by integrating out the momentum of the spin- $\uparrow$  particle and the azimuthal angle of  $\vec{\mathbf{p}}_{\text{COM}}$  to obtain  $C_c^{(2)}(p_{\text{COM}})$  which depends only on the magnitude of the relative momentum  $p_{\text{COM}}$ .

$$C_c^{(2)}(p_{\text{COM}}) = \frac{1}{2\pi N_1 N_2} \times \int d^2 \vec{\mathbf{p}}_1 d\phi_{\text{COM}} [\langle \mathbf{n}_1(\vec{\mathbf{p}}_1) \mathbf{n}_2(\vec{\mathbf{p}}_{\text{COM}} - \vec{\mathbf{p}}_1) \rangle - \langle \mathbf{n}_1(\vec{\mathbf{p}}_1) \rangle \langle \mathbf{n}_2(\vec{\mathbf{p}}_{\text{COM}} - \vec{\mathbf{p}}_1) \rangle] \quad (5.12)$$

$N_1(N_2)$  is the total number of spin- $\uparrow(\downarrow)$  fermions and normalization with the number of possible pairs  $N_1 N_2$  enables comparison to a spin-balanced system. This correlator is plotted in Figure 5.15 for two regimes  $E_B < E_F$  and  $E_B > E_F$  for both the imbalanced 3+6 and balanced 6+6 case. In the balanced case, irrespective of  $E_B$  the distribution of  $p_{\text{COM}}$  is peaked around zero momentum. In the imbalanced case, the mismatch in Fermi surfaces makes pairing harder which reflects in the lower amplitude peak of the correlation function. In the regime where  $E_B < E_F$  there isn't a significant difference in the COM momentum at which the correlator peaks. However, when  $E_B > E_F$  the correlation function has a peak at a finite momentum. This observation is interesting in the light of proposals where the FFLO phase appears as molarons with finite COM momentum[142], [143].

## 5.8 Conclusions

Spin-imbalanced systems are host to an array of interesting phenomena and predictions. The case of mismatched Fermi surfaces is connected to two limits namely a spin-balanced system and the extreme case of imbalance featuring a single impurity immersed in a Fermi sea. The interesting regime in all of these systems concerns the ground state of an attractively interacting system. The case of a spin-balanced few-body system was explored in the previous chapters and in this chapter experiments in the single impurity limit were presented.

The preparation of few-fermion systems with spin-imbalance in the motional ground state presents challenges. RF transitions between hyperfine states with motional resolution were presented. While for spin-polarized samples coupling between motional sidebands is non-existent, interaction mediated coupling between them was used to prepare spin-imbalanced

systems in the motional ground state. Using adiabatic RF sweeps a spin-imbalanced system in the motional ground state was deterministically prepared.

The extreme case of spin-imbalance featuring a single impurity in a Fermi sea consisting of a few closed shells was first presented. Complementary microscopic measurements of in situ fermion bath densities in position and momentum space demonstrated the presence of particle-hole excitations across interaction strengths. Access to second-order correlations of in situ positions points to accumulation of bath fermions around the impurity. Third-order correlations between the impurity and two fermions points to the formation of a molaron state at large interaction strengths  $E_B > E_F$ . The asymmetric pairing associated with a molaron state qualitatively distinguishes it from the polaron state. The effect of fermion number on the molaron pairing asymmetry was then quantified. Excited repulsive states of a single impurity were then explored. Correlations in such an excited system point to a decay close to the Feshbach resonance position. Introducing finite impurity concentrations connects the single impurity limit to the case of mismatched Fermi surfaces. In this limit correlation functions in momentum space were accessed and compared to the case of a spin-balanced system. In contrast to the spin-balanced system where a peak appears at zero values of COM momentum, for  $E_B > E_F$  the spin-imbalanced system features a peak at finite momentum.

In conclusion, we have studied microscopic correlations in a minimal instance of a single impurity immersed in a few-body Fermi sea. Preparing the system in the ground state we demonstrated how the interaction mediated by the impurity causes shifts in momenta of the bath particles to higher values reminiscent of particle-hole excitations while at the same time reducing the size of the fermion cloud in position space indicative of binding. We further demonstrated how microscopic correlations involving the impurity and two fermions indicate the formation of an asymmetric state reminiscent of a molecule at higher interaction strengths. The transition to such a molaron state occurs at interaction strengths comparable to theoretical predictions[49].

The polaron is a quasi-particle and its presence in a few-body system at weak coupling would show up in the excitation spectrum of the system. In the foreseeable future this could be implemented by looking at the RF spectrum with the motional resolution achieved for preparing the system. Since this RF transfer also depends on motional overlap, it can be used to obtain the quasi-particle residue. However such an ejection spectroscopy scheme would only probe the ground state of the system. This could then be coupled with a molecular injection spectroscopy[142] scheme to demonstrate the presence of an excited molaron state in the system thereby providing more evidence for the polaron-molaron transition. Alternatively, the ground and excited many-body states of the few-body system can be coupled with interaction modulation spectroscopy[80] to indicate a gap closing around the polaron-molaron transition. The properties of the polaron quasi-particle could also be probed by measuring its effective mass. This would require exciting only the impurity selectively by making use of state dependent potentials in  ${}^6\text{Li}$ [152]. These experiments and the possibility to prepare few-body imbalanced systems in the motional ground state coupled

with microscopic observables could also be used to probe exotic forms of superfluidity[53].



## 6 Conclusions and Outlook

Even though few-body systems are far from the many-body limit, they already possess collective properties reminiscent of their many-body counterparts. Starting with spin-balanced few-body systems, preparation of low entropy samples of up to 6+6 fermions in a quasi-2D harmonic oscillator potential were presented. In 2D symmetries lead to degeneracies of motional orbitals leading to the formation of shell structure which was demonstrated(Figure 3.4). The effect of interactions on the shell structure was explored(Figure 3.5). As the interaction strength was increased, the shell structure vanishes leading to stable even fermion numbers since in that way the system can increase the binding energy per particle. Collective modes were excited in such a system by modulating interactions. Since interactions change the amount of pairing in the system, they were used to couple ground and excited motional states with different amount of pairing enabling the extraction of the excitation spectrum. The excitation spectrum showed a non-trivial asymptotic gap closing feature reminiscent of the normal-superfluid transition in the many-body limit(Figure 3.7). The dependence of this mode on particle number(Figure 3.8) and coherence properties were presented(Figure 3.9). Since these modes arise due to pair excitations, they occur only at the Fermi surface due to a frozen inner core. Subsequently microscopic observations demonstrating Pauli blocking through correlations called Pauli Crystals were summarized(Figure 3.11). The ability to access microscopic correlation functions were then used to demonstrate the formation of Cooper pairs at the Fermi surface as interactions were tuned in the system(Figure 3.13). These observations provided evidence in favor of emergent many-body properties already at these mesoscopic scales.

While previous microscopic measurements were performed to obtain in situ momenta of the particles, the size of the system being smaller than the effective imaging resolution prohibits a direct measurement of in situ positions. A technical scheme to magnify the many-body wavefunction of the system using matterwave techniques was presented(Figure 4.1). The scheme depended on evolving a non-interacting many-body state in two harmonic traps with different trap frequencies. An implementation of nearly harmonic Gaussian traps was presented to perform these matterwave transformations. The various parameters of these traps which affect the performance of the matterwave microscope were provided. Key performance attributes of this matterwave microscope - magnification, anharmonicity, anisotropy and resolution - were experimentally determined. With the range of accessible optical powers for the matterwave lenses, magnifications in the range 30 to 42 were achieved. The effect of trap parameters on anharmonicity was estimated and experimentally determined(Figure 4.6). The anisotropy of the matterwave microscope was experimentally

obtained by measuring in situ correlations of a single Feshbach molecule(Figure 4.7). The resolution was experimentally obtained by imaging systems of various sizes and the resolution was found to be sufficient to explore quasi-2D mesoscopic systems(Figure 4.8). A spin-balanced mesoscopic system consisting of 6+6 fermions was used to demonstrate the performance of the matterwave microscope(Figure 4.9). At moderate interaction strengths, Cooper pairs were found previously in momentum space. Increasing the interactions and measuring in situ positions provided evidence for the formation of a molecular state thus realizing the few-body analog of the BEC-BCS crossover. In situ position correlations were quantified as a function of interaction strength(Figure 4.10) and were used to demonstrate a monotonic increase in correlations at short distances(Figure 4.11).

Going beyond spin-balanced systems, we then explored few-body systems with spin-imbalance. Since interesting phases involving imbalance in the many-body limit occur in the motional ground state, the challenges involved in the preparation of such few-body systems were presented. Using interaction induced spin-motion coupling, the motional states were coupled using RF transitions(Figure 5.4). Adiabatic RF sweeps were used to deterministically prepare a spin-imbalanced system in the motional ground state(Figure 5.5). The extreme case of imbalance featuring a single impurity immersed in a Fermi sea was experimentally realized. Microscopic density measurements of in situ position and momenta revealed broadening of the fermion cloud in momentum space and narrowing in position space as attractive interactions were increased(Figure 5.6). This is reminiscent of particle-hole excitations of the Fermi sea caused by the immersed impurity in the many-body limit. The resulting dressing of the impurity results in the formation of a polaron or molaron quasi-particle in the many-body limit. While the polaron is a free impurity dressed by the Fermi sea, the molaron is a molecule (comprised of the impurity and a fermion) which is dressed by the surrounding Fermi sea. A polaron-molaron transition is expected to occur as the interaction strength is tuned in the many-body limit. Accessing correlation functions of second(Figures 5.7, 5.8) and third order(Figures 5.9, 5.10), evidence for the formation of a molecule like state at large interaction strengths was provided. The third-order correlation function between an impurity and two fermions indicates the formation of an asymmetric paired state where the impurity is closer to one of the fermions(Figures 5.9, 5.10). The effect of fermion density on this molecular state was studied by varying the number of fermions(Figure 5.14). The metastability of the repulsive excited state mixture was also explored with these microscopic correlations and it was found to have a larger decay closer to the scattering resonance position(Figures 5.11, 5.12). Since the finite impurity concentration scenario leads to a system with mismatched Fermi surfaces, this was then studied. The fate of pairing and the characteristics of the pairs were studied by comparing the distribution of COM momentum correlations with the spin-balanced case(Figure 5.15). In contrast to the spin-balanced case, in a regime where the two-body interactions are larger than the many-body energy scales given by the Fermi energy, the COM momentum correlation appears to have a peak at finite momentum.

In the following paragraphs, a few possible future directions are alluded to starting with

---

spin-balanced systems followed by their imbalanced counterparts. Symmetries play a very important role in physics as they are associated with conservation laws. Systems with scaling symmetry are ubiquitous near phase transitions and are responsible for universal behaviours. The unitary Fermi gas is a non-relativistic system which exhibits conformal symmetry. The symmetry is encapsulated by the Schrödinger group which consists of invariance under spatio-temporal translations, spatial rotations, Galilean boosts, scale and conformal transformations[153]. These symmetries have far reaching consequences and impose constraints on thermodynamic and transport properties[154]–[156]. A 2D-Fermi gas with contact interactions possess scale invariance similar to a unitary Fermi gas so long as interactions are not too strong[157], [158]. For such a harmonically trapped system, non-relativistic conformal invariance is satisfied and as a result the excitation spectrum is predicted to form a conformal tower of states[159]. The states are distinguished by the amount of angular momentum( $m$ ) and energy they possess leading to a classification into breathing and COM modes. The breathing modes( $\Delta m = 0$ ) can be excited by isotropic modulation of the trap while COM modes( $\Delta \neq 0$ ) can be excited by anisotropic trap modulation. The different angular momentum states  $\pm m$  can be further possibly distinguished by rotational modulation along clockwise or counter-clockwise directions. A few-fermion system subject to rotation is already being investigated in the other experiment. In addition to spectroscopic investigations of this system with a conformal tower of states, deterministic preparation into these excited states opens us avenues for direct observation of the effect of conformal symmetry. A remarkable prediction of conformal symmetry in such systems is the factorization of the total wavefunction into a product of the COM and hyperradial parts[159]. Using in situ position measurements developed in this thesis, the many-body wavefunction of the system can be sampled and this consequence of conformal symmetry can be directly tested.

Spin-imbalanced Fermi gases feature a rich phase diagram and only a small region was explored in the previous chapter. Complementary spectroscopic measurements would be invaluable in the single impurity limit to explore the emergence of quasi-particle properties in the few-body limit. Using interaction modulation or RF spectroscopy the energy gap between the few-body ground and excited state can be measured. The presence of an asymptotic gap closing would be further evidence for the polaron and molaron states with a transition between them. State dependent optical potentials can be further used to selectively modulate the impurity enabling access to quasi-particle properties like the effective mass. While only a single instance of mismatched Fermi surfaces was explored, the effect of mismatch on the qualitative and quantitative aspects of pairing would be an invaluable direction of enquiry. The FFLO phase is expected to occupy a larger region of the phase diagram in lower dimensions and is more pronounced in 1D[135]. In the few-body limit, there have been a couple of theoretical predictions in this direction[136], [137]. Using the ability to tailor optical potentials, 1D traps with the elongated axis perpendicular to the imaging direction can be created. This can then be used to measure correlations in momentum space where clear predictions as a function of Fermi surface mismatch exist.



# Acknowledgements

I would like to first thank Selim for giving me this opportunity to be part of the Ultracold group. It has indeed been an immense learning experience being part of the research group over the years. His support from even before I joined the group has always been extremely generous and I really don't know if I deserve it! Thanks also to Matthias for being very generous with this time and providing advice at tough times.

I'm very thankful to the examiners Prof. Markus Oberthaler, Prof. Tilman Enss and Prof. André Butz for agreeing to be part of the committee. Special thanks to Markus for agreeing to be the second reviewer at such short notice.

Over the years I have been fortunate to have worked with a number of exceptional people. Luca was probably the reason I decided to join the New experiment. He always had a knack for simplifying complicated things into their most essential parts and would strip away unnecessary details until the solution stared at one directly in the face. I could ask him anything and it was always a pleasure to discuss physics with him. Having been successful with spin-balanced systems and taking inspiration from Gerhard's work with sideband resolved RF transfers, it was Luca who realized that interaction induced spin-motion coupling could be used to prepare spin-imbalanced systems in the interesting ground state regime. He was also responsible for making us think systematically about the regime in which it would work. Marvin's command over Labview was stellar and I owe my knowledge of the Actor framework to him. Luca and Marvin brought together complementary skills from which I greatly benefited. During my later years Carl joined the efforts first as a Master student and then as a PhD. Sandra then joined us and I thank both of them for the work we did together in the lab and for scientific discussions. The experiment also benefited a lot from our then Postdoc Philipp Preiss before he moved to start his own research group. When we were scratching our heads on implementing the potential for the matterwave microscope using existing traps, his suggestion to use an additional larger trap was what made it possible. Thanks a lot to all of you!

A steady flux of people through the ultracold group during my stay have created a vibrant atmosphere here. Thanks to you all for your support over the years. It was great discussing entanglement between two interacting Fermions with Andrea. Vincent transferred all the knowledge he had about the design of Feshbach coils. Puneet's infectious enthusiasm for anything many-body was palpable. Antonia was welcoming, Lukas got me interested in laser galvos, additive and subtractive manufacturing. Jan-Hendrik was very friendly, got me started when I joined and along with Paul contributed a lot to make the Phase Lock loop a reality. Ralf's pedagogical skills were amazing. Based on Lukas's design Ram-Janik made

professional laser shutters and drivers inspired by the work from the Vuletić group. Philipp Lunt took over the PLL and made sure Toptica made it a workable product. Laurin's skills with Python inspired many in the group to switch. Johannes and Paul have been valuable additions to the Old experiment. Experiments Sebastian did with Jan-Hendrik helped us understand which Raman transitions wouldn't work. Tobi and Max have been driving forces behind HQA and I wish them success. Armin, Jonas, Malaika, Leo, Diana, Jonas, Hüseyin, Marlene, Vivienne, Jan, Juan, Johanna, Suraj and Martha have contributed to the group's research endeavors. Conversations with Leo have been fun but some offshoot projects might have burnt a hole in his pocket! I've looked forward to Malaika's concerts nearly every semester and they have been very nice! Conversations with Suraj have been wide-ranging and interesting. Maciej has been the latest addition to the group as a Postdoc and all the experiments are already benefiting from him. Gerhard has been a great person to discuss physics with and his e-Lego modules have made setting up a lot of electronics very easy. Though Thomas was long gone before I joined the group, it was always fun to discuss physics whenever our paths crossed and I learnt a lot from him, besides inheriting some stuff from his former apartment that I shouldn't really have!

It has also been a pleasure to interact with collaborators over the years. For the Higgs project, we were fortunate to work with the people who proposed the few-body precursor - Johannes, Steffi and Georg. We learnt a lot from you and you helped us realize that there's a lot of things which could be done.

The inspiration for the impurity project came from Richard and his group. It was Richard's interest in the few-body impurity problem that got us to figure out a way to prepare ground state systems. I was very fortunate for the Zoom meetings with Jonas, Rui-Peng, Rafał where I learnt a lot about their work on the trimer-dimer transition. It was great to have Paul join the project offering his expertise with Quany and make a lot of progress. I learnt a lot from long discussions in Richard's office with him and Paul.

I was extremely fortunate to learn about quantum gases, scattering and Feshbach resonances from Jook Walraven twice! Once during the HGSFP grad days and later during a very memorable time at Les Houches. Jook's enthusiasm for teaching the subject was only matched by his knowledge of the content. His ability to connect theory to experiment was unique. Every time I look at this lecture notes, I learn something new!

Groups of Matthias and Lauriane create a vibrant cold atoms presence at the PI and it has been fun interacting with them. I learnt a lot about LiCs mixtures from Manuel, Eleonora, Kilian and Michael. Manuel helped me understand p-wave resonances and lunch plans with Eleonora always led to interesting conversations about work and beyond. Discussions with Shuwei about physics and many more things have been illuminating.

Financial support from the Landesgraduiertenförderung in the form of a scholarship is gratefully acknowledged. Thanks also to the HGSFP for travel grants enabling me to attend a summer school.

The secretaries at the Institute made sure that the administrative stuff was taken care of. Thanks to Claudia keeping track of holidays, Frau. Schneyder and Alexandra for making

---

sure that I get my contracts on time. Frau. Pachomowa hat um das Timesheets gekümmert and ich möchte sie dafür bedanken.

Ich möchte auch allen Mitarbeiter\*innen des Werkstatts für ihre Unterstützung während meiner Zeit hier bedanken.

Away from work a lot of people have made sure my time in Heidelberg was enjoyable. Anna, Barbara and Mario have been family and I will cherish all the Christmases, Easters, New Years we celebrated together, the countless meals we had, board games we played, the concerts we went to and vacations together. It's only due to Anusha that I've had a vibrant social life in Heidelberg. Weekend plans with Michelle, Coco, Mukti, Seba, Melvin and Ann have been fun. Kuba's knowledge about anything was only matched by his unlimited collection of board games which we had fun playing with him and Ewa. Your departure from Heidelberg is solely missed. Lunch and dinner plans with Dorothy were fun and helped explore the restaurant scene in Heidelberg. Thanks to Sid we explored nearly authentic Indian food here. The Core and CroXY communities with their various offshoots were a fun place to hang out and was inspiration for many projects outside work. After not having visited my folks for a long time since Covid, Amma and Kru's visit were most welcome and cheered my spirits. I've been lucky to have very supportive parents and grandparents who inculcated in me the importance of curiosity and learning from a very young age. Kru has been unwavering in her support when I have been away and I never had to worry. Anusha has been a great source of strength, support and inspiration. Thanks a lot for being there for me during the happy as well as hard times!



# Bibliography

- [1] P. W. Anderson, “[More is different: Broken symmetry and the nature of the hierarchical structure of science.](#)” *Science*, vol. 177, no. 4047, pp. 393–396, 1972.
- [2] C. Chin, R. Grimm, P. Julienne, and E. Tiesinga, “[Feshbach resonances in ultracold gases,](#)” *Reviews of Modern Physics*, vol. 82, no. 2, p. 1225, 2010.
- [3] C. Gross and W. S. Bakr, “[Quantum gas microscopy for single atom and spin detection,](#)” *Nature Physics*, vol. 17, no. 12, pp. 1316–1323, 2021.
- [4] I. Bloch, J. Dalibard, and W. Zwerger, “[Many-body physics with ultracold gases,](#)” *Reviews of modern physics*, vol. 80, no. 3, p. 885, 2008.
- [5] A. Bohr, B. R. Mottelson, and D. Pines, “[Possible analogy between the excitation spectra of nuclei and those of the superconducting metallic state,](#)” *Physical Review*, vol. 110, no. 4, p. 936, 1958.
- [6] A. Bohr and B. Mottelson, *Nuclear Structure, Vol. I and II*. Benjamin Inc., Massachusetts, 1975.
- [7] S. Grebenev, J. P. Toennies, and A. F. Vilesov, “[Superfluidity within a small helium-4 cluster: The microscopic andronikashvili experiment,](#)” *Science*, vol. 279, no. 5359, pp. 2083–2086, 1998.
- [8] W. Zwerger, *The BCS-BEC crossover and the unitary Fermi gas*. Springer Science & Business Media, 2011, vol. 836.
- [9] S. Jochim, M. Bartenstein, A. Altmeyer, G. Hendl, S. Riedl, C. Chin, J. Hecker Denschlag, and R. Grimm, “[Bose-einstein condensation of molecules,](#)” *Science*, vol. 302, no. 5653, pp. 2101–2103, 2003.
- [10] M. W. Zwierlein, C. A. Stan, C. H. Schunck, S. M. Raupach, S. Gupta, Z. Hadzibabic, and W. Ketterle, “[Observation of bose-einstein condensation of molecules,](#)” *Physical review letters*, vol. 91, no. 25, p. 250 401, 2003.
- [11] M. Greiner, C. A. Regal, and D. S. Jin, “[Emergence of a molecular bose–einstein condensate from a fermi gas,](#)” *Nature*, vol. 426, no. 6966, pp. 537–540, 2003.
- [12] M. Zwierlein, C. Stan, C. Schunck, S. Raupach, A. Kerman, and W. Ketterle, “[Condensation of pairs of fermionic atoms near a feshbach resonance,](#)” *Physical Review Letters*, vol. 92, no. 12, p. 120 403, 2004.
- [13] C. Regal, M. Greiner, and D. S. Jin, “[Observation of resonance condensation of fermionic atom pairs,](#)” *Physical review letters*, vol. 92, no. 4, p. 040 403, 2004.

- [14] C. Chin, M. Bartenstein, A. Altmeyer, S. Riedl, S. Jochim, J. H. Denschlag, and R. Grimm, “[Observation of the pairing gap in a strongly interacting fermi gas](#),” *Science*, vol. 305, no. 5687, pp. 1128–1130, 2004.
- [15] A. J. Leggett, “[Cooper pairing in spin-polarized fermi systems](#),” *Le Journal de Physique Colloques*, vol. 41, no. C7, pp. C7–19, 1980.
- [16] P. Nozieres and S. Schmitt-Rink, “[Bose condensation in an attractive fermion gas: From weak to strong coupling superconductivity](#),” *Journal of Low Temperature Physics*, vol. 59, pp. 195–211, 1985.
- [17] L. N. Cooper, “[Bound electron pairs in a degenerate fermi gas](#),” *Physical Review*, vol. 104, no. 4, p. 1189, 1956.
- [18] J. Bardeen, L. N. Cooper, and J. R. Schrieffer, “[Theory of superconductivity](#),” *Physical review*, vol. 108, no. 5, p. 1175, 1957.
- [19] F. Serwane, G. Zürn, T. Lompe, T. Ottenstein, A. Wenz, and S. Jochim, “[Deterministic preparation of a tunable few-fermion system](#),” *Science*, vol. 332, no. 6027, pp. 336–338, 2011.
- [20] A. Wenz, G. Zürn, S. Murmann, I. Brouzos, T. Lompe, and S. Jochim, “[From few to many: Observing the formation of a fermi sea one atom at a time](#),” *Science*, vol. 342, no. 6157, pp. 457–460, 2013.
- [21] M. Gajda, J. Mostowski, T. Sowiński, and M. Załuska-Kotur, “[Single-shot imaging of trapped fermi gas](#),” *Europhysics Letters*, vol. 115, no. 2, p. 20 012, 2016.
- [22] F. Chen, P. W. Tillberg, and E. S. Boyden, “[Expansion microscopy](#),” *Science*, vol. 347, no. 6221, pp. 543–548, 2015.
- [23] L. Asteria, H. P. Zahn, M. N. Kosch, K. Sengstock, and C. Weitenberg, “[Quantum gas magnifier for sub-lattice-resolved imaging of 3d quantum systems](#),” *Nature*, vol. 599, no. 7886, pp. 571–575, 2021.
- [24] E. Braaten, “[Universal relations for fermions with large scattering length](#),” in *The BCS-BEC Crossover and the Unitary Fermi Gas*, Springer, 2011, pp. 193–231.
- [25] E. Gubankova, W. V. Liu, and F. Wilczek, “[Breached pairing superfluidity: Possible realization in qcd](#),” *Physical review letters*, vol. 91, no. 3, p. 032 001, 2003.
- [26] W. V. Liu and F. Wilczek, “[Interior gap superfluidity](#),” *Physical review letters*, vol. 90, no. 4, p. 047 002, 2003.
- [27] S.-T. Wu and S. Yip, “[Superfluidity in the interior-gap states](#),” *Physical Review A*, vol. 67, no. 5, p. 053 603, 2003.
- [28] P. F. Bedaque, H. Caldas, and G. Rupak, “[Phase separation in asymmetrical fermion superfluids](#),” *Physical review letters*, vol. 91, no. 24, p. 247 002, 2003.

- 
- [29] H. Caldas, “Cold asymmetrical fermion superfluids,” *Physical Review A*, vol. 69, no. 6, p. 063 602, 2004.
- [30] J. Carlson and S. Reddy, “Asymmetric two-component fermion systems in strong coupling,” *Physical review letters*, vol. 95, no. 6, p. 060 401, 2005.
- [31] B. Chandrasekhar, “A note on the maximum critical field of high-field superconductors,” *Applied Physics Letters*, vol. 1, no. 1, pp. 7–8, 1962.
- [32] A. M. Clogston, “Upper limit for the critical field in hard superconductors,” *Physical Review Letters*, vol. 9, no. 6, p. 266, 1962.
- [33] G. Sarma, “On the influence of a uniform exchange field acting on the spins of the conduction electrons in a superconductor,” *Journal of Physics and Chemistry of Solids*, vol. 24, no. 8, pp. 1029–1032, 1963.
- [34] P. Fulde and R. A. Ferrell, “Superconductivity in a strong spin-exchange field,” *Physical Review*, vol. 135, no. 3A, A550, 1964.
- [35] A. Larkin and Y. N. Ovchinnikov, “Nonuniform state of superconductors,” *Zh. Eksperim. i Teor. Fiz.*, vol. 47, 1964.
- [36] M. W. Zwierlein, C. H. Schunck, A. Schirotzek, and W. Ketterle, “Direct observation of the superfluid phase transition in ultracold fermi gases,” *nature*, vol. 442, no. 7098, pp. 54–58, 2006.
- [37] M. W. Zwierlein, A. Schirotzek, C. H. Schunck, and W. Ketterle, “Fermionic superfluidity with imbalanced spin populations,” *Science*, vol. 311, no. 5760, pp. 492–496, 2006.
- [38] G. B. Partridge, W. Li, R. I. Kamar, Y.-a. Liao, and R. G. Hulet, “Pairing and phase separation in a polarized fermi gas,” *Science*, vol. 311, no. 5760, pp. 503–505, 2006.
- [39] F. Chevy, “Universal phase diagram of a strongly interacting fermi gas with unbalanced spin populations,” *Physical Review A*, vol. 74, no. 6, p. 063 628, 2006.
- [40] L. Landau and S. Pekar, “Effective mass of a polaron,” *Zh. Eksp. Teor. Fiz*, vol. 18, no. 5, pp. 419–423, 1948.
- [41] H. Fröhlich, “Electrons in lattice fields,” *Advances in Physics*, vol. 3, no. 11, pp. 325–361, 1954.
- [42] N. Prokof’ev and B. Svistunov, “Fermi-polaron problem: Diagrammatic monte carlo method for divergent sign-alternating series,” *Physical Review B*, vol. 77, no. 2, p. 020 408, 2008.
- [43] A. Schirotzek, C.-H. Wu, A. Sommer, and M. W. Zwierlein, “Observation of fermi polarons in a tunable fermi liquid of ultracold atoms,” *Physical review letters*, vol. 102, no. 23, p. 230 402, 2009.

- [44] S. Nascimbene, N. Navon, K. Jiang, L. Tarruell, M. Teichmann, J. McKeever, F. Chevy, and C. Salomon, “Collective oscillations of an imbalanced fermi gas: Axial compression modes and polaron effective mass,” *Physical review letters*, vol. 103, no. 17, p. 170 402, 2009.
- [45] P. A. Lee, N. Nagaosa, and X.-G. Wen, “Doping a mott insulator: Physics of high-temperature superconductivity,” *Reviews of modern physics*, vol. 78, no. 1, p. 17, 2006.
- [46] M. Koschorreck, D. Pertot, E. Vogt, B. Fröhlich, M. Feld, and M. Köhl, “Attractive and repulsive fermi polarons in two dimensions,” *Nature*, vol. 485, no. 7400, pp. 619–622, 2012.
- [47] S. Zöllner, G. M. Bruun, and C. Pethick, “Polarons and molecules in a two-dimensional fermi gas,” *Physical Review A*, vol. 83, no. 2, p. 021 603, 2011.
- [48] M. M. Parish, “Polaron-molecule transitions in a two-dimensional fermi gas,” *Physical Review A*, vol. 83, no. 5, p. 051 603, 2011.
- [49] J. Levinsen and S. K. Baur, “High-polarization limit of the quasi-two-dimensional fermi gas,” *Physical Review A*, vol. 86, no. 4, p. 041 602, 2012.
- [50] J. Vlietinck, J. Ryckebusch, and K. Van Houcke, “Diagrammatic monte carlo study of the fermi polaron in two dimensions,” *Physical Review B*, vol. 89, no. 8, p. 085 119, 2014.
- [51] P. Kroiss and L. Pollet, “Diagrammatic monte carlo study of quasi-two-dimensional fermi polarons,” *Physical Review B*, vol. 90, no. 10, p. 104 510, 2014.
- [52] J. Koepsell, J. Vijayan, P. Sompet, F. Grusdt, T. A. Hilker, E. Demler, G. Salomon, I. Bloch, and C. Gross, “Imaging magnetic polarons in the doped fermi–hubbard model,” *Nature*, vol. 572, no. 7769, pp. 358–362, 2019.
- [53] L. Radzihovsky and D. E. Sheehy, “Imbalanced feshbach-resonant fermi gases,” *Reports on Progress in Physics*, vol. 73, no. 7, p. 076 501, 2010.
- [54] F. Chevy and C. Mora, “Ultra-cold polarized fermi gases,” *Reports on Progress in Physics*, vol. 73, no. 11, p. 112 401, 2010.
- [55] L. X. Bayha, “Emergence of many-body physics in two-dimensional few-fermion systems,” Ph.D. dissertation, 2020.
- [56] M. Holten, “From pauli blocking to cooper pairs: Emergence in a mesoscopic 2d fermi gas,” Ph.D. dissertation, 2022.
- [57] C. J. Foot, *Atomic physics*. OUP Oxford, 2004, vol. 7.
- [58] M. E. Gehm, “Preparation of an optically-trapped degenerate fermi gas of 6 li: Finding the route to degeneracy,” Ph.D. dissertation, 2003.

- 
- [59] E. Arimondo, M. Inguscio, and P. Violino, “[Experimental determinations of the hyperfine structure in the alkali atoms,](#)” *Reviews of Modern Physics*, vol. 49, no. 1, p. 31, 1977.
- [60] B. Shore, *The Theory of Coherent Atomic Excitation*. Taylor & Francis, 1991.
- [61] J. T. M. Walraven, *Atomic Physics*. Lecture Notes, 2023.
- [62] R. Wei and E. J. Mueller, “[Magnetic-field dependence of raman coupling in alkali-metal atoms,](#)” *Physical Review A*, vol. 87, no. 4, p. 042514, 2013.
- [63] P. Hill, *Implementation of a versatile optical phase locked loop for experiments with ultracold lithium*, Bachelor Thesis, 2018.
- [64] P. Duarte, R. Hart, J. Hitchcock, T. Corcovilos, T.-L. Yang, A. Reed, and R. Hulet, “[All-optical production of a lithium quantum gas using narrow-line laser cooling,](#)” *Physical Review A*, vol. 84, no. 6, p. 061406, 2011.
- [65] H. Feshbach, “[Unified theory of nuclear reactions,](#)” *Annals of Physics*, vol. 5, no. 4, pp. 357–390, 1958.
- [66] U. Fano, “[Effects of configuration interaction on intensities and phase shifts,](#)” *Physical review*, vol. 124, no. 6, p. 1866, 1961.
- [67] J. T. M. Walraven, *Quantum Gases*. Lecture Notes, 2019.
- [68] H. Bethe, “[Theory of the effective range in nuclear scattering,](#)” *Physical Review*, vol. 76, no. 1, p. 38, 1949.
- [69] C. Kohstall, M. Zaccanti, M. Jag, A. Trenkwalder, P. Massignan, G. M. Bruun, F. Schreck, and R. Grimm, “[Metastability and coherence of repulsive polarons in a strongly interacting fermi mixture,](#)” *Nature*, vol. 485, no. 7400, pp. 615–618, 2012.
- [70] E. Fermi, *Nuclear physics: a course given by Enrico Fermi at the University of Chicago*. University of Chicago Press, 1950.
- [71] N. R. Thomas, N. Kjærgaard, P. S. Julienne, and A. C. Wilson, “[Imaging of s and d partial-wave interference in quantum scattering of identical bosonic atoms,](#)” *Physical review letters*, vol. 93, no. 17, p. 173201, 2004.
- [72] J. Levinsen and M. M. Parish, “[Strongly interacting two-dimensional fermi gases,](#)” *Annual review of cold atoms and molecules*, pp. 1–75, 2015.
- [73] E. Tiesinga, B. Verhaar, and H. Stoof, “[Threshold and resonance phenomena in ultracold ground-state collisions,](#)” *Physical Review A*, vol. 47, no. 5, p. 4114, 1993.
- [74] G. Zürn, T. Lompe, A. N. Wenz, S. Jochim, P. Julienne, and J. Hutson, “[Precise characterization of li 6 feshbach resonances using trap-sideband-resolved rf spectroscopy of weakly bound molecules,](#)” *Physical review letters*, vol. 110, no. 13, p. 135301, 2013.

- [75] M. Holten, L. Bayha, K. Subramanian, S. Brandstetter, C. Heintze, P. Lunt, P. M. Preiss, and S. Jochim, “[Observation of cooper pairs in a mesoscopic two-dimensional fermi gas](#),” *Nature*, vol. 606, no. 7913, pp. 287–291, 2022.
- [76] [Nüevüe hnü512 datasheet](#).
- [77] A. Bergschneider, V. M. Klinkhamer, J. H. Becher, R. Klemt, G. Zürn, P. M. Preiss, and S. Jochim, “[Spin-resolved single-atom imaging of li 6 in free space](#),” *Physical Review A*, vol. 97, no. 6, p. 063613, 2018.
- [78] D. Pekker and C. Varma, “[Amplitude/higgs modes in condensed matter physics](#),” *Annu. Rev. Condens. Matter Phys.*, vol. 6, no. 1, pp. 269–297, 2015.
- [79] J. Bjerlin, S. Reimann, and G. Bruun, “[Few-body precursor of the higgs mode in a fermi gas](#),” *Physical Review Letters*, vol. 116, no. 15, p. 155302, 2016.
- [80] L. Bayha, M. Holten, R. Klemt, K. Subramanian, J. Bjerlin, S. M. Reimann, G. M. Bruun, P. M. Preiss, and S. Jochim, “[Observing the emergence of a quantum phase transition shell by shell](#),” *Nature*, vol. 587, no. 7835, pp. 583–587, 2020.
- [81] M. Holten, L. Bayha, K. Subramanian, C. Heintze, P. M. Preiss, and S. Jochim, “[Observation of pauli crystals](#),” *Physical Review Letters*, vol. 126, no. 2, p. 020401, 2021.
- [82] T. Busch, B.-G. Englert, K. Rzażewski, and M. Wilkens, “[Two cold atoms in a harmonic trap](#),” *Foundations of Physics*, vol. 28, no. 4, pp. 549–559, 1998.
- [83] Y. Chen, D.-W. Xiao, R. Zhang, and P. Zhang, “[Analytical solution for the spectrum of two ultracold atoms in a completely anisotropic confinement](#),” *Physical Review A*, vol. 101, no. 5, p. 053624, 2020.
- [84] Z. Idziaszek and T. Calarco, “[Analytical solutions for the dynamics of two trapped interacting ultracold atoms](#),” *Physical Review A*, vol. 74, no. 2, p. 022712, 2006.
- [85] G. M. Bruun, “[Long-lived higgs mode in a two-dimensional confined fermi system](#),” *Physical Review A*, vol. 90, no. 2, p. 023621, 2014.
- [86] M. C. Marchetti, J.-F. Joanny, S. Ramaswamy, T. B. Liverpool, J. Prost, M. Rao, and R. A. Simha, “[Hydrodynamics of soft active matter](#),” *Reviews of modern physics*, vol. 85, no. 3, p. 1143, 2013.
- [87] S. Sachdev, *Quantum phase transitions*. Cambridge University Press, 2011.
- [88] M. Endres, T. Fukuhara, D. Pekker, M. Cheneau, P. Schauß, C. Gross, E. Demler, S. Kuhr, and I. Bloch, “[The ‘higgs’ amplitude mode at the two-dimensional superfluid/mott insulator transition](#),” *Nature*, vol. 487, no. 7408, pp. 454–458, 2012.
- [89] D. M. Brink and R. A. Broglia, *Nuclear Superfluidity: pairing in finite systems*. Cambridge University Press, 2005.

- 
- [90] R. G. Scott, F. Dalfovo, L. Pitaevskii, and S. Stringari, “Rapid ramps across the beccs crossover: A route to measuring the superfluid gap,” *Physical Review A*, vol. 86, no. 5, p. 053 604, 2012.
- [91] G. Bruun and H. Heiselberg, “Cooper pairing and single-particle properties of trapped fermi gases,” *Physical Review A*, vol. 65, no. 5, p. 053 407, 2002.
- [92] J. J. Sakurai and E. D. Commins, *Modern quantum mechanics, revised edition*. American Association of Physics Teachers, 1995.
- [93] N. W. Ashcroft and N. D. Mermin, *Solid state physics*. Cengage Learning, 2022.
- [94] B. DeMarco and D. S. Jin, “Onset of fermi degeneracy in a trapped atomic gas,” *science*, vol. 285, no. 5434, pp. 1703–1706, 1999.
- [95] B. DeMarco, S. Papp, and D. Jin, “Pauli blocking of collisions in a quantum degenerate atomic fermi gas,” *Physical review letters*, vol. 86, no. 24, p. 5409, 2001.
- [96] A. G. Truscott, K. E. Strecker, W. I. McAlexander, G. B. Partridge, and R. G. Hulet, “Observation of fermi pressure in a gas of trapped atoms,” *science*, vol. 291, no. 5513, pp. 2570–2572, 2001.
- [97] T. Jelte, J. M. McNamara, W. Hogervorst, W. Vassen, V. Krachmalnicoff, M. Schellekens, A. Perrin, H. Chang, D. Boiron, A. Aspect, *et al.*, “Comparison of the hanbury brown–twiss effect for bosons and fermions,” *Nature*, vol. 445, no. 7126, pp. 402–405, 2007.
- [98] T. Rom, T. Best, D. Van Oosten, U. Schneider, S. Fölling, B. Paredes, and I. Bloch, “Free fermion antibunching in a degenerate atomic fermi gas released from an optical lattice,” *Nature*, vol. 444, no. 7120, pp. 733–736, 2006.
- [99] T. Müller, B. Zimmermann, J. Meineke, J.-P. Brantut, T. Esslinger, and H. Moritz, “Local observation of antibunching in a trapped fermi gas,” *Physical review letters*, vol. 105, no. 4, p. 040 401, 2010.
- [100] C. Sanner, E. J. Su, A. Keshet, R. Gommers, Y.-i. Shin, W. Huang, and W. Ketterle, “Suppression of density fluctuations in a quantum degenerate fermi gas,” *Physical review letters*, vol. 105, no. 4, p. 040 402, 2010.
- [101] A. Omran, M. Boll, T. A. Hilker, K. Kleinlein, G. Salomon, I. Bloch, and C. Gross, “Microscopic observation of pauli blocking in degenerate fermionic lattice gases,” *Physical review letters*, vol. 115, no. 26, p. 263 001, 2015.
- [102] C. Foot and M. Shotton, “Double well potentials and quantum gates,” *American Journal of Physics*, vol. 79, no. 7, pp. 762–768, 2011.
- [103] W. Heitler and F. London, “Wechselwirkung neutraler atome und homöopolare bindung nach der quantenmechanik,” *Zeitschrift für Physik*, vol. 44, no. 6-7, pp. 455–472, 1927.

- [104] A. Auerbach, *Interacting electrons and quantum magnetism*. Springer Science & Business Media, 1998.
- [105] P. M. Preiss, J. H. Becher, R. Klemt, V. Klinkhamer, A. Bergschneider, N. Defenu, and S. Jochim, “[High-contrast interference of ultracold fermions](#),” *Physical Review Letters*, vol. 122, no. 14, p. 143602, 2019.
- [106] D. Rakshit, J. Mostowski, T. Sowiński, M. Załuska-Kotur, and M. Gajda, “[On the observability of pauli crystals in experiments with ultracold trapped fermi gases](#),” *Scientific Reports*, vol. 7, no. 1, p. 15004, 2017.
- [107] N. Metropolis, A. W. Rosenbluth, M. N. Rosenbluth, A. H. Teller, and E. Teller, “[Equation of state calculations by fast computing machines](#),” *The journal of chemical physics*, vol. 21, no. 6, pp. 1087–1092, 1953.
- [108] D. J. Wineland, J. Bergquist, W. M. Itano, J. Bollinger, and C. Manney, “[Atomic-ion coulomb clusters in an ion trap](#),” *Physical review letters*, vol. 59, no. 26, p. 2935, 1987.
- [109] R. Bücker, A. Perrin, S. Manz, T. Betz, C. Koller, T. Plisson, J. Rottmann, T. Schumm, and J. Schmiedmayer, “[Single-particle-sensitive imaging of freely propagating ultracold atoms](#),” *New Journal of Physics*, vol. 11, no. 10, p. 103039, 2009.
- [110] T. Gericke, P. Würtz, D. Reitz, T. Langen, and H. Ott, “[High-resolution scanning electron microscopy of an ultracold quantum gas](#),” *Nature Physics*, vol. 4, no. 12, pp. 949–953, 2008.
- [111] M. Schellekens, R. Hoppeler, A. Perrin, J. V. Gomes, D. Boiron, A. Aspect, and C. I. Westbrook, “[Hanbury brown twiss effect for ultracold quantum gases](#),” *Science*, vol. 310, no. 5748, pp. 648–651, 2005.
- [112] W. S. Bakr, A. Peng, M. E. Tai, R. Ma, J. Simon, J. I. Gillen, S. Foelling, L. Pollet, and M. Greiner, “[Probing the superfluid-to-mott insulator transition at the single-atom level](#),” *Science*, vol. 329, no. 5991, pp. 547–550, 2010.
- [113] J. F. Sherson, C. Weitenberg, M. Endres, M. Cheneau, I. Bloch, and S. Kuhr, “[Single-atom-resolved fluorescence imaging of an atomic mott insulator](#),” *Nature*, vol. 467, no. 7311, pp. 68–72, 2010.
- [114] M. Boll, T. A. Hilker, G. Salomon, A. Omran, J. Nespolo, L. Pollet, I. Bloch, and C. Gross, “[Spin-and density-resolved microscopy of antiferromagnetic correlations in fermi-hubbard chains](#),” *Science*, vol. 353, no. 6305, pp. 1257–1260, 2016.
- [115] A. Mazurenko, C. S. Chiu, G. Ji, M. F. Parsons, M. Kanász-Nagy, R. Schmidt, F. Grusdt, E. Demler, D. Greif, and M. Greiner, “[A cold-atom fermi-hubbard antiferromagnet](#),” *Nature*, vol. 545, no. 7655, pp. 462–466, 2017.

- 
- [116] J. Koepsell, J. Vijayan, P. Sompet, F. Grusdt, T. A. Hilker, E. Demler, G. Salomon, I. Bloch, and C. Gross, “[Imaging magnetic polarons in the doped fermi-hubbard model](#),” *Nature*, vol. 572, no. 7769, pp. 358–362, 2019.
- [117] A. Bergschneider, V. M. Klinkhamer, J. H. Becher, R. Klemt, L. Palm, G. Zürn, S. Jochim, and P. M. Preiss, “[Experimental characterization of two-particle entanglement through position and momentum correlations](#),” *Nature Physics*, vol. 15, no. 7, pp. 640–644, 2019.
- [118] D. Rakshit, J. Mostowski, T. Sowiński, M. Załuska-Kotur, and M. Gajda, “[On the observability of pauli crystals in experiments with ultracold trapped fermi gases](#),” *Scientific Reports*, vol. 7, no. 1, pp. 1–11, 2017.
- [119] I. Shvarchuck, C. Buggle, D. Petrov, K. Dieckmann, M. Zielonkowski, M. Kemmann, T. Tiecke, W. Von Klitzing, G. Shlyapnikov, and J. Walraven, “[Bose-einstein condensation into nonequilibrium states studied by condensate focusing](#),” *Physical review letters*, vol. 89, no. 27, p. 270 404, 2002.
- [120] S. Tung, G. Lamporesi, D. Lobser, L. Xia, and E. A. Cornell, “[Observation of the presuperfluid regime in a two-dimensional bose gas](#),” *Physical review letters*, vol. 105, no. 23, p. 230 408, 2010.
- [121] P. Murthy, D. Kedar, T. Lompe, M. Neidig, M. Ries, A. Wenz, G. Zürn, and S. Jochim, “[Matter-wave fourier optics with a strongly interacting two-dimensional fermi gas](#),” *Physical Review A*, vol. 90, no. 4, p. 043 611, 2014.
- [122] R. Grimm, M. Weidemüller, and Y. B. Ovchinnikov, “[Optical dipole traps for neutral atoms](#),” in *Advances in atomic, molecular, and optical physics*, vol. 42, Elsevier, 2000, pp. 95–170.
- [123] R. Dubessy, C. De Rossi, T. Badr, L. Longchambon, and H. Perrin, “[Imaging the collective excitations of an ultracold gas using statistical correlations](#),” *New Journal of Physics*, vol. 16, no. 12, p. 122 001, 2014.
- [124] K. Hueck, N. Luick, L. Sobirey, J. Siegl, T. Lompe, and H. Moritz, “[Two-dimensional homogeneous fermi gases](#),” *Physical review letters*, vol. 120, no. 6, p. 060 402, 2018.
- [125] M. G. Ries, “A two-dimensional fermi gas in the bec-bcs crossover,” Ph.D. dissertation, 2015.
- [126] L. Pricoupenko and P. Pedri, “[Universal \(1+ 2\)-body bound states in planar atomic waveguides](#),” *Physical Review A*, vol. 82, no. 3, p. 033 625, 2010.
- [127] M. W. Zwierlein, “High-temperature superfluidity in an ultracold fermi gas,” Ph.D. dissertation, Massachusetts Institute of Technology, 2006.
- [128] S. Tan, “[Large momentum part of a strongly correlated fermi gas](#),” *Annals of Physics*, vol. 323, no. 12, pp. 2971–2986, 2008.

- [129] S. Tan, “Energetics of a strongly correlated fermi gas,” *Annals of Physics*, vol. 323, no. 12, pp. 2952–2970, 2008.
- [130] S. Tan, “Generalized virial theorem and pressure relation for a strongly correlated fermi gas,” *Annals of Physics*, vol. 323, no. 12, pp. 2987–2990, 2008.
- [131] G. B. Partridge, K. E. Strecker, R. I. Kamar, M. W. Jack, and R. G. Hulet, “Molecular probe of pairing in the bec-bcs crossover,” *Physical Review Letters*, vol. 95, no. 2, p. 020 404, 2005.
- [132] G. Veeravalli, E. Kuhnle, P. Dyke, and C. Vale, “Bragg spectroscopy of a strongly interacting fermi gas,” *Physical review letters*, vol. 101, no. 25, p. 250 403, 2008.
- [133] J. Stewart, J. Gaebler, T. Drake, and D. Jin, “Verification of universal relations in a strongly interacting fermi gas,” *Physical Review Letters*, vol. 104, no. 23, p. 235 301, 2010.
- [134] M. M. Parish and J. Levinsen, “Highly polarized fermi gases in two dimensions,” *Physical Review A*, vol. 87, no. 3, p. 033 616, 2013.
- [135] Y.-a. Liao, A. S. C. Rittner, T. Paprotta, W. Li, G. B. Partridge, R. G. Hulet, S. K. Baur, and E. J. Mueller, “Spin-imbalance in a one-dimensional fermi gas,” *Nature*, vol. 467, no. 7315, pp. 567–569, 2010.
- [136] D. Peçak and T. Sowiński, “Signatures of unconventional pairing in spin-imbanced one-dimensional few-fermion systems,” *Physical Review Research*, vol. 2, no. 1, p. 012 077, 2020.
- [137] L. Rammelmüller, J. E. Drut, and J. Braun, “Pairing patterns in one-dimensional spin-and mass-imbanced fermi gases,” *SciPost Physics*, vol. 9, no. 1, p. 014, 2020.
- [138] F. Scazza, G. Valtolina, P. Massignan, A. Recati, A. Amico, A. Burchianti, C. Fort, M. Inguscio, M. Zaccanti, and G. Roati, “Repulsive fermi polarons in a resonant mixture of ultracold li 6 atoms,” *Physical review letters*, vol. 118, no. 8, p. 083 602, 2017.
- [139] G. Ness, C. Shkedrov, Y. Florshaim, O. K. Diessel, J. von Milczewski, R. Schmidt, and Y. Sagi, “Observation of a smooth polaron-molecule transition in a degenerate fermi gas,” *Physical Review X*, vol. 10, no. 4, p. 041 019, 2020.
- [140] J. Koepsell, D. Bourgund, P. Sompert, S. Hirthe, A. Bohrdt, Y. Wang, F. Grusdt, E. Demler, G. Salomon, C. Gross, *et al.*, “Microscopic evolution of doped mott insulators from polaronic metal to fermi liquid,” *Science*, vol. 374, no. 6563, pp. 82–86, 2021.
- [141] C. S. Chiu, G. Ji, A. Bohrdt, M. Xu, M. Knap, E. Demler, F. Grusdt, M. Greiner, and D. Greif, “String patterns in the doped hubbard model,” *Science*, vol. 365, no. 6450, pp. 251–256, 2019.

- 
- [142] O. K. Diessel, J. von Milczewski, A. Christianen, and R. Schmidt, “Probing molecular spectral functions and unconventional pairing using raman spectroscopy,” *arXiv preprint arXiv:2209.11758*, 2022.
- [143] C. J. Mathy, M. M. Parish, and D. A. Huse, “Trimers, molecules, and polarons in mass-imbalanced atomic fermi gases,” *Physical review letters*, vol. 106, no. 16, p. 166 404, 2011.
- [144] D. Petrov, C. Salomon, and G. Shlyapnikov, “Scattering properties of weakly bound dimers of fermionic atoms,” *Physical Review A*, vol. 71, no. 1, p. 012 708, 2005.
- [145] R. Li, J. von Milczewski, A. Imamoglu, R. Ołdziejewski, and R. Schmidt, “Impurity-induced pairing in two-dimensional fermi gases,” *arXiv preprint arXiv:2211.12495*, 2022.
- [146] F. Mintert and C. Wunderlich, “Ion-trap quantum logic using long-wavelength radiation,” *Physical Review Letters*, vol. 87, no. 25, p. 257 904, 2001.
- [147] C. Ospelkaus, C. E. Langer, J. M. Amini, K. R. Brown, D. Leibfried, and D. J. Wineland, “Trapped-ion quantum logic gates based on oscillating magnetic fields,” *Physical review letters*, vol. 101, no. 9, p. 090 502, 2008.
- [148] S. Gupta, Z. Hadzibabic, M. Zwierlein, C. Stan, K. Dieckmann, C. Schunck, E. Van Kempen, B. Verhaar, and W. Ketterle, “Radio-frequency spectroscopy of ultracold fermions,” *Science*, vol. 300, no. 5626, pp. 1723–1726, 2003.
- [149] Z. Yan, P. B. Patel, B. Mukherjee, R. J. Fletcher, J. Struck, and M. W. Zwierlein, “Boiling a unitary fermi liquid,” *Physical Review Letters*, vol. 122, no. 9, p. 093 401, 2019.
- [150] P. Massignan, M. Zaccanti, and G. M. Bruun, “Polarons, dressed molecules and itinerant ferromagnetism in ultracold fermi gases,” *Reports on Progress in Physics*, vol. 77, no. 3, p. 034 401, 2014.
- [151] K. Kinjo, M. Manago, S. Kitagawa, Z. Mao, S. Yonezawa, Y. Maeno, and K. Ishida, “Superconducting spin smecticity evidencing the fulde-ferrell-larkin-ovchinnikov state in  $\text{Sr}_2\text{RuO}_4$ ,” *Science*, vol. 376, no. 6591, pp. 397–400, 2022.
- [152] L. Corman, P. Fabritius, S. Häusler, J. Mohan, L. H. Dogra, D. Husmann, M. Lebrat, and T. Esslinger, “Quantized conductance through a dissipative atomic point contact,” *Physical Review A*, vol. 100, no. 5, p. 053 605, 2019.
- [153] Y. Nishida and D. T. Son, “Nonrelativistic conformal field theories,” *Physical Review D*, vol. 76, no. 8, p. 086 004, 2007.
- [154] P. K. Kovtun, D. T. Son, and A. O. Starinets, “Viscosity in strongly interacting quantum field theories from black hole physics,” *Physical review letters*, vol. 94, no. 11, p. 111 601, 2005.

- [155] D. Son, “[Vanishing bulk viscosities and conformal invariance of the unitary fermi gas,](#)” *Physical review letters*, vol. 98, no. 2, p. 020 604, 2007.
- [156] T. Enss, R. Haussmann, and W. Zwerger, “[Viscosity and scale invariance in the unitary fermi gas,](#)” *Annals of Physics*, vol. 326, no. 3, pp. 770–796, 2011.
- [157] M. Holten, L. Bayha, A. C. Klein, P. A. Murthy, P. M. Preiss, and S. Jochim, “[Anomalous breaking of scale invariance in a two-dimensional fermi gas,](#)” *Physical review letters*, vol. 121, no. 12, p. 120 401, 2018.
- [158] T. Peppler, P. Dyke, M. Zamorano, I. Herrera, S. Hoinka, and C. Vale, “[Quantum anomaly and 2d-3d crossover in strongly interacting fermi gases,](#)” *Physical review letters*, vol. 121, no. 12, p. 120 402, 2018.
- [159] V. Bekassy and J. Hofmann, “[Nonrelativistic conformal invariance in mesoscopic two-dimensional fermi gases,](#)” *Physical Review Letters*, vol. 128, no. 19, p. 193 401, 2022.